ABSTRACT

Title of dissertation: A STRAIN-BASED EXPERIMENTAL METHODOLOGY FOR MEASURING SECTIONAL STIFFNESS PROPERTIES OF COMPOSITE BLADES

Tyler Sinotte
Doctor of Philosophy, 2020

Dissertation directed by: Professor Olivier Bauchau
Department of Aerospace Engineering

Sectional stiffness properties of composite rotor blades, such as the axial, torsional, and bending stiffness, play an important role in the design and analysis of rotorcraft, as they impact the predicted rotor dynamics, structural loads, and stress and strain fields. Multiple numerical tools exist for predicting the sectional stiffness properties based on the cross-sectional geometries and materials; however, rotor blades are often made of composite materials and require complex manufacturing procedures, making it challenging to provide an accurate prediction of the inputs needed for these numerical tools. This dissertation therefore focuses on developing an experimental technique for calculating the sectional stiffness properties, based on the measurement of a detailed strain field using digital image correlation.

Two primary features distinguish the developed methodology from currently existing techniques. First, this method is based upon measured strain fields, as opposed to measurements of displacements or frequencies that are traditionally used. The strain field provides a description of the local deformation of the blades, thereby allowing measurements of the sectional stiffness properties to be made at discrete spanwise locations along the blade and providing the capability to predict

changes in properties due to features commonly associated with helicopter rotors, such as twist or taper. Second, this method can be used to calculate the full cross-sectional stiffness matrix based on a combination of experimental measurements and a numerical warping function, as opposed to only a subset of these properties that are typically measured in displacement or frequency based approaches.

The developed methodology is first validated using numerical results from 3-D FEA for cross-sections that have received extensive study in literature. A test setup is then developed for experimental implementation of the proposed method and applied to five different beams. The material properties and geometries of these beams were selected to place an emphasis on the unique capabilities of the method, including the measurement of elastic coupling stiffness components and spanwise variations in the stiffness properties, with results compared against analytic solutions and predictions from *SectionBuilder*. A detailed uncertainty analysis is also implemented for estimating the impact of measurement errors on the stiffness properties.

A STRAIN-BASED EXPERIMENTAL METHODOLOGY FOR MEASURING SECTIONAL STIFFNESS PROPERTIES OF COMPOSITE BLADES

by

Tyler Mel Sinotte

Dissertation submitted to the Faculty of the Graduate School of the
University of Maryland, College Park in partial fulfillment
of the requirements for the degree of
Doctor of Philosophy
2020

Advisory Committee:
Professor Olivier A Bauchau, Chair/Advisor
Professor James Baeder
Professor Inderjit Chopra
Professor Anubhav Datta
Professor Peter W. Chung, Dean's Representative

Dedication

To my family for their love and support throughout my academic journey.

Acknowledgments

My PhD research has not been a sole endeavor and I would have never reached this point without the help, guidance, and support of many individuals. First and foremost, I would like to thank my PhD advisor, Dr. Olivier A. Bauchau, for giving me the opportunity to work on a challenging and interesting project. His wealth of knowledge in structures and rotorcraft has been invaluable and he has guided me at many points throughout my research. I would also like to thank the other members of my committee Dr. James Baeder, Dr. Inderjit Chopra, Dr. Anubhav Datta, and Dr. Peter Chung for their expertise and guidance throughout my graduate school career. Their insights have been extremely helpful in the formulation of this dissertation and their classes have proven instrumental in providing me with a solid understanding of structural analysis and rotorcraft. I would also like to specifically thank Dr. Chopra for his effort in recruiting me to come to the University of Maryland, despite the fact that I had no previous experience in the field of rotorcraft.

This work would not have been possible without the financial support of the U.S. Army Aviation Development Directorate (ADD) Vertical Lift Research Center of Excellence (VLRCOE) under cooperative agreement W911W6-17-2-0004 and the UMD Clark doctoral fellowship program. The VLRCOE yearly reviews served as great progress checks throughout my studies and I would especially like to thank Dr. Mahendra Bhagwat (Program Manager and Technical Agent), Dr. Will Staruk, and Dr. Joon Lim for their contributions and feedback.

My educational experience at UMD would not have been nearly as smooth without the many staff and senior students who took the time to help me. Dr. VT Nagaraj is owed many thanks for the countless times he was willing to listen to me and provide guidance when something wasn't working in my research. The aerospace staff members, Otto, Laura, LaVita, Gabby, Tom, Matt, and Leslie, among others, are also owed thanks for always staying on top of things such as placing orders for

any parts needed in my experiments or making sure I had all the correct paperwork filled out. Thank you to the senior students in the cube farm, Will, Elizabeth, and Joe among others, for getting me familiar with UMD when I first arrived and providing guidance on courses. A special thanks to my fellow labmates within Dr. Bauchau's group. Valentin and Alfonso, and more recently Matteo, Giuseppe, and Minghe, provided much needed guidance and friendship throughout this research. Nishant, Sheng-wei, Shilei, Ray, and Andrew were always willing to sit through my presentations and were supportive and helpful whenever I ran into problems. Several other students, such as Amy, James, Jon, and Lex are also owed many thanks for their guidance in manufacturing the various test articles, particularly for assistance in making the composite blades.

Thank you to all my cube farm and aerospace friends from throughout the years, there are too many of you to list, but you have really made Maryland feel like a second home and I will greatly miss our interactions. The intramural sports teams provided a much needed reprieve from research and helped forge many friendships. A special thanks to Emily, Katie, Laura, and Wanyi – I have been fortunate to have you as both friends and roommates at various points over the past several years. I would also like to specifically thank Bharath, Brandyn, Dan, and Dylan, whose friendship since I first arrived at Maryland provided many much needed breaks, whether it was the hiking and camping trips, getting together to play games, or just hanging out.

Last, but certainty not least, I would like to thank my family. Mom, Dad, Holly, Shaun, and Breanna, you have always been there for me and I would never have made it this far without your love and support. My parents are my role models and have always been there for me throughout more than two decades of school. I will never forget all the sacrifices you have made to help me get to where I am today and I hope to have made you proud.

Table of Contents

List of Tables

List of Figures

List of Abbreviations

BECAS	Beam Cross Section Analysis Software
CAMRAD	Comprehensive Analytical Model of Rotor Aerodynamics and Dynamics
CCD	Charge-Coupled Device
CFD	Computational Fluid Dynamics
CMOS	Complementary Metal-Oxide-Semiconductor
DIC	Digital Image Correlation
ESPI	Electronic Speckle Pattern Interferometry
FEA	Finite Element Analysis
FEM	Finite Element Method
FFT	Fast Fourier Transform
HART	Higher harmonic control Aeroacoustics Rotor Test
MCM	Monte Carlo Method
NACA	National Advisory Committee for Aeronautics
PMI	Projection Moiré Interferometry
RCAS	Rotorcraft Comprehensive Analysis System
SVD	Singular Value Decomposition
TRAM	Tilt Rotor Aeroacoustic Model
TSM	Taylor Series Method
UMARC	University of Maryland Advanced Rotorcraft Code
VABS	Variational Asymptotic Beam Sectional analysis
VAM	Variational Asymptotic Method
X3D	Experimental 3-D Dynamic solver

Chapter 1: Introduction

1.1 Motivation

The design and analysis of rotorcraft is primarily governed by the aeromechanic behavior of the rotor, including aerodynamics, structural dynamics, and stability and control. For rotorcraft, these disciplines are strongly coupled and an accurate model is required for each to accurately predict the response of the rotor. The earliest aerodynamic models were first developed by Glauert in 1926 [2] which introduced blade element theory for rotorcraft; since then, a variety of aerodynamics models have been developed for application to rotorcraft. These aerodynamics models range from simple steady 2-D linear airfoil theory, to full unsteady models, to 3-D computational fluid dynamics (CFD), with extensive work done to account for the unique rotorcraft aerodynamic environment, such as treatment of dynamic stall, in which flow separation is delayed beyond the expected angle of attack from static flow conditions due to the dynamic pitching of the aircraft, as well as treatment of non-uniform inflow, through dynamic inflow models and more accurate free-wake models.

For the structural dynamics analysis, the blades are conventionally modeled using beam theory, as rotor blades typically have a much greater radial dimension than the cross-sectional dimensions. The use of beam theory to model the blades requires sectional stiffness properties, such as the bending and torsional stiffness, as well as sectional mass properties, which are both typically predicted through numerical

analysis. The aerodynamics and structural dynamics models are then coupled together to study the aeromechanic behavior of the rotorcraft using a comprehensive analysis, which also incorporates vehicle trim to determine the controls needed to maintain a steady flight and to predict the blade deformations, airloads, and rotor performance in desired flight conditions.

While the capabilities of comprehensive analysis codes have greatly improved over the past several decades, particularly with the coupling of CFD with comprehensive analysis [3], there is still a large amount of uncertainty in the sectional stiffness properties for composite blades, which play a pivotal role in the accuracy of comprehensive analysis. Since the blades are typically made of anisotropic materials and present complex cross-sectional geometries that require complicated manufacturing procedures, the accurate prediction of their stiffness properties using numerical tools can often be quite challenging. Recent numerical studies have shown the importance that uncertainties in the sectional stiffness properties can have on the analysis. Using a Monte-Carlo analysis, Murugan et al. [4] showed the effect of random uncertainty in the stiffness properties of a BO-105 rotor on the vibratory hub loads, with up to a 400% variations from baseline values. Pfumm et al. [5] performed a similar study for a UH-60A rotor, which showed up to 12% variations on the elastic blade deflections in hover and up to 200% variations in vibratory hub forces in forward flight from their respective baselines.

Because of these uncertainties, it is not uncommon to arbitrarily adjust the predicted blade stiffness properties to better match experimental data; for example, Yeo and Johnson [6] found that it was necessary to reduce the predicted flap bending, chord bending, and torsional stiffness values of the scaled BO-105 blade by 10% to match the measured nonrotating natural frequencies. While these adjustments can lead to a satisfactory prediction of the rotor dynamics, inaccuracies in other rotor component models such as the blade grips or control system components may be the

actual cause of the discrepancies between the predicted and measured results, which can still lead to inaccuracies in structural and vibratory loads and the resulting stress and strain fields that are critical for the design and analysis of the rotor.

Ultimately, there is a dearth of structural data for actual composite rotor blades, in spite of its importance for comprehensive analysis. Publicly available stiffness properties for actual helicopter blades is limited to a few rotors, such as the H-34 [7], Puma [8], SA 349/2 [9], UH-60A [10–12], and the BO-105 (HART-I and HART-II) [13, 14], with only the BO-105 model containing experimental measurements in addition to numerical predictions. Even in these cases, the properties are limited to the axial, torsional, flap bending, and lag bending stiffness at best, which represents only a subset of the full sectional stiffness characterization. Due to this lack of available structural data, the overall objective of this research is to develop a new experimental method that can provide a more complete measurement of the sectional stiffness properties, so that numerical analysis tools can be used more confidently.

1.2 Rotor Structural Modeling

The response of a helicopter in flight is often computed using comprehensive analysis, which couples the rotor aerodynamics and structural dynamics with the full vehicle flight dynamics and controls [15, 16]. While the aerodynamics and vehicle flight dynamics and controls are critical components of a comprehensive analysis, this dissertation primarily focuses on the structural modeling and properties of the blade, which are discussed in the subsequent sections.

1.2.1 Review of 3-D Beam Theory

Beam theory is widely used in the analysis of aerospace structures and specifically in rotorcraft analysis. For a structure to be defined as a beam, it must have one

of its characteristic dimensions significantly larger than the other two. A depiction of a typical helicopter blade is shown in Fig. 1.1; typically the ratio of the radial dimension R to the chord c, referred to as the aspect ratio, is on the order of 12 to 16 for a rotor blade, thereby making it well suited to be analyzed as a beam. Ultimately, the aim of beam theory is to solve Saint-Venant's problem, which refers to the problem of determining elastic deformations of a three-dimensional beam loaded at its end sections only. The earliest solutions to this problem were by Saint-Venant, who derived exact elasticity solutions for these beams under torsion [17] and bending [18].

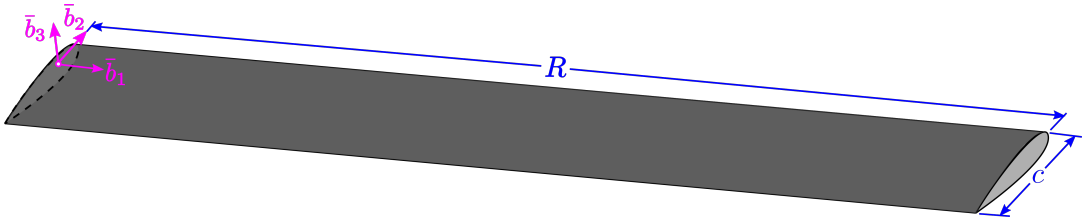

Figure 1.1: Representative rotor blade.

One of the simplest and most well-known beam theories is the Euler-Bernoulli beam theory; three underlying assumptions of this theory are that *(1)* there are no deformations in the plane of the cross-section, *(2)* the cross-section remains planar after deformation, and *(3)* the cross-section remains normal to the deformed axis of the beam. Under these assumptions, the displacements can be represented as rigid-body translations and rotations which lead to a simple kinematic description of the displacements and strains. These can then be combined with the constitutive laws and the equilibrium equations to give the following relationships

$$\begin{Bmatrix} F_1(x) \\ M_2(x) \\ M_3(x) \end{Bmatrix} = \begin{bmatrix} K_{11} & K_{15} & K_{16} \\ K_{15} & K_{55} & K_{56} \\ K_{16} & K_{56} & K_{66} \end{bmatrix} \begin{Bmatrix} \bar{\epsilon}_1(x) \\ \kappa_2(x) \\ \kappa_3(x) \end{Bmatrix} \tag{1.1}$$

where $\bar{\epsilon}_1(x)$ is the sectional axial strain, $\kappa_2(x)$ and $\kappa_3(x)$ are the sectional curvatures about axis $\bar{b}_2$ and $\bar{b}_3$ respectively, and $F_1(x)$, $M_2(x)$, and $M_3(x)$ are the axial force

and bending moments about axis $\bar{b}_2$ and $\bar{b}_3$, respectively. The K_{ij} terms are the sectional stiffness properties, whose measurement are the objective of this thesis. For an uncoupled beam the off-diagonal stiffness properties become zero leaving the axial stiffness, K_{11}, the bending stiffness about $\bar{b}_2$, K_{55}, and the bending stiffness about $\bar{b}_3$, K_{66}. In rotorcraft applications, K_{55} and K_{66} are commonly referred to as the flap bending and lag bending stiffnesses, respectively.

The beam formulation developed by Timoshenko [19], commonly referred to as Timoshenko beam theory, relaxed the third assumption from the Euler-Bernoulli beam theory that the cross-section must remain perpendicular to the beam axis, meaning that transverse shear deformation was taken into account and no longer considered negligible. In addition to the three equilibrium equations from Euler-Bernoulli beam theory, this gave rise to two more equilibrium equations

$$\begin{Bmatrix} F_2(x) \\ F_3(x) \end{Bmatrix} = \begin{bmatrix} K_{22} & 0 \\ 0 & K_{33} \end{bmatrix} \begin{Bmatrix} \bar{\gamma}_{12}(x) \\ \bar{\gamma}_{13}(x) \end{Bmatrix} \tag{1.2}$$

where $\bar{\gamma}_{12}(x)$ and $\bar{\gamma}_{13}(x)$ are the sectional shear strains and $F_2(x)$ and $F_3(x)$ are the shear forces in the $\bar{b}_2$ and $\bar{b}_3$, respectively. This provides two additional stiffness properties, K_{22} and K_{33}, which are the shear stiffness in directions $\bar{b}_2$ and $\bar{b}_3$, respectively. Finally, the constitutive law for the torsional behavior of the beam is

$$M_1(x) = K_{44}\kappa_1(x) \tag{1.3}$$

where $\kappa_1(x)$ is the sectional twist rate, $M_1(x)$ is the torque, and K_{44} is the torsional stiffness.

While Euler-Bernoulli beam theory and Timoshenko beam theory provide a useful basis for the analysis of beams, it is important to have a beam theory that unifies all aspects of the deformation – the axial and bending, shear, and torsional –

into a single system of equations. One of the key steps in having a more complete structural theory was the development of a beam theory for heterogeneous and anistropic materials. Ieşan [20, 21] developed a method to obtain the solutions of Saint-Venant's problem for straight beams made of heterogeneous materials. Dong et al. [22–24] then generalized Iesan's method using a semi-finite element discretization for the cross-section, while calculating both the warping displacements and sectional properties of the beam.

The next advancements in a unified beam theory came through the Variational Asymptotic Method (VAM) pioneered by Berdichevsky [25], in which asymptotic analysis is applied to the energy functional. In this approach, the three-dimensional Saint-Venant's problem is reduced to a two-dimensional analysis over the beam's cross-section and a one-dimensional analysis of the nonlinear beam equations. Further refinements to this method were then made by Atilgan et al. [26,27], Hodges [28], Yu et al. [29], and Kim et al. [30] to deal with beams with small initial curvatures and made of anisotropic, composite materials and to account for end effects. These refinements ultimately lead to a 6×6 sectional stiffness matrix defining the cross-section.

An alternative to the variational asymptotic method is an approach first developed by Giavotto et al. [31] for beams with arbitrary cross-sectional geometry and material properties. In this approach, two types of solutions for Saint-Venant's problem are identified: the central solution, which defines the behavior through the entire length of the beam, and extremity solutions, which decay exponentially away from the boundaries. Taking the central solutions into account leads to a two-dimensional analysis of the beam's cross-section using finite elements which also yields a 6×6 sectional stiffness matrix. Furthermore, this approach allows the three-dimensional stress and strain fields to be evaluated at any point in the cross-section once the sectional deformations – the sectional axial and shear strains and three curvatures – are known. This approach was further refined by Borri

et al. [32, 33] to introduce the concept of intrinsic warping and also generalized to initially curved and twisted beams, where the magnitudes of the beam's initial curvatures are not required to be small.

Additional refinements have been made over the past several decades to the method initially proposed by Giavotto. Mielke [34, 35] found the center manifold of Saint-Venant's problem for a straight beam and showed that it is a finite-dimensional manifold spanned by twelve generalized eigenvectors associated with the null and purely imaginary eigenvalues. Six of the modes correspond to the rigid-body modes of the beam and the other six correspond to the fundamental deformation modes of the beam (extension, shearing, torsion, and bending). Zhong [36] then developed a novel analytical technique based on Hamilton's formalism and showed that the null and purely imaginary eigenvalues of the Hamiltonian operator give rise to the solution of Saint-Venant's problem. He later produced analytical solutions for planar elasticity problems and three-dimensional straight beams made of anisotropic materials in which he outlined procedures for determining the twelve generalized eigenvectors [37].

More recently, Morandini et al. [38] developed a similar approach based on Hamilton's formalism using numerical techniques to evaluate the generalized eigenvectors for straight beams made of both isotropic and anisotropic materials. Druz et al. [39, 40] then accounted for naturally twisted beams and obtained a sectional stiffness matrix relating the components of the generalized forces and displacement. Bauchau and Han [41] then developed an approach based on Hamilton's formalism that decomposes the solution into its central and extremity components through a sequence of structure preserving transformations using symplectic matrices. This leads to a set of linear equations for the nodal warping and sectional compliance matrix whose solutions are found by projecting the governing equations onto the subspace associated with the Hamiltonian matrix's null and purely imaginary eigenvalues. Bauchau and Han [42] then further generalized the approach to initially

curved beams undergoing large motion but small strains.

1.2.2 Review of Rotorcraft Beam Analysis

The previous section discussed the development of beam theory in a general sense; the application of beam theory to rotorcraft analysis, and specifically the rotor itself, is further discussed in this section. The earliest use of beam theory for rotorcraft analysis was in the NACA technical report in 1957 by Houbolt and Brooks [43], which formulated linearized equations of motion for elastic blades while accounting for the coupling between flap and lag bending and torsional deformation. This was followed up by a general nonlinear beam formulation (accurate up to the second-order) by Hodges and Dowell in 1974 for the coupled flap/lag/torsion dynamics of rotor blades [44]. Subsequent efforts over the next decade primarily focused on consideration of higher-order terms and exact beam kinematics, including work by Rosen and Friedmann [45] and Hodges et al. [46, 47].

While these efforts were comprehensive in studying the structural response of a helicopter rotor, they relied on Euler-Bernoulli formulations for isotropic materials. However, the use of composite materials in rotor blades was starting to become common by the 1980s and the development of beam models for anisotropic materials was required. Some of the earliest developments of an anistropic beam theory for rotorcraft applications occurred in the late 1980s and early 1990s, including efforts by Bauchau [48] to develop a beam theory for anisotropic materials; Bauchau and Hong [49] to develop a nonlinear composite beam theory that included warping effects and elastic couplings; Hodges [50] to apply variational principles to anisotropic beams with closed cross-sections and unrestrained warping, and Smith and Chopra [51] to develop an analysis for blades with elastic couplings. A more complete summary of the development of nonlinear composite beam theory and its applications to rotorcraft can be found in the book "Nonlinear Composite Beam Theor" by Hodges [28].

The final key challenge in applying beam theory to rotorcraft was the inclusion of a multibody dynamics formulation. Helicopter rotors often incorporate kinematic mechanisms to connect various flexible components and control the blades, with multibody dynamics playing a particularly important role in advanced concepts such as tiltrotors, where the rotor and wing have strong interactions, as well as coaxial rotor systems. One of the earliest efforts was performed by Bauchau and Kang in 1993 [52], who presented a multibody formulation for the nonlinear dynamic analysis of a helicopter rotor and considered the ground resonance problem. Since then, multibody dynamics have become commonplace in rotorcraft analysis and the combination of these key features, a finite element based beam theory for anisotropic materials and flexible multibody dynamics analysis, has lead to the current state-of-the-art in rotorcraft comprehensive analysis tools, including *Dymore* [53], CAMRAD II [54], RCAS [55], and UMARC [56].

1.2.3 Cross-sectional Analysis

As previously described in Sec 1.2.1, the 3-D Saint-Venant's problem can be reduced into a 2-D cross-sectional analysis and 1-D system of nonlinear equations using either the variational asymptotic method (VAM) or the approach pioneered by Giavotto et al. [31]. In both cases, the 2-D cross-sectional analysis is performed using a finite element model on a cross-section whose geometry and material can be arbitrary (heterogeneous and anisotropic), to obtain sectional stiffness matrices. The sectional stiffness matrix $\underline{\underline{K}}$ provides a means of relating the sectional stress resultants $\underline{\mathcal{F}}$ to the sectional deformation measures $\underline{\mathcal{E}}$ according to

$$\underline{\mathcal{F}} = \underline{\underline{K}}\,\underline{\mathcal{E}} \tag{1.4}$$

The sectional stress resultants is the vector of forces and moments defined by $\underline{\mathcal{F}}^T = \{F_1, F_2, F_3, M_1, M_2, M_3\}^T$, where F_1 denotes the axial forces and F_2 and F_3 denote the two shear forces while M_1 denotes the torque and M_2 and M_3 the two bending moments. The sectional deformation measures is the vector of sectional strains and curvatures defined by $\underline{\mathcal{E}}^T = \{\bar{\epsilon}_{11}, \bar{\gamma}_{12}, \bar{\gamma}_{13}, \kappa_1, \kappa_2, \kappa_3\}^T$, where $\bar{\epsilon}_{11}$ is the sectional axial strain and $\bar{\gamma}_{12}$ and $\bar{\gamma}_{13}$ are the sectional shear strains while κ_1, κ_2 and κ_3 are the curvatures about their respective axes. The sectional stiffness matrix is a symmetric, 6×6 matrix of the form

$$\underline{\underline{K}} = \begin{bmatrix} K_{11} & K_{12} & K_{13} & K_{14} & K_{15} & K_{16} \\ K_{12} & K_{22} & K_{23} & K_{24} & K_{25} & K_{26} \\ K_{13} & K_{23} & K_{33} & K_{34} & K_{35} & K_{36} \\ K_{14} & K_{24} & K_{34} & K_{44} & K_{45} & K_{46} \\ K_{15} & K_{25} & K_{35} & K_{45} & K_{55} & K_{56} \\ K_{16} & K_{26} & K_{36} & K_{46} & K_{56} & K_{66} \end{bmatrix} \tag{1.5}$$

where the subscripts 1 through 6 correspond to the extension, shear about axis $\bar{b}_2$, shear about axis $\bar{b}_3$, torsion, bending about axis $\bar{b}_2$, and bending about axis $\bar{b}_3$, respectively. Any term with mixed subscripts (*i.e.* K_{ij} where $i \neq j$) represents a coupling between the deformation modes of the beam; in the case that no coupling is present, the stiffness matrix becomes diagonal and reduces to the simple expressions discussed in Sec 1.2.1.

Once determined, either through measurement or numerically, the sectional stiffness matrices can then be used as an input to the comprehensive analysis codes and the resulting sectional forces and moments can be reapplied to the 2-D cross-sectional models to predict the 3-D stress and strain distributions. For numerical calculations, the engineering software variational asymptotic beam sectional analysis (VABS) developed by Hodges et al. [57–59] provides a cross-sectional modeling

capability using the variational asymptotic method. For the approach pioneered by Giavotto, the software *SectionBuilder* developed by Bauchau et al. [60, 61] is commonly used, with the beam cross section analysis software (BECAS) [62] also used in the wind turbine industry.

1.2.4 Advanced Rotor Analysis

Most conventional rotor blades are primarily straight and consist of quasi-isotropic layups making them well suited for analysis using the beam theories implemented in comprehensive analysis codes; however, advanced designs that can also be treated with beam theory have received considerable attention, particularly blades that are elastically tailored to introduce coupling between deformation modes as well as curved and twisted blades. Early work by Mansfield and Sobey [63] and Winkler [64] showed that through a careful selection of the composite layup, elastically tailored blades can be designed to introduce extension/torsion coupling (*i.e.* a non-zero K_{14} stiffness component) when using an antisymmetric ply sequence or to introduce bending/torsion coupling (*i.e.* non-zero K_{45} and K_{46} stiffness components) when using a symmetric ply sequence.

Extension/torsion coupling is of considerable interest in rotorcraft and specifically for tilt-rotors. Tilt-rotors operate at two different rotational speeds, one for hover and another for cruise, and have substantially different optimal twist distributions for each flight mode. Since the rotational environment of the rotor generates significant extensional loads due to the centrifugal forces, extension-torsion coupling can be utilized to provide a more optimal twist distribution for the rotor in both operational conditions. Early application of extension/torsion coupling to a tiltrotor analysis was performed in 1986 by Bauchau et al. [65] which considered two rotor designs that matched baseline XV-15 stiffness properties but still provided passive twist change through extension-torsion coupling. Smith and Chopra [66] in 1991

then formulated an analytical model for elastically tailored composite box-beams, including prediction of a full 6×6 stiffness matrix, which was correlated with experimental displacement measurements of elastically tailored box beams from Chandra, Stemple, and Chopra [67]. Significant research since then has focused on the structural analysis of blades with extension-torsion coupling, including by Soykasap and Hodges [68], Ozbay et al. [69], and Haynes and Armanios [70], as well as experimental measurements using an articulated NACA0012 model rotor by Lake et al. [71].

Bending/torsion coupling, in which bending deformation introduces a change in twist, has also been studied both for rotorcraft and wind turbine applications. For rotorcraft, Bao and Chopra [72, 73] performed a study using UMARC and correlated with experiments for five rotors with composite couplings, showing that bending/torsion coupling could provide notable reductions to vibratory hub loads. For wind turbines, Fedorov and Berggreen [74] used an Euler-Bernoulli beam formulation and the cross-sectional analysis BECAS to study bending/torsion coupling and correlated with experimental results for composite beams. Stablein [75] also considered bend-twist coupling using a Timoshenko beam element and showed that the coupling should only be included in certain regions of the blade to ensure tower clearance is maintained.

While most studies introduce structural coupling by elastic tailoring of the ply layups, these effects can also be introduced through implementation of twist or curvature in the blades, known as geometric coupling. An early study in 1987 by Bauchau and Hong [76] presented a nonlinear beam analysis for initially curved and twisted beams and correlated the tip displacements arising from the geometric couplings with analytical and experimental solutions. In 1994, Cesnik and Hodges [77] extended the variational asymptotical method to consider initially curved and twisted composite beams and showed the importance of accounting for the curvature measures

in the 2D cross-sectional analysis; Hodges [78] later correlated results against 3D FEM for initially curved and twisted beams using VABS, comparing the extension/torsion and shear/bending couplings with a pre-twisted anistropic beam and the shear/torsion and extension/bending couplings with an initially curved anistropic beam. Epps and Chandra [79] in 1996 measured frequencies of rotating composite beams with tip sweep and compared to predictions using beam theory. Recently, Sinotte and Bauchau [80] correlated the curved beam models in *Dymore* and *SectionBuilder* with experimental strain results for beams undergoing centrifugal loading in a vacuum, showing that beam models could accurately capture measured strains in initially curved beams as long as the curvature is included in the cross-sectional analysis.

1.2.5 Higher-order Structural Models

While beam models are predominately used in computational aeromechanics analyses, higher order models have also been considered, including shell elements and fully 3-D finite element models. Bauchau et al. [81–83] investigated the use of shell elements in a multibody dynamic paradigm and presented energy preserving time integration schemes. Analysis using shell elements has been applied to wind turbines; Branner et al. studied the use of shell elements for determining stresses [84] and compared deformations to experimental data [85]. Bazilevs et al. [86] implemented a Kirchhoff-Love shell based structural model coupled with 3D computational fluid dynamics to study the airloads and structural deformations and stresses for a full scale offshore wind turbine rotor. Application of shell elements to rotorcraft analysis was performed by Kang et al. [87], in which a shell element was developed within RCAS. This element was designed to be connected to the existing nonlinear beam elements to allow for a mixed element model by using shell elements over only a portion of the blade, which could significantly reduce computational time compared to that of a full shell model. Comparisons of natural frequencies and deflections

for the combined shell and beam models were made to both experimental data and models consisting of only beam elements.

Analysis using 3-D finite element models for the blades has also been performed for the aeromechanical response of the rotor. Ortun et al. [88] investigated the ERATO rotor, a blade which features a double swept profile, using 3D hexahedral elements for the blade in the finite element code MSC/Marc. The 3-D structural model was coupled with a 3-D computational fluid dynamics (CFD) model to compare with a high-speed level flight case (at advance ratio $\mu = 0.423$) from a wind tunnel experiment. Yeo and Truong et al. [89, 90] also studied the use of 3-D FEA for rotor analysis using MSC/Marc and comparing the rotating beam frequencies to an RCAS beam analysis. Most recently, a 3-D finite element method (FEM) solver called X3D has been developed for the structural analysis of rotor blades based on the work by Datta and Johnson [91, 92]. The code was further refined by Staruk et al. [93] and coupled with both low-order aerodynamic models as well as a full CFD model to study the NASA tiltrotor aeroacoustic model (TRAM). Additional studies using the X3D solver have also been conducted by Ward et al. [94] using a notional UH-60A like rotor with a free-wake aerodynamics model.

Although these higher-order models have the potential to improve the fidelity of the analysis, most of these models are still being developed. Moreover, since the rotor, which dominates the dynamic response of the entire aircraft, can often be well captured using beam elements in a multibody formulation, at a significant computation cost savings compared to higher-order structural models, the comprehensive analysis tools such as *Dymore*, CAMRAD II, RCAS, and UMARC are still widely used today. The fact that beam-based comprehensive analyses are still predominately used and the interest in advanced geometry blades with structural coupling further underscores the need for more accurate cross-sectional stiffness properties to improve the accuracy of the aeromechanics calculations.

1.3 Sectional Stiffness Measurements

While beam theory is well suited for the structural dynamics analysis of rotor blades, determining the sectional stiffness properties for use in these codes is a challenging task. The fact that the blades are typically made of anisotropic materials and present cross-sectional geometries, often composed of multiple internal components, can present difficulties in defining an accurate model for use in numerical cross-sectional analysis tools. Moreover, variations in the material properties that arise from the manufacturing and curing processes may not be well known. In view of these difficulties, an experimental measurement of the sectional stiffness properties seems desirable – to ensure that the blade cross-section is being modeled correctly and provide a more accurate analysis.

Traditionally, stiffness properties are calculated based on a measurement of global parameters, such as deflection or frequency, which are then related to the stiffness using a beam model, usually from Euler-Bernoulli beam theory. The main existing measurement techniques can generally be categorized into three groups: deflection based, rotation based measurements, and frequency based measurements, with the first two measurement types being static (or quasi-static) and the last one being dynamic.

1.3.1 Deflection Based Measurements

Deflection based measurements rely on a measurement of the beam's deflection, normally at either the tip or the mid-span, to calculate the bending stiffness properties, with two simple approaches based on this measurement illustrated in Fig. 1.2. The setup in Fig. 1.2(a) measures the tip displacement w_{tip} of a cantilevered blade of length L under a static tip force F, while the setup in Fig. 1.2(b), referred to as a three-point bending test, measures the mid-span displacement w_{mid} of a cantilevered

beam simply supported at both ends with a force F applied at the mid-span. From Euler-Bernoulli theory, the curvature of the beam can be related to the second derivative of the beam's deflection ($\kappa(x) = d^2w(x)/dx^2$) and the cross-sectional stiffness can then be found using

$$M(x) = EI\frac{d^2w}{dx^2} \tag{1.6}$$

where $M(x)$ is the cross-sectional moment due to the applied force, and EI is the bending stiffness. Equation (1.6) must then be integrated twice to obtain a relationship for the bending stiffness in terms of the displacement. Normally, the properties must be assumed to be uniform along the span, so that EI can therefore be brought outside the integration. For the case of the cantilevered beam setup, the bending moment is $M(x) = F(L - x)$ and the displacement and slope at the root are both zero, $w(x = 0) = 0$ and $dw(x = 0)/dx$, respectively, and the cross-sectional bending stiffness can then be determined by

$$EI = \frac{FL^3}{3w_{\text{tip}}}. \tag{1.7}$$

For the case of the three-point bending setup, the bending moment over the first half of the beam ($0 < x < L/2$) is $M(x) = -Fx/2$ while the displacement at the root and the slope at the mid-span of the beam are both zero, $w(x = 0) = 0$ and $dw(x = L/2)/dx$, respectively, and the cross-sectional bending stiffness can then be determined by

$$EI = \frac{FL^3}{48w_{\text{mid}}}. \tag{1.8}$$

In the case of the cantilevered setup, the bending stiffness is derived under the assumption that the slope at the root is zero; however, it can be difficult to achieve a perfect clamp in an experimental setup, particularly if the blade is very

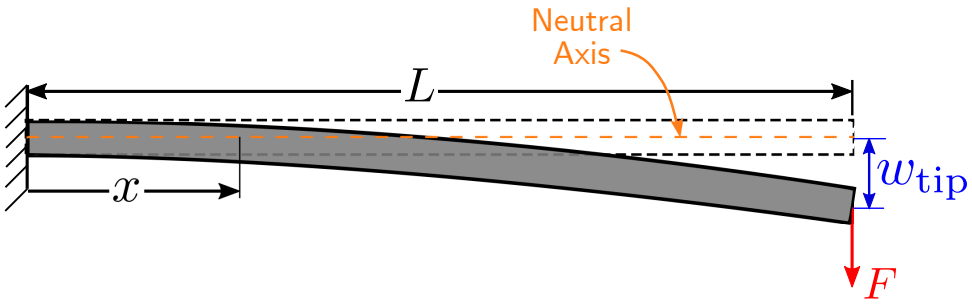

(a) Cantilever setup

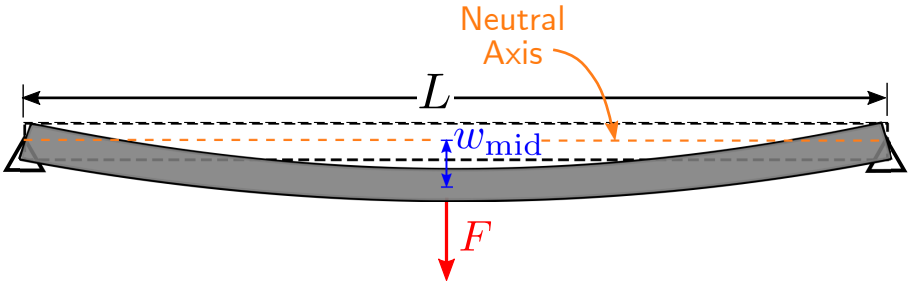

(b) Three-point bending setup

Figure 1.2: Illustrative setups for measurement of bending stiffness based on deflection.

stiff. In this case, the slope boundary condition may no longer be satisfied, resulting in a measured stiffness that is lower than the expected value. For the three-point bending setup, it is easier to enforce only a displacement boundary condition at both ends and errors in the simply supported boundary condition (that $M(x) = 0$ at the boundaries) have less of an impact on the measured properties, making it better suited for measurement of large bending stiffnesses. In the past, these methods have primarily been applied to measure the bending stiffnesses of the HART I and HART II rotors in the outboard region of the blade, starting at about 20% of the radius, where the properties are assumed to be uniform. For the HART II blade [14], the flap bending stiffness was measured using a cantilever setup with an optical measurement of the tip displacement. A three point bending setup was also used to measure the flap and chordwise bending stiffnesses of the Hart I rotor [13], as well as the chordwise bending stiffness of the HART II rotor [14].

1.3.2 Rotation Based Measurements

Rotation based stiffness measurements rely on a measurement of the cross-sectional rotations, either of the slope to calculate the bending stiffness or of the twist to calculate the torsional stiffness. One simple method for calculating the rotation is to measure the displacement at multiple locations on the blade. In the case of a bending stiffness, the displacement w can be measured at multiple locations along the span using a cantilever setup similar to Fig. 1.2(a) and the slope can be calculated between measurement locations using a finite difference approximation according to

$$\frac{dw}{dx} = w'(x) = \frac{w(x_2) - w(x_1)}{x_2 - x_1} \tag{1.9}$$

where x_1 and x_2 are the spanwise locations of the measurements. The bending stiffness can then be determined from a single integration of the Euler-Bernoulli moment-curvature relation (Eq. (1.6)) which gives

$$EI = \frac{Fx(L - x/2)}{w'(x)} \tag{1.10}$$

where $x = (x_2 + x_1)/2$. If the slope is measured at the tip, the stiffness can be approximated by $EI = FL^2/(2w'(L))$.

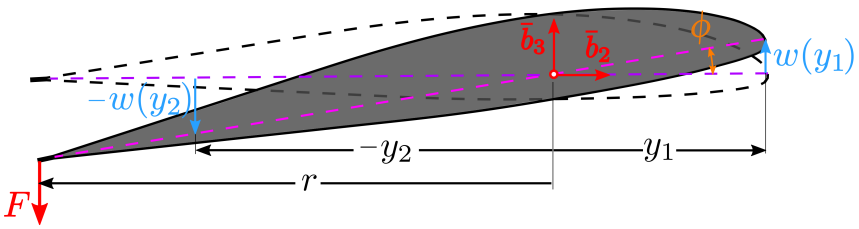

Figure 1.3: Illustrative setup for measurement of torsional stiffness based on measured rotation angle ϕ.

In a similar fashion, the torsional stiffness can also be measured by applying a torque and measuring the displacement at multiple locations along the chord.

While the twist angle could be approximated using a measurement of displacement at a single location along the chord, the torque is normally not applied as a force couple but by a single force, offset along the chordwise direction as shown in Fig. 1.3, so a single displacement measurement would not be able to eliminate the flap displacement arising from the non-zero vertical force. By obtaining displacement measurements at two different chord locations and making the assumption that the cross-section deforms rigidly, the flap displacement can be filtered out and the twist angle – measured positive nose-up – can be calculated according to

$$\phi = \tan^{-1}\left(\frac{w(y_1) - w(y_2)}{y_1 - y_2}\right) \tag{1.11}$$

where ϕ is the rotation angle and y_1 and y_2 the chordwise measurement locations. The torsional stiffness GJ is related to the applied torque $M_1 = Fr$ and the twist rate $\kappa_1(x) = d\phi/dx$ using Eq. (1.3) – namely $GJ = M_1/(d\phi/dx)$. If the blade is fixed at its root ($\phi(x = 0) = 0$), this relationship can be integrated along the span to give the torsional stiffness in terms of the measured twist angle as

$$GJ = \frac{Frx}{\phi}. \tag{1.12}$$

This method, using a slope calculated based on measured displacements, has been applied to measure both the bending and torsional stiffness of several Mach scale rotors at the University of Maryland using a digital height gauge [95,96]. Photogrammetric techniques, which capture the blade motion using cameras, can also be used to measure the displacement at a finer resolution compared to a height gauge. A Vicon motion capture system was used to measure the torsional, flap bending, and chordwise bending stiffness of a Mach scaled NACA 0012 blade at the University of Maryland [97]. Digital Image Correlation (DIC), another type of photogrammetric method, was used to measure the flap bending and torsional stiffness of the Hart II

rotor in the region near the root (up to $0.22R$) where there were significant variations in properties due to taper and geometry changes [14]. DIC was also used to measure blade deformations and calculate the torsional as well as flap and lag bending stiffness in the reinforced root section of Mach scaled VR-12 rotors at the University of Texas at Austin [98].

An alternative approach to measure the rotation is through the use of the "mirror method," in which mirrors are attached to the surface of a beam and laser light is reflected off the mirror to measure rotation under loading as shown in Fig. 1.4 for a cantilever beam in bending. The deflection of the reflected laser light δ is then measured on a target surface at a distance d from the blade, normally containing a grid for easy measurement, and used to calculate the reflection angle $\beta = \tan^{-1}(\delta/d)$. In the case of bending, the beam slope is equal to half the reflection angle ($w' = 0.5\beta$), and for an applied torque, the twist is also equal to half of the reflection angle ($\phi = 0.5\beta$). These measured angles can then be substituted into Eq. (1.10) and Eq. (1.12) to determine the bending stiffness and torsional stiffness, respectively. This technique was first applied for the measurement of the torsional stiffness of composite I-beams by Chandra and Chopra [99]. It has also been applied for measurements of the torsional, flap bending, and chord bending stiffness values of Mach scaled VR-12 coaxial rotors at the University of Texas at Austin [98, 100]. In this case, significant differences were observed between the calculated and measured torsional stiffness values, although a simplified numerical model was used to calculate the properties. A rigorous uncertainty analysis was also applied to the measurement of the stiffness properties, which is largely neglected in most other studies.

The mirror method helps reduce some of the errors that can arise from an imperfect experimental condition compared to a deflection based method; however, the equations as written still require the assumption that the properties are uniform along the span if only a single mirror is used in the measurement. If multiple mirrors

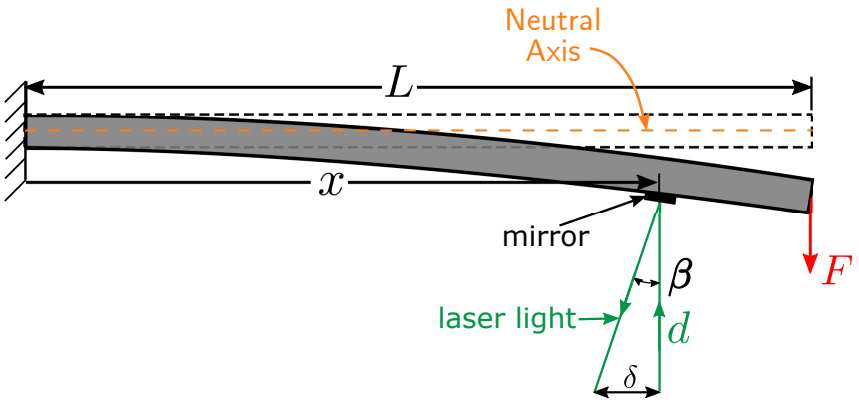

Figure 1.4: Illustrative setup for measurement of bending stiffness based on the "mirror method."

are included along the span and in close proximity to one another, the bending curvature can instead be approximated using a finite difference method with the slope measurements of two adjacent mirrors and the bending stiffness can be calculated using

$$EI = \frac{P(x_2^2 - x_1^2)}{\beta_2 - \beta_1} \tag{1.13}$$

where x_1 and x_2 indicate the adjacent locations of two spanwise mirrors and β_1 and β_2 the measured laser reflection angle at those locations. The twist rate can also be approximated in a similar manner between two mirrors to give an updated torsional stiffness of

$$GJ = \frac{2Pr(x_2 - x_1)}{\beta_2 - \beta_1}. \tag{1.14}$$

This modified approach has been applied to measure both the torsional and flap bending stiffness of the Hart I rotor in the region near the root (up to $0.22R$) where there were significant variations in properties due to taper and geometry changes [13]. This modified "mirror method" approach relaxes the assumption of uniform properties along the span, as integration of the Euler-Bernoulli bending-curvature relation is no longer required, as well as essentially eliminating inaccuracies arising from imperfect boundary conditions, since the difference of the two measured slopes will eliminate any rigid body motion present in both measurements. However,

the implementation and data collection process using this modified "mirror method" for an entire blade can be quite difficult and time consuming due to the large number of mirrors required and extensive data tracking requirements. In addition, the most accurate results require a large measurement distance d from the blade, which may not always be feasible.

1.3.3 Frequency Based Measurements

The previous techniques focused on static deformation measurements for calculating the stiffness properties, but dynamic measurements can also be used to measure the stiffness properties. The blade frequencies can be measured under different excitations and boundary conditions, with a shaker commonly used to excite a cantilever blade as shown in Fig. 1.5. The oscillations of the beam under excitation must then be recorded, through devices such as laser vibrometers or accelerometers, and a Fast Fourier Transform (FFT) can be used to extract the natural frequencies. Typically the blade frequencies are measured since the rotor dynamics play such an important role in the aeromechanics, regardless of whether the frequencies are used to calculate the stiffness. Based on the extracted frequencies, the assumption that properties are uniform along the span, and assumptions on the mass and inertia distributions, the stiffness can then be calculated from the frequency according to

$$\begin{aligned} EI &= \frac{\omega_b^2 m L^4}{f_{i,b}^4} \\ GJ &= \frac{\omega_t^2 I_\phi L^2}{f_{i,t}^2} \end{aligned} \tag{1.15}$$

where ω_b and ω_t are the non-rotating natural frequencies for bending and torsion, respectively, m is the mass per unit span, I_ϕ the mass moment of inertia per unit span, and $f_{1,b} = 1.87$ and $f_{1,t} = \pi/2$ for the first natural frequencies with a cantilever boundary condition. Because frequency measurements are highly impacted by

boundary conditions and require assumptions on the mass distributions, they have primarily only been used to measure stiffness values in cases when a static test is hard to perform, such as for the chordwise bending stiffness of the NACA 0012 blade at the University of Maryland [96]. In addition, there are no simple modifications that can be performed to account for spanwise variations and frequency based measurements are only realistically suited for blades with uniform property distributions.

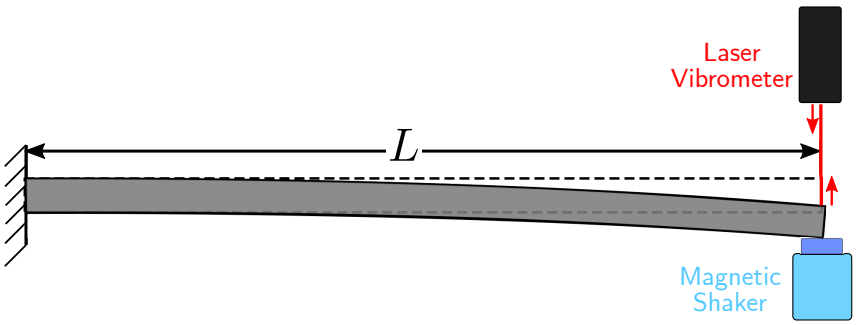

Figure 1.5: Illustrative setup for measurement of sectional stiffness based on measured frequencies using a shaker and laser vibrometer.

1.3.4 Other Notable Measurements

In addition to the above methods, there have also been a few special purpose efforts to measure stiffness properties. Jung et al. [101] used an X-ray CT scan technique to determine the post manufactured geometries and surface boundaries of the HART II rotor, which were then used in a cross-sectional analysis to evaluate the cross-sectional stiffness properties and compare with the experimental measurements from the static discrepancies. While this technique drastically reduced discrepancies between the actual blade and numerical model in terms of the geometric description of the cross-section, uncertainties can still exist in the material properties which can impact the predicted sectional stiffness values. In the wind turbine industry, Fedorov and Berggreen [74] analyzed the torsional, flap bending, and flap bending/torsion coupled stiffness values by fitting displacements and rotations measured using DIC with polynomials up to order 12 and then calculating the curvature and twist rate

from the fitted deformations. This is the only known attempt to measure the actual coupling stiffness for a composite beam, but the equations were specifically derived under the Euler-Bernoulli assumptions.

1.3.5 Limitations of Existing Measurement Techniques

Previous experiments have focused on measuring the sectional stiffness properties of beams primarily through static deformations or frequencies. While these techniques have proven effective, they also have multiple limitations. The first, and most fundamental, drawback is that none of the existing measurement techniques can provide the full 6×6 stiffness matrix. Existing methods have only been used to calculate torsional and two bending stiffness values and, in the special case of the wind turbine study by Fedorov and Berggreen [74], also the flap bending/torsion coupled stiffness. While these stiffness values are generally adequate for an accurate prediction of the rotor dynamics, they do not provide sufficient information for an accurate calculation of the stress and strain fields within the blade. Indeed, the rotational environment of the helicopter rotor generates significant axial strains due to the centrifugal forces, necessitating an accurate measure of the axial stiffness to predict.

In addition, most existing measurement techniques rely on the assumption that the stiffness properties are uniform along the span. While this assumption is normally true of model scale rotors used for wind tunnel testing, it is not true of most full-scale helicopter rotors. Finally, when using a single global parameter to measure stiffness, inaccuracies in the experimental and theoretical boundary conditions can significantly impact the results; however, several of the methods have been extended to include multiple measurements along the span to help filter out any rigid body motion.

1.4 Strain Measurement Techniques

Development of a methodology that provides a more complete and accurate measurement of the beam sectional stiffness requires more than just a measurement of frequencies or static displacements. Measurement of the strain field within the beam provides an alternative approach to existing measurement methodologies and can help address some of their shortcomings. Strain is a measure of the differential deformation in a structure; while a rigid body motion results in a observable displacement, it produces no strain and imperfect boundary conditions will have a minimal impact on the strain and therefore stiffness property measurement. In addition, all six sectional deformation measures given by $\underline{\mathcal{E}}$ can be related to the strain field, meaning that the full 6×6 stiffness matrix can be calculated from the strain field, as opposed to just a subset of the matrix. Finally, since strain is a local measurement within the beam, it can be used to predict spanwise variations in properties that most existing methods aren't capable of handling. Various techniques exist for measuring the strain field and can be broadly classified as contact based or non-contact based methods.

1.4.1 Contact Based Strain Measurements

Contact based techniques are those that require direct contact with the surface of a test article in order to obtain the strain measurements. This includes instrumentation such as strain gauges, extensometers, wire sensors, or fiber optic sensors. Strain gauges, due to their relatively low cost and versatility, are probably the most widely used strain measurement technique in aerospace applications. Strain gauges measure the change in resistance under an applied load to determine the strain and commonly come in two varieties: metallic foil gauges and semiconductor gauges [102]. Metallic foil gauges make use of a thin metallic wire looped back and forth and attached to an insulating film, as shown in Fig. 1.6(a), and are bonded to

a structure using an adhesive. When subjected to a tensile strain, the thin metallic wire stretches, decreasing its cross-sectional area thereby increasing its resistance; conversely, when subjected to a compressive strain, the metallic wire contracts, increasing its cross-sectional area and decreasing its resistance. Semiconductor strain gauges, shown in Fig. 1.6(b), consist of a bar or strip of a semiconductor, normally silicon or germanium, whose peizoresistive properties result in a change in resistance under deformation. Semiconductor strain gauges are much more sensitive than metallic foil gauges making them well suited for measurement of small strains, but are also significantly more expensive, are extremely temperature-sensitive, and typically more fragile. While both gauge types are designed to measure the strain in only the longitudinal direction, a strain rosette, with an example layout shown in Fig. 1.6(c), can be used to measure the shear strain and lateral strain.

Strain gauges have been used extensively within rotorcraft applications. In 1993-1994, full scale testing of the UH-60a airloads included 21 strain gauges for measuring the flap, lag, and torsional moments [103]. Subsequent testing of the same rotor system in 2010 included 28 strain gauges for measuring the structural loads [104]. For model scale rotors, strain gauges have also seen extensive use, including multiple tests at the University of Maryland to measure the blade loads in bending/torsion coupled blades [73] and in high advance ratio testing [96, 105, 106].

Although strain gauges have seen significant applications in rotorcraft, their use for measurement of the sectional stiffness properties can be problematic. Measurement of the detailed strain field along the span of the blade would require a large number of gauges, especially if stiffness measurements are desired for any non-uniform section of the blade. While an individual gauge typically costs $5 to $10, instrumenting the large number of required gauges would end up being both costly and very labor-intensive. Moreover, if the blade is to be tested in a wind tunnel or flown on an actual helicopter, the inclusion of a large number of gauges could significantly impact

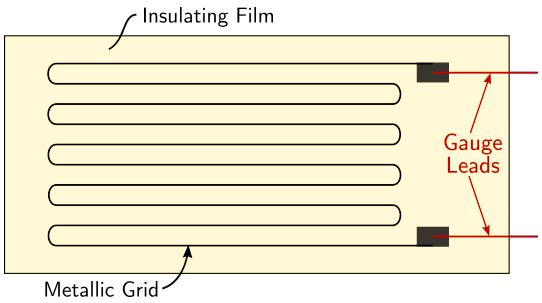

(a) Metallic foil strain gauge

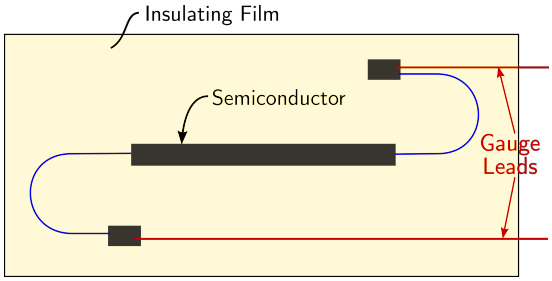

(b) Semiconductor strain gauge

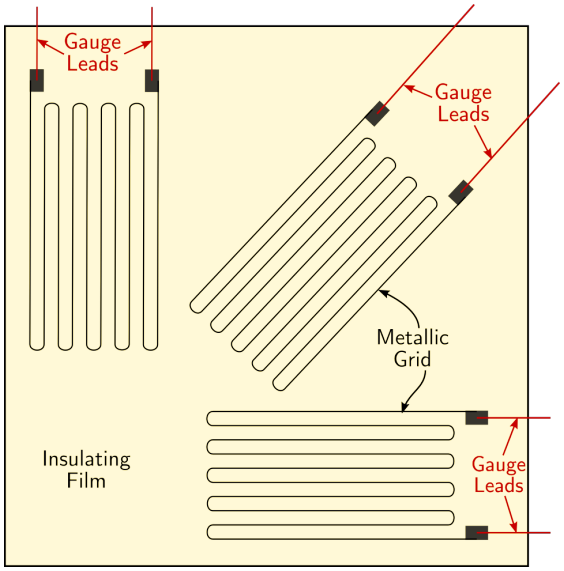

(c) Strain gauge rosette

Figure 1.6: Illustrative strain gauges.

the aerodynamic performance of the rotor. Finally, measurement of strain in the rotational environment typically requires a slip-ring to pass electrical signals from the rotating to non-rotating systems and, because slip-rings introduce additional noise and have a limited number of signal channels, would therefore limit the practicality of utilizing all the strain gauges for additional testing.

An alternative method to strain gauges is distributed wire sensors, which are shape memory wires that are normally embedded into the structure. The changes in electrical resistance are measured at multiple points along the wire sensor, as shown in Fig. 1.7, and the displacement and strain field within the beam are interpolated from these measurements using a finite element formulation. Baz and Poh [107] devised a wire sensor for measuring distributed bending deformations and strains.

Copp [108] extended this to measure the elastic twist of a rotating blade, using a sawtooth shaped wire sensor. While the embedded nature of distributed wire sensors is aerodynamically advantageous, these wire sensors require Euler-Bernoulli assumptions with a finite element formulation to calculate the strains and have seen limited use in rotorcraft.

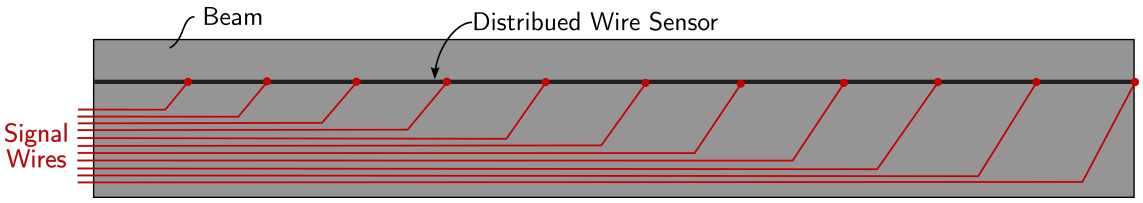

Figure 1.7: Schematic setup of distributed wire sensor.

Fiber optic sensors can also be utilized as a distributed strain sensor, usually through the use of a fiber bragg gratings as shown in Fig. 1.8. As the structure deforms, the fiber, which is either attached to the external surface or embedded internally if using composite materials, also deforms. This deformation modifies the wavelength of the transmitted light which can be directly related to the strain. In 2007, Liu et al. [109] developed a fiber optic strain and pressure sensor for use in rotors and obtained strain field measurements under centrifugal loading. Fairbanks-Smith [110] also used fiber-optic strain sensors on a section of a CH-47 rotor blade to study the impact of ballistic damage, finding good correlation between strain measurements using a fiber optic sensor and conventional strain gauges. Unlike the previously mentioned contact based strain sensors, fiber optic strain sensors do not require an excitation voltage to operate which drastically simplifies their installation. Fiber-optic sensors are also very lightweight and small and therefore will have a minimal impact on the blade mass and stiffness properties; however, a network of fiber optical sensors is still required to get a detailed strain field.

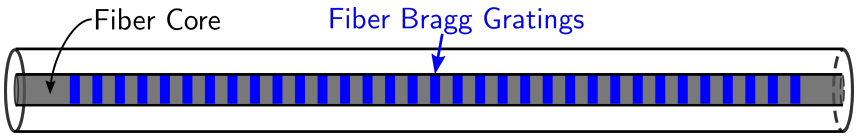

Figure 1.8: Example of Fiber Bragg Gratings.

1.4.2 Non-Contact Based Strain Measurements

Non-contact techniques for measuring strains have significantly advanced in the past several decades due to the advent of the digital camera and increased computer capabilities. Non-contact techniques have the capability for a much higher spatial resolution than conventional contact based strain measurements, which is advantageous for measuring spanwise distributions of stiffness properties. Many varieties of these optical methods exist, including electronic speckle pattern interferometry (ESPI), projection Moiré interferometry (PMI), and digital image correlation (DIC). Note that all optical methods directly measure the object contour and 3-D displacements; strain is then calculated from this information using an approach similar to 3-D finite element analysis.

Electronic speckle pattern interferometry (ESPI), uses the fact that when a rough surface is illuminated with laser light, a high contrast speckle pattern is observed, as shown in Fig. 1.9(a). An interferogram is then created by superimposing a reference beam from the same laser source on the speckles. When the structure is subjected to a load, the surface deforms and the observed speckle interferogram changes; comparison of the interferograms before and after applying the load generates a fringe pattern, as shown in Fig. 1.9(b), which provides a measure of the 3-D displacement that is subsequently used to calculate the strain field on the surface of the blade. Originally the interferograms were recorded using TV cameras; however, it is now common to collect digital images using a CCD or CMOS camera and the method is also referred to as digital speckle pattern interferometry (DSPI) [1]. For rotorcraft applications, ESPI has primarily been used for nondestructive inspection;

Gryzagoridis [111] used ESPI to detect composite de-lamination in a rotor blade.

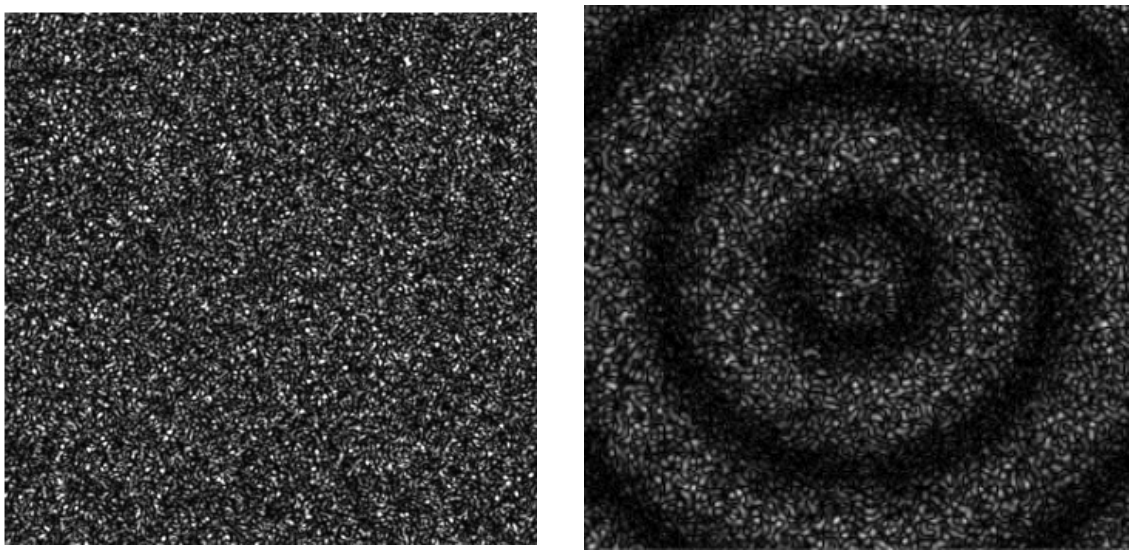

(a) Example speckle pattern **(b) Example fringe pattern**

Figure 1.9: Example of results produced using ESPI (from Rastogi 2015 [1]).

Projection Moiré interferometry (PMI) is another optical interferometric measurement method that uses an incoherent light source, normally pulsed laser diodes, to project a grid of parallel lines onto the test object. Images of the projected grid lines are then captured in both a baseline undeformed state and a deformed state under loading, which are compared to a computer generated phase shifted grid, resulting in interferograms with Moiré fringes. These fringe patterns are then digitally processed to measure the object contour and displacement field. PMI has been used in a variety of rotorcraft studies. Fleming and Gorton [112] applied PMI on a four-bladed, Mach-scaled rotor to measure mean and unsteady blade bending and twist deformations. Subsequent testing by Fleming et al. [113] on active twist rotor blades measured the spanwise distribution of flap bending deformation at multiple azimuthal locations and the tip twist under various actuation amplitudes. Sekula [114] measured blade deflections using PMI at several different thrust levels and heights for a rotor in ground effect. While PMI has seen more extensive use in rotorcraft applications than ESPI, both methods have primarily been used to

measure the displacements and not strains.

Alternatively, stereoscopic digital image correlation (DIC) can be used to measure the 3-D displacements on the surface of an object. DIC uses pairs of cameras to capture images of an object in an undeformed reference state and a deformed state; displacements are then calculated by cross correlation of a stochastic speckle pattern using stereo photogrammmetry. Unlike the interferometric methods, which generate their patterns optically using lasers, the speckle pattern for DIC is directly applied to the surface, usually using paint. Of the non-contact, optical measurement methods, DIC has been used most extensively in rotorcraft applications. Sirohi and Lawson [115] used DIC to measure the flap and twisting deformation, showing good correlations with measurements obtained using both a laser displacement sensor and inclinometer. Sicard and Sirohi [116] extended this study to measure the extension, lag and flap bending, and torsional deformations of an extremely flexible spinning rotor, showing that the elastic twist deformation was on the same order of magnitude as the blade pitch. Uehara and Sirohi [117] then applied DIC to measure the deformation of a rotating blade, extracting the mode shapes and frequencies from these measurements using operational modal analysis. For full-scale rotorcraft, Annett and Littell [118] used DIC to measure the structural response of two CH-46E airframes during impact testing. The 3-D displacement field was measured throughout the impact and the residual strains from the impact were also evaluated.

Optical non-contact measurement techniques provide significant advantages over traditional contact based strain measurements for evaluating the sectional stiffness. Minimal preparation is required for measurement of strains using optical techniques, meaning that the blades can still be used for wind tunnel or flight testing, without significantly impacting its aerodynamic profile or structural integrity. In addition, optical measurement techniques provide very high spatial resolution,

which is desirable for predicting any spanwise variations in properties. Of the optical measurement methods, DIC provides a good tradeoff between cost and strain measurement capabilities and has seen the most widespread use in rotorcraft, including to measure stiffness properties (based on displacements) and the modal characteristics of rotating blades, and was thus selected for obtaining the strain measurements in this work.

1.5 Objectives

The overall objective of the present work is to develop a new measurement technique for a more complete characterization of the sectional stiffness properties – to provide better accuracy in the structural loads predicted from comprehensive analysis codes and the resulting stress and strain fields. The technical approach to accomplish this can be categorized into the following tasks.

- *Develop a new strain-based methodology for measuring the sectional stiffness properties.* This is the main objective of the present dissertation. By using a strain-based method, as opposed to the displacement or frequency based methods commonly applied in rotorcraft analysis, the dependency on an accurate experimental implementation of the expected boundary condition can be significantly reduced. Moreover, because the strain is a local property within the beam, this allows the stiffness properties to be measured at discrete radial locations along the blade which can be used to measure spanwise variations arising from blade attributes like taper and twist. However, an accurate measurement of the stiffness properties, particularly of the shear and torsional terms, using a strain-based approach also requires the definition of a warping field, which generally needs to be calculated numerically.

- *Develop and implement an uncertainty analysis for error estimation.* An

uncertainty quantification based on a Taylor series method is used to propagate expected errors in the experimental measurements into the calculated stiffness properties. The implementation is compared with a Monte Carlo simulation to verify the accuracy.

- *Verify the methodology and implementation.* Since a new experimental method is being explored, the data reduction equations are verified using numerical strain data from 3-D FEM. This eliminates any unexpected errors that may arise from experimental measurements and evaluates the methodology under ideal circumstances.

- *Implement an experimental setup for measuring the strains and loads for model scale rotor blades.* A test stand is built to apply six independent load cases of sufficient magnitude to generate strains with large signal to noise ratios. Since DIC is used to measure the displacement and strain fields and requires a view of the surface of the beam for measurement, a system of pulleys is used to generate loads to keep the view of the beam unobstructed. The mounting adapters to the test stand and for load application are kept modular to accommodate beams with a variety of cross-sectional geometries.

- *Apply the methodology to experimentally measure the stiffness properties of various beams.* The methodology is evaluated using a variety of test articles, specifically beams that present elastic coupling terms, beams with spanwise variations in properties, and model scale composite rotor blades. The experimental results are then used to provide a comparison with existing 2-D cross-sectional analysis tools.

1.6 Contributions

With these objectives in mind, the following are the key contributions of the present work

1. Development of a new strain-based method for measuring the cross-sectional stiffness properties of composite rotor blades. This differs from the conventional techniques utilizing displacement or frequency measurements.

2. Measurements of the full 6×6 sectional stiffness matrix. Existing measurement techniques focus on only a subset of the matrix and generally include measurements of only the torsional and flap and lag bending stiffnesses for the blade.

3. Comparison of results from proposed method to existing displacement based measurement techniques. This shows some of the advantages that a strain-based methodology can provide.

4. Detailed uncertainty analysis for predicting expected errors of the stiffness property measurements. Previous studies have only focused on the measurement of the stiffness properties itself without focusing on error estimation.

5. Experimental evaluation of 2-D cross-sectional analysis tools, specifically *SectionBuilder*. In the past, 2-D cross-sectional analysis codes (both *SectionBuilder* and VABS) have primarily been validated with analytic solutions and 3-D FEM.

6. Detailed strain measurement data sets for model scale composite rotors. These data sets can be used to validate the stress and strain predictive capabilities of both 2-D cross-sectional analysis codes as well as 3-D FEM tools, such as X3D.

1.7 Organization of the Dissertation

The present chapter provided the motivation for the current work and an overview of the existing methodologies for predicting and measuring the sectional stiffness matrices of composite rotor blades, needed for an accurate comprehensive analysis. Chapter 2 describes the development of a new methodology, combining both experimental and numerical data, to improve on the measurement of the sectional stiffness properties. This chapter summarizes the key aspects of this methodology and highlights the information needed for an accurate measurement. The proposed approach combines experimental data with the warping field predicted by *SectionBuilder* to eliminate restrictions on the cross-sectional geometry or materials.

Chapter 3 focuses on validation of the new methodology using strain data simulated from 3-D finite element models. Models were specifically selected to address some of the key features of composite rotor blades, including spanwise variations in properties, elastic coupling, and twist. Chapter 4 then presents a detailed error analysis for providing uncertainty quantification on the experimental measurements of the stiffness properties.

Chapter 5 discusses the experimental setup for obtaining the strain and force measurements needed to calculate the local, sectional stiffness properties. Results of simple calibration procedures are discussed, to assess the expected errors for each of the measurements. Chapter 6 then details the stiffness measurements obtained for various beams using this experimental setup, starting with results for simple isotropic cross-sections and moving up to more complex composite blades. Finally, Chap. 7 gives a summary of the present work, provides the key conclusions and suggestions for future work.

Chapter 2: Methodology

This chapter focuses on the mathematical and numerical methodology for the presented dissertation research. The governing equations for the cross-sectional analysis are first presented, followed by a discussion of the process to calculate the stiffness matrix from these equations.

2.1 Cross-Sectional Analysis

The cross-sectional stiffness matrix, $\underline{\underline{K}}$, provides a direct relationship between the sectional deformation measures $\underline{\mathcal{F}}$ and the sectional stress resultants $\underline{\mathcal{E}}$, as defined by Eq. (1.4) ($\underline{\mathcal{F}} = \underline{\underline{K}}\,\underline{\mathcal{E}}$). While the sectional stress resultants can be measured experimentally, Eq. (1.4) can not be used to directly calculate the stiffness matrix as the sectional deformation measures can not be obtained experimentally. Instead, this relationship must be rewritten in terms of a measurable quantity, the local strains, through the use of a numerical model. For this thesis, the cross-sectional analysis tool *SectionBuilder* was used for the numerical model.

SectionBuilder is a finite element based tool for the analysis of cross-sections with arbitrary geometry made of anistropic materials, based on a solution approach of Saint-Venant's problem using Hamilton's formalism developed by Bauchau and Han [41, 60]. It provides an exact solution of the 3D theory of elasticity under several assumptions: *(1)* small strains and small warping displacements; *(2)* uniform geometry and material properties along the span of the beam; *(3)* cross-sectional dimensions are much smaller than the beam's span. The first two assumptions

imply that the beam can be analyzed using Saint Venant's beam theory, while the third assumption implies that extremity effects are negligible [119]. A full discussion of the derivation of the solution process for *SectionBuilder* can be found in [120]; the following subsections will introduce the key variables and highlight the main principles needed for providing the relationship between the strains, stiffness matrix, and sectional stress resultants.

2.1.1 Beam Configuration

In aerospace applications, a beam will generally have a cross-section of arbitrary geometry and may be initially curved and twisted for aerodynamic purposes, as depicted in Fig. 2.1. The beam is defined by an arbitrary curve in space, denoted $\mathcal{C}$, which forms a reference line along the span of the beam. The total length of curve $\mathcal{C}$ is L, with the curvilinear coordinate α_1 defining the intrinsic parameterization of the curve.

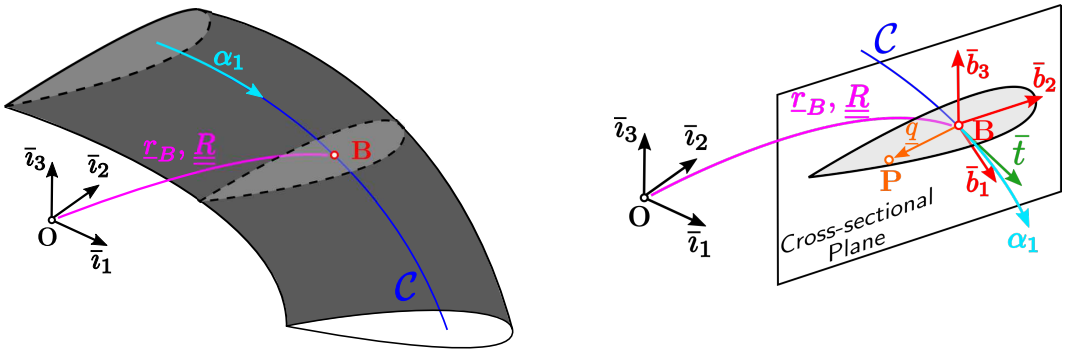

(a) Full beam configuration **(b) Cross-sectional configuration**

Figure 2.1: Configuration of a naturally curved and twisted beam.

The cross-sectional configuration is defined by frame $\mathcal{F}_B = \left[\mathbf{B}, \mathcal{B} = (\bar{b}_1, \bar{b}_2, \bar{b}_3)\right]$, where point **B** lies at the intersection of the cross-sectional plane with the reference line of the beam. The plane of the cross-section is therefore determined by the two mutually orthogonal unit vectors, $\bar{b}_2$ and $\bar{b}_3$. A point within the cross-section can be defined using the material coordinates α_1, y, and z, where y and z measure the

location along $\bar{b}_2$ and $\bar{b}_3$, respectively.

In general, the orientation of the cross-section will change as it moves along curve $\mathcal{C}$ due to the natural twist and curvature of the beam and basis $\mathcal{B}$ will therefore be a function of α_1. The location of point **B** with respect to the reference frame $\mathcal{F}_I = [\mathbf{O}, \mathcal{I} = (\bar{\imath}_1, \bar{\imath}_2, \bar{\imath}_3)]$ is defined by $\underline{r}_B$ and the rotation tensor that brings basis $\mathcal{I}$ to basis $\mathcal{B}$ is $\underline{\underline{R}}(\alpha_1)$. The motion tensor that brings frame $\mathcal{F}_I$ to frame $\mathcal{F}_B$ is then defined by

$$\underline{\underline{C}} = \begin{bmatrix} \underline{\underline{R}} & \tilde{r}_B \underline{\underline{R}} \\ \underline{\underline{0}} & \underline{\underline{R}} \end{bmatrix} \tag{2.1}$$

where $\tilde{r}_B$ is the skew-symmetric matrix defined by

$$\tilde{r}_B = \begin{bmatrix} 0 & -r_{B,3} & r_{B,2} \\ r_{B,3} & 0 & -r_{B,1} \\ -r_{B,2} & r_{B,1} & 0 \end{bmatrix} \tag{2.2}$$

with $r_{B,i}$ denoting the i^{th} component of $\underline{r}_B$. The components of the beam's curvature tensor in frame $\mathcal{F}_B$ are then defined from the motion tensor by

$$\tilde{\mathcal{K}} = \underline{\underline{C}}^{-1} \underline{\underline{C}}' = \begin{bmatrix} \tilde{k} & \tilde{t} \\ \underline{\underline{0}} & \tilde{k} \end{bmatrix} \tag{2.3}$$

where notation $(\cdot)'$ indicates a derivative with respect to α_1, $\underline{k}$ is the curvature vector of the beam, and $\bar{t}$ is the unit tangent vector to curve $\mathcal{C}$. For a straight, untwisted beam, the unit tangent vector is $\bar{t} = \{1, 0, 0\}^T$ and the curvature vector is $\underline{k} = \{0, 0, 0\}^T$. For an initially curved or twisted beam, the curvature vector becomes $\underline{k} = \{\kappa_1, \kappa_2, \kappa_3\}^T$, where κ_1 is the twist rate, κ_2 the curvature about axis b_2 (*i.e.* the anhedral or dihedral), and κ_3 the curvature about axis b_3 (*i.e.* sweep).

2.1.2 Stress and Strain Components

In the formulation of *SectionBuilder*, the strains are defined in terms of the Green-Lagrange strain tensor denoted by

$$\underline{\gamma} = \left\{ \begin{array}{c} \underline{\gamma}_O \\ \underline{\gamma}_I \end{array} \right\} \tag{2.4}$$

where $\underline{\gamma}_O^T = \{\gamma_{11}, 2\gamma_{12}, 2\gamma_{13}\}$ are the out-of-plane strain components and $\underline{\gamma}_I^T = \{\gamma_{22}, \gamma_{23}, 2\gamma_{23}\}$ are the in-plane strain components. The strain components can be written in terms of an arbitrary displacement field $\underline{u}(\alpha_1, y, z)$, which describes the relative displacement of a material point $\mathbf{P}$ within the cross-section, according to

$$\underline{\gamma}_O = \frac{1}{\sqrt{g}}\underline{u}' + \frac{1}{\sqrt{g}}\underline{\underline{D}}_O\,\underline{u} \tag{2.5a}$$

$$\underline{\gamma}_I = \frac{1}{\sqrt{g}}\underline{\underline{D}}_I\,\underline{u} \tag{2.5b}$$

where $\underline{\underline{D}}_O$ and $\underline{\underline{D}}_I$ are differential operators defined by

$$\underline{\underline{D}}_O = \begin{bmatrix} d & -k_3 & k_2 \\ k_3 + \sqrt{g}\dfrac{\partial}{\partial y} & d & -k_1 \\ -k_2 + \sqrt{g}\dfrac{\partial}{\partial z} & k_1 & d \end{bmatrix}, \quad \underline{\underline{D}}_I = \begin{bmatrix} 0 & \sqrt{g}\dfrac{\partial}{\partial y} & 0 \\ 0 & 0 & \sqrt{g}\dfrac{\partial}{\partial z} \\ 0 & \sqrt{g}\dfrac{\partial}{\partial z} & \sqrt{g}\dfrac{\partial}{\partial y} \end{bmatrix} \tag{2.6}$$

with $\sqrt{g} = t_1 - k_3 y + k_2 z$ and $d = -\left(t_2 - k_1 z\right)\partial(\cdot)/\partial y - \left(t_3 + k_1 y\right)\partial(\cdot)/\partial z$. For the case of a straight untwisted beam, the expressions are simplified since $\sqrt{g} = 1$ and k_1, k_2, k_3, and d are all zero. Using this notation, the Green-Lagrange strain tensor from Eq. (2.4) can be written as

$$\underline{\gamma} = \underline{\underline{A}}\,\underline{u}' + \underline{\underline{B}}\,\underline{u} \tag{2.7}$$

where

$$\underline{\underline{A}} = \frac{1}{\sqrt{g}} \begin{bmatrix} \underline{\underline{I}} \\ \underline{\underline{0}} \end{bmatrix}, \quad \underline{\underline{B}} = \frac{1}{\sqrt{g}} \begin{bmatrix} \underline{\underline{D}}_O \\ \underline{\underline{D}}_I \end{bmatrix} \tag{2.8}$$

Although the strains must remain small at all times, due to the first assumption for *SectionBuilder*, the beam can still undergo large displacements and rotations.

The stress in the beam is represented using the Cauchy stress tensor, denoted by $\underline{\tau}^T = \left\{\underline{\tau}_o^T, \underline{\tau}_I^T\right\}$, where $\underline{\tau}_o^T = \{\tau_{11}, \tau_{12}, \tau_{13}\}$ are the out-of-plane components and $\underline{\tau}_I = \{\tau_{22}, \tau_{33}, \tau_{23}\}$ are the in-plane components. Assuming that the beam is made of linearly elastic, but generally anisotropic materials, the constitutive relationship between the Cauchy stress tensor and the Green-Lagrange strain tensor is defined as

$$\underline{\tau} = \underline{\underline{D}}\,\underline{\gamma} \tag{2.9}$$

where $\underline{\underline{D}}$ is the 6×6 material stiffness matrix resolved in the basis $\mathcal{B}$.

When defining the constitutive relationships, the stress and strain tensors are commonly partitioned by the normal $\{(\cdot)_{11}, (\cdot)_{22}, (\cdot)_{33}\}$ and shear $\{(\cdot)_{23}, (\cdot)_{13}, (\cdot)_{12}\}$ components; however, because the current partitioning scheme uses out-of-plane and in-plane components, it is important to make sure the material stiffness matrix is defined correctly. When resolved in basis $\mathcal{B}^*$, whose axis are aligned with the axes of the material, the material stiffness matrix for an orthotropic material can be written as

$$\underline{\underline{D}}^* = \frac{1}{\Delta} \begin{bmatrix} E_1\left(1-\nu_{23}\nu_{32}\right) & 0 & 0 & E_1\left(\nu_{21}+\nu_{23}\nu_{31}\right) & E_1\left(\nu_{31}+\nu_{21}\nu_{32}\right) & 0 \\ 0 & G_{12}\Delta & 0 & 0 & 0 & 0 \\ 0 & 0 & G_{13}\Delta & 0 & 0 & 0 \\ E_1\left(\nu_{21}+\nu_{23}\nu_{31}\right) & 0 & 0 & E_2\left(1-\nu_{13}\nu_{32}\right) & E_2\left(\nu_{32}+\nu_{12}\nu_{31}\right) & 0 \\ E_1\left(\nu_{31}+\nu_{21}\nu_{32}\right) & 0 & 0 & E_2\left(\nu_{32}+\nu_{12}\nu_{31}\right) & E_3\left(1-\nu_{12}\nu_{21}\right) & 0 \\ 0 & 0 & 0 & 0 & 0 & G_{23}\Delta \end{bmatrix} \tag{2.10}$$

where $\Delta = (1 - \nu_{23}\nu_{32} - \nu_{13}\nu_{31} - \nu_{12}\nu_{21} - 2\nu_{32}\nu_{13}\nu_{21})$ and the relationships $\nu_{21} =$

$\nu_{12}E_2/E_1$, $\nu_{31} = \nu_{13}E_3/E_1$, and $\nu_{32} = \nu_{23}E_3/E_2$ were used to simplify the matrix. For a transversely isotropic material, such as a unidirectional layer of composite, the material stiffness can be simplified using the fact that $E_3 = E_2$, $G_{13} = G_{12}$, $\nu_{13} = \nu_{12}$, and $G_{23} = E_2/\left[2\left(1+\nu_{23}\right)\right]$. For an isotropic material, the material stiffness can be further simplified using the fact that $E_1 = E_2 = E_3 = E$, $\nu_{12} = \nu_{13} = \nu_{23} = \nu$, and $G_{12} = G_{13} = G_{23} = E/\left[2\left(1+\nu\right)\right]$. Generally, the material basis $\mathcal{B}^*$ and the reference basis $\mathcal{B}$ are not aligned, and the material stiffness matrix must therefore be rotated into the reference basis. Figure 2.2(a) shows an example cross-section made of several layers of composite material. A rotation of θ about b_1 brings the reference basis $\mathcal{B}$ to the local basis $\mathcal{E}$. As seen in Fig. 2.2(b), a second rotation of γ about axis $\bar{e}_3$ brings the basis $\mathcal{E}$ to the material basis $\mathcal{B}^*$, which is aligned with the fibers of the composite material. The material stiffness matrix in reference basis $\mathcal{B}$ is then

$$\underline{\underline{D}} = \underline{\underline{R}}^*_\sigma \, \underline{\underline{D}}^* \, \underline{\underline{R}}^{*T}_\sigma \tag{2.11}$$

where

$$\underline{\underline{R}}^*_\sigma = \begin{bmatrix} C_\gamma^2 & -S_{2\gamma} & 0 & S_\gamma^2 & 0 & 0 \\ \frac{C_\theta S_{2\gamma}}{2} & C_{2\gamma}C_\theta & -C_\gamma S_\theta & -\frac{C_\theta S_{2\gamma}}{2} & 0 & S_\theta S_\gamma \\ \frac{S_\theta S_{2\gamma}}{2} & C_{2\gamma}S_\theta & C_\gamma C_\theta & -\frac{S_\theta S_{2\gamma}}{2} & 0 & -C_\theta S_\gamma \\ C_\theta^2 S_\gamma^2 & C_\theta^2 S_{2\gamma} & -S_{2\theta}S_\gamma & C_\theta^2 C_\gamma^2 & S_\theta^2 & -S_{2\theta}C_\gamma \\ S_\theta^2 S_\gamma^2 & S_{2\gamma}S_\theta^2 & S_{2\theta}S_\gamma & C_\gamma^2 S_\theta^2 & C_\theta^2 & C_\gamma S_{2\theta} \\ \frac{S_{2\theta}S_\gamma^2}{2} & \frac{S_{2\theta}S_{2\gamma}}{2} & S_\gamma C_{2\theta} & \frac{C_\gamma^2 S_{2\theta}}{2} & -\frac{S_{2\theta}}{2} & C_\gamma C_{2\theta} \end{bmatrix} \tag{2.12}$$

with the shorthand notation $S_{(\cdot)} = \sin(\cdot)$ and $C_{(\cdot)} = \cos(\cdot)$

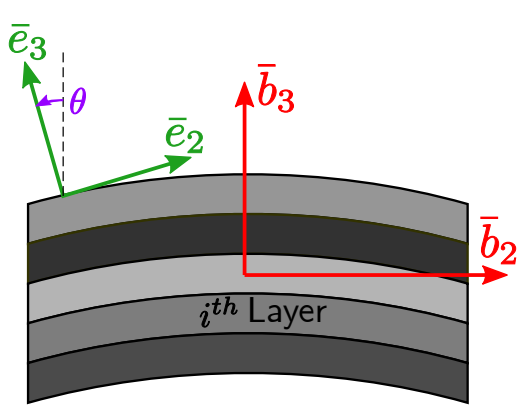

(a) Cross-section composed of multiple composite layers

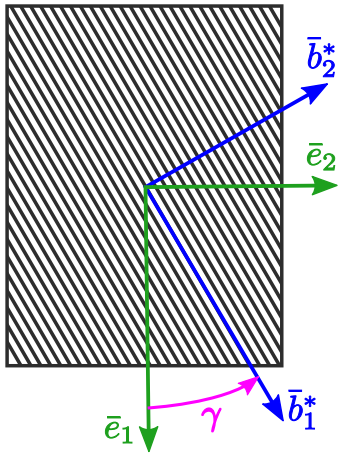

(b) Ply orientation in the i^{th} layer

Figure 2.2: Cross-section showing rotation angles between the reference basis $\mathcal{B}$ and material basis $\mathcal{B}^*$.

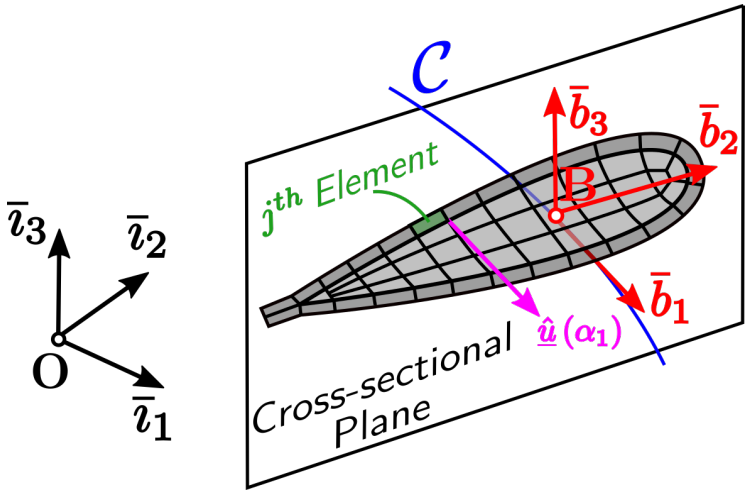

Figure 2.3: Discretized cross-section.

2.1.3 Semi-Discretization of the Displacement Field

In the previous paragraphs, the displacement and warping fields were treated as general vectors depending on three independent variables, the curvilinear coordinate, α_1, and the cross-sectional coordinates, y and z. However, the equations governing the displacement field in beam theory are one-dimensional, ordinary differential equations that are a function of α_1 only. Therefore, to obtain a one-dimensional formulation, the cross-section of the beam is discretized using two-dimensional

elements, as shown in Fig. 2.3. The displacement fields can then be written as

$$\underline{u}\,(\alpha_1, y, z) = \underline{\underline{N}}\,(y, z)\,\underline{\hat{u}}\,(\alpha_1) \tag{2.13}$$

where $\underline{\underline{N}}\,(y, z)$ are the two-dimensional shape functions used for the discretization and $\underline{\hat{u}}\,(\alpha_1)$ stores the nodal values of the displacement field. This discretization can then be introduced in Eq.(2.7) for the Green-Lagrange strain tensor, which gives

$$\underline{\gamma} = \underline{\underline{A}}_L \underline{\hat{u}}' + \underline{\underline{B}}_L \underline{\hat{u}} \tag{2.14}$$

where the strain interpolation matrices, $\underline{\underline{A}}_L$ and $\underline{\underline{B}}_L$, are defined by

$$\underline{\underline{A}}_L = \underline{\underline{A}}\,\underline{\underline{N}} = \frac{1}{\sqrt{g}} \left[\begin{array}{c|ccc|c} & N_i & 0 & 0 & \\ & 0 & N_i & 0 & \\ \dots & 0 & 0 & N_i & \dots \\ & 0 & 0 & 0 & \\ & 0 & 0 & 0 & \\ & 0 & 0 & 0 & \end{array}\right] \tag{2.15a}$$

$$\underline{\underline{B}}_L = \underline{\underline{B}}\,\underline{\underline{N}} = \frac{1}{\sqrt{g}} \left[\begin{array}{c|ccc|c} & d & -k_3 N_i & k_2 N_i & \\ & k_3 N_i + \sqrt{g} N_{i,y} & d & -k_1 N_i & \\ \dots & -k_2 N_i + \sqrt{g} N_{i,z} & k_1 N_i & d & \dots \\ & 0 & \sqrt{g} N_{i,y} & 0 & \\ & 0 & 0 & \sqrt{g} N_{i,z} & \\ & 0 & \sqrt{g} N_{i,z} & \sqrt{g} N_{i,y} & \end{array}\right] \tag{2.15b}$$

with $N_i(\xi, \eta)$ being the Lagrange shape functions, ξ and η being the local spatial variables over the element, and $N_{i,y}$ and $N_{i,z}$ indicating the derivatives with respect to y and z, respectively. Since the shape functions and derivatives are only non-zero

for the j^{th} element, the strain interpolation matrices $\underline{\underline{A}}_L$ and $\underline{\underline{B}}_L$ are of size $6 \times 3n$, where n is the number of nodes per element.

2.1.4 The Central Solution

Under the assumption that the beam's span is much greater than the cross-sectional dimensions, the extremity solutions, which decay exponentially with the distance from the beam's ends, can be neglected. The remaining part of the solution is the central or "Saint-Venant's" solution, which propagates along the beam's span without decaying. The central solution is an exact solution of the linear theory of 3-D elasticity for beams with uniform geometric and material characteristics along their span, with the accuracy only limited by the discretization used for the finite element method.

The detailed derivation of the central solution can be found in Bauchau and Han [41, 60]; an important feature of the central solution is the fact that the nodal displacements, $\underline{\hat{u}}$ can be expressed as

$$\underline{\hat{u}} = \underline{\underline{Z}}\,\underline{\mathcal{U}}_R + \underline{\underline{W}}\,\underline{\mathcal{F}}_c \tag{2.16}$$

where $\underline{\underline{Z}}\,\underline{\mathcal{U}}_R$ represents the rigid-body motion of the nodes and $\underline{\underline{W}}\,\underline{\mathcal{F}}_c$ represents the warping displacement. For the rigid-body motion, $\underline{\mathcal{U}}_R^T = \left\{\underline{u}_R^T, \underline{\phi}_R^T\right\}$ stores the rigid-body displacement and rotation of the entire cross-section, respectively. Matrix $\underline{\underline{Z}}$ is a $3m \times 6$ matrix, with m being the total number of nodes in the model, storing the nodal locations for all the nodes in the cross-sectional model, with the rows corresponding to the i^{th} node defined by

$$\underline{\underline{Z}}_i = \begin{bmatrix} 1 & 0 & 0 & 0 & z_i & -y_i \\ 0 & 1 & 0 & -z_i & 0 & 0 \\ 0 & 0 & 1 & y_i & 0 & 0 \end{bmatrix} \tag{2.17}$$

where y_i and z_i are the y and z locations of the node, respectively. For the warping displacement, $\underline{\mathcal{F}}_c^T = \left\{\underline{F}^T, \underline{M}^T\right\}$ denotes the stress resultants at the current apanwise location, where $\underline{F}$ contains the three sectional force, consisting of the axial force and two transverse shear forces, and $\underline{M}$ contains the sectional moments, consisting of the twisting and two bending moments, all of which are resolved in the reference basis $\mathcal{B}$. Matrix $\underline{\underline{W}}(y,z)$ is a $3m\times$ 6 matrix, which stores the nodal warping field, with each column of the matrix representing the warping induced by the respective unit component of the sectional stress resultant.

For Saint-Venant's problem, the governing equations reduce to

$$\underline{\mathcal{U}}_R' + \tilde{\mathcal{K}}\underline{\mathcal{U}}_R = \underline{\underline{S}}\,\underline{\mathcal{F}}_c \tag{2.18a}$$

$$\underline{\mathcal{F}}_c' - \tilde{\mathcal{K}}^T\underline{\mathcal{F}}_c = \underline{0} \tag{2.18b}$$

where $\underline{\underline{S}}$ is the sectional compliance matrix and the inverse of the sectional stiffness matrix (*i.e.* $\underline{\underline{K}} = \underline{\underline{S}}^{-1}$). Substituting Eqs.(2.16) and (2.18) into the discretized version of the strain tensor given by Eq.(2.14) and using the fact that a rigid body motion induces no strain (*i.e.* the coefficient of $\underline{\mathcal{U}}_R$ must vanish), the strain tensor at any point in the beam is

$$\underline{\gamma}(\alpha_1, y, z) = \left[\underline{\underline{A}}_L\left(\underline{\underline{Z}}\,\underline{\underline{S}} + \underline{\underline{W}}\,\tilde{\mathcal{K}}^T\right) + \underline{\underline{B}}_L\,\underline{\underline{W}}'\right]\underline{\mathcal{F}}_c(\alpha_1) \tag{2.19}$$

Equation (2.19) implies that, with knowledge of the nodal warping field, the complete strain field at any point of the cross-section can be expressed in terms of the six sectional stress resultants.

2.2 Data Reduction Equation

Equation (2.19) provides the basic relationship used to solve for the sectional compliance matrix. By rearranging the expression on the right-hand side of Eq. (2.19), the strain tensor can be expressed as

$$\underline{\gamma} = \underline{\underline{A}}_L \underline{\underline{Z}}\, \underline{\underline{S}}\, \underline{\mathcal{F}}_c + \left(\underline{\underline{A}}_L \underline{\underline{W}} \tilde{\mathcal{K}}^T + \underline{\underline{B}}_L \underline{\underline{W}} \right) \underline{\mathcal{F}}_c \tag{2.20}$$

The first portion of the equation, $\underline{\gamma} = \underline{\underline{A}}_L \underline{\underline{Z}}\, \underline{\underline{S}}\, \underline{\mathcal{F}}_c$, provides a direct relationship between the sectional strains and stress resultants, $\underline{\gamma}$ and $\underline{\mathcal{F}}_c$, respectively, which can both be experimentally measured and the sectional compliance matrix, $\underline{\underline{S}}$. The remaining expression, $\left(\underline{\underline{A}}_L \underline{\underline{W}} \tilde{\mathcal{K}}^T + \underline{\underline{B}}_L \underline{\underline{W}} \right) \underline{\mathcal{F}}_c$, is a correction factor dependent on the nodal warping field. Since the warping field, which is dependent on both the geometric and material properties of the cross-section, cannot be measured directly and an analytical solution cannot be obtained for an arbitrary cross-section, it must be determined numerically. *SectionBuilder* is used to calculate the warping field, whose predominant role is to provide a correction to the shearing and torsional stiffness properties that would otherwise not be able to be determined experimentally. Thus, with knowledge of the sectional strains and stress resultants and the nodal warping field, the sectional compliance matrix, and therefore sectional stiffness matrix, can be calculated at discrete spanwise locations. However, several additional steps must be performed to put Eq. (2.20) into a form solvable for the compliance matrix.

2.2.1 Rotation of the Strain Components

In the current work, DIC is used to measure the deformation and strain on the external surface of the beam, with the strain measured in the directions normal and

tangent to the surface, denoted by basis $\mathcal{E} = (\bar{e}_1, \bar{e}_2, \bar{e}_3)$. Consider two representative cross-sections, as shown in Fig. 2.4. For the triangular cross-section, shown in Fig. 2.4(a), there are three discrete edges, whose tangent bases $\mathcal{E}$ are all generally rotated with respect to the reference basis $\mathcal{B}$. For the airfoil shaped cross-section, shown in Fig. 2.4(b), the external profile is a continuous curve whose tangent basis $\mathcal{E}$ is constantly changing orientation around the cross-section. Since the strain given by Eq. (2.20) is in basis $\mathcal{B}$, it is necessary to bring the data into a common basis. While strain measurements using DIC are the focus of this thesis, other common measurement techniques, such as strain gauges, also output strains in basis $\mathcal{E}$ and the change in basis will still be necessary, regardless of the measurement technique.

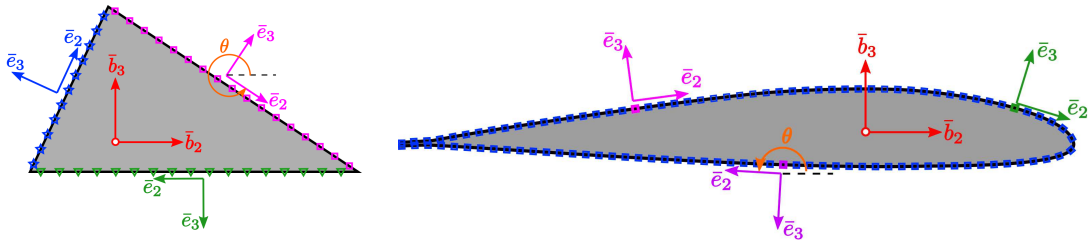

(a) Triangular cross-section.

(b) Airfoil cross-section.

Figure 2.4: External edge bases for example cross-sections.

The transformation between bases $\mathcal{B}$ and $\mathcal{E}$ consists of single rotation of θ about axis $\bar{b}_1$, as shown in Fig. 2.4. The rotation tensor that brings basis $\mathcal{B}$ to $\mathcal{E}$ is therefore defined by

$$\underline{\underline{R}}_\theta = \begin{bmatrix} 1 & 0 & 0 \\ 0 & C_\theta & -S_\theta \\ 0 & S_\theta & C_\theta \end{bmatrix} \tag{2.21}$$

and the strain rotation can be expressed as

$$\begin{bmatrix} \gamma_{11}^+ & \gamma_{12}^+ & \gamma_{13}^+ \\ \gamma_{12}^+ & \gamma_{22}^+ & \gamma_{23}^+ \\ \gamma_{13}^+ & \gamma_{23}^+ & \gamma_{33}^+ \end{bmatrix} = \underline{\underline{R}}_\theta^T \begin{bmatrix} \gamma_{11} & \gamma_{12} & \gamma_{13} \\ \gamma_{12} & \gamma_{22} & \gamma_{23} \\ \gamma_{13} & \gamma_{23} & \gamma_{33} \end{bmatrix} \underline{\underline{R}}_\theta \tag{2.22}$$

where notation $(\cdot)^+$ indicates the strain components resolved in basis $\mathcal{E}$. However, Eq. (2.20) uses the strain tensor in vectoral form and in terms of the engineering shear strain components instead of the tensor shear strain components (*i.e.* in terms of $2\gamma_{12}$, $2\gamma_{13}$, and $2\gamma_{23}$). By expanding the product on the right-hand side and rearranging into a vector equation, the relationship between the strain vector in basis $\mathcal{B}$ and basis $\mathcal{E}$ can be expressed as

$$\underline{\gamma}^+ = \underline{\underline{R}}_\epsilon^{-1} \underline{\gamma} \tag{2.23}$$

where

$$\underline{\underline{R}}_\epsilon = \begin{bmatrix} 1 & 0 & 0 & 0 & 0 & 0 \\ 0 & C_\theta & -S_\theta & 0 & 0 & 0 \\ 0 & S_\theta & C_\theta & 0 & 0 & 0 \\ 0 & 0 & 0 & C_\theta^2 & S_\theta^2 & -S_{2\theta} \\ 0 & 0 & 0 & S_\theta^2 & C_\theta^2 & S_{2\theta} \\ 0 & 0 & 0 & S_{2\theta}/2 & -S_{2\theta}/2 & C_{2\theta} \end{bmatrix} \tag{2.24}$$

There are two possible ways to bring the measured strains and Eq. (2.20) into a common basis. The first option is to bring the measured strain components into basis $\mathcal{B}$ using the relationship $\underline{\gamma} = \underline{\underline{R}}_\epsilon \underline{\gamma}^+$. While this relationship is straightforward, only three of the six strain components can actually be measured using DIC – γ_{11}^+, γ_{12}^+, and γ_{22}^+. The remaining three strain components can be calculated using the constitutive relationship and the fact that no surface traction is being applied; however, this requires knowledge of the material stiffness in basis $\mathcal{E}$ and the uncertainties in the assumed material properties and the measured strains will propagate into the calculation of the strains in basis $\mathcal{B}$. The second option is to rewrite Eq. (2.20) in basis $\mathcal{E}$, which can be accomplished by multiplying the entire equation by $\underline{\underline{R}}_\epsilon^{-1}$ to

give

$$\underline{\gamma}^{+} = \underline{\underline{R}}_{\epsilon}^{-1}\underline{\underline{A}}_{L}\underline{\underline{Z}}\,\underline{\underline{S}}\,\underline{\mathcal{F}} + \underline{\underline{R}}_{\epsilon}^{-1}\left(\underline{\underline{A}}_{L}\underline{\underline{W}}\tilde{\mathcal{K}}^{T} + \underline{\underline{B}}_{L}\underline{\underline{W}}\right)\underline{\mathcal{F}} \tag{2.25}$$

In this case, the rotation is applied only to the matrix of nodal locations, $\underline{\underline{A}}_{L}\underline{\underline{Z}}$, and the warping correction terms, $\underline{\underline{A}}_{L}\underline{\underline{W}}\tilde{\mathcal{K}}^{T} + \underline{\underline{B}}_{L}\underline{\underline{W}}$, which minimizes the impact on the uncertainties in the final stiffness properties.

2.2.2 Local Equilibrium Equations

Although the transformation applied in Eq. (2.20) is correct, the problem still remains that only three of the six strain components in $\underline{\gamma}^{+}$ can be measured. It will be shown later that, in most cases, the non-measured components will not be required; however, special cases may arise where these components are desired. These three strain components can be calculated using the local equilibrium conditions on the outer surface of the beam; since there is no applied surface traction, Newton's laws imply the vanishing of the stress component normal to the surface (τ_{33}^{+}) and of the two shear stress components acting in the surface plane (τ_{23}^{+} and τ_{13}^{+}). These three conditions provide the additional information needed to evaluate the three strain components that were not directly measured.

The constitutive relationship can be used to relate the stresses and strains but needs to be written in basis $\mathcal{E}$, which gives

$$\underline{\tau}^{+} = \underline{\underline{D}}^{+}\underline{\gamma}^{+} \tag{2.26}$$

The material stiffness matrix, $\underline{\underline{D}}$, is naturally defined in the material basis $\mathcal{B}^{*}$, as given by Eq. (2.10), and needs to be rotated into the local basis $\mathcal{E}$. This consists only of a rotation of γ about axis $\bar{e}_3$, which gives

$$\underline{\underline{D}}^{+} = \underline{\underline{R}}_{\sigma}^{+}\underline{\underline{D}}^{*}\underline{\underline{R}}_{\sigma}^{+T} \tag{2.27}$$

where

$$\underline{\underline{R}}_{\sigma}^{+} = \begin{bmatrix} C_\gamma^2 & -S_{2\gamma} & 0 & S_\gamma^2 & 0 & 0 \\ S_{2\gamma}/2 & C_{2\gamma} & 0 & -S_{2\gamma}/2 & 0 & 0 \\ 0 & 0 & C_\gamma & 0 & 0 & -S_\gamma \\ S_\gamma^2 & S_{2\gamma} & 0 & C_\gamma^2 & 0 & 0 \\ 0 & 0 & 0 & 0 & 1 & 0 \\ 0 & 0 & S_\gamma & 0 & 0 & C_\gamma \end{bmatrix} \tag{2.28}$$

In this form, the stresses and strains are partitioned according to the out-of-plane and in-plane components, respectively. An alternative means of partitioning the strains is by the measured and non-measured components, denoted by the subscripts $(\cdot)_m$ and $(\cdot)_n$, respectively, leading to

$$\begin{Bmatrix} \underline{\tau}_m^+ \\ \underline{\tau}_n^+ \end{Bmatrix} = \begin{bmatrix} \underline{\underline{D}}_{mm}^+ & \underline{\underline{D}}_{nm}^+ \\ \underline{\underline{D}}_{nm}^{+T} & \underline{\underline{D}}_{nn} \end{bmatrix} \begin{Bmatrix} \underline{\gamma}_m^+ \\ \underline{\gamma}_n^+ \end{Bmatrix} \tag{2.29}$$

where $\underline{\gamma}_m^{+T} = \left\{\gamma_{11}^+, \gamma_{12}^+, \gamma_{22}^+\right\}$, $\underline{\gamma}_n^{+T} = \left\{\gamma_{13}^+, \gamma_{33}^+, \gamma_{23}^+\right\}$, $\underline{\tau}_m^{+T} = \left\{\tau_{11}^+, \tau_{12}^+, \tau_{22}^+\right\}$, and $\underline{\tau}_n^{+T} = \left\{\tau_{13}^+, \tau_{33}^+, \tau_{23}^+\right\}$. With this partitioning, $\underline{\underline{D}}_{mm}^+$ contains the data initially in the first, second, and fourth rows and columns of Eq. (2.27), $\underline{\underline{D}}_{nm}^+$ contains the data from the first, second, and fourth rows, and third, fifth, and sixth columns, and $\underline{\underline{D}}_{nn}^+$ contains the data from the third, fifth, and sixth rows and columns. Using this notation, the local equilibrium conditions on the surface imply that $\underline{\tau}_n^{+T} = \underline{0}$, and substituting this into the bottom set of relationships in Eq. 2.29 gives

$$\underline{\gamma}_n^+ = \underline{\underline{D}}_{nn}^{+-1} \underline{\underline{D}}_{nm}^{+T} \underline{\gamma}_m^+ \tag{2.30}$$

and the complete strain tensor can thus be determined at any measurement location.

2.2.3 Compliance Matrix Equations

As written, Eq. (2.25) contains the sectional compliance in matrix form and thus can not readily be solved for these properties. Therefore, it is necessary to restructure the equations such that they represent a linear system of equations for the compliance matrix entries. The compliance matrix is symmetric, meaning that of the 36 terms, only 21 of them should be independent. The symmetry can therefore be imposed either before or after calculating the individual compliance properties from the measured values; both options will be considered below.

When the symmetry is assumed before calculating the compliance matrix entries, the product $\underline{\underline{S}}\,\underline{\mathcal{F}}_c$ from Eq. (2.25) can be recast as

$$\begin{aligned}\underline{\underline{S}}\,\underline{\mathcal{F}}_c &= \begin{bmatrix} S_{11} & S_{12} & S_{13} & S_{14} & S_{15} & S_{16} \\ S_{12} & S_{22} & S_{23} & S_{24} & S_{25} & S_{26} \\ S_{13} & S_{23} & S_{33} & S_{34} & S_{35} & S_{36} \\ S_{14} & S_{24} & S_{34} & S_{44} & S_{45} & S_{46} \\ S_{15} & S_{25} & S_{35} & S_{45} & S_{55} & S_{56} \\ S_{16} & S_{26} & S_{36} & S_{46} & S_{56} & S_{66} \end{bmatrix} \\ &= \underline{\underline{G}}_s\,\underline{S}_s \end{aligned} \tag{2.31}$$

where the following terms were defined

$$\underline{\underline{\mathbb{F}}}_1 = \begin{bmatrix} F_1 & F_2 & F_3 & M_1 & M_2 & M_3 \\ 0 & F_1 & 0 & 0 & 0 & 0 \\ 0 & 0 & F_1 & 0 & 0 & 0 \\ 0 & 0 & 0 & F_1 & 0 & 0 \\ 0 & 0 & 0 & 0 & F_1 & 0 \\ 0 & 0 & 0 & 0 & 0 & F_1 \end{bmatrix}, \quad \underline{\underline{\mathbb{F}}}_2 = \begin{bmatrix} 0 & 0 & 0 & 0 & 0 \\ F_2 & F_3 & M_1 & M_2 & M_3 \\ 0 & F_2 & 0 & 0 & 0 \\ 0 & 0 & F_2 & 0 & 0 \\ 0 & 0 & 0 & F_2 & 0 \\ 0 & 0 & 0 & 0 & F_2 \end{bmatrix}$$

$$\underline{\underline{\mathbb{F}}}_3 = \begin{bmatrix} 0 & 0 & 0 & 0 \\ 0 & 0 & 0 & 0 \\ F_3 & M_1 & M_2 & M_3 \\ 0 & F_3 & 0 & 0 \\ 0 & 0 & F_3 & 0 \\ 0 & 0 & 0 & F_3 \end{bmatrix}, \quad \underline{\underline{\mathbb{F}}}_4 = \begin{bmatrix} 0 & 0 & 0 \\ 0 & 0 & 0 \\ 0 & 0 & 0 \\ M_1 & M_2 & M_3 \\ 0 & M_1 & 0 \\ 0 & 0 & M_1 \end{bmatrix},$$

$$\underline{\underline{\mathbb{F}}}_5 = \begin{bmatrix} 0 & 0 \\ 0 & 0 \\ 0 & 0 \\ 0 & 0 \\ M_2 & M_3 \\ 0 & M_2 \end{bmatrix}, \quad \underline{\underline{\mathbb{F}}}_6 = \begin{bmatrix} 0 \\ 0 \\ 0 \\ 0 \\ 0 \\ M_3 \end{bmatrix}, \quad \underline{\underline{G}}_s = \left[\begin{array}{c|c|c|c|c|c} \underline{\underline{\mathbb{F}}}_1 & \underline{\underline{\mathbb{F}}}_2 & \underline{\underline{\mathbb{F}}}_3 & \underline{\underline{\mathbb{F}}}_4 & \underline{\underline{\mathbb{F}}}_5 & \underline{\underline{\mathbb{F}}}_6 \end{array} \right],$$

$$\underline{S}_s^T = \left\{ S_{11},S_{12},S_{13},S_{14},S_{15},S_{16} \middle| S_{22},S_{23},S_{24},S_{25},S_{26} \middle| S_{33},S_{34},S_{35},S_{36} \middle| S_{44},S_{45},S_{46} \middle| S_{55},S_{56} \middle| S_{66} \right\}$$

If the symmetry is assumed after the compliance matrix entries are calculated, the product $\underline{\underline{S}}\,\underline{\mathcal{F}}_c$ can be recast as

$$\begin{aligned} \underline{\underline{S}}\,\underline{\mathcal{F}}_c &= \begin{bmatrix} S_{11} & S_{12} & S_{13} & S_{14} & S_{15} & S_{16} \\ S_{21} & S_{22} & S_{23} & S_{24} & S_{25} & S_{26} \\ S_{31} & S_{32} & S_{33} & S_{34} & S_{35} & S_{36} \\ S_{41} & S_{42} & S_{43} & S_{44} & S_{45} & S_{46} \\ S_{51} & S_{52} & S_{53} & S_{54} & S_{55} & S_{56} \\ S_{61} & S_{62} & S_{63} & S_{64} & S_{65} & S_{66} \end{bmatrix} \begin{Bmatrix} F_1 \\ F_2 \\ F_3 \\ M_1 \\ M_2 \\ M_3 \end{Bmatrix} \\ &= \underline{\underline{G}}_u\,\underline{S}_u \end{aligned} \tag{2.32}$$

where

$$\underline{S}_u^T = \left\{ S_{11},S_{12},S_{13},S_{14},S_{15},S_{16} \middle| S_{21},S_{22},S_{23},S_{24},S_{25},S_{26} \middle| S_{31},S_{32},S_{33},S_{34},S_{35},S_{36} \middle| \cdots \right.$$
$$\left. S_{41},S_{42},S_{43},S_{44},S_{45},S_{46} \middle| S_{51},S_{52},S_{53},S_{54},S_{55},S_{56} \middle| S_{61},S_{62},S_{63},S_{64},S_{65},S_{66} \right\},$$

$$\underline{\underline{G}}_u = \left[\begin{array}{c|c|c|c|c|c} \underline{\mathcal{F}}_c^T & \underline{0} & \underline{0} & \underline{0} & \underline{0} & \underline{0} \\ \underline{0} & \underline{\mathcal{F}}_c^T & \underline{0} & \underline{0} & \underline{0} & \underline{0} \\ \underline{0} & \underline{0} & \underline{\mathcal{F}}_c^T & \underline{0} & \underline{0} & \underline{0} \\ \underline{0} & \underline{0} & \underline{0} & \underline{\mathcal{F}}_c^T & \underline{0} & \underline{0} \\ \underline{0} & \underline{0} & \underline{0} & \underline{0} & \underline{\mathcal{F}}_c^T & \underline{0} \\ \underline{0} & \underline{0} & \underline{0} & \underline{0} & \underline{0} & \underline{\mathcal{F}}_c^T \end{array}\right]$$

with $\underline{0}$ being a 1×6 vector of zeros. Using these expressions, Eq. (2.25) can be recast to a linear system of equations for the compliance properties as

$$\underline{\underline{R}}_\epsilon^{-1}\underline{\underline{A}}_L\underline{\underline{Z}}\,\underline{\underline{G}}\,\underline{S} = \underline{\gamma}^+ - \underline{\underline{R}}_\epsilon^{-1}\left(\underline{\underline{A}}_L\underline{\underline{W}}\tilde{\mathcal{K}}^T + \underline{\underline{B}}_L\underline{\underline{W}}\right)\underline{\mathcal{F}}_c \tag{2.33}$$

where for the term $\underline{\underline{G}}\,\underline{S}$, either the symmetric or unsymmetric form, $\underline{\underline{G}}_s\,\underline{S}_s$ or $\underline{\underline{G}}_u\,\underline{S}_u$, respectively, can be used.

2.2.4 *SectionBuilder* Data

Equation (2.33) was derived using the discretized equations for the finite element solution for the strain field – before trying to solve for the compliance properties it is therefore important to consider what each of the matrices and matrix products represents. In the experiments, the strains are measured at discrete locations around the cross-section, with the measurement locations indicated by the circles (●) in Fig. 2.5(a). The strain measurement at the i^{th} location in the cross-section, indicated by subscript $(\cdot)_i, i = 1, 2, \ldots, N$ where N is the number of strain measurements, is contained within the j^{th} element of the finite element mesh. Because the shape functions and their derivatives are only non-zero within the current element, the interpolation matrices $\underline{\underline{A}}_L$ and $\underline{\underline{B}}_L$ are only non-zero for the nodes within the current element.

Consider first the matrix product $\underline{\underline{A}}_L\underline{\underline{Z}}$; $\underline{\underline{A}}_L$ contains the shape functions as

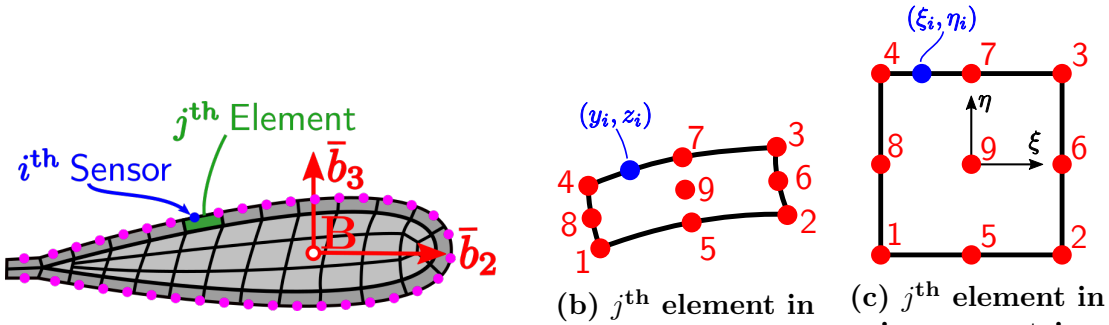

(a) Discretized airfoil cross-section. **(b) j^{th} element in physical space.** **(c) j^{th} element in isoparametric space.**

Figure 2.5: i^{th} measurement location in the finite element mesh.

defined by Eq. (2.15a) and $\underline{\underline{Z}}$ contains the nodal locations as defined by Eq. (2.17). The i^{th} strain measurement is defined at the location (ξ_i, η_i) within the isoparametric space corresponding to the location (y_i, z_i) in basis $\mathcal{B}$ for the j^{th} element, as seen in Fig. 2.5(b-c), and the shape functions are evaluated at these isoparametric coordinates. Expanding the product of theses matrices leads to

$$\left(\underline{\underline{A}}_L \underline{\underline{Z}}\right)_i = \begin{bmatrix} \sum N_l & 0 & 0 & 0 & \sum N_l z_l & -\sum N_l y_l \\ 0 & \sum N_l & 0 & -\sum N_l z_l & 0 & 0 \\ 0 & 0 & \sum N_l & \sum N_l y_l & 0 & 0 \\ 0 & 0 & 0 & 0 & 0 & 0 \\ 0 & 0 & 0 & 0 & 0 & 0 \\ 0 & 0 & 0 & 0 & 0 & 0 \end{bmatrix} \tag{2.34}$$

where all summations go from $l = 1$ to $l = n$, with n being the number of nodes per element. Using the basic properties of the shape functions, these individual expressions can be simplified to $\sum_{l=1}^{n} N_l = 1$, $\sum_{l=1}^{n} N_l y_l = y_i$, and $\sum_{l=1}^{n} N_l z_l = z_i$. Substituting in the above expressions and premultiplying by the inverse of the strain rotation matrix, given by Eq. (2.24), results in

$$\underline{\underline{U}}_i = \left(\underline{\underline{R}}_\epsilon^{-1}\underline{\underline{A}}_L\underline{\underline{Z}}\right)_i = \begin{bmatrix} 1 & 0 & 0 & 0 & z_i & -y_i \\ 0 & C_\theta & -S_\theta & -z_iC_\theta - y_iS_\theta & 0 & 0 \\ 0 & S_\theta & C_\theta & y_iC_\theta - z_iS_\theta & 0 & 0 \\ 0 & 0 & 0 & 0 & 0 & 0 \\ 0 & 0 & 0 & 0 & 0 & 0 \\ 0 & 0 & 0 & 0 & 0 & 0 \end{bmatrix} \tag{2.35}$$

The structure of $\underline{\underline{U}}_i$ leads to some important implications when solving for the compliance matrix. Since the last three rows of $\underline{\underline{U}}_i$ are all null, only three of the initial six equations provided by Eq. (2.33) for the compliance properties are nontrivial. These equations correspond to the first three strain components in $\underline{\gamma}^+$, which are the out-of-plane strains γ_{11}^+, γ_{12}^+, and γ_{13}^+; therefore, the in-plane strains γ_{22}^+, γ_{33}^+, and γ_{23}^+ have no impact on the calculation of the compliance properties. In addition, the j^{th} column of $\underline{\underline{U}}_i$ corresponds to data used to calculate the j^{th} row of the compliance matrix. Of the three out-of-plane strains, only the first two components, γ_{11}^+ and γ_{12}^+, are measured while the third component would need to be determined from the constitutive equations. However, from the structure of $\underline{\underline{U}}_i$, the first two rows contain non-zero entries in all columns and therefore all the compliance properties can be predicted using only the measured strains, as long as θ is sufficiently far from integer multiples of 90° such that both the cosine and sine components are non-zero.

To illustrate the importance of these properties of $\underline{\underline{U}}_i$, consider two types of representative cross-sectional geometries. The first type consists of external edges that are curved, such as a circular tube or rotor blade. In this case, the tangent basis $\mathcal{E}$ is constantly changing orientation around the cross-section and the angle θ can be sufficiently far from the integer multiples of 90° over a significant portion of the cross-section. Consider, for instance, a NACA 0012 and VR-7 airfoil profile as shown in Fig 2.6(a) The sine and cosine components of θ are shown in Fig. 2.6(b) for both

profiles as a function of the position along the external edge, s. For both airfoils, the curvature near the leading edge ($s \approx 0.4$ to 0.6) leads to significant sine and cosine components. For a symmetric airfoil, the sine component is close to zero for only a small portion of the external edge, which for a NACA 0012 profile occurs near the quarter chord location. For an unsymmetric airfoil, such as the VR-7 profile, the top surface tends to exhibit larger curvatures with a greater sine component, while the bottom surface tends to be flatter with a smaller sine component.

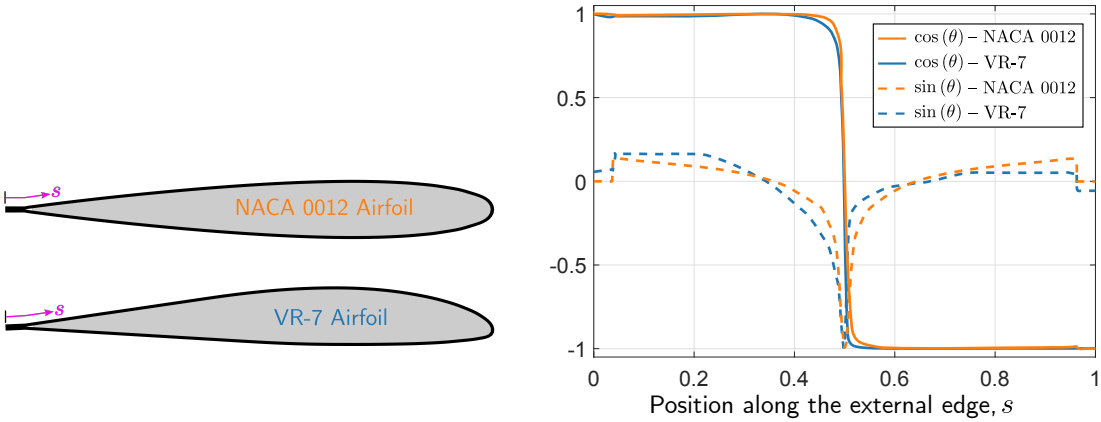

(a) Example airfoil profiles. **(b) Sine and cosine of θ for airfoils.**

Figure 2.6: Basis rotation components along external edge for NACA 0012 and VR-7 airfoils.

The second type of cross-section contains four perpendicular edges, such as a beam with a solid rectangular cross-section or a box-beam, which can be representative of certain rotor blade spars. While much simpler geometrically than the airfoil, these types of cross-sections can present more challenges when trying to measure all the compliance properties. When the edges are aligned parallel to the reference basis as shown in Fig. 2.7, the angle $\theta = 0°$, 90°, 180°, or 270°. If the strain were measured on at least two of the perpendicular edges, all 36 components of the compliance matrix could be measured. However, if one of the cross-sectional dimensions is sufficiently small, it may not be possible to measure the strain on these faces. For instance, with the DIC setup used in this thesis, strain measurements can only be obtained on faces with a minimum edge dimension of about 7 mm to 10 mm.

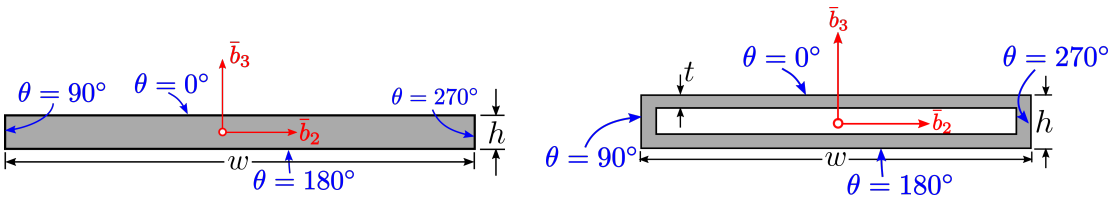

(a) Solid rectangular cross-section. **(b) Hollow rectangular cross-section.**

Figure 2.7: Example rectangular sections depicting rotation angles on external edges.

Although the current DIC setup is limited to measurements on faces with edge dimensions of at least 7 mm to 10 mm, if the beam is sufficiently thinner in one dimension, there will be minimal shear flow in that direction and therefore the shear strain in that direction will be small on the perpendicular edges. To illustrate this, the strains in the cross-sections shown in Fig. 2.7 were simulated for a shear force, F_3, in the direction of $\bar{b}_3$. The shear strain under this force is used to measure the compliance matrix component S_{33}, which is also related to the $-S_\theta$ component from the second row and third column of $\underline{\underline{U}}_i$. For the solid rectangular cross-section, widths of $w = 25$ mm and $w = 100$ mm and heights, h, varying from 0.5 mm to 25 mm were selected, while for the hollow rectangular cross-section, widths of $w = 25$ mm and $w = 100$ mm, a thickness of $t = 1.5$ mm and heights, h, varying from 4.5 mm to 25 mm were selected, which are representative of some commercially available beams. A total length of $l = 600$ mm was defined for the beams, with the magnitude of the shear force constrained by the resulting bending moment $M_2 = -F_3 l$ that resulted in a maximum bending strain of 3000 $\mu\epsilon$. For both types of cross-sections, an aluminum ($E = 68.9$ GPa, $\nu = 0.33$) and a composite material, with unidirectional plies of carbon-fiber ($E_1 = 130$ GPa, $E_2 = 8.69$ GPa, $\nu_{12} = 0.28$, $\nu_{23} = 0.33$, $G_{12} = 4.60$ GPa) in a ply sequence of $[-45°/45°/0°/90°]_s$, were considered.

The resulting shear strains under the shear force F_3 are shown in Fig. 2.8 for varying heights for both the aluminum and composite solid rectangular cross-sections. Figure 2.8(a) shows the mean shear strain component, $\bar{\gamma}^+_{13} = \frac{1}{n}\sum_{i=1}^{n}|\gamma^+_{13,i}|$, on the top

and bottom edges, at $\theta = 0°$ and $\theta = 180°$, which is not directly measurable using DIC (or most other strain measurement techniques) and must be calculated using the constitutive relationships. Figure 2.8(b) shows the mean shear strain component, $\bar{\gamma}^+_{12} = \frac{1}{n}\sum_{i=1}^{n}|\gamma^+_{12,i}|$, on the side edges, at $\theta = 90°$ and $\theta = 270°$, which can be directly measured using DIC if the height is $h \gtrapprox 10$ mm. Similarly, the shear strains for the hollow rectangular cross-section are shown in Fig. 2.9 for varying cross-sectional heights. Figure 2.9(a) shows the mean shear strain $\bar{\gamma}^+_{13}$ on the top and bottom edges of the hollow rectangular section, which is not directly measurable, while Fig. 2.9(b) shows the mean shear strain $\bar{\gamma}^+_{12}$ on the side edges, which can be measured if the height is $h \gtrapprox 10$ mm.

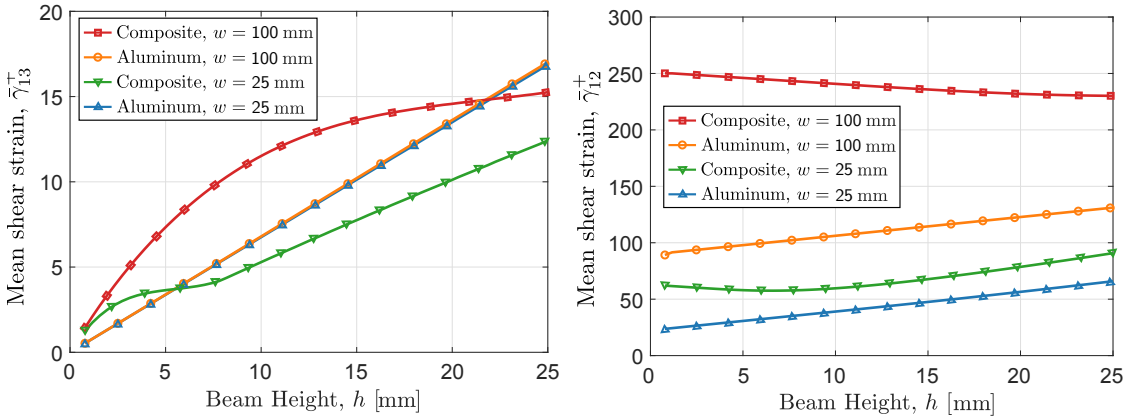

(a) Shear strain $\bar{\gamma}^+_{13}$ on top and bottom edges.

(b) Shear strain $\bar{\gamma}^+_{12}$ on the side edges.

Figure 2.8: Shear strain components used to predict the compliance matrix component S_{33} for the solid rectangular cross-section.

For both the solid and hollow rectangular cross-sections and for both material types, the shear strain component used for predicting the compliance matrix component S_{33} is much greater on the side edges than on the top and bottom edges. The shear strain component γ^+_{13} on the top and bottom edges can not be directly measured and, although it can be calculated from the constitutive equations, since it is on the order of 10 $\mu\epsilon$, it will have a very small signal to noise ratio. Because of this low signal to noise ratio, when the beam height is too small ($h \lessapprox 10$ mm) to

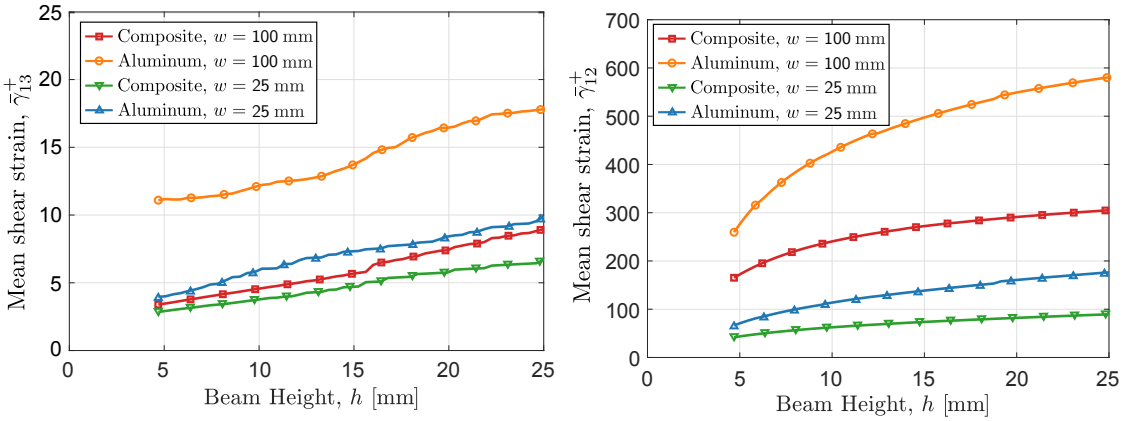

(a) Shear strain $\bar{\gamma}_{13}^{+}$ on top and bottom edges.

(b) Shear strain $\bar{\gamma}_{12}^{+}$ on the side edges.

Figure 2.9: Shear strain components used to predict the compliance matrix component S_{33} for the hollow rectangular cross-section.

be able to measure the strains on the side faces, the compliance matrix component S_{33} will need to be determined directly from the numerical model. While the airfoil and rectangular cross-sections considered here are not representative of all possible cross-sectional geometries, these results show that in most cases, the constitutive equations provide no additional information for measuring the compliance and stiffness matrices, either because the non-measured strain component is too close to 0 $\mu\epsilon$ or because the surface has enough curvature such that both the sine and cosine components of θ are non-zero.

When solving for the compliance matrix entries, $\underline{\underline{U}}_i$ is also multiplied by the load matrix $\underline{\underline{G}}$. The strain is measured under a discrete loading condition, which is indicated by superscript $(\cdot)^{(k)}, k = 1, 2, \cdots, L$ where L is the number of different loading conditions. If using the form of the force matrix in which symmetry is not initially assumed, given by Eq. (2.32), the product $\underline{\underline{H}}_i^{(k)} = \underline{\underline{U}}_i \underline{\underline{G}}_u^{(k)}$ becomes

$$\underline{\underline{H}}_i^{(k)} = \begin{bmatrix} \underline{\mathcal{F}}_c^{(k)^T} & 0 & 0 & 0 & z_i\underline{\mathcal{F}}_c^{(k)^T} & -y_i\underline{\mathcal{F}}_c^{(k)^T} \\ 0 & C_\theta\underline{\mathcal{F}}_c^{(k)^T} & -S_\theta\underline{\mathcal{F}}_c^{(k)^T} & (-z_iC_\theta - y_iS_\theta)\,\underline{\mathcal{F}}_c^{(k)^T} & 0 & 0 \\ 0 & S_\theta\underline{\mathcal{F}}_c^{(k)^T} & C_\theta\underline{\mathcal{F}}_c^{(k)^T} & (y_iC_\theta - z_iS_\theta)\,\underline{\mathcal{F}}_c^{(k)^T} & 0 & 0 \\ 0 & 0 & 0 & 0 & 0 & 0 \\ 0 & 0 & 0 & 0 & 0 & 0 \\ 0 & 0 & 0 & 0 & 0 & 0 \end{bmatrix} \tag{2.36}$$

Several important implications also arise from the form of $\underline{\underline{H}}_i^{(k)}$ when solving for the compliance matrix. Each entry in $\underline{\underline{H}}_i^{(k)}$ contains $\underline{\mathcal{F}}_c^{(k)^T}$ and the j^{th} component of $\underline{\mathcal{F}}_c^{(k)^T}$ is therefore used to calculate all six components in the j^{th} column of the compliance matrix. Because each row is dependent on all six components of the stress resultants, $\underline{\mathcal{F}}_c$, six linearly independent load cases must be applied during testing in order to measure all components of the compliance matrix uniquely. In addition, since each row of $\underline{\underline{H}}_i^{(k)}$ has three non-zero entries which are dependent on z_i and y_i, the strain measurements must be made at a minimum of three locations around the cross-section, with at least two different values of y_i and z_i for the measurements. For a cross-section with a curved external edge such as an airfoil, this means that data only needs to be measured over a portion of the entire external profile such that a sufficient variation in both y_i and z_i is obtained, which can be accomplished by measuring strain along only the upper or lower portion of the profile. However, for a rectangular cross-section, strains must be measured on at least two of the four edges to satisfy these requirements.

The remaining terms in Eq. (2.33) are the matrices corresponding to the warping correction, $\underline{\underline{R}}_\epsilon^{-1}\left(\underline{\underline{A}}_L\underline{\underline{W}}\tilde{\mathcal{K}}^T + \underline{\underline{B}}_L\underline{\underline{W}}\right)\underline{\mathcal{F}}_c$. The first part of the expression in parenthesis, $\underline{\underline{A}}_L\underline{\underline{W}}$, evaluates to a 6×6 matrix containing the components of the warping field at the i^{th} measurement location, with the last three rows all null. The second part, $\underline{\underline{B}}_L\underline{\underline{W}}$, contains the spatial derivatives of the components of the warping field. The warping correction is generally complicated for a curved beam with an

arbitrary cross-section; however, some insight can be provided by first considering the simple case of a straight beam (*i.e.* $|\underline{k}| = 0$). Because the curvature is zero, the majority of the terms in both the curvature tensor $\tilde{\mathcal{K}}$ and strain interpolation matrix $\underline{\underline{B}}_L$ also evaluate to zero and the warping correction, $\underline{\underline{V}}_i = \underline{\underline{R}}_\epsilon^{-1}\left(\underline{\underline{A}}_L\underline{\underline{W}}\tilde{\mathcal{K}}^T + \underline{\underline{B}}_L\underline{\underline{W}}\right)$ becomes

$$\underline{\underline{V}}_i = \begin{bmatrix} 0 & -W_{\alpha_1,6,i} & W_{\alpha_1,5,i} & 0 & 0 & 0 \\ A_{1,i} & A_{2,i} - W_{y,6,i} & A_{3,i} + W_{y,5,i} & A_{4,i} & A_{5,i} & A_{6,i} \\ B_{1,i} & B_{2,i} - W_{z,6,i} & B_{3,i} + W_{z,5,i} & B_{4,i} & B_{5,i} & B_{6,i} \\ C_{1,i} & C_{2,i} & C_{3,i} & C_{4,i} & C_{5,i} & C_{6,i} \\ D_{1,i} & D_{2,i} & D_{3,i} & D_{4,i} & D_{5,i} & D_{6,i} \\ E_{1,i} & E_{2,i} & E_{3,i} & E_{4,i} & E_{5,i} & E_{6,i} \end{bmatrix} \tag{2.37}$$

where $W_{k,l,i}$ corresponds to the component of the warping field in the k^{th} direction, induced by the l^{th} unit component of the sectional stress resultant, evaluated at the i^{th} measurement location on the cross-section and the following notation was introduced

$$\begin{aligned} A_{l,i} &= \frac{\partial W_{\alpha_1,l,i}}{\partial y}C_{\theta_i} - \frac{\partial W_{\alpha_1,l,i}}{\partial z}S_{\theta_i}, \qquad B_{l,i} = \frac{\partial W_{\alpha_1,l,i}}{\partial y}S_{\theta_i} + \frac{\partial W_{\alpha_1,l,i}}{\partial z}C_{\theta_i} \\ C_{l,i} &= \frac{\partial W_{y,l,i}}{\partial y}C_{\theta_i}^2 + \frac{\partial W_{z,l,i}}{\partial z}S_{\theta_i}^2 - \left(\frac{\partial W_{z,l,i}}{\partial y} + \frac{\partial W_{y,l,i}}{\partial z}\right)\frac{S_{2\theta_i}}{2} \\ D_{l,i} &= \frac{\partial W_{y,l,i}}{\partial y}S_{\theta_i}^2 + \frac{\partial W_{z,l,i}}{\partial z}C_{\theta_i}^2 + \left(\frac{\partial W_{z,l,i}}{\partial y} + \frac{\partial W_{y,l,i}}{\partial z}\right)\frac{S_{2\theta_i}}{2} \\ E_{l,i} &= \frac{\partial W_{y,l,i}}{\partial y}S_{2\theta_i} - \frac{\partial W_{z,l,i}}{\partial z}S_{2\theta_i} + \left(\frac{\partial W_{z,l,i}}{\partial y} + \frac{\partial W_{y,l,i}}{\partial z}\right)C_{2\theta_i} \end{aligned}$$

When calculating the entries of the compliance matrix, $\underline{\underline{V}}_i$ is multiplied by $\underline{\mathcal{F}}_c^{(k)}$ and this quantity then gets subtracted from the strain $\underline{\epsilon}^+$ to determine the full right-hand side of the linear system of equations. From the previous discussion of $\underline{\underline{H}}_i^{(k)}$, rows 1, 5, and 6 of the compliance matrix are calculated from the axial strain γ_{11}^+ while rows 2, 3, and 4 of the compliance matrix are calculated from the shear

strain γ_{12}^{+}. In addition, the j^{th} column of the compliance matrix is predicted from the j^{th} component of the sectional stress resultants. With this information and the nature of the first two rows of $\underline{\underline{V}}_i$ – corresponding to $\gamma_{11,i}^{+}$ and $\gamma_{12,i}^{+}$, respectively – it can be seen that the compliance matrix entries in rows 1, 5, and 6 and columns 1, 4, 5, and 6 have no dependencies on the warping terms and can therefore be calculated entirely from experimental data. For the simpler case of a cross-section made of an isotropic material, the warping field components $W_{\alpha_1,l,i}$ are 0 for $l = 1, 5$, and 6, and therefore only the compliance matrix entries in the smaller subset of rows 2, 3, and 4 and columns 2, 3, and 4 are dependent on the numerical warping correction.

For beams that are initially curved, $\underline{\underline{V}}_i$ will generally be fully populated and all the compliance matrix terms will therefore be impacted by the warping correction. However, the warping correction will not effect the calculation of each term from the compliance matrix equally and its importance can be considered by comparing the ratio of the first and second entries of $\underline{\underline{V}}_i\underline{\mathcal{F}}_c$ to the axial and shear strains, $\gamma_{11,i}^{+}$ and $\gamma_{12,i}^{+}$, respectively, for each component of the sectional stress resultant. Since the strains and $\underline{\underline{V}}_i$ are evaluated at each of the measurement locations around the external profile of the cross-section, the average ratio of these terms can be used, defined by

$$f_{\gamma_{11}^{+},j} = \frac{1}{N}\sum_{i=1}^{N}\left|\frac{\underline{\underline{V}}_{i,(1,j)}\underline{\mathcal{F}}_{c,j}}{\gamma_{11,i,j}^{+}}\right|, \qquad f_{\gamma_{12}^{+},j} = \frac{1}{N}\sum_{i=1}^{N}\left|\frac{\underline{\underline{V}}_{i,(2,j)}\underline{\mathcal{F}}_{c,j}}{\gamma_{12,i,j}^{+}}\right|, \tag{2.38}$$

where notation $\underline{\underline{V}}_{i,(1,j)}$ and $\underline{\underline{V}}_{i,(2,j)}$ is used to indicate the j^{th} column of the first and second rows of $\underline{\underline{V}}_i$, respectively, and notation $\gamma_{11,i,j}^{+}$ and $\gamma_{12,i,j}^{+}$ is used to indicate the total axial and shear strains, respectively, at the i^{th} measurement location and under loading from the j^{th} component of the sectional stress resultants. A ratio of zero indicates that the warping has no influence on the strain component under the current loading condition and the compliance matrix entries corresponding to that

strain and load are determined entirely from the experimental data. A ratio between 0 and 1 indicates that the warping induced strain is non-zero and of the same sign as the total strain, with a value of 0.5 indicating that the warping induced strain accounts for half of the total strain and a value of 1 indicating that the strain is entirely due to warping effects. A ratio greater than 1 indicates that the strain due to warping has an opposite effect from the classical strain measurement, given by $\underline{\underline{U}}_i \underline{\underline{S}} \underline{\mathcal{F}}_c$, and the warping correction will significantly impact the calculation of the corresponding compliance properties.

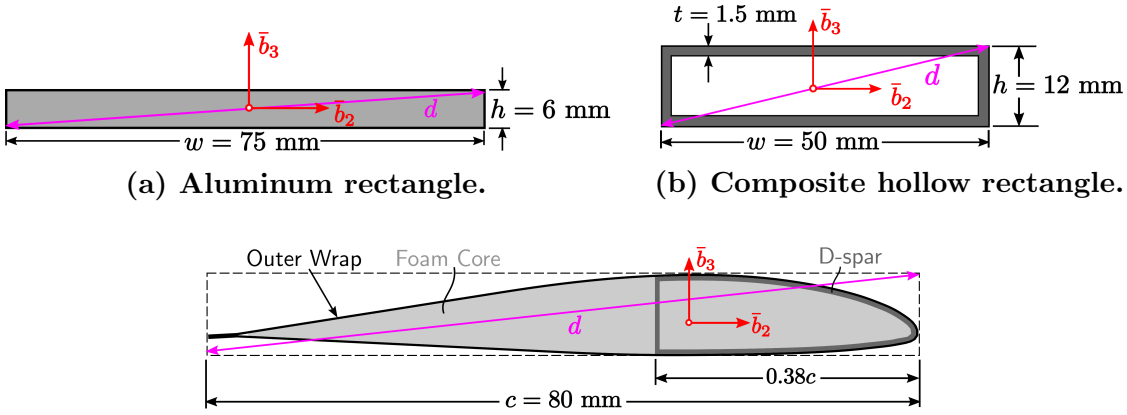

(a) Aluminum rectangle. **(b) Composite hollow rectangle.**

(c) VR-7 airfoil with a D-spar.

Figure 2.10: Cross-sections used for determining the ratio of warping induced strain to total strain.

These ratios were evaluated for beams with varying curvatures in each of the three directions, for three representative cross-sections. A non-dimensional form of the curvature, defined by $\bar{\kappa}_j = \kappa_j d$, was used to compare the results for different cross-sections, where d is the diagonal of the minimal box that fully encompasses the entire cross-section. An aluminum beam (E =68.9 GPa, nu = 0.33) with a solid rectangular cross-section, as shown in Fig. 2.10(a), was first considered, with dimensions of $h = 6$ mm and $w = 75$ mm. Next, a beam with a hollow rectangular cross-section was considered, as shown in Fig. 2.10(b), with dimensions of $h = 12$ mm, $w = 50$ mm, and $t = 1.5$ mm and made of a composite material, with unidirectional plies of carbon-fiber (E_1 =130 GPa, E_2 =8.69 GPa, $\nu_{12} = 0.28$, $\nu_{23} = 0.33$, G_{12} =4.60

GPa) in a ply sequence of $[-30°/90°/-45°/0°]_s$. The ply sequence was selected to produce extension-torsion and shear-bending coupling, which results in non-zero expressions for $S_{14/41}$, $S_{25/52}$, and $S_{36/63}$. Finally, a beam with a VR-7 profile was considered, as shown in Fig. 2.10(c), with a chord of 80 mm, an outer wrap consisting of a two layers of carbon-fiber at ±45°, a d-shaped spar going from the leading edge to $0.38c$ and composed of two layers of carbon-fiber at ±45°, and an internal foam core ($E = 3.6$ MPa, $\nu = 0.38$), with the carbon-fiber having the same material properties as that of the hollow rectangular section. For each cross-section, a beam with a moderate curvature, $\bar{\kappa}_j = 0.1$, and a large curvature, $\bar{\kappa}_j = 1$ were evaluated, with Fig. 2.11 showing the two levels of curvature for a beam curved in the plane of $\left(\bar{b}_1, \bar{b}_2\right)$. The moderate level of curvature is representative of that seen in some modern helicopter rotors, where, for example, the V-22 blades, which have a 47.5° twist over a 5.8 m radius, have an average non-dimensional twist of $\bar{\kappa}_1 \approx 0.105$ [121].

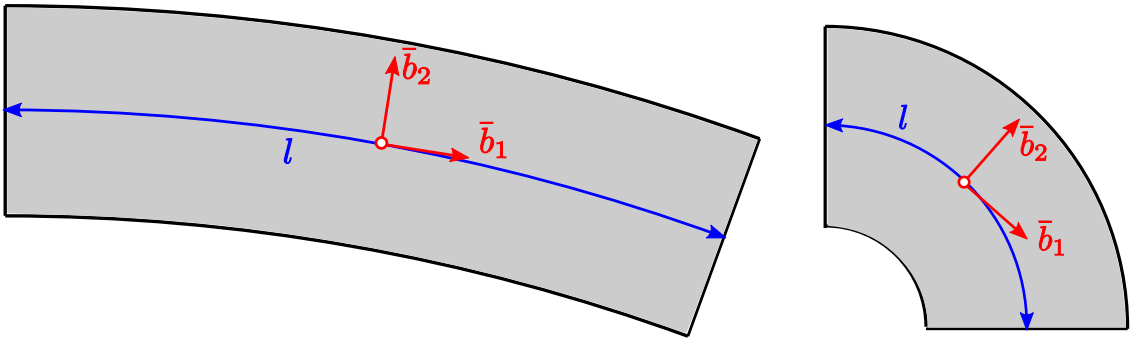

(a) $\bar{\kappa}_3 = 0.1$ **(b)** $\bar{\kappa}_3 = 1$

Figure 2.11: Example beams curved in the plane of $\left(\bar{b}_1, \bar{b}_2\right)$.

The ratios of the warping induced strain to the total strain under a load from the j^{th} component of the sectional stress resultants are shown in Table 2.1 for the aluminum beam with the rectangular cross-section. As stated earlier, the first, fifth, and sixth rows of the compliance matrix are calculated using the measured axial strains, $\gamma^+_{11,i}$, and the second, third, and fourth rows are calculated using the measured shear strains, $\gamma^+_{12,i}$, while the j^{th} column of the compliance matrix is calculated from a load in the j^{th} component of the sectional stress resultants. For

the straight beam, the axial strain components have no dependency on the warping correction, so the first, fifth and sixth rows of the compliance matrix, corresponding to the axial and bending behavior of the beam, can be determined entirely from the experimental measurements. For moderately curved beams with $\bar{\kappa}_j = 0.1$, the effect of warping remains relatively small on these terms, which means that the axial and bending behavior is still almost entirely determined by the experimental data, with the exception of the bending compliance about $\bar{b}_3$ when the beam is curved about axis $\bar{b}_2$, where the ratio is $f_{\gamma^+_{11,6}} = 0.365$. For very highly curved beams, where $\bar{\kappa}_j = 1$, these ratios begin to approach and, in some cases, exceed values of 1 and the warping correction becomes a significant factor for calculating the axial and bending compliances. For the straight beam, the second components of the second, third, and fourth rows have a ratio $f_{\gamma^+_{12,2}} \approx 0.2$, which means that the warping effects will account for about 20% of the total compliance, and therefore shear stiffness, about axis $\bar{b}_2$. Since $f_{\gamma^+_{13,2}} = 1$, the shear compliance about axis $\bar{b}_3$, will be entirely determined from the warping effects. The ratio $f_{\gamma^+_{12,4}} \approx 0.5$, which means that the torsional compliance would be calculated at twice its expected value (*i.e.* the torsional stiffness would be 50% of its expected value) if the numerical warping correction were not included. For moderate levels of curvature where $\bar{\kappa}_j = 0.1$, the ratios $f_{\gamma^+_{12,2}}$, $f_{\gamma^+_{12,3}}$, and $f_{\gamma^+_{12,4}}$ all remain similar to those of the straight beam and the warping effect on the shear and torsional compliance terms will remain similar. However, for highly curved beams with $\bar{\kappa}_j = 1$, the warping induced strains are significantly impacted by the curvature, which can be seen in the ratios $f_{\gamma^+_{12,2}}$ and $f_{\gamma^+_{12,4}}$.

Table 2.1: Ratios of warping induced to total strain for the aluminum rectangular cross-section with various beam curvatures

	Straight	Twisted		Curved about $\bar{b}_2$		Curved about $\bar{b}_3$	
	$\bar{\kappa} = 0$	$\bar{\kappa}_1 = 0.1$	$\bar{\kappa}_1 = 1$	$\bar{\kappa}_2 = 0.1$	$\bar{\kappa}_2 = 1$	$\bar{\kappa}_3 = 0.1$	$\bar{\kappa}_3 = 1$
$f_{\gamma^+_{11,1}}$	0	0.068	1.273	0.078	1.214	0.006	0.595
$f_{\gamma^+_{11,2}}$	0	0.497	1.033	0	0	0	0
$f_{\gamma^+_{11,3}}$	0	2.253	1.090	0	0	0	0
$f_{\gamma^+_{11,4}}$	0	1.571	1.749	0	0	0	0
$f_{\gamma^+_{11,5}}$	0	0.002	0.134	0	0	0.016	0.741
$f_{\gamma^+_{11,6}}$	0	0.012	1.190	0.365	1.101	0.005	0.121
$f_{\gamma^+_{12,1}}$	0	0.507	0.498	0	0	0	0
$f_{\gamma^+_{12,2}}$	0.199	0.233	8.592	0.228	1.736	0.206	0.675
$f_{\gamma^+_{12,3}}$	1.000	1.000	1.000	1.000	1.000	0.984	0.976
$f_{\gamma^+_{12,4}}$	0.500	0.499	0.450	0.520	1.220	0.499	0.752
$f_{\gamma^+_{12,5}}$	0	23.180	12.233	0	0	0	0
$f_{\gamma^+_{12,6}}$	0	1.000	1.000	0	0	0	0

The ratios of the warping induced strains to the total strains for the composite hollow rectangular and composite VR-7 airfoil cross-sections are shown in Table 2.2 and Table 2.3, respectively. For the straight beam with a composite hollow rectangular cross-section, the ratios that correspond to the shear and torsional compliance terms, $f_{\gamma^+_{12,2}} = 0.159$, $f_{\gamma^+_{12,3}} = 1.000$, and $f_{\gamma^+_{12,4}} = 0.409$ are of similar magnitudes to those of the aluminum rectangular cross-section. The ratios $f_{\gamma^+_{11,4}}$ and $f_{\gamma^+_{12,1}}$, used when calculating S_{14} and S_{41}, $f_{\gamma^+_{11,2}}$ and $f_{\gamma^+_{12,5}}$, used when calculating S_{25} and S_{52}, and $f_{\gamma^+_{11,3}}$ and $f_{\gamma^+_{12,6}}$, used when calculating S_{36} and S_{63}, are all important due to the elastic coupling introduced by the ply layup. While the compliance matrix should be symmetric, the warping induced strain does not equally impact

the corresponding symmetric terms, which can be seen when comparing the ratios $f_{\gamma^+_{11,4}} = 0$ and $f_{\gamma^+_{12,1}} = 0.411$ used for computing the symmetric terms S_{14} and S_{41}, respectively. Generally, one of these symmetric compliance terms can be calculated with very little influence from the warping correction, as seen by the fact that $f_{\gamma^+_{11,4}} = 0$, $f_{\gamma^+_{12,5}} = 0.022$, and $f_{\gamma^+_{11,3}} = 0.022$, while the other compliance component is more heavily influenced by the warping correction. For the straight beam with the VR-7 airfoil, the selected layup presents no elastic coupling terms and the only ratios that effect the calculation of the non-zero compliance properties are $f_{\gamma^+_{11,1}}$, $f_{\gamma^+_{12,2}}$, $f_{\gamma^+_{12,3}}$, $f_{\gamma^+_{12,}}$, $f_{\gamma^+_{11,5}}$, and $f_{\gamma^+_{11,6}}$. For the airfoil, the warping induced strain only accounts for about 20% of the total strain from a torsional load used when calculating the torsional compliance, which is much smaller than the 40% to 50% in the rectangular cross-sections. In addition, the ratio $f_{\gamma^+_{12,3}}$ becomes 0.586 compared to 1.000 for both rectangular sections, and the shear compliance about axis $\bar{b}_3$ will no longer be entirely determined from warping effects. For both the composite hollow rectangular and

Table 2.2: Ratios of warping induced to total strain for the composite hollow rectangular cross-section with various beam curvatures

	Straight	Twisted		Curved about $\bar{b}_2$		Curved about $\bar{b}_3$	
	$\bar{\kappa} = 0$	$\bar{\kappa}_1 = 0.1$	$\bar{\kappa}_1 = 1$	$\bar{\kappa}_2 = 0.1$	$\bar{\kappa}_2 = 1$	$\bar{\kappa}_3 = 0.1$	$\bar{\kappa}_3 = 1$
$f_{\gamma^+_{11,1}}$	0	0.058	1.824	0.151	0.737	0.011	1.321
$f_{\gamma^+_{11,2}}$	0.231	0.664	1.046	0.461	1.034	0.446	1.108
$f_{\gamma^+_{11,3}}$	0.022	0.458	1.309	0.136	0.932	0.050	1.069
$f_{\gamma^+_{11,4}}$	0	0.233	2.329	0.009	0.851	0.023	1.250
$f_{\gamma^+_{11,5}}$	0	0.005	1.183	0.000	0.000	0.030	1.171
$f_{\gamma^+_{11,6}}$	0	0.116	2.288	0.118	1.328	0.009	0.203
$f_{\gamma^+_{12,1}}$	0.411	0.422	0.418	0.484	1.064	0.428	0.922
$f_{\gamma^+_{12,2}}$	0.159	0.717	1.105	0.942	1.013	0.218	1.339
$f_{\gamma^+_{12,3}}$	1.000	1.000	1.000	1.000	1.000	0.992	0.981
$f_{\gamma^+_{12,4}}$	0.409	0.320	1.533	0.423	0.965	0.412	0.948
$f_{\gamma^+_{12,5}}$	0.022	0.021	1.106	0.126	1.133	0.046	0.580
$f_{\gamma^+_{12,6}}$	1.000	1.000	1.000	1.000	1.000	1.016	0.832

airfoil cross-sections, moderate levels of curvature only have a minor impact on most of the ratios important for calculating the non-zero compliance components, with exception to the ratios $f_{\gamma^+_{11,2}}$, $f_{\gamma^+_{11,3}}$, and $f_{\gamma^+_{12,2}}$ for the composite hollow rectangular cross-section and $f_{\gamma^+_{12,2}}$ and $f_{\gamma^+_{12,3}}$ for the composite airfoil.

Table 2.3: Ratios of warping induced to total strain for the composite VR-7 airfoil cross-section with various beam curvatures

	Straight	Twisted		Curved about $\bar{b}_2$		Curved about $\bar{b}_3$	
	$\bar{\kappa} = 0$	$\bar{\kappa}_1 = 0.1$	$\bar{\kappa}_1 = 1$	$\bar{\kappa}_2 = 0.1$	$\bar{\kappa}_2 = 1$	$\bar{\kappa}_3 = 0.1$	$\bar{\kappa}_3 = 1$
$f_{\gamma^+_{11,1}}$	0	0.025	1.236	0.066	0.496	0.046	0.815
$f_{\gamma^+_{11,2}}$	0.398	0.396	0.954	0.562	1.022	0.689	0.918
$f_{\gamma^+_{11,3}}$	0.910	3.481	1.251	0.840	0.902	0.973	1.002
$f_{\gamma^+_{11,4}}$	0	0.927	2.816	0.025	0.882	0.159	1.045
$f_{\gamma^+_{11,5}}$	0	0.007	0.168	0.000	0.000	0.024	0.328
$f_{\gamma^+_{11,6}}$	0	0.126	1.363	0.022	0.631	0.018	0.212
$f_{\gamma^+_{12,1}}$	0.364	4.294	5.585	0.938	0.976	0.358	1.074
$f_{\gamma^+_{12,2}}$	0.506	1.850	1.338	0.978	1.053	0.659	1.023
$f_{\gamma^+_{12,3}}$	0.586	0.710	0.974	0.902	1.055	0.704	1.051
$f_{\gamma^+_{12,4}}$	0.198	0.196	0.839	0.203	1.106	0.182	1.042
$f_{\gamma^+_{12,5}}$	0.790	28.003	0.527	1.388	0.847	0.976	0.721
$f_{\gamma^+_{12,6}}$	1.358	0.557	0.943	1.261	0.994	1.340	1.563

Overall, the axial and bending compliances can be measured directly in the experiments with little impact from the numerical warping correction for beams of arbitrary cross-section that are either straight or have moderate levels of curvature. However, the shear and torsional compliances require both the experimental measurements and the numerical warping correction, with the impact of the warping correction dependent on the type of cross-section.

2.3 Solution Procedure

The equations discussed up to this point have been for a measurement at a discrete location within the cross-section under a single loading condition, which provides at most three linearly independent equations for the 36 unknown terms in the compliance matrix. In the actual experiment, data needs to be acquired at multiple locations within the cross-section and under multiple loading conditions to provide enough information to fully determine the compliance matrix components. This complete set of data then needs to be collected to provide a fully determined system of equations that can be used to solve for the compliance properties. Once the compliance matrix has been calculated, the sectional stiffness matrix can then be determined.

2.3.1 Matrix Assembly

Using the notation introduced in Sec. 2.2.4, the equations for a single measurement at the i^{th} location and under the k^{th} load can be written in a compact form as

$$\underline{\underline{H}}_i^{(k)} \underline{S} = \underline{\gamma}_i^{+,(k)} - \underline{\underline{V}}_i \underline{\mathcal{F}}_c^{(k)} \tag{2.39}$$

While this represents a 6×6 system of equations, it was shown that the last three rows of $\underline{\underline{H}}_i^{(k)}$ are null and the row corresponding to the shear strain component γ_{13}^{+} often provides no additional information. Therefore, only the first two rows in Eq. 2.39 will be used for calculating the compliance properties. This will be indicated using the subscript $(\cdot)_{(1:2,1:6)}$ for the matrices, $\underline{\underline{H}}_{i,(1:2,1:6)}^{(k)}$ and $\underline{\underline{V}}_{i,(1:2,1:6)}$, to indicate the first two rows and all 6 columns of these matrices and $\underline{\gamma}_{i,(1:2)}^{+,(k)}$ to indicate the first two entries in the strain vector, $\gamma_{11,i}^{+,(k)}$ and $\gamma_{12,i}^{+,(k)}$. The measurements are made at N locations around the cross-section under L loading conditions and the total data can

be collected into a single set of linear equations defined by

$$\begin{bmatrix} \underline{\underline{H}}^{(1)}_{1,(1:2,1:6)} \\ \vdots \\ \underline{\underline{H}}^{(1)}_{N,(1:2,1:6)} \\ \hline \underline{\underline{H}}^{(2)}_{1,(1:2,1:6)} \\ \vdots \\ \underline{\underline{H}}^{(2)}_{N,(1:2,1:6)} \\ \hline \vdots \\ \hline \underline{\underline{H}}^{(L)}_{1,(1:2,1:6)} \\ \vdots \\ \underline{\underline{H}}^{(L)}_{N,(1:2,1:6)} \end{bmatrix} \underline{S} = \left\{ \begin{array}{c} \underline{\gamma}^{+,(1)}_{1,(1:2)} \\ \vdots \\ \underline{\gamma}^{+,(1)}_{N,(1:2)} \\ \hline \underline{\gamma}^{+,(2)}_{1,(1:2)} \\ \vdots \\ \underline{\gamma}^{+,(2)}_{N,(1:2)} \\ \hline \vdots \\ \hline \underline{\gamma}^{+,(L)}_{1,(1:2)} \\ \vdots \\ \underline{\gamma}^{+,(L)}_{N,(1:2)} \end{array} \right\} - \left\{ \begin{array}{c} \underline{\underline{V}}_{1,(1:2,1:6)} \underline{\mathcal{F}}^{(1)}_{c} \\ \vdots \\ \underline{\underline{V}}_{N,(1:2,1:6)} \underline{\mathcal{F}}^{(1)}_{c} \\ \hline \underline{\underline{V}}_{1,(1:2,1:6)} \underline{\mathcal{F}}^{(2)}_{c} \\ \vdots \\ \underline{\underline{V}}_{N,(1:2,1:6)} \underline{\mathcal{F}}^{(2)}_{c} \\ \hline \vdots \\ \hline \underline{\underline{V}}_{1,(1:2,1:6)} \underline{\mathcal{F}}^{(L)}_{c} \\ \vdots \\ \underline{\underline{V}}_{N,(1:2,1:6)} \underline{\mathcal{F}}^{(L)}_{c} \end{array} \right\} - \tag{2.40}$$

which can be recast into a compact form as

$$\underline{\underline{\mathbb{H}}}\,\underline{S} = \underline{\mathbb{E}} - \underline{\mathbb{V}} \tag{2.41}$$

where $\underline{\underline{\mathbb{H}}}$ will be of size $m \times n$, where $m = 2NL$ and n is either 21 or 36, depending on whether or not the compliance matrix is initially assumed to be symmetric.

2.3.2 Compliance Matrix Calculation

Since DIC provides data at a significant number of locations around the cross-section, Eq. (2.41) will generally represent an over-determined set of linear equations for the components of the sectional compliance matrix. Because there will also be noise in the experimental measurements, there is no $\underline{S}$ that will exactly satisfy Eq. (2.41) and a solution that minimizes the residual

$$\underline{r} = \underline{\underline{\mathbb{H}}}\,\underline{S} - (\underline{\mathbb{E}} - \underline{\mathbb{V}}) \tag{2.42}$$

is therefore desired. This represents a linear least squares problem for the compliance matrix components, which can be solved using several numerical approaches. Since the problem is unconstrained but ill-conditioned, with condition numbers generally between 10^4 and 10^6, a method such as the singular value decomposition (SVD) or QR decomposition is best suited for calculating the solution. The SVD is numerically stable and less sensitive to perturbations than the QR factorization, but is more expensive to compute, with a cost of $\approx 2mn^2 + 11n^3$ floating point operations (flops) compared to a cost of $\approx 2mn^2 - 2n^3/3$ flops for the QR factorization [122]. However, because the minimum number of load cases is six and DIC will generally provide at least 100 strain measurements for a given cross-section, $m \gtrapprox 1200 \gg n$ and the cost for both methods will be dominated by the $2mn^2$ term with the total cost ending up being similar. Thus, the SVD is used to solve the linear system of equations for $\underline{S}$, since it is numerically stable and has a similar cost to the QR decomposition for the large problem sizes expected when using DIC.

Applying the singular value decomposition to $\underline{\underline{\mathbb{H}}}$ gives

$$\underline{\underline{\mathbb{H}}} = \underline{\underline{\mathcal{U}}}\,\underline{\underline{\Sigma}}\,\underline{\underline{\mathcal{V}}}^T \tag{2.43}$$

where matrix $\underline{\underline{\Sigma}}$ is a $m \times n$ matrix with the singular values along its diagonal and $\underline{\underline{\mathcal{U}}}$ and $\underline{\underline{\mathcal{V}}}$ are unitary matrices, of size $m \times m$ and $n \times n$, respectively, containing the left and right singular vectors, as discussed in Appendix A. Substituting Eq. (2.43) into Eq. (2.41) leads to

$$\underline{\underline{\mathcal{U}}}\,\underline{\underline{\Sigma}}\,\underline{\underline{\mathcal{V}}}^T\,\underline{S} = \underline{\mathbb{E}} - \underline{\mathbb{V}} \tag{2.44}$$

and the solution for the compliance matrix components becomes

$$\underline{S} = \underline{\underline{\mathcal{V}}}\,\underline{\underline{\Sigma}}^{-1}\,\underline{\underline{\mathcal{U}}}^T\,(\underline{\mathbb{E}} - \underline{\mathbb{V}}) \tag{2.45}$$

In $\underline{\underline{\Sigma}}$ there are only n non-zero singular values, corresponding to the number of unknowns in the compliance matrix, and only a subset of the left singular vectors in $\underline{\underline{\mathcal{U}}}$ are needed for the calculation of $\underline{S}$ as the majority will multiplied by the null vectors in $\underline{\underline{\Sigma}}$. Since $m \gg n$, the computation of these extra left singular vectors is very costly, both in terms of time and storage, and a reduced form of the SVD can be calculated that contains only the first n left singular vectors in $\underline{\underline{\mathcal{U}}}$, as described in Appendix A.2. Implementations of the reduced SVD are readily available through tools like the Fortran package *PROPACK* and the MATLAB routine *svd*, with Fig. 2.12 showing the increased efficiency of the compact SVD over the full SVD in terms of wall clock time in MATLAB for different values of m in $\underline{\underline{\mathbb{H}}}$. For the experiments in the current work, most beams will be subjected to between 10 and 12 load cases and strain measurements will be obtained at around 250 point per cross-section, meaning that the total number of rows in $\underline{\underline{\mathbb{H}}}$ will be around $m \approx 2500$ to 3000. This means that the total time to calculate the SVD would be about 3 s if using the full SVD compared to about 5 to 10 ms if using the reduced SVD, which is a reduction in run time by about three orders of magnitude. While additional time is required for the matrix assembly and multiplications in the full solution process, the full SVD takes up about 90% of the total solution time and switching to a compact SVD still reduces the total solution by an order of magnitude. This is especially important when considering the fact that the DIC data is obtained across a significant portion of the span of the beam and, if calculating the cross-sectional properties at multiple span-wise locations, this can reduce the total run time from several minutes down to several seconds.

The final stage in then to reconstruct the compliance matrix from the solution given by Eq. (2.45). If the form of the equations in which symmetry was assumed at the onset was used, corresponding to $\underline{\underline{G}}_s$ and $\underline{S}_s$, the compliance matrix can simply be reconstructed by substituting the entries S_{ij} into the i^{th} row and j^{th} column and

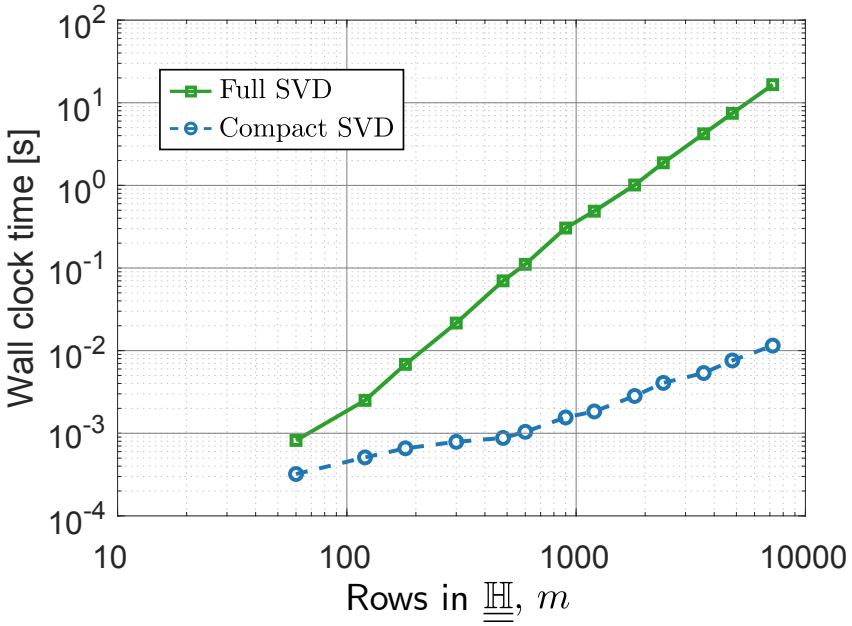

Figure 2.12: Run time of SVD implementations for different problem sizes m.

j^{th} row and i^{th} column. If the form of the equations in which symmetry was not initially assumed was used, corresponding to $\underline{\underline{G}}_u$ and $\underline{S}_u$, some additional steps must be taken to enforce symmetry. In this case, the terms that should be equivalent in the compliance matrix (S_{ij} and S_{ji}) are calculated from different combinations of the applied loads and strains, which have different errors associated with them, and are impacted differently by the numerical warping correction, as discussed in Sec. 2.2.4. Asymmetries will then be introduced because one of the terms is calculated using measurements that have relatively low signal to noise ratios, where a small error can easily produce a significant compliance component that would otherwise be small or zero. This situation can often arise in terms calculated from applied shear forces, F_2 and F_3, that have small expected strains, as the bending moments resulting from these applied shear forces typically generate much larger strains. Therefore, the

following two conditions are applied to eliminate significant asymmetries

$$\text{if } sgn(S_{u,ij}) \neq sgn(S_{u,ji}) \qquad \text{then } S_{u,ij} = S_{u,ji} = 0 \tag{2.46a}$$

$$\text{if } \frac{S_{u,ij}}{S_{u,ji}} > 10 \text{ or } \frac{S_{u,ji}}{S_{u,ij}} > 10 \qquad \text{then } S_{u,ij} = S_{u,ji} = 0 \tag{2.46b}$$

where the first condition eliminates terms of opposite signs and the second condition eliminates terms that differ by more than an order of magnitude. Finally, the symmetric compliance matrix can be calculated from the unsymmetric form by

$$\underline{\underline{S}} = \frac{\underline{\underline{S}}_u + \underline{\underline{S}}_u^T}{2} \tag{2.47}$$

which averages the non-zero off-diagonal terms. Since the form in which symmetry is initially assumed has no way of eliminating off-diagonal compliance components that arise solely from error in a measurement with a very low signal to noise ratio, the unsymmetric form is used for all the experimental data in this thesis.

2.3.3 Stiffness Matrix Calculation

Once the sectional compliance matrix has been calculated, it becomes straightforward to calculate the stiffness matrix as its inverse defined by

$$\underline{\underline{K}} = \underline{\underline{S}}^{-1} \tag{2.48}$$

While the dimensional form of the stiffness matrix given by Eq. (2.48) is the format required for most beam codes, it is also useful to consider the stiffness matrix in a non-dimensional form, where the term in the i^{th} row and j^{th} column is normalized according to

$$K_{n,ij} = \sqrt{\frac{K_{ij}^2}{K_{ii}K_{jj}}} \tag{2.49}$$

With this definition, the terms along the diagonal, where $i = j$, evaluate to 1 and the terms on the off-diagonal, where $i \neq j$, take on a value between 0 and 1. When the normalized off-diagonal terms are much less than 1, they are insignificant to the overall response of the beam, in terms of the static or dynamic behavior and the resultant stresses and strains. Therefore, this provides a means of determining the significance of the measured off-diagonal components of the stiffness matrix.

2.3.4 Principal Axes of Bending

The principal axes of bending are defined by frame $\mathcal{F}_C = [\mathbf{C}, \mathcal{C} = (\bar{c}_1, \bar{c}_2, \bar{c}_3)]$, as shown in Fig. 2.13. Their origin $\mathbf{C}$ is at the centroid of the cross-section, the location where an applied axial load, in the direction $\bar{b}_1 = \bar{c}_1$, produces no bending deformation. The axes are also oriented at an angle α_{pb} with respect to basis $\mathcal{B}$, with the angle defined such that the cross-bending stiffness K_{56} becomes zero and the bending stiffness components K_{55} and K_{66} are maximized [119].

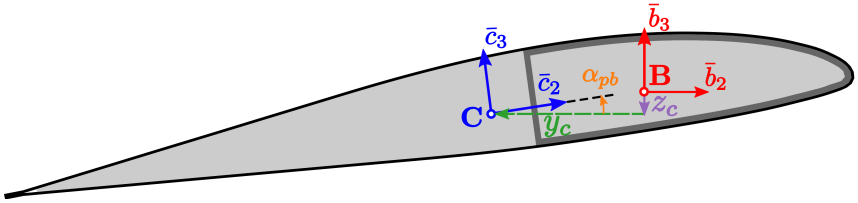

Figure 2.13: Centroid and principal axes of bending.

The location of the centroid can be determined from the stiffness components relating the axial and bending behavior, K_{15} and K_{16}, according to

$$y_c = -\frac{K_{16}}{K_{11}}, \quad z_c = \frac{K_{15}}{K_{11}} \tag{2.50}$$

where y_c and z_c are the distances along axis $\bar{b}_2$ and $\bar{b}_3$, respectively. Defining an intermediate frame $\mathcal{F}_{C^*} = [\mathbf{C}, \mathcal{C}^* = (\bar{c}_1^*, \bar{c}_2^*, \bar{c}_3^*)]$ whose origin is at the centroid but whose axes $\bar{c}_2^*$ and $\bar{c}_3^*$ are parallel to $\bar{b}_2$ and $\bar{b}_3$, respectively, the axial and bending

stiffness components become

$$\begin{aligned} K_{11}^{c*} &= K_{11}, \qquad K_{15}^{c*} = 0, \qquad K_{16}^{c*} = 0, \\ K_{55}^{c*} &= K_{55} - \frac{K_{15}^2}{K_{11}} = K_{55} - z_c K_{15}, \\ K_{56}^{c*} &= K_{56} - \frac{K_{15}K_{16}}{K_{11}}, \\ K_{66}^{c*} &= K_{66} - \frac{K_{16}^2}{K_{11}} = K_{66} + y_c K_{16} \end{aligned} \tag{2.51}$$

where $(\cdot)^{c*}$ indicates components resolved in basis $\mathcal{C}^*$. The orientation of the principal axes, defined by angle α_{pb}, is then determined by

$$\alpha_{pb} = 0.5 \tan^{-1}\left(\frac{-2K_{56}^{c*}}{K_{66}^{c*} - K_{55}^{c*}}\right) \tag{2.52}$$

and the corresponding axial and bending stiffness components in basis $\mathcal{C}$ become

$$\begin{aligned} K_{11}^{c} &= K_{11}, \qquad K_{15}^{c} = K_{16}^{c} = K_{56}^{c} = 0, \\ K_{55}^{c} &= \frac{K_{55}^{c*} + K_{66}^{c*}}{2} - \sqrt{\left(\frac{K_{66}^{c*} - K_{55}^{c*}}{2}\right)^2 + (K_{56}^{c*})^2}, \\ K_{66}^{c} &= \frac{K_{55}^{c*} + K_{66}^{c*}}{2} + \sqrt{\left(\frac{K_{66}^{c*} - K_{55}^{c*}}{2}\right)^2 + (K_{56}^{c*})^2}. \end{aligned} \tag{2.53}$$

These definitions imply that the principal axes of bending will always be oriented such that the bending stiffness K_{55}^c about axis $\bar{c}_2$ will always be less than or equal to the bending stiffness K_{66}^c about axis $\bar{c}_3$.

2.3.5 Shear Center

The shear center **S** of the cross-section is the location where an applied shear force, F_2 or F_3, produces no torsional deformation [119]. This implies that at this location, the coupling terms between the shear and torsional behavior, K_{24} and K_{34}, must vanish. A set of principal axes can then be defined by the frame

$\mathcal{F}_S = [\mathbf{S}, \mathcal{S} = (\bar{s}_1, \bar{s}_2, \bar{s}_3)]$, as shown in Fig. 2.14, such that the cross-shear stiffness K_{23} also vanishes and the shear stiffness components K_{22} and K_{33} are maximized.

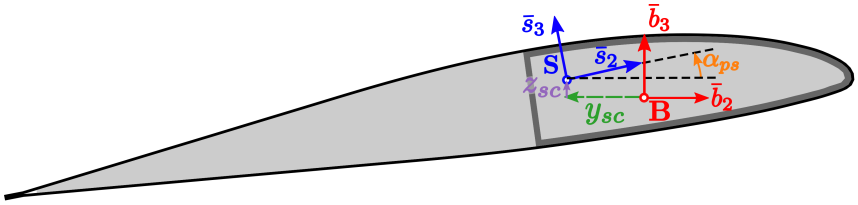

Figure 2.14: Shear center and principal axes of shear.

The location of the shear center can be determined from the stiffness components relating the shear and torsional behavior according to

$$y_{sc} = \frac{K_{22}K_{34} - K_{23}K_{24}}{K_{22}K_{33} - K_{23}^2}, \qquad z_{sc} = \frac{K_{23}K_{34} - K_{33}K_{24}}{K_{22}K_{33} - K_{23}^2} \tag{2.54}$$

where y_{sc} and z_{sc} are the distances along axis $\bar{b}_2$ and $\bar{b}_3$, respectively. Defining an intermediate frame $\mathcal{F}_{S^*} = [\mathbf{S}, \mathcal{S}^* = (\bar{s}_1^*, \bar{s}_2^*, \bar{s}_3^*)]$ whose origin is at the shear center, but whose axes $\bar{s}_2^*$ and $\bar{s}_3^*$ are aligned parallel to $\bar{b}_2$ and $\bar{b}_3$, respectively, the shear and torsional stiffness components become

$$\begin{gathered} K_{22}^{s*} = K_{22}, \qquad K_{33}^{s*} = K_{33}, \qquad K_{23}^{s*} = K_{23}, \\ K_{24}^{s*} = 0, \qquad K_{34}^{s*} = 0, \\ K_{44}^{s*} = K_{44} - y_{sc}K_{34} + z_{sc}K_{24} \end{gathered} \tag{2.55}$$

where $(\cdot)^{s*}$ indicates components resolved in basis $\mathcal{S}^*$. The orientation of the principal axes, defined by angle α_{ps}, is then determined by

$$\alpha_{ps} = 0.5 \tan^{-1}\left(\frac{2K_{23}}{K_{22} - K_{33}}\right). \tag{2.56}$$

and the corresponding axial and bending stiffness components in basis $\mathcal{S}$ become

$$\begin{aligned} K^s_{22} &= \frac{K_{22}+K_{33}}{2} + \sqrt{\left(\frac{K_{22}-K_{33}}{2}\right)^2 + K^2_{23}}, \\ K^s_{33} &= \frac{K_{22}+K_{33}}{2} - \sqrt{\left(\frac{K_{22}-K_{33}}{2}\right)^2 + K^2_{23}}, \\ K^s_{23} = K^s_{24} = K^s_{34} &= 0, \qquad K^s_{44} = K^{s*}_{44} = K_{44} - y_{sc}K_{34} + z_{sc}K_{24}. \end{aligned} \tag{2.57}$$

These definitions imply that the principal axes of shear will always be oriented such that the shear stiffness K^s_{22} in direction $\bar{s}_2$ will always be greater than or equal to the shear stiffness K^s_{33} in direction $\bar{s}_3$.

2.3.6 Change in Cross-Sectional Frame

Depending on the type of analysis, it may be desired to have the stiffness and compliance properties evaluated at the shear center, the centroid, or another arbitrary point within the cross-section. In general, this will consist of both a translation and a rotation into a new cross-sectional frame $\mathcal{F}_P = [\mathbf{P}, \mathcal{P} = (\bar{p}_1, \bar{p}_2, \bar{p}_3)]$, where $\mathbf{P}$ is the location within the cross-section about which the stiffness components are desired and $\mathcal{P}$ is the basis in which the stiffness components should be resolved, as shown in Fig. 2.15. The change in frame consists first of the translation from the origin of basis $\mathcal{B}$, denoted by $\mathbf{B}$, to point $\mathbf{P}$ defined by

$$\underline{r}_p = 0\bar{b}_1 + y_p\bar{b}_2 + z_p\bar{b}_3 \tag{2.58}$$

with y_p and z_p both resolved in basis $\mathcal{B}$. The change from basis $\mathcal{B}$ into basis $\mathcal{P}$ also consists of a rotation by angle α about axis $\bar{b}_1$, with the rotation matrix defined by

$$\underline{\underline{R}}_\alpha = \begin{bmatrix} 1 & 0 & 0 \\ 0 & C_\alpha & -S_\alpha \\ 0 & S_\alpha & C_\alpha \end{bmatrix}. \tag{2.59}$$

The motion tensor $\underline{\underline{C}}_P$ that brings frame $\mathcal{F}_B$ into frame $\mathcal{F}_P$ is then defined by

$$\underline{\underline{C}}_P = \begin{bmatrix} \underline{\underline{R}}_\alpha & \tilde{r}_p \underline{\underline{R}}_\alpha \\ \underline{\underline{0}} & \underline{\underline{R}}_\alpha \end{bmatrix} \tag{2.60}$$

with $\tilde{r}_p$ the skew-symmetric representation of $\underline{r}_p$ defined by

$$\tilde{r}_p = \begin{bmatrix} 0 & -z_p & y_p \\ z_p & 0 & 0 \\ -y_p & 0 & 0 \end{bmatrix}. \tag{2.61}$$

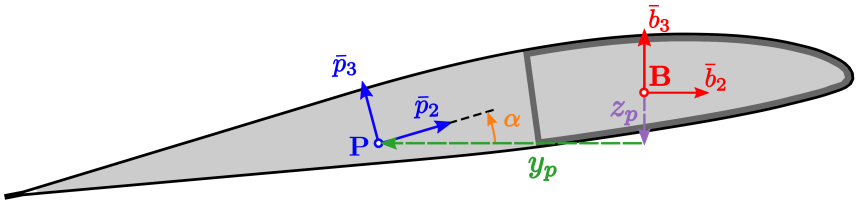

Figure 2.15: Translation and rotation into cross-sectional frame $\mathcal{F}_P$.

Using the motion tensor $\underline{\underline{C}}_P$, the stiffness matrix can be brought into frame $\mathcal{F}_P$ according to

$$\underline{\underline{K}}_P = \underline{\underline{C}}_P^T \underline{\underline{K}}\, \underline{\underline{C}}_P. \tag{2.62}$$

Since the compliance matrix is the inverse of the stiffness matrix, it can be brought into frame $\mathcal{F}_P$ by inverting Eq. 2.62 according to

$$\underline{\underline{S}}_P = \underline{\underline{C}}_p^{-1} \underline{\underline{S}} \left(\underline{\underline{C}}_p^T \right)^{-1}. \tag{2.63}$$

Chapter 3: Verification and Validation

This chapter presents the verification and validation of the main data reduction procedure highlighted in Chapter 2. The data reduction procedure is analyzed for its capability to handle two key features not found in most other measurement techniques: the ability to calculate the full 6×6 stiffness matrix as well as spanwise variations in properties associated with features common to rotor blades such as twist and taper. For the purposes of validation, the experimental results will be simulated using the 3-D finite element code *ANSYS* in order to eliminate any uncertainties and errors that will be introduced through an experimental setup. Three different beams will be considered, each one with increasing complexity, to address the key features of the method.

The first validation model considers an aluminum beam with a rectangular cross-section. For this simple geometry and material, an analytic solution exists for all the non-zero stiffness components that can be used to verify the data reduction procedure. For the second model, an aluminum beam with a rectangular cross-section is also considered, with the dimensions of the cross-section changing linearly along the length of the beam to verify the prediction of spanwise variations in properties. The third model considers a composite box-beam, using geometric and material properties that have been previously studied in literature. Three different ply layups were considered, to verify the capability to measure various elastic coupling terms.

3.1 Aluminum Rectangular Beam

The aluminum beam with a rectangular cross-section provided a useful validation case, since an analytic solution exists for all the non-zero stiffness components for a rectangular cross-section made of an isotropic material. The beam, shown in Fig. 3.1, had a length of $l = 60$ cm, a cross-sectional width of $w = 5$ cm, and a cross-sectional height of $h = 2.5$ cm, which provided a ratio of the beam length to the maximum cross-sectional dimension of 12. The beam was made of 6061-T6 aluminum, with a Young's modulus of $E = 68.9$ GPa and Poisson's ratio of $\nu = 0.33$.

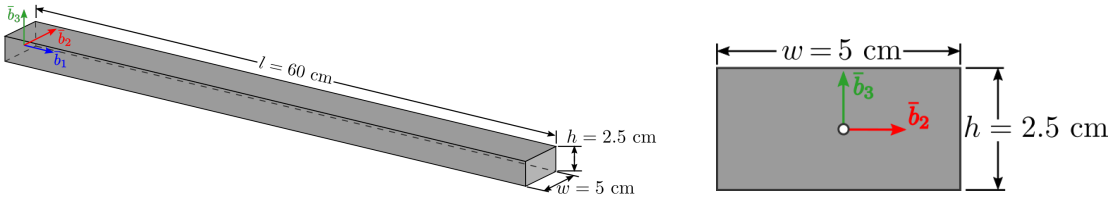

(a) 3-D view of beam **(b) Cross section geometry**

Figure 3.1: Aluminum beam with rectangular cross-section.

3.1.1 Analytical Solution

For a beam with a rectangular cross-section and made of an isotropic material, there are only six non-zero stiffness terms as long as the cross-sectional axes ($\bar{b}_2$, $\bar{b}_3$) are at the center of the cross-section, as shown in Fig. 3.1(b). For the axial and bending behavior, the stiffness can be readily determined by

$$K_{11} = EA = Ewh \qquad K_{55} = EI_{\text{flap}} = \frac{Ewh^3}{12} \qquad K_{66} = EI_{\text{lag}} = \frac{Ew^3h}{12} \tag{3.1}$$

The torsional stiffness can then be determined from Saint Venant's solution for the torsion of a bar, with the exact solution taking the form of an infinite sum of

trigonometric functions given by [123]

$$K_{44} = GJ = \frac{32Gw^3h}{\pi^4} \sum_{k=\text{odd}}^{\infty} \frac{1}{k^4} \left(1 - \frac{2w}{hk\pi} \tanh\left(\frac{hk\pi}{2w}\right)\right) \tag{3.2}$$

The two shear stiffnesses can be determined by equating the sectional strain energy from 3-D elasticity and beam theory [124], which gives

$$\begin{aligned} K_{22} &= \left(\frac{6}{5Gwh} + \frac{36\nu^2Gh^2}{\pi^4E^2w^6} \sum_{k=1}^{\infty} \left(hH_k + 4\sum_{m=1}^{\infty} H_{km}\right)\right)^{-1} \\ K_{33} &= \left(\frac{6}{5Gwh} + \frac{36\nu^2Gw^2}{\pi^4E^2h^6} \sum_{r=1}^{\infty} \left(wH_r + 4\sum_{s=1}^{\infty} H_{rs}\right)\right)^{-1} \end{aligned} \tag{3.3}$$

where the expressions for H_k and H_r are given by

$$\begin{aligned} H_k &= \left(\frac{h}{2k\pi}\sinh\left(\frac{2k\pi w}{h}\right) - w\right)\left(k^4\cosh\left(\frac{k\pi w}{h}\right)\right)^{-1} \\ H_r &= \left(\frac{w}{2k\pi}\sinh\left(\frac{2k\pi h}{w}\right) - h\right)\left(k^4\cosh\left(\frac{k\pi h}{w}\right)\right)^{-1} \end{aligned}$$

and the expressions for H_{km} and H_{rs} are given by

$$\begin{aligned} H_{km} &= \frac{h}{2k^4}\left(w - \frac{2h}{k\pi}\tanh\left(\frac{k\pi w}{h}\right) + \frac{h}{4k\pi}\frac{\sinh\left(2k\pi w/h\right)}{\cosh\left(2k\pi w/h\right)} + \frac{w}{2\cosh\left(k\pi w/h\right)}\right) \quad \text{if } k = m \\ H_{km} &= \frac{(-1)^{k+m}\,h\left[(k+m)\sin\left((k-m)\,\pi\right) + (k-m)\sin\left((k+m)\,\pi\right)\right]}{k^2m^2\left(k^2-m^2\right)\pi} W_{km} \quad \text{if } k \neq m \\ H_{rs} &= \frac{w}{2k^4}\left(h - \frac{2w}{k\pi}\tanh\left(\frac{k\pi h}{w}\right) + \frac{w}{4k\pi}\frac{\sinh\left(2k\pi h/w\right)}{\cosh\left(2k\pi h/w\right)} + \frac{h}{2\cosh\left(k\pi h/w\right)}\right) \quad \text{if } r = s \\ H_{rs} &= \frac{(-1)^{k+m}\,w\left[(k+m)\sin\left((k-m)\,\pi\right) + (k-m)\sin\left((k+m)\,\pi\right)\right]}{k^2m^2\left(k^2-m^2\right)\pi} W_{rs} \quad \text{if } r \neq s \end{aligned}$$

with W_{km} and W_{rs} given by

$$\begin{aligned} W_{km} =& w - \frac{2h}{m\pi}\tanh\left(\frac{m\pi w}{h}\right) - \frac{2h}{k\pi}\tanh\left(\frac{k\pi w}{h}\right) + \\ &+ \frac{h\left[(k+m)\sinh\left((k-m)\,\pi w/h\right) + (k-m)\sinh\left((k+m)\,\pi w/h\right)\right]}{2\left(k^2-m^2\right)\pi\cosh\left(k\pi w/h\right)\cosh\left(m\pi w/h\right)} \end{aligned}$$

$$W_{rs} = h - \frac{2w}{m\pi}\tanh\left(\frac{m\pi h}{w}\right) - \frac{2w}{k\pi}\tanh\left(\frac{k\pi h}{w}\right) + \\ + \frac{w\left[(k+m)\sinh\left((k-m)\,\pi h/w\right) + (k-m)\sinh\left((k+m)\,\pi h/w\right)\right]}{2\left(k^2-m^2\right)\pi\cosh\left(k\pi h/w\right)\cosh\left(m\pi h/w\right)}$$

3.1.2 3-D Finite Element Model

To numerically simulate the experimental results, *ANSYS* was used to generate a 3-D finite element model and calculate the surface strains under a set of 6 linearly independent loads. The model was meshed using 6000 SOLID186 (20-node hexahedral) elements, with 120 elements along the length, 10 elements along the width, and 5 elements along the height as shown in Fig. 3.2. The nodes at the left end ($x = 0$ cm) were fully constrained in all three degrees of freedom to simulate a clamped boundary condition, and the loads were then applied at the right end of the beam ($x = 60$ cm). The applied loads for the six loading conditions are summarized in Table 3.1 and shown in Fig. 3.3 and Fig. 3.4 for the forces and moments, respectively, with the load levels selected to provide a maximum strain of about 500 $\mu\epsilon$ under an axial load and between 2000 and 2500 $\mu\epsilon$ for the remaining loads. For the torsional load case, a point load was applied at the four nodes at the corner of the cross-section in the $\pm\bar{b}_3$ direction, for a net zero force but a 360 N-m moment about $\bar{b}_1$. For the bending moments, the load was applied as a linearly varying surface traction in the $\bar{b}_1$ direction, with the variation in the $\bar{b}_3$ direction for the flap bending moment and in the $\bar{b}_2$ direction for the lag bending moment. For

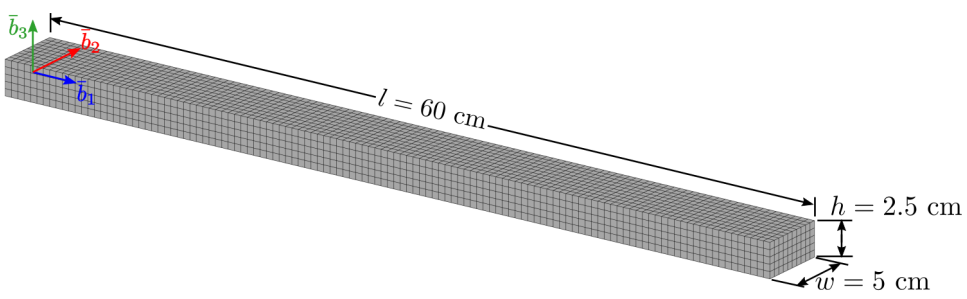

Figure 3.2: Mesh of the aluminum beam with rectangular cross-section.

the three forces, the loads were applied as a constant surface traction in the $\bar{b}_1$, $\bar{b}_2$, and $\bar{b}_3$ direction for the axial, lag shear, and flap shear forcing, respectively.

After the boundary conditions were applied for each of the six loading conditions, the displacements and strains were then calculated with a few representative results shown in Figs. 3.5 and 3.6. By default, the strains from the finite element model are calculated in the global basis $\mathcal{B} = (\bar{b}_1, \bar{b}_2, \bar{b}_3)$ as shown in Fig. 3.5; however, to be consistent with results from an experimental measurement, these strains must be rotated into the local surface basis $\mathcal{E} = (\bar{e}_1, \bar{e}_2, \bar{e}_3)$ using Eq. (2.23) as shown in Fig. 3.6. It is important to note that the two in-plane shear strains are impacted

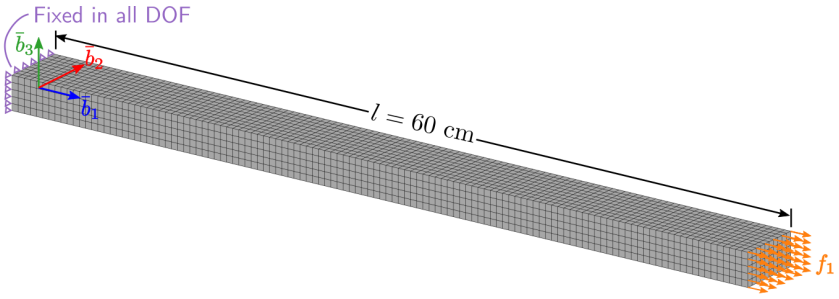

(a) Axial force

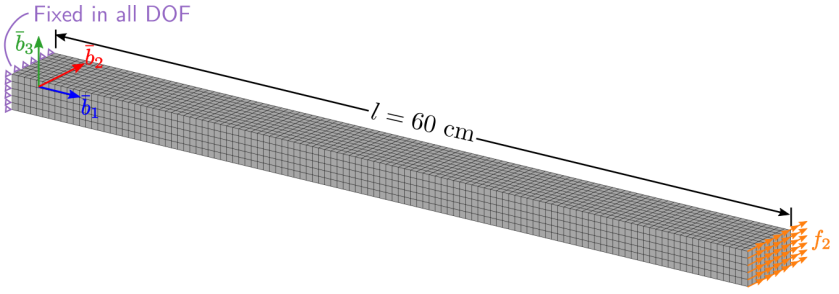

(b) Lag shear force

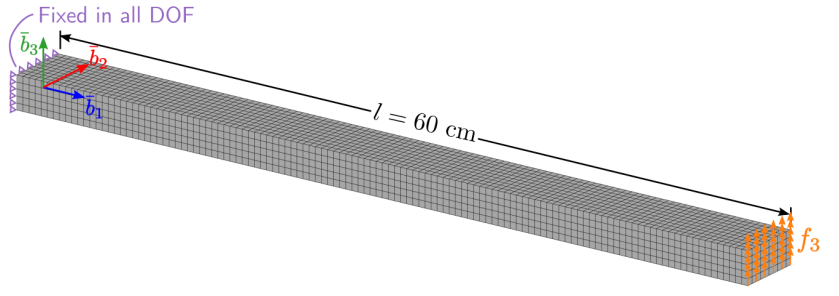

(c) Flap shear force

Figure 3.3: Applied boundary conditions for the three forces.

Table 3.1: Applied loads for the 3-D finite element model of the aluminum beam with a rectangular cross-section

Loading	Surface Traction (3-D model)	Equivalent Beam Load
Axial	$f_1 = 3.445 \times 10^7$ N/m^2	$F_1 = 4.306 \times 10^4$ N
Lag shear	$f_2 = 2.392 \times 10^6$ N/m^2	$F_2 = 2.991 \times 10^3$ N
Flap shear	$f_3 = 1.196 \times 10^6$ N/m^2	$F_3 = 1.495 \times 10^3$ N
Torsional	$f_{1,t} = 3598$ N	$M_1 = 360$ N-m
Flap bending	$m_2 = 1.378 \times 10^{10} z$ N/m^2	$M_2 = 897$ N-m
Lag bending	$m_3 = 6.89 \times 10^9 y$ N/m^2	$M_3 = 1794$ N-m

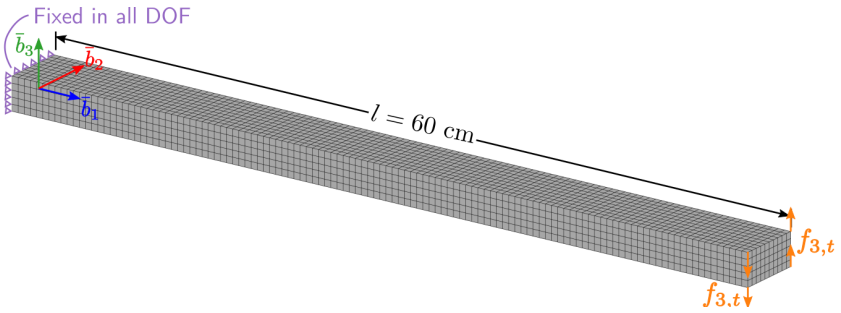

(a) Torque

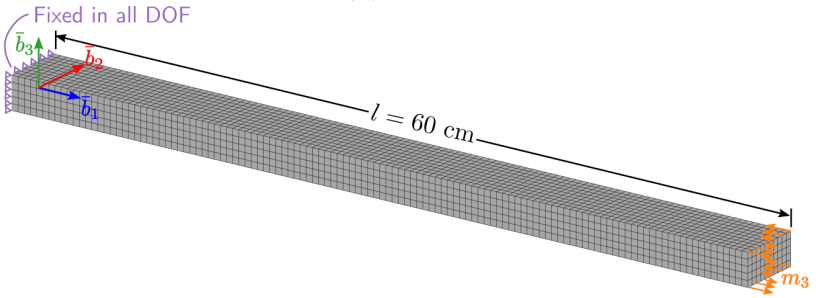

(b) Flap bending moment

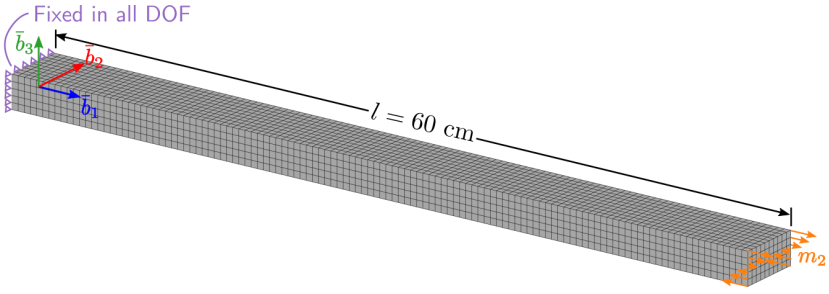

(c) Lag bending moment

Figure 3.4: Applied boundary conditions for the three moments.

by the rotation, while the axial strain remains the same. While the displacements are not used explicitly in the calculation of the compliance and stiffness matrices (Eq. (2.41)), they are needed in order to accurately calculate the sectional stress resultants, $\underline{\mathcal{F}}_c$, from the equivalent beam load applied at the tip of the beam (see Sec. 5.3.3).

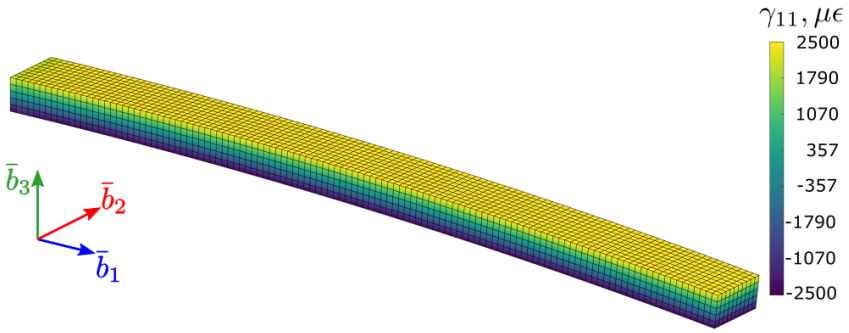

(a) Axial strain, γ_{11}, under flap bending load, m_2

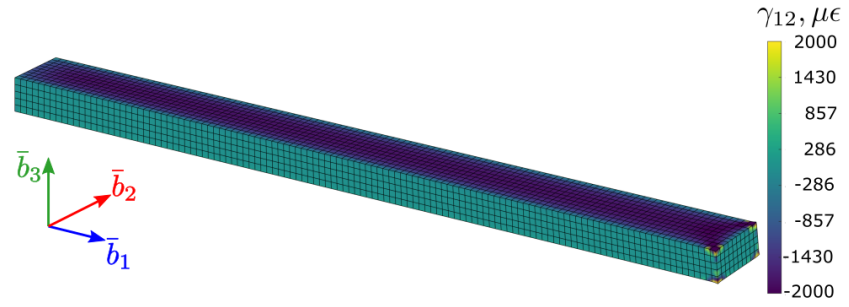

(b) Shear strain, γ_{12}, under torsional load, $f_{1,t}$

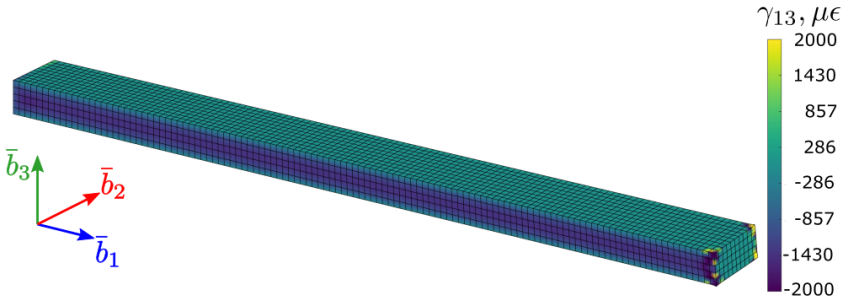

(c) Shear strain, γ_{13}, under torsional load, $f_{1,t}$

Figure 3.5: Strains in the global basis $\mathcal{B} = (\bar{b}_1, \bar{b}_2, \bar{b}_3)$ under flap bending and torsional loads for the aluminum beam with a rectangular cross-section.

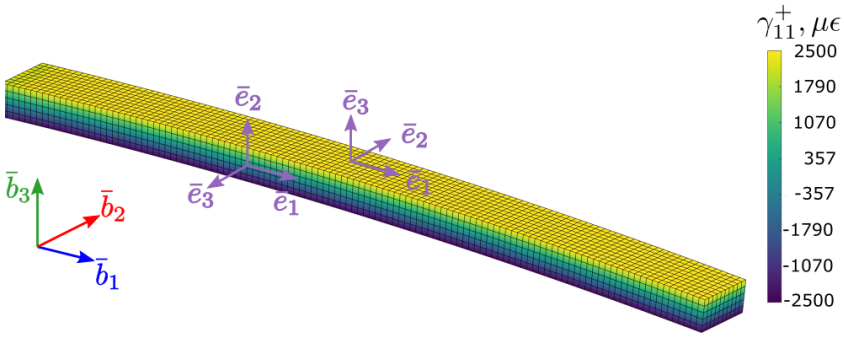

(a) Axial strain, γ_{11}^{+}, under flap bending load, m_2

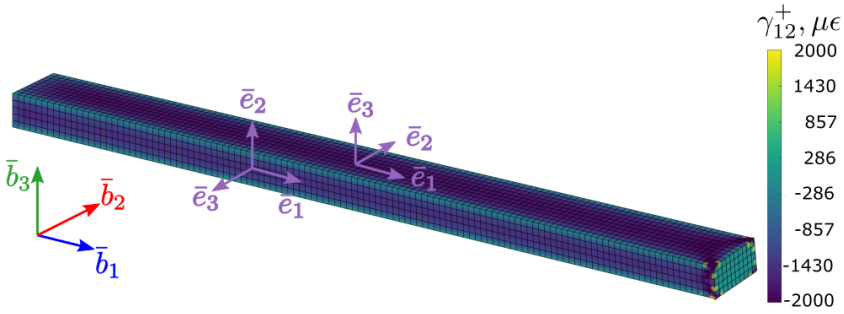

(b) Shear strain, γ_{12}^{+}, under torsional load, $f_{1,t}$

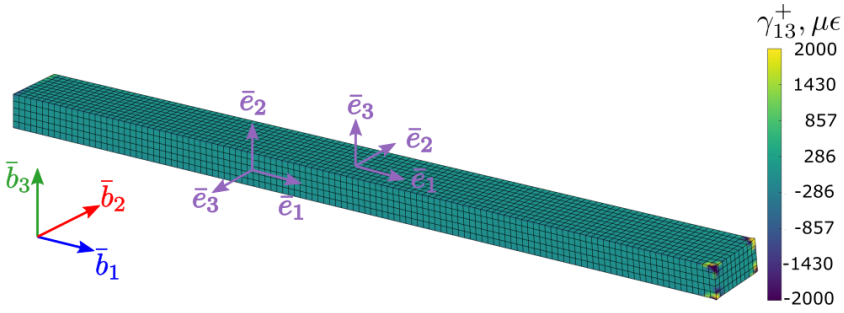

(c) Shear strain, γ_{13}^{+}, under torsional load, $f_{1,t}$

Figure 3.6: Strains in the surface basis $\mathcal{E} = (\bar{e}_1, \bar{e}_2, \bar{e}_3)$ under flap bending and torsional loads for the aluminum beam with a rectangular cross-section.

3.1.3 Stiffness Results

Using the sectional stress resultants calculated along the span, the strains in basis $\mathcal{E}$, and the numerical warping field, the matrices from Eq. (2.41) can be assembled and used to calculate the compliance and stiffness matrices at discrete spanwise locations. The strain data was extracted at the nodes along the external edges of the elements resulting in strain data at every 1 cm along the span. The

average stiffness values for the entire beam are shown in Table 3.2 and compared against the analytic solutions from Sec. 3.1.1. Note that because the beam is isotropic and the reference axes of the beam are at the geometric center of the cross-section, which is coincident with both the shear center and centroid for the rectangular cross-section, all the off-diagonal terms are zero and are omitted in Table 3.2. All six stiffness values calculated from the 3-D FEM strains showed great agreement with their respective analytic solutions. The largest difference was in the flap shearing stiffness K_{33}, which had a discrepancy of 5.3%, while the torsional stiffness had a discrepancy of 1.9% and the remaining four stiffness components all had differences of less than 0.5% compared to their respective analytic solutions.

One of the main goals of this thesis was to develop a procedure that could predict the stiffness coefficients at discrete locations along the beam. Since the strain data was extracted from the *ANSYS* model at 1 cm intervals along the span, the stiffness matrix could also be calculated discretely at each of these spanwise locations with the results shown in Fig. 3.7 and Fig. 3.8. For each of the six non-zero stiffness matrix entries, the value calculated using the strains from the 3-D finite element model are shown as points, with the analytic solution shown as a solid line. For all six stiffness values, the calculated stiffness has some variations along the first few centimeters due to the strain concentrations that result from the clamped boundary

Table 3.2: Average stiffness of the aluminum rectangular beam

Stiffness Term	**Calculated from 3-D FEM Strains**	**Analytic Solution**
K_{11}	8.619×10^7 N	8.613×10^7 N
K_{22}	2.688×10^7 N	2.697×10^7 N
K_{33}	2.650×10^7 N	2.517×10^7 N
K_{44}	4716 N-m^2	4628 N-m^2
K_{55}	4489 N-m^2	4486 N-m^2
K_{66}	1.795×10^4 N-m^2	1.794×10^4 N-m^2

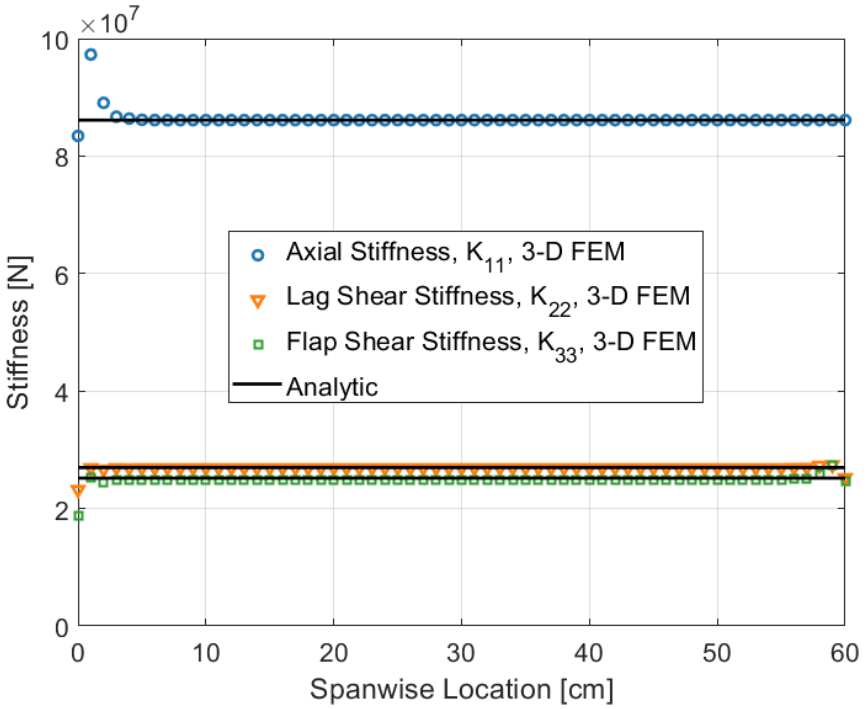

Figure 3.7: Spanwise variations of the axial (K_{11}), lag shear (K_{22}), and flap shear (K_{33}) stiffness using 3-D FEM strains for the aluminum beam with rectangular cross-section.

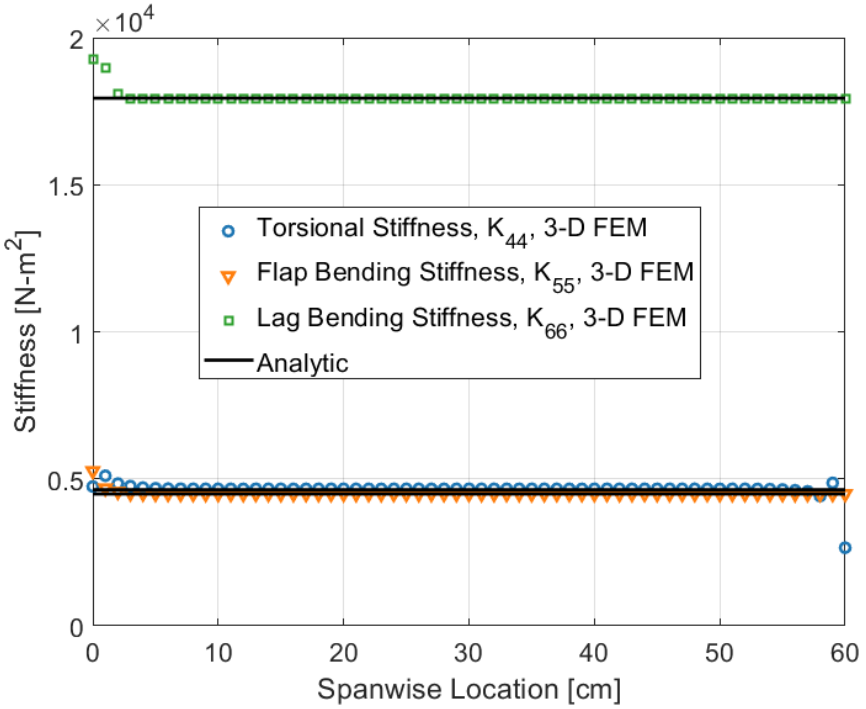

Figure 3.8: Spanwise variations of the torsional (K_{44}), flap bending (K_{55}), and lag bending (K_{66}) stiffness using 3-D FEM strains for the aluminum beam with rectangular cross-section.

condition at the root. In addition, the torsional stiffness is affected by the applied load at the tip, due to the fact that the moment for this loading condition was generated using loads applied at only four nodes. However, the overall trends for the local stiffness values are similar to those of the average or global stiffness values highlighted in Table 3.2 – with the values calculated from the 3-D FEM strains showing overall excellent agreement with the analytic solution.

3.2 Tapered Aluminum Rectangular Beam

The tapered aluminum beam with a rectangular cross-section was also considered in order to verify the capability to predict spanwise variations in properties. The beam, shown in Fig. 3.9, had a length of $l = 60$ cm, and a cross-sectional width and height that decreased linearly along the span, with the greatest dimensions at the root of the beam. To determine the impact, if any, of the magnitude of the taper, beams with two different taper ratios, the ratio of the cross-sectional dimensions at the root to the those at the tip, were considered: the first beam had a moderate taper ratio of two, while the second beam had a more extreme taper ratio of five. For both beams, the cross-section at the root had a width of $w_{\text{root}} = 6$ cm and height of $h_{\text{root}} = 2.5$ cm. Thus, for the beam with a taper ratio of two, the dimensions at the tip were $w_{\text{tip}} = 3$ cm and $h_{\text{tip}} = 1.25$ cm, while for the beam with a taper ratio of five, the dimensions at the tip were $w_{\text{tip}} = 1.2$ cm and $h_{\text{tip}} = 0.5$ cm. The two beams were again made of 6061-T6 aluminum, with a Young's modulus of $E = 68.9$ GPa and Poisson's ratio of $\nu = 0.33$.

3.2.1 3-D Finite Element Model

To numerically simulate the experimental results, *ANSYS* was again used to generate a 3-D finite element model and calculate the surface strains under a set of 6

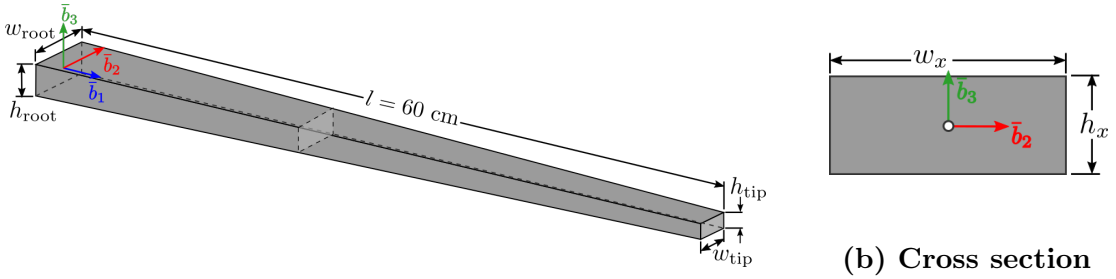

(a) 3-D view of beam **(b) Cross section geometry**

Figure 3.9: Tapered aluminum beam with rectangular cross-section.

linearly independent loads. Both tapered models were meshed using 3240 SOLID186 elements, with 120 elements along the length, 9 elements along the width, and 3 elements along the height as shown in Fig. 3.10. The nodes at the left end ($x = 0$ cm) were all fully constrained in all three degrees of freedom to simulate a clamped boundary condition, and the loads were then applied at the right end of the beam ($x = 60$ cm), using the same loading procedure discussed in Sec. 3.1.2 for the prismatic aluminum beam. However, for the tapered beams, the loading magnitudes were selected such that the maximum strains at mid-span ($x = 30$ cm) were about $500\mu\epsilon$ under an axial load and between 2000 and 2500 $\mu\epsilon$ for the remaining five loading conditions, with the actual applied loads defined in Table 3.3 and Table 3.4 for the models with taper ratios of two and five, respectively.

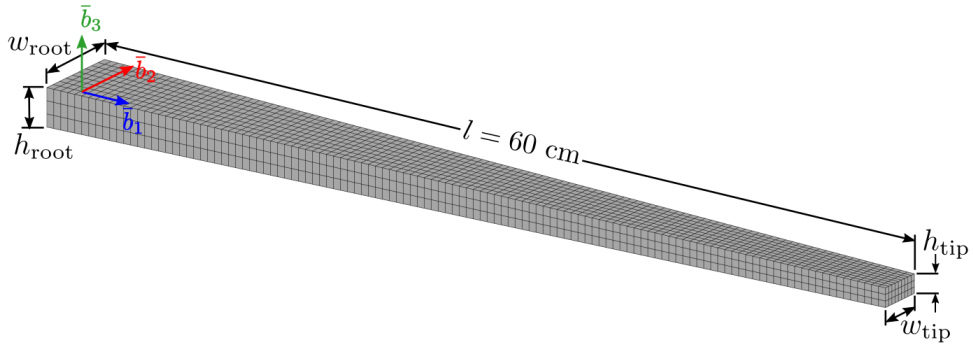

Figure 3.10: Mesh of the tapered aluminum beam with rectangular cross-section.

Once the boundary conditions were applied for both models under each of the six loading conditions, the displacements and strains were then calculated with a few

representative results shown in Fig. 3.11. The axial strain γ_{11}^{+} under the axial load for both taper ratios is shown in Fig. 3.11(a-b), while the shear strain γ_{12}^{+} under the torsional load is shown in Fig. 3.11(c-d), with all strain components shown in the local surface basis $\mathcal{E} = (\bar{e}_1, \bar{e}_2, \bar{e}_3)$.

Table 3.3: Applied loads for the aluminum beam with a taper ratio of 2

Loading	Surface Traction (3-D model)	Equivalent Beam Load
Axial	$f_1 = 7.751 \times 10^7$ N/m^2	$F_1 = 2.907 \times 10^4$ N
Lag shear	$f_2 = 4.845 \times 10^6$ N/m^2	$F_2 = 1.817 \times 10^3$ N
Flap shear	$f_3 = 2.019 \times 10^6$ N/m^2	$F_3 = 757$ N
Torsional	$f_{1,t} = 6466$ N	$M_1 = 388$ N-m
Flap bending	$m_2 = 9.301 \times 10^{10} z$ N/m^3	$M_2 = 454$ N-m
Lag bending	$m_3 = 3.876 \times 10^{10} y$ N/m3	$M_3 = 1090$ N-m

Table 3.4: Applied loads for the aluminum beam with a taper ratio of 5

Loading	Surface Traction (3-D model)	Equivalent Beam Load
Axial	$f_1 = 3.101 \times 10^8$ N/m^2	$F_1 = 1.860 \times 10^4$ N
Lag shear	$f_2 = 1.550 \times 10^7$ N/m^2	$F_2 = 930$ N
Flap shear	$f_3 = 6.459 \times 10^6$ N/m^2	$F_3 = 388$ N
Torsional	$f_{1,t} = 8277$ N	$M_1 = 199$ N-m
Flap bending	$m_2 = 1.860 \times 10^{12} z$ N/m^3	$M_2 = 233$ N-m
Lag bending	$m_3 = 7.751 \times 10^{11} y$ N/m3	$M_3 = 558$ N-m

3.2.2 Stiffness Results

After rotating the strains from *ANSYS* into basis $\mathcal{E}$ and combining these with the sectional stress resultants calculated along the span and the numerical warping field, the data reduction matrices were assembled and used to calculate the compliance and stiffness matrices at discrete spanwise locations. The spanwise variations in the stiffness properties are shown in Figs. 3.12 - 3.17 for the six non-zero components for both tapered beams, with the results for the beam with a taper ratio

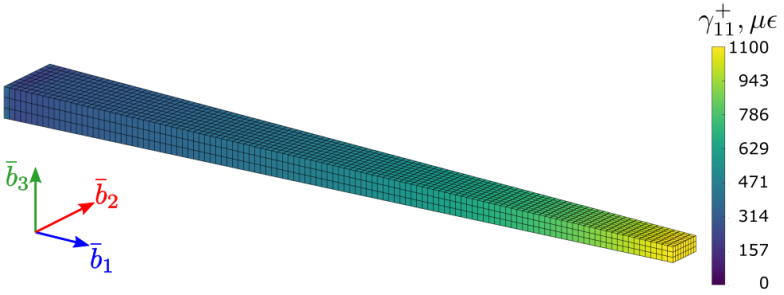

(a) Axial strain, γ_{11}^{+}, under axial load, f_1, for a taper ratio of 2

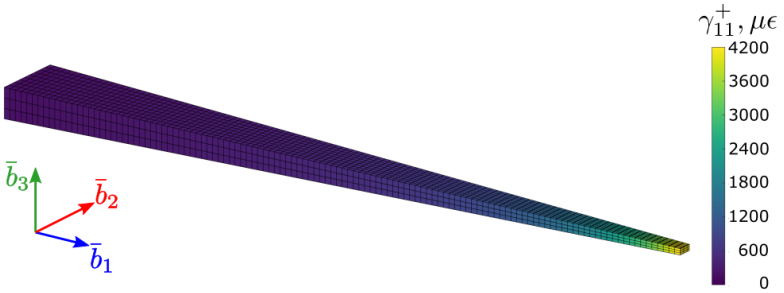

(b) Axial strain, γ_{11}^{+}, under axial load, f_1, for a taper ratio of 5

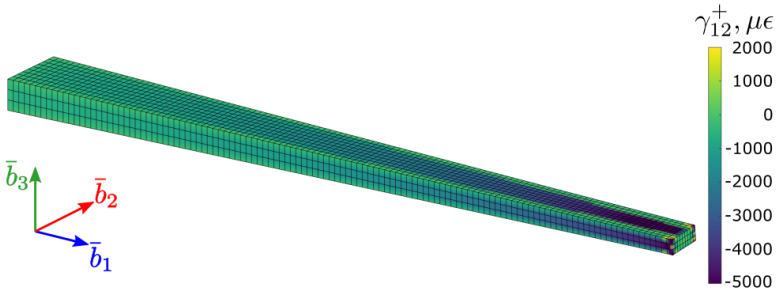

(c) Shear strain, γ_{13}^{+}, under torsional load, $f_{1,t}$, for a taper ratio of 2

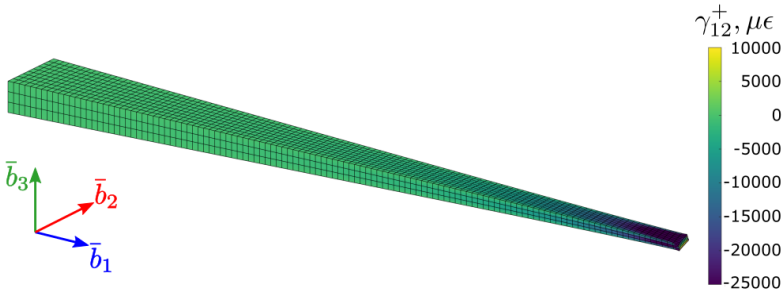

(d) Shear strain, γ_{13}^{+}, under torsional load, $f_{1,t}$, for a taper ratio of 5

Figure 3.11: Strains in surface basis $\mathcal{E} = (\bar{e}_1, \bar{e}_2, \bar{e}_3)$ under axial and torsional loads for the tapered aluminum beams with a rectangular cross-section.

of 2 shown as hollow circles (○) and for the beam with a taper ratio of 5 shown as hollow squares (□). Although the analytic solutions from Sec. 3.1.1 are derived under the assumption that the beam is prismatic, meaning it has a constant cross-section along the span, they still provide a useful reference for comparing the stiffness properties calculated from the *ANSYS* strain fields. With the exception of the flap shear stiffness shown in Fig. 3.14, it can be seen that with there is good agreement between the reference analytic solution and the stiffness properties calculated from the *ANSYS* results. For the axial and flap and lag bending properties, the calculated stiffnesses are all within 1% of the reference solution, except for near the root where strain concentrations arise due to the clamped boundary condition. For the lag shear stiffness K_{22}, the calculated stiffness was on average about 1.5% greater than the reference stiffness with a maximum difference of about 2% near the root. For the flap shear stiffness K_{33}, the calculated and reference stiffness had their largest differences near the root of the beam but showed much better agreement moving closer to the tip; on average the calculated flap shear stiffness was about 6.5% higher than the reference stiffness but close to the root was about 13.5% greater. The torsional stiffness K_{44} followed a similar trend to the flap shear stiffness with the greatest differences occurring near the clamped end of the beam but showed smaller overall discrepancies; the maximum difference was about 9.5% near the root and on average was about 3.8% greater than the reference stiffness. Overall, these results show that the data reduction algorithm presented in this thesis is capable of calculating the cross-sectional stiffness properties locally along the beam, even when significant spanwise variations in the cross-sectional geometry are present.

3.3 Composite Box Beam

The final beam considered was a thin-walled composite box beam, whose cross-sectional dimensions and material properties were modeled using the experiments of

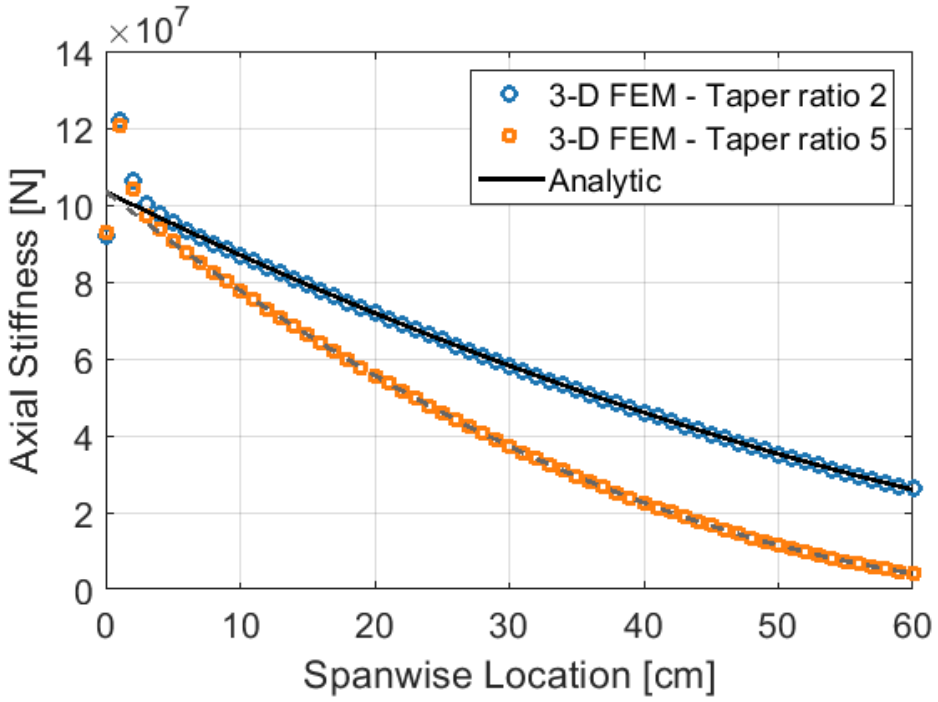

Figure 3.12: Spanwise variations of the axial stiffness, K_{11}, for the tapered aluminum beams.

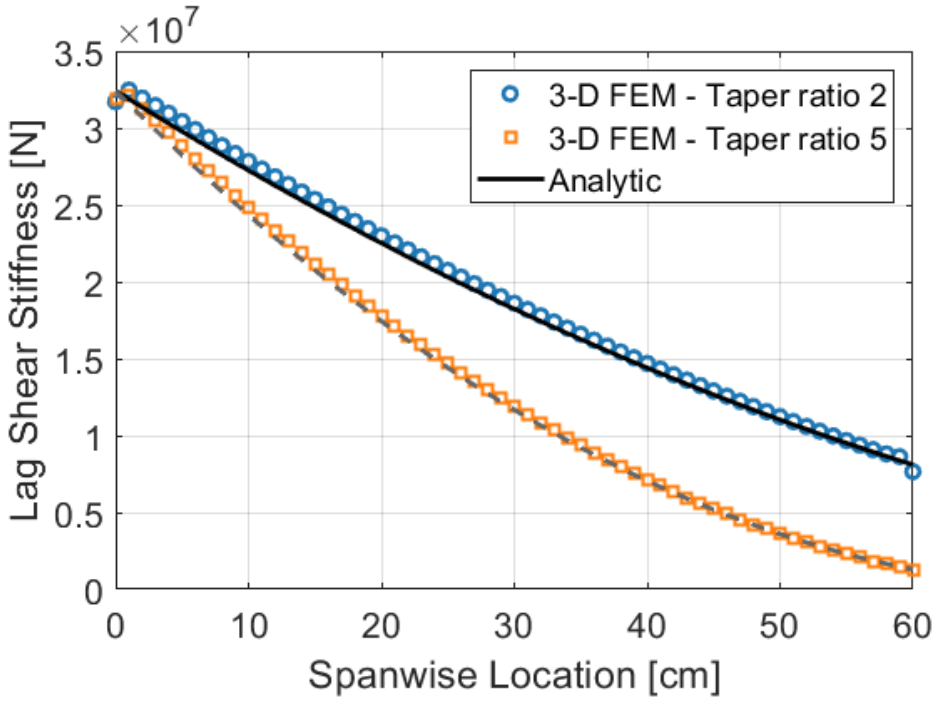

Figure 3.13: Spanwise variations of the lag shear stiffness, K_{22}, for the tapered aluminum beams.

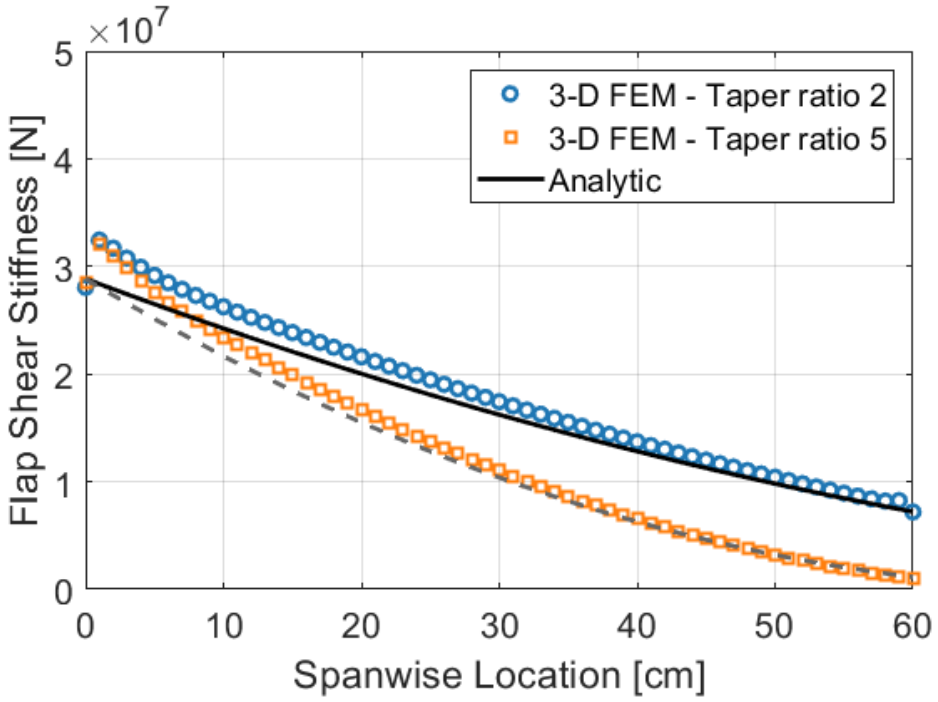

Figure 3.14: Spanwise variations of the flap shear stiffness, K_{33}, for the tapered aluminum beams.

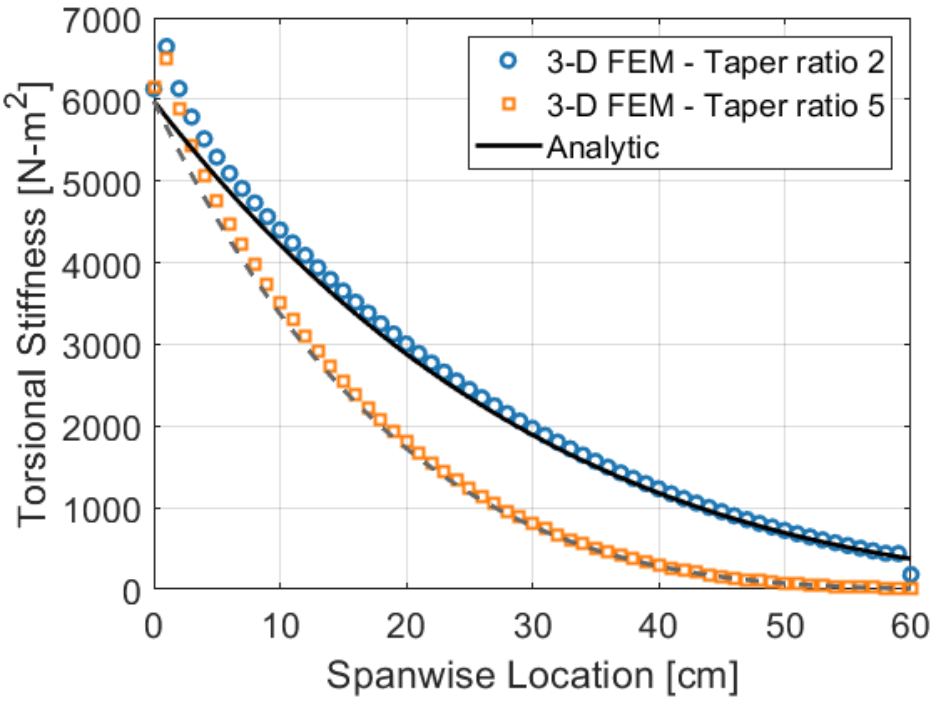

Figure 3.15: Spanwise variations of the torsional stiffness, K_{44}, for the tapered aluminum beams.

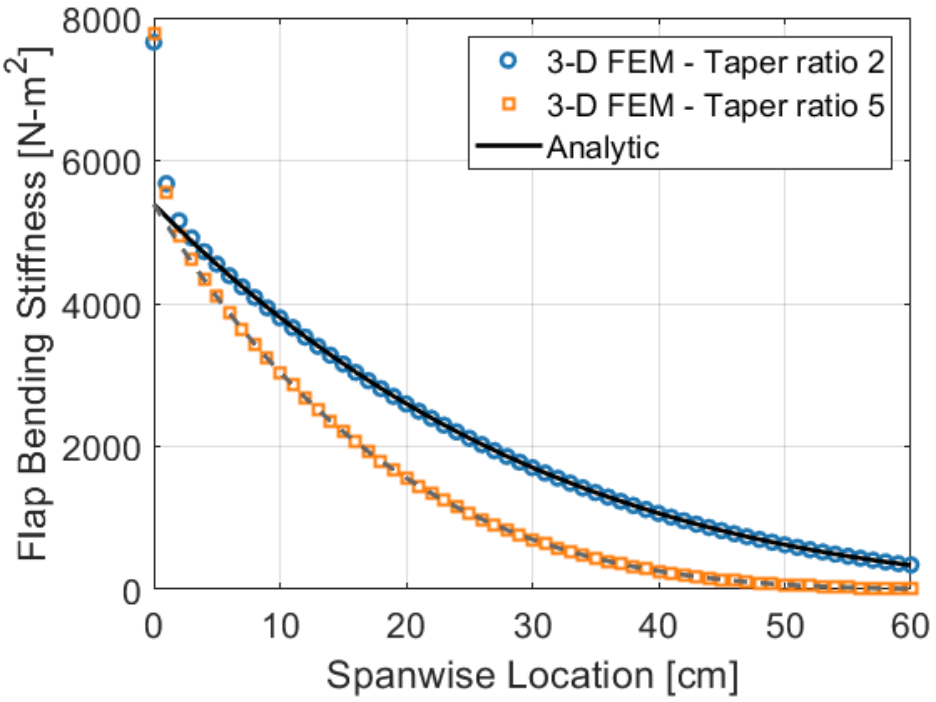

Figure 3.16: Spanwise variations of the flap bending stiffness, K_{55}, for the tapered aluminum beams.

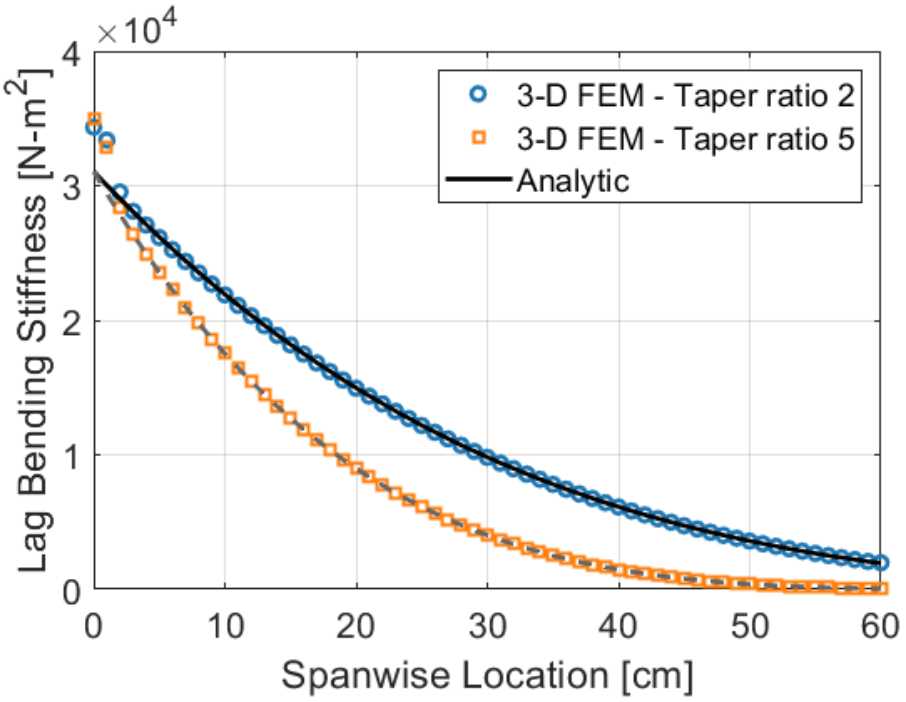

Figure 3.17: Spanwise variations of the lag bending stiffness, K_{66}, for the tapered aluminum beams.

Chandra and Chopra from 1990 [67]. The composite box beam, shown in Fig. 3.18, had a length of $l = 60$ cm, an external width of $w = 24.206$ mm, an external height of $h = 13.640$ mm, and a wall thickness of $t = 0.762$ mm. This type of box beam has been widely studied in literature and used to evaluate a variety of numerical and analytic cross-sectional analyses including those of Smith and Chopra [66], Bauchau and Hodges [125], Popescu and Hodges [126], Jung et al. [127], and Yu et al. [29]. For this dissertation, three different ply layups, shown in Table 3.5, were considered to study the ability to measure elastic coupling terms introduced by both symmetric and antisymmetric ply layups. The lay-up definitions are defined starting with the innermost ply and ending with the outermost ply with 0° plies oriented with the axis of the beam ($\bar{b}_1$) and a positive ply angle indicating a right-hand rotation about the local normal to the wall. For all beams, the walls consisted of six plies of unidirectional AS4/3501-6 graphite/epoxy, with each ply being 0.127 mm thick and with a longitudinal Young's modulus of $E_{1^*} = 141.96$ GPa, transverse Young's modulus of $E_{2^*} = 9.79$ GPa, shear moduli of $G_{12^*} = 6$ GPa and $G_{23^*} = 4.80$ GPa, and Poisson's ratios of $\nu_{12^*} = \nu_{13^*} = \nu_{23^*} = 0.42$, where notation $(\cdot)^*$ is used to indicate that properties are in the material basis $\mathcal{B}^*$ with $\bar{b}_1^*$ aligned with the material fibers.

Table 3.5: Composite Box-Beam Layups

Lay-up	Upper wall	Right wall	Lower wall	Left wall
Uncoupled	$[0°]_6$	$[0°]_6$	$[0°]_6$	$[0°]_6$
Symmetric	$[20°]_6$	$[0°]_6$	$[-20°]_6$	$[0°]_6$
Antisymmetric	$[15°]_6$	$[15°]_6$	$[15°]_6$	$[15°]_6$

The first beam considered had a symmetric, uncoupled layup consisting of six plies with their fibers all oriented along the axis of the beam ($[0°]_6$), meaning that the six deformation modes were completely uncoupled and the stiffness and compliance matrices should be diagonal, as was the case for the previously considered isotropic

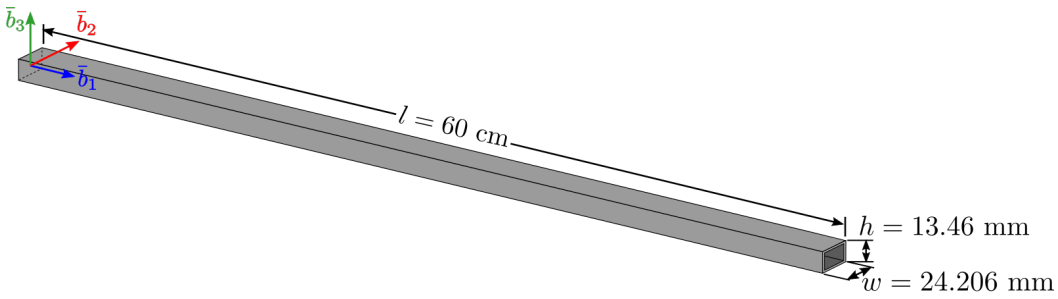

(a) 3-D view of beam

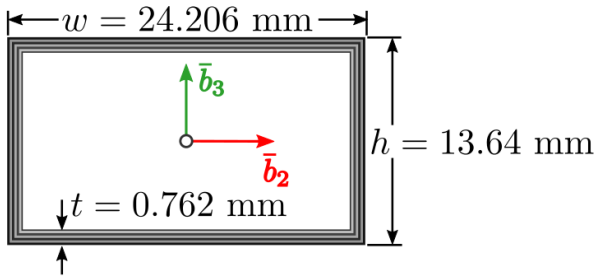

(b) Cross-section geometry

Figure 3.18: Composite beam with rectangular box cross-section.

beams. The calculated stiffness results for this layup were presented by Popescu and Hodges [126] using both *VABS* and *NABSA*, and can be used to compare with the results from the 3-D FEM. The second beam consisted of a symmetric, but coupled, layup with six plies oriented at 0° on the two side walls, six plies oriented at 20° on the upper wall and six plies oriented at -20° on the lower wall. Generally, a symmetric layup with not all plies at 0° or 90° will present coupling between the extension and shear behavior and the torsional and bending behavior. Since the plies oriented at a non-zero angle are only on the upper and lower walls, it is expected that a bending/torsion coupling will only be present for the bending about axis $\bar{b}_2$ – which in rotorcraft is commonly referred to as flap bending – and not for the bending about axis $\bar{b}_3$ – commonly referred to as lag bending. The third and final layup was an antisymmetric layup consisting of all six plies oriented at 15° for the entire cross-section. Generally, an antisymmetric layup will present coupling between the extension and torsional behavior and the shearing and bending behavior. The

stiffness values for this layup were calculated by Yu et al. using *VABS* and *NABSA* and by Jung et al. using a refined analytical model, which can both be used to compare with the results obtained here from the 3-D FEM strains. For all three layups, the analytic expressions for the various stiffness values based on a classical laminated plate theory presented by Smith and Chopra [66] will also be used for comparison.

3.3.1 Classical Laminated Plate Theory

A composite laminate is an assembly of plies, each possibly having different elastic properties, and defined by a stacking sequence describing the orientation of the composite fibers in each layer. For a ply made of unidirectional composite material, the material can be assumed to be transversely isotropic meaning that it has two orthogonal planes of symmetry and is therefore defined by only four independent material constants, E_{1^*}, E_{2^*}, G_{12^*}, and ν_{12^*}. Due to the small thickness of an individual ply, it can be assumed that each ply is in a state of plane stress with the stress-strain relationship defined by

$$\begin{Bmatrix} \sigma_{11^*} \\ \sigma_{22^*} \\ \sigma_{12^*} \end{Bmatrix} = \begin{bmatrix} Q_{11} & Q_{12} & 0 \\ Q_{12} & Q_{22} & 0 \\ 0 & 0 & Q_{66} \end{bmatrix} \begin{Bmatrix} \gamma_{11^*} \\ \gamma_{22^*} \\ \gamma_{12^*} \end{Bmatrix} = \underline{\underline{Q}} \begin{Bmatrix} \gamma_{11^*} \\ \gamma_{22^*} \\ \gamma_{12^*} \end{Bmatrix} \tag{3.4}$$

where Q_{11}, Q_{12}, Q_{22}, and Q_{66} are related to the material properties by

$$Q_{11} = \frac{E_{1^*}}{1 - \nu_{12^*}\nu_{21^*}}, \qquad Q_{12} = \frac{\nu_{21^*}E_{1^*}}{1 - \nu_{12^*}\nu_{21^*}}, \qquad Q_{22} = \frac{E_{2^*}}{1 - \nu_{12^*}\nu_{21^*}}$$
$$Q_{66} = G_{12^*}, \qquad \nu_{21^*} = \frac{E_{2^*}\nu_{12^*}}{E_{1^*}}$$

This stress-strain relationship is derived in the material basis of a single ply; however a lamina consists of multiply plies that may have different orientations. The stress-

strain relationship can be rotated into a consistent frame using the rotation tensor

$$\underline{\underline{R}}_{\sigma} = \begin{bmatrix} C_\gamma^2 & S_\gamma^2 & -2S_\gamma C_\gamma \\ S_\gamma^2 & C_\gamma^2 & 2S_\gamma C_\gamma \\ S_\gamma C_\gamma & -S_\gamma C_\gamma & C_\gamma^2 - S_\gamma^2 \end{bmatrix} \tag{3.5}$$

where γ is the orientation of the fibers with respect to the global coordinate axes. The stress-strain relationship for an individual ply in the global coordinate system can then be written as

$$\begin{Bmatrix} \sigma_{11} \\ \sigma_{22} \\ \sigma_{12} \end{Bmatrix} = \underline{\underline{R}}_{\sigma} \underline{\underline{Q}} \underline{\underline{R}}_{\sigma}^T \begin{Bmatrix} \gamma_{11} \\ \gamma_{22} \\ \gamma_{12} \end{Bmatrix} = \begin{bmatrix} \bar{Q}_{11} & \bar{Q}_{12} & \bar{Q}_{16} \\ \bar{Q}_{12} & \bar{Q}_{22} & \bar{Q}_{26} \\ \bar{Q}_{16} & \bar{Q}_{26} & \bar{Q}_{66} \end{bmatrix} \begin{Bmatrix} \gamma_{11} \\ \gamma_{22} \\ \gamma_{12} \end{Bmatrix} \tag{3.6}$$

3.3.1.1 Sectional Stiffness Properties

Using the constitutive relationships from the classical laminate plate theory, defined by Eq. (3.6), some assumptions on the warping of the cross-section and the transverse in-plane normal stresses, and the equilibrium equations, Smith and Chopra [66] derived expressions for the cross-sectional stiffness properties of a beam with a thin-walled composite box cross-section. While the derived expressions do not provide an exact solution of 3-D elasticity, they do provide a useful check on both the sign and magnitude of the stiffness coefficients. These expressions for the stiffness properties are

$$K_{11} = \iint_{h,v} \bar{Q}_{11} dA - \frac{\iint_{h,v} \bar{Q}_{12} dA}{\iint_{h,v} \bar{Q}_{22} dA} \iint_{h,v} \bar{Q}_{12} dA \tag{3.7a}$$

$$K_{12} = -\iint_{h} \bar{Q}_{16} dA + \frac{\iint_{h} \bar{Q}_{26} dA}{\iint_{h} \bar{Q}_{22} dA} \iint_{h} \bar{Q}_{12} dA \tag{3.7b}$$

$$K_{13} = -\iint_{v} \bar{Q}_{16} dA + \frac{\iint_{v} \bar{Q}_{26} dA}{\iint_{v} \bar{Q}_{22} dA} \iint_{v} \bar{Q}_{12} dA \tag{3.7c}$$

$$K_{14} = (1+\beta)\iint_h \bar{Q}_{16}\zeta dA + (1-\beta)\iint_v \bar{Q}_{16}\eta dA + \\ + \frac{(1+\beta)\iint_h \bar{Q}_{26}\zeta dA - (1-\beta)\iint_v \bar{Q}_{26}\eta dA}{\iint_{h,v} \bar{Q}_{22} dA} \iint_{h,v} \bar{Q}_{12} dA \tag{3.7d}$$

$$K_{22} = \iint_h \bar{Q}_{66} dA - \frac{\iint_h \bar{Q}_{26} dA}{\iint_h \bar{Q}_{22} dA} \iint_h \bar{Q}_{26} dA \tag{3.7e}$$

$$K_{25} = -\iint_h \bar{Q}_{16}\zeta dA + \frac{\iint_h \bar{Q}_{26}\zeta dA}{\iint_h \bar{Q}_{22}\zeta^2 dA} \iint_h \bar{Q}_{12}\zeta^2 dA \tag{3.7f}$$

$$K_{33} = \iint_v \bar{Q}_{66} dA - \frac{\iint_v \bar{Q}_{26} dA}{\iint_v \bar{Q}_{22} dA} \iint_v \bar{Q}_{26} dA \tag{3.7g}$$

$$K_{36} = -\iint_v \bar{Q}_{16}\eta dA + \frac{\iint_v \bar{Q}_{26}\eta dA}{\iint_v \bar{Q}_{22}\eta^2 dA} \iint_v \bar{Q}_{12}\eta^2 dA \tag{3.7h}$$

$$K_{44} = (1+\beta)^2 \iint_h \bar{Q}_{66}\zeta^2 dA + (1-\beta)^2 \iint_v \bar{Q}_{66}\eta^2 dA + \\ + \frac{(1+\beta)\iint_h \bar{Q}_{26}\zeta dA - (1-\beta)\iint_v \bar{Q}_{26}\eta dA}{\iint_{h,v} \bar{Q}_{22} dA} \Bigg[(1-\beta)\iint_v \bar{Q}_{26}\eta dA + \\ -(1+\beta)\iint_h \bar{Q}_{26}\zeta dA\Bigg] - (1-\beta)^2 \frac{\iint_v \bar{Q}_{26}\eta^2 dA}{\iint_{h,v} \bar{Q}_{22}\eta^2 dA} \iint_v \bar{Q}_{26}\eta^2 dA + \\ - (1+\beta)^2 \frac{\iint_h \bar{Q}_{26}\zeta^2 dA}{\iint_{h,v} \bar{Q}_{22}\zeta^2 dA} \iint_h \bar{Q}_{26}\zeta^2 dA \tag{3.7i}$$

$$K_{45} = (1+\beta)\iint_v \bar{Q}_{16}\zeta^2 dA - (1+\beta)\frac{\iint_h \bar{Q}_{26}\zeta^2 dA}{\iint_{h,v} \bar{Q}_{22}\zeta^2 dA} \iint_{h,v} \bar{Q}_{12}\zeta^2 dA \tag{3.7j}$$

$$K_{46} = -(1-\beta)\iint_v \bar{Q}_{16}\eta^2 dA + (1-\beta)\frac{\iint_v \bar{Q}_{26}\eta^2 dA}{\iint_{h,v} \bar{Q}_{22}\eta^2 dA} \iint_{h,v} \bar{Q}_{12}\eta^2 dA \tag{3.7k}$$

$$K_{55} = \iint_{h,v} \bar{Q}_{11}\zeta^2 dA - \frac{\iint_{h,v} \bar{Q}_{12}\zeta^2 dA}{\iint_{h,v} \bar{Q}_{22}\zeta^2 dA} \iint_{h,v} \bar{Q}_{12}\zeta^2 dA \tag{3.7l}$$

$$K_{66} = \iint_{h,v} \bar{Q}_{11}\eta^2 dA - \frac{\iint_{h,v} \bar{Q}_{12}\eta^2 dA}{\iint_{h,v} \bar{Q}_{22}\eta^2 dA} \iint_{h,v} \bar{Q}_{12}\eta^2 dA \tag{3.7m}$$

where $\iint_h$ denotes an integral over the upper and lower walls, $\iint_v$ denotes an integral over the side walls, η is the chordwise coordinate, ζ is the heightwise coordinate, $\beta = (\alpha - 1)/(1 + \alpha)$ and $\alpha = (w/h)(G_v/G_h)$. G_v and G_h are the effective shear stiffnesses defined by

$$G_{h,v} = \frac{1}{t}\left(\bar{A}_{66(h,v)} - \frac{\bar{A}^2_{16(h,v)}}{\bar{A}_{11(h,v)}}\right) \tag{3.8}$$

where

$$\bar{A}_{11(h,v)} = A_{11(h,v)} - \frac{A_{12(h,v)}^2}{A_{22(h,v)}}, \qquad \bar{A}_{16(h,v)} = A_{16(h,v)} - \frac{A_{12(h,v)}A_{26(h,v)}}{A_{22(h,v)}}$$

$$\bar{A}_{66(h,v)} = A_{66(h,v)} - \frac{A_{26(h,v)}^2}{A_{22(h,v)}}, \qquad A_{ij(h,v)} = \sum_{n=1}^{6} \bar{Q}_{ij}^{(n)} t_{\text{ply}}^{(n)}$$

3.3.2 3-D Finite Element Model

The 3-D finite element models for all three ply layups were generated in *ANSYS* using 14400 SOLID186 elements, with 120 elements along the length, 10 elements along the width, 6 elements along the height, and 2 elements through the thickness, with the mesh of the cross-section shown in Fig. 3.19. Using the same loading procedure discussed in Sec. 3.1.2, the loads were applied at the right end ($x = 60$ cm) of the composite box beams with the left end ($x = 0$ cm) fully constrain in all three degrees of freedom. For all three ply layups, the same loading magnitudes were applied, as summarized in Table 3.6, which were selected to produce maximum strains of about 500 $\mu\epsilon$ under an axial load and about 2500 $\mu\epsilon$ under the remaining five loading conditions.

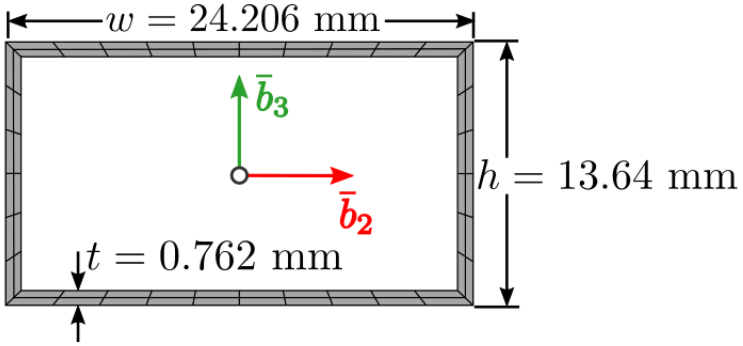

Figure 3.19: Cross-sectional mesh of the composite box beams.

After the boundary conditions were applied for the beams under all six loading conditions, the displacements and strains were calculated with a few representative results shown in Fig. 3.20 and Fig. 3.21. The shear strain γ_{12}^{+} under an axial load

for all three ply layups is shown in Fig. 3.20. For the uncoupled beam, shown in Fig. 3.20(a), the shear strain is nearly zero throughout the entire beam. For the beam with the symmetric layup under an axial load, shown in Fig. 3.20(b), the shear strain is non-zero on both the top and bottom walls where the plies are oriented at 20° and -20°, respectively. This shear strain arises due to the extension/shear coupling and results in a small shear deformation in the chordwise direction ($\bar{b}_2$). For the beam with an antisymmetric layup under an axial load, shown in Fig. 3.20(e), the shear strain is again non-zero on both the top and bottom walls and the beam exhibits a negative torsional rotation about the beam's axis ($\bar{b}_1$) due to the extension/torsion coupling.

Table 3.6: Applied loads for the composite box-beams

Loading	Surface Traction (3-D model)	Equivalent Beam Load
Axial	$f_1 = 7.10 \times 10^7$ N/m^2	$F_1 = 3930$ N
Lag shear	$f_2 = 1.92 \times 10^6$ N/m^2	$F_2 = 106$ N
Flap shear	$f_3 = 1.38 \times 10^6$ N/m^2	$F_3 = 76.1$ N
Torsional	$f_{1,t} = 39.0$ N	$M_1 = 1.89$ N-m
Flap bending	$m_2 = 2.60 \times 10^7 z$ N/m^2	$M_2 = 45.7$ N-m
Lag bending	$m_3 = 1.47 \times 10^7 y$ N/m^2	$M_3 = 63.5$ N-m

The axial strain γ_{11}^{+} under a flap bending load for all three ply layups is shown in Fig. 3.21. For the uncoupled beam shown in Fig. 3.21(a), the axial strain distribution was nearly constant along the span but varied linearly in the flapwise direction ($\bar{b}_3$) from about -1250 $\mu\epsilon$ to about 1250 $\mu\epsilon$. For the beams with the symmetric and antisymmetric layups, shown in Fig. 3.21(b-c), both the displacement and axial strain were about 2.5 times as much as the for the uncoupled beam. For the antisymmetric layup, the axial strain was still nearly constant along the span but varied linearly from about -3300 $\mu\epsilon$ to about 3300 $\mu\epsilon$ in the flapwise direction ($\bar{b}_3$); however for the symmetric layup, strain concentrations arose near both the root and tip of the beam where the boundary conditions were applied causing larger variations

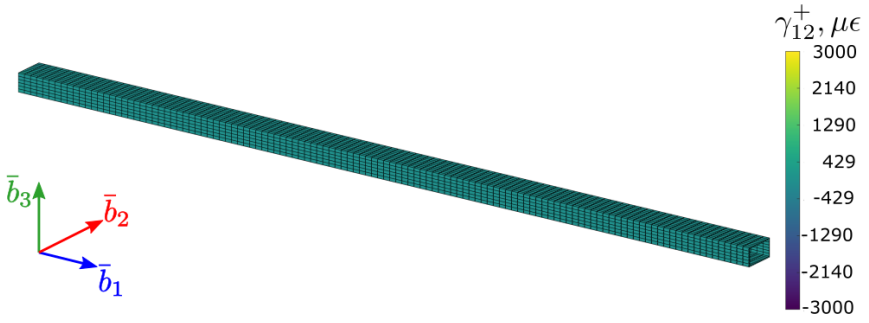

(a) Uncoupled layup

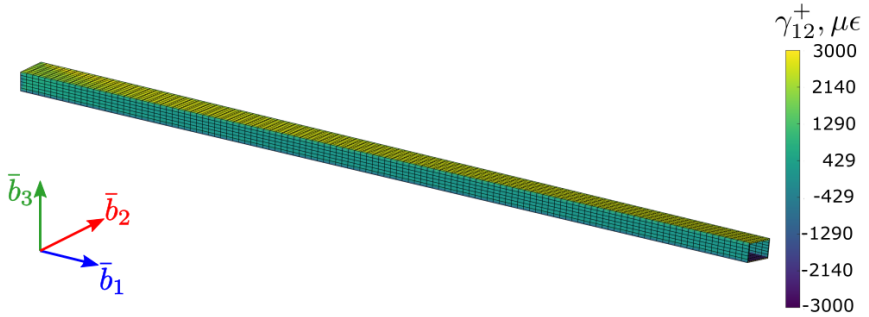

(b) Symmetric layup

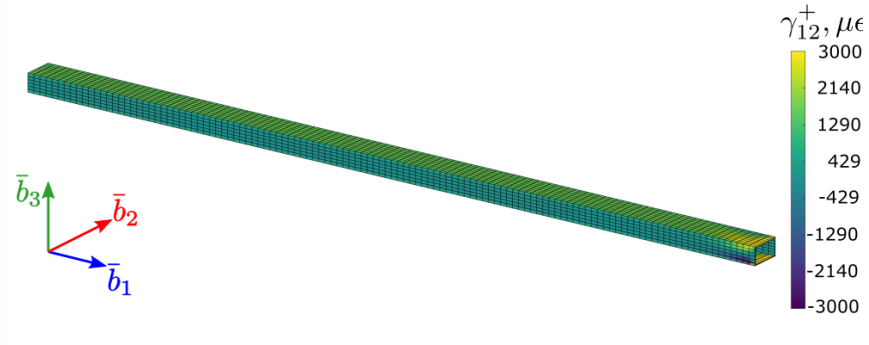

(c) Antisymmetric layup

Figure 3.20: Shear strain γ_{12}^{+} in surface basis $\mathcal{E} = (\bar{e}_1, \bar{e}_2, \bar{e}_3)$ under an axial load, f_1 for the three composite box beam layups.

along the span. In addition, for the antisymmetric layup, the beam exhibited a small amount of lateral deflection in the chordwise direction ($\bar{b}_2$) due to the shear/bending coupling, while for the symmetric layup, the beam exhibited a significant rotation about the beam's axis ($\bar{b}_1$) due to the torsion/bending coupling present in the beam.

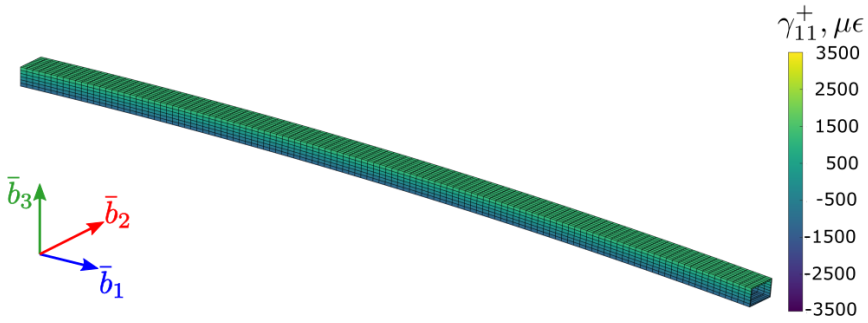

(a) Uncoupled layup

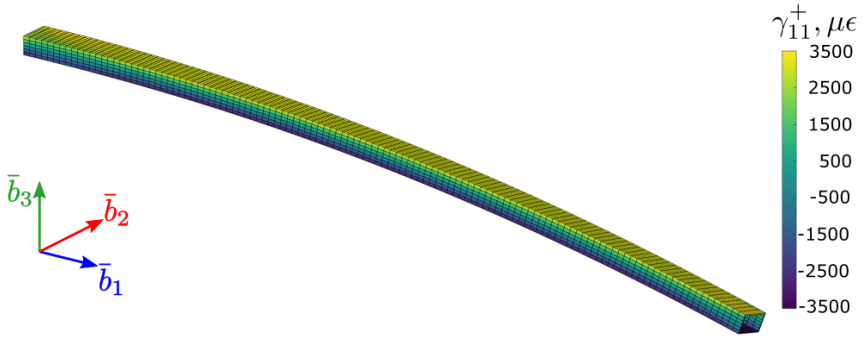

(b) Symmetric layup

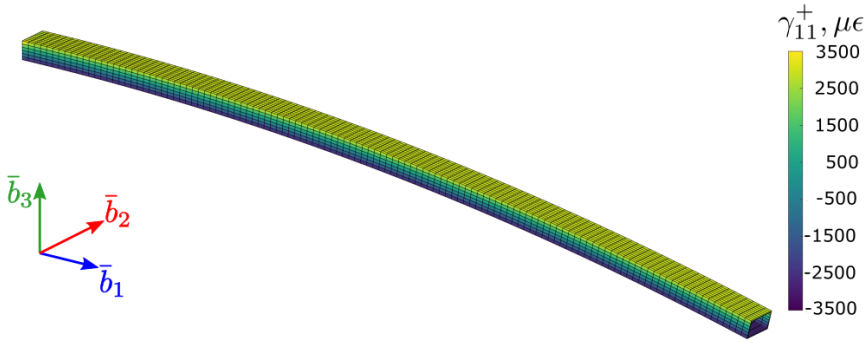

(c) Antisymmetric layup

Figure 3.21: Axial strain γ_{11}^{+} in surface basis $\mathcal{E} = (\bar{e}_1, \bar{e}_2, \bar{e}_3)$ under a flap bending load, m_2, for the three composite box beam layups.

3.3.3 Stiffness Results

Once the data reduction matrices were assembled, using the sectional stress resultants along the span, the rotated strains from the *ANSYS* models, and the numerical warping field, the compliance and stiffness matrices were calculated at discrete locations every cm along the span, with the results for the diagonal entries of the stiffness matrices shown in Figs. 3.22-3.27 for all three composite layups. Since

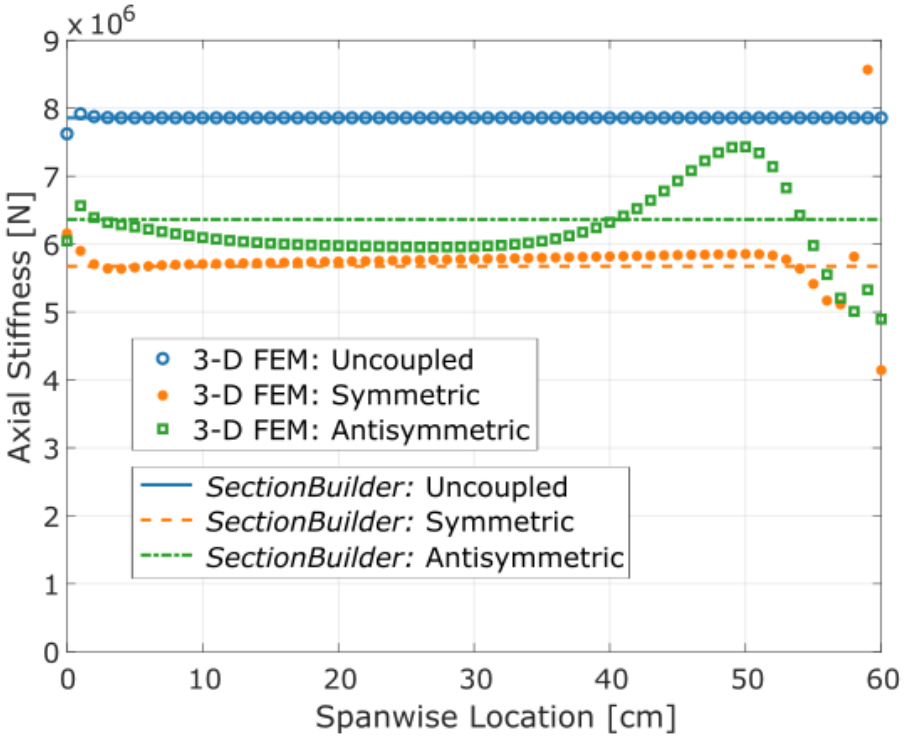

Figure 3.22: Spanwise variations of the axial stiffness, K_{11}, for the composite box beams.

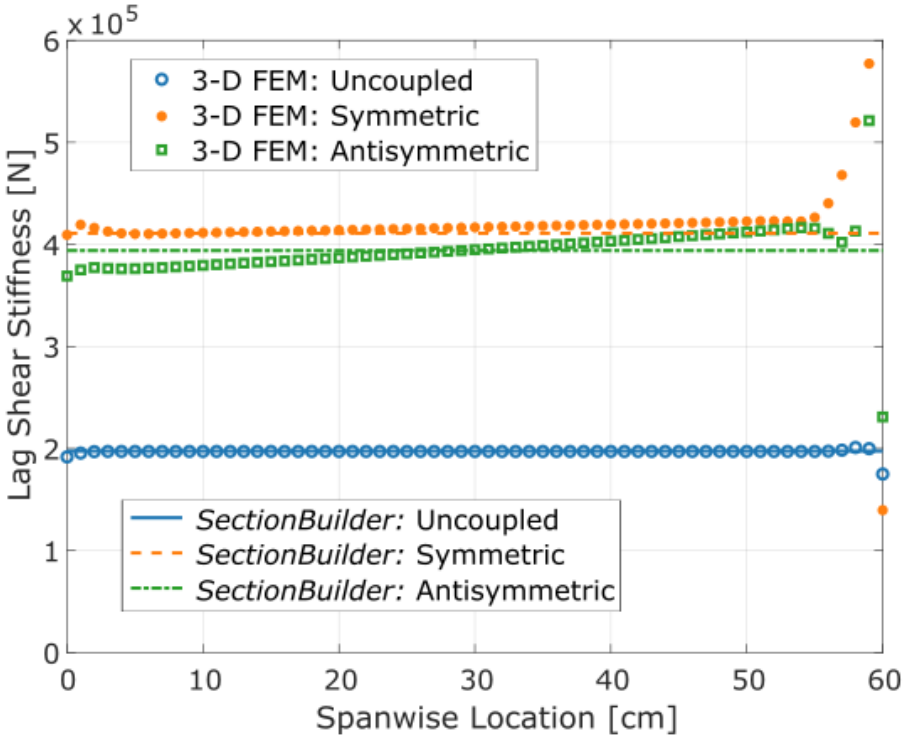

Figure 3.23: Spanwise variations of the lag shear stiffness, K_{22}, for the composite box beams.

no analytic solution exists for the composite beams, the stiffness results were all compared to their predicted values from *SectionBuilder* and predictions available in literature. For the uncoupled beam, whose values from the 3-D FEM strains are shown as hollow blue circles (○), the calculated stiffnesses were all nearly constant along the span and overall showed great agreement with the stiffness values predicted from *SectionBuilder*, shown as solid lines. Only in the case of the flap shear stiffness (K_{33}) and torsional stiffness (K_{44}) are discrepancies observed, with the values calculated from the 3-D FEM strains about 7% lower than the predicted values. In the case of the coupled beam with a symmetric layup, whose calculated results from the 3-D FEM strains are shown as filled orange circles (●), the stiffness values showed some variations along the span, particularly near the tip of the beam ($x = 60$ cm). Overall the calculated stiffness values and those predicted from *SectionBuilder*, shown as dashed lines, showed good agreement except for in the flap shear (K_{22}) and torsional (K_{44}) stiffnesses, which both had discrepancies of about 10%. For the coupled beam with the antisymmetric layup, whose results are shown as hollow green squares (□), the stiffness values calculated from the 3-D FEM strains showed the greatest spanwise variations. Overall, the calculated stiffness values for the antisymmetric layup show fairly good agreement with the results predicted by *SectionBuilder*, shown as dashed-dotted lines; however, the lag bending (K_{66}) and flap shear (K_{33}) were both about 20% less than the predicted values.

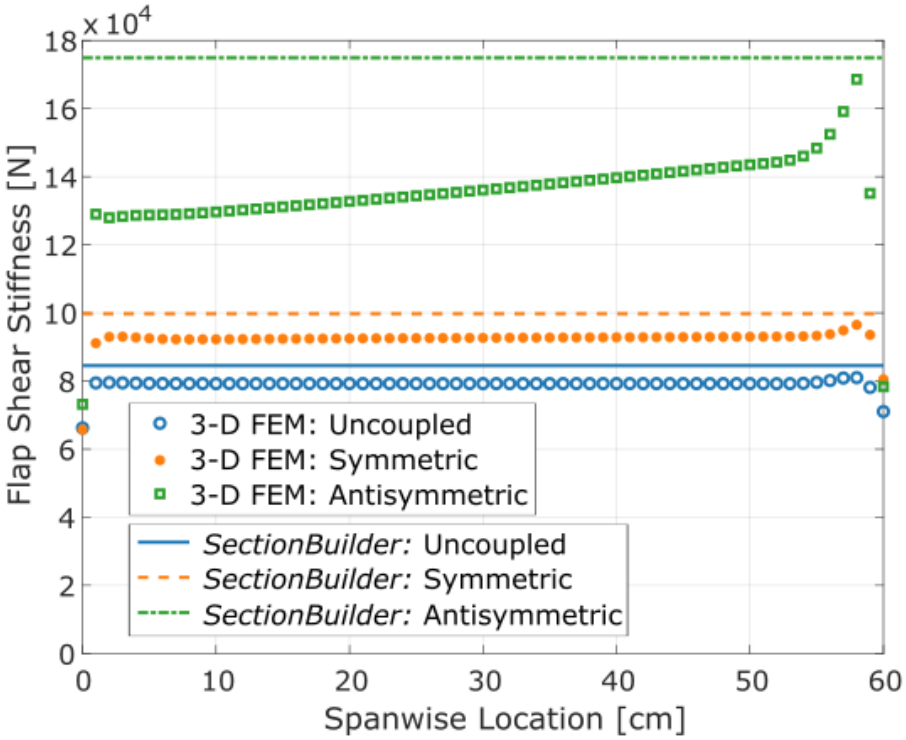

Figure 3.24: Spanwise variations of the flap shear stiffness, K_{33}, for the composite box beams.

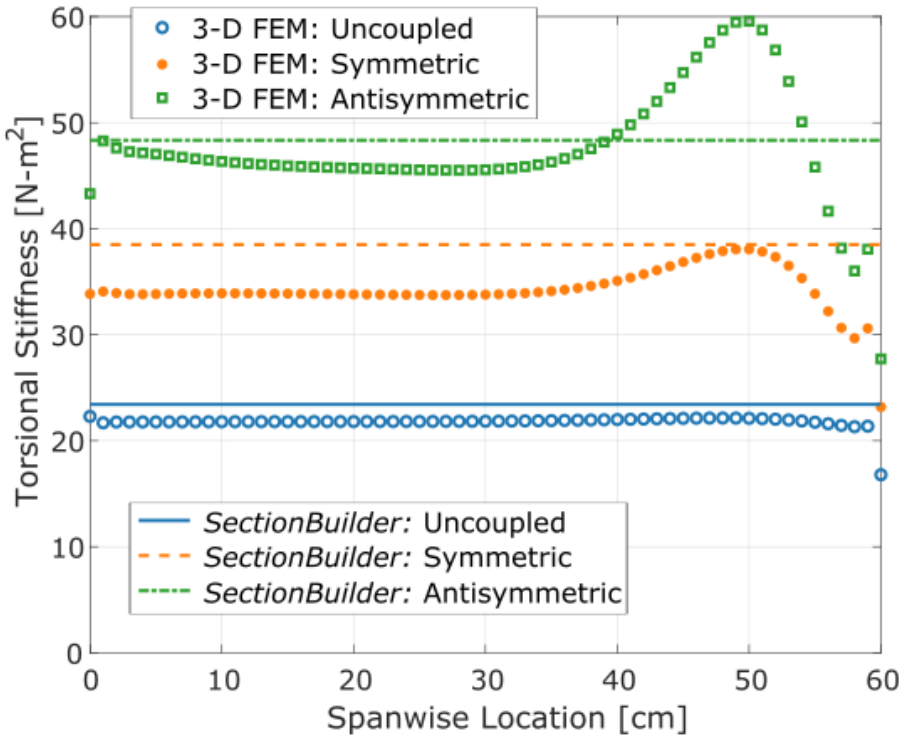

Figure 3.25: Spanwise variations of the torsional stiffness, K_{44}, for the composite box beams.

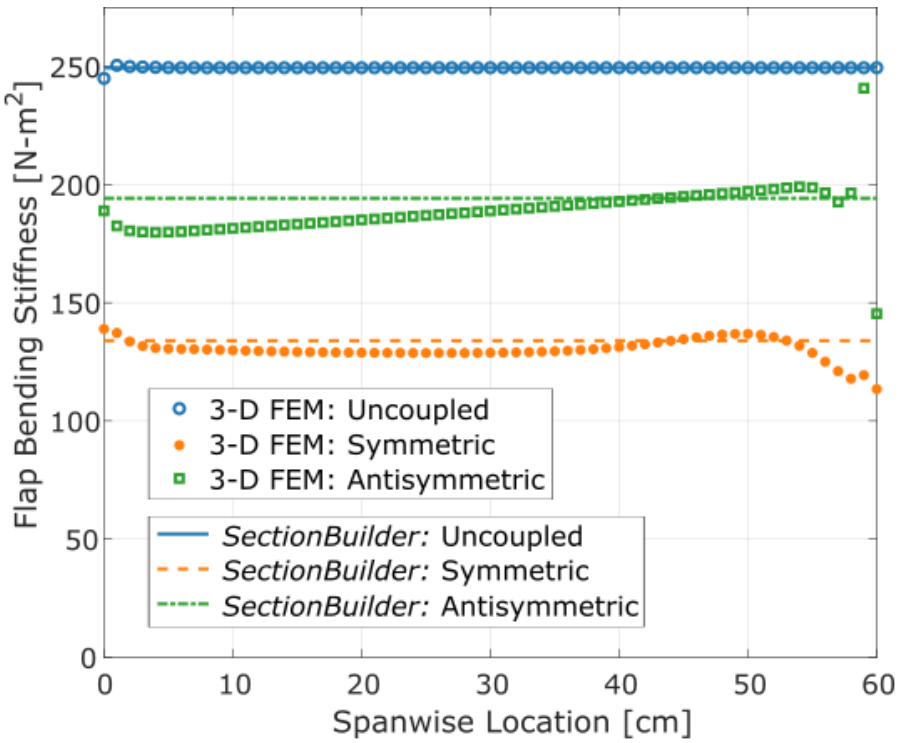

Figure 3.26: Spanwise variations of the flap bending stiffness, K_{55}, for the composite box beams.

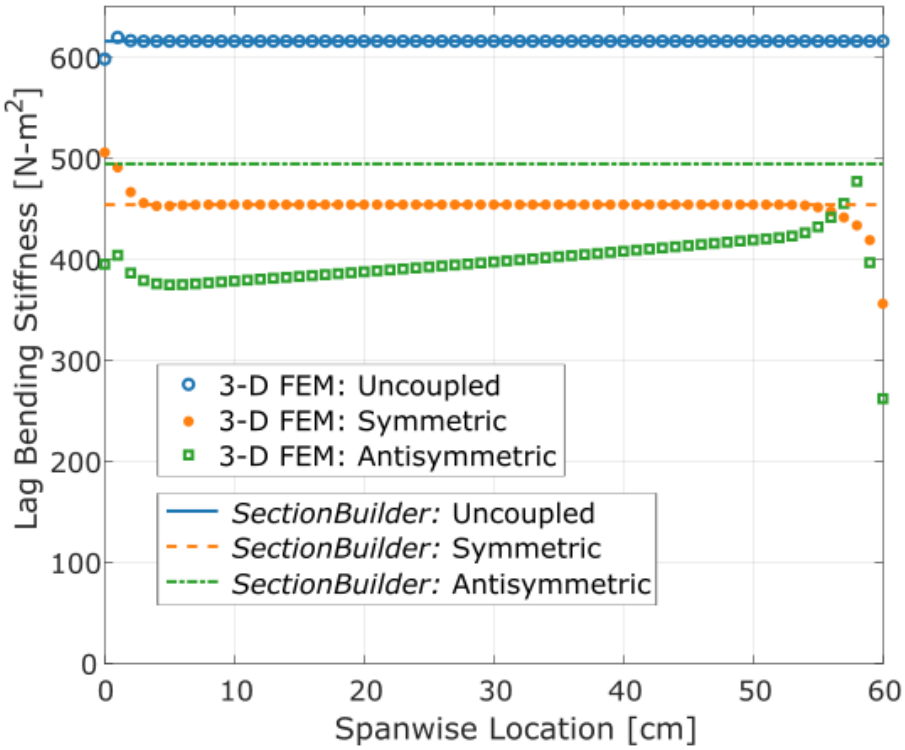

Figure 3.27: Spanwise variations of the lag bending stiffness, K_{66}, for the composite box beams.

While the diagonal entries of the stiffness matrices for the three composite beams showed generally good agreement with the predicted values from *SectionBuilder*, the goal in selecting multiple layups was to also verify the capability to measure the elastic coupling terms that appear in the off-diagonal entries of the stiffness matrix. For the beam with the symmetric layup, there should be both a coupling between the flap bending and torsional deformations, represented by a non-zero stiffness K_{45}, and between the extension and lag shear deformations, represented by a non-zero stiffness K_{12}. The spanwise variations of both of these elastic coupling stiffnesses are shown in Fig. 3.28; the extension/shear coupling stiffness (○) showed overall good agreement with the value predicted by *SectionBuilder*, but with some variations near the beams edges. The bending/torsion coupling (□) showed a discrepancy of about 10% between the calculated and predicted stiffness value, with significant spanwise variations near the tip of the beam that mirror the calculated torsional stiffness

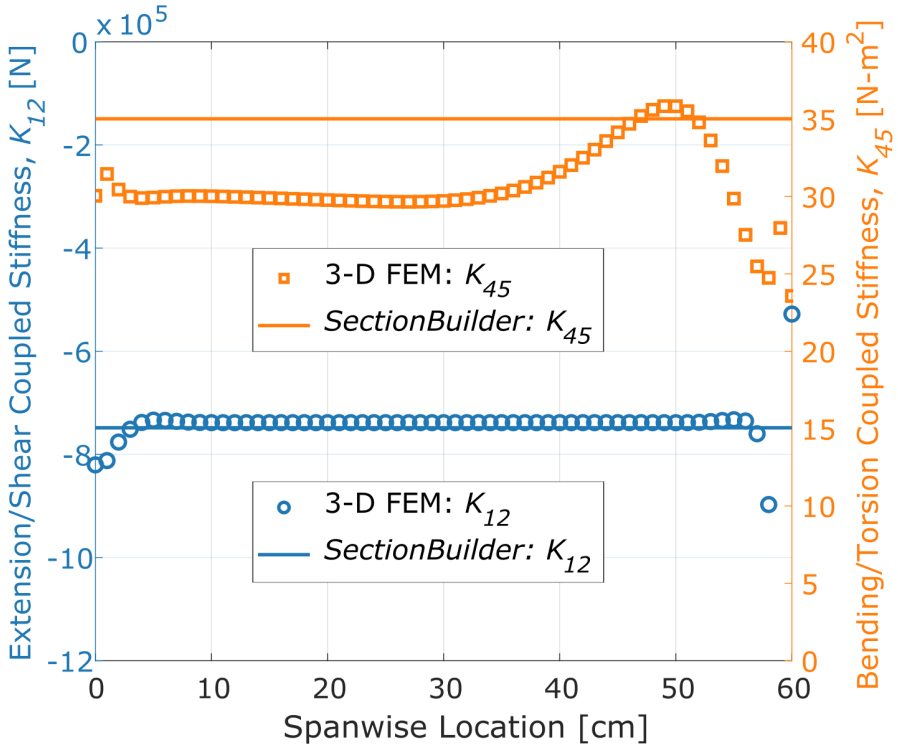

Figure 3.28: Spanwise variations of the extension/shear coupling stiffness, K_{12}, and the bending/torsion coupling stiffness, K_{45}, for the symmetric composite box beam layup.

distribution from Fig. 3.25.

For the beam with the antisymmetric layup, there should be three coupling terms present; an extension/torsion coupling, represented by a non-zero stiffness K_{14}, and two elastic couplings between the shear and bending deformations, with a flap bending/lag shear coupling given by K_{25} and a lag bending/flap shear coupling given by K_{36}, with the spanwise distributions shown in Fig. 3.29. Although there are significant spanwise variations in the extension/torsion coupling stiffness(○), the mean of the variations was close to the value predicted by *SectionBuilder*, shown as a solid line. For the shear bending couplings, the flap bending/lag shear coupling K_{25}(●) had good agreement with the value predicted by *SectionBuilder* shown as a dashed line, but with some variation along the span; however, the lag bending/flap shear coupling K_{36}(□) showed a discrepancy of about 30%.

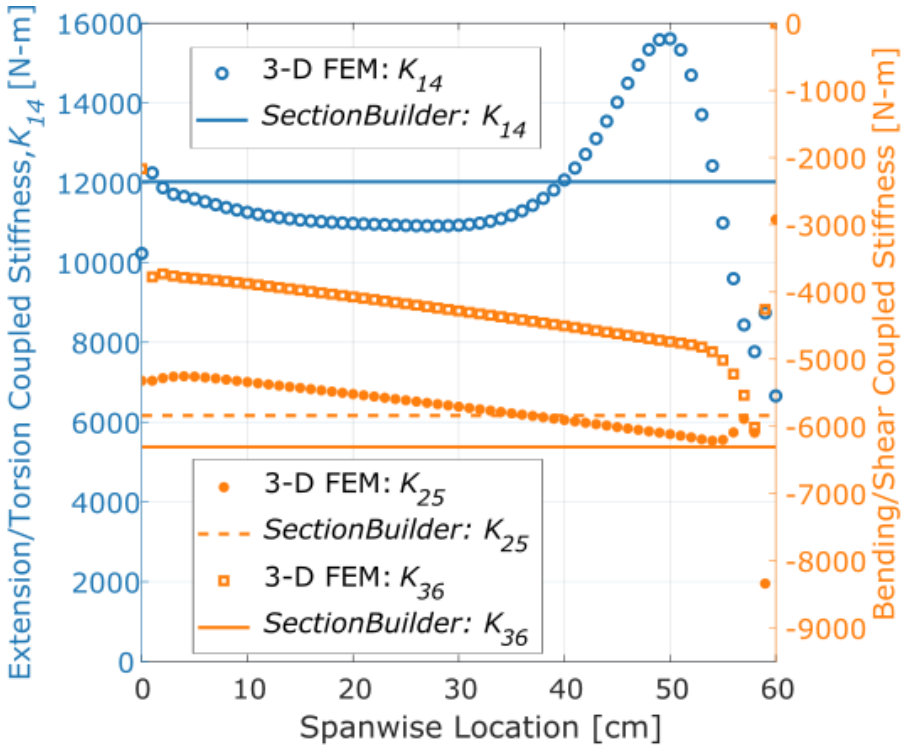

Figure 3.29: Spanwise variations of the extension/torsion coupling stiffness, K_{14}, and the bending/shear coupling stiffnesses, K_{25} and K_{36} n, for the antisymmetric composite box beam layup.

Although there are some spanwise variations in the stiffness properties cal-

culated from the 3-D FEM strains, which arise from the boundary conditions and the longer diffusion lengths inherent to composite materials, the cross-sectional geometry and material distribution was constant along the span and it can also be useful to compare the average stiffness properties along the entire span with numerical predictions. The uncoupled beam with the $[0^\circ]_6$ layup on all four sides has been extensively studied in past literature and the calculated results are compared with those from *SectionBuilder*, the reported results from VABS [126], and those calculated using the equations from Smith and Chopra [66] that are summarized in Sec. 3.3.1 and denoted by CLPT (Composite Laminate Plate Theory). For the uncoupled beam, the only non-zero stiffnesses were the six entries along the diagonal, whose average values are compared in Table 3.7. The calculated stiffnesses from 3-D FEM show good agreement with the numerical predictions, except for in the flap shear (K_{33}) and torsional (K_{44}) terms which have discrepancies of about 7%. Note that the stiffness values calculated by treating the walls as composite laminated plates (CLPT) also show good correlation with the other numerical methods, except for in the shear stiffness terms which are both overpredicted.

For the symmetric layup, the beam presented non-zero stiffness values for the extension/shear coupling (K_{12}) and the bending/torsion coupling (K_{45}), whose average values are compared in Table 3.8 along with the diagonal components. Since

Table 3.7: Average stiffness of the uncoupled composite box beam

Stiffness Term	Calculated from 3-D FEM Strains	Numerical Predictions		
		SectionBuilder	***VABS***	**CLPT**
K_{11} [N]	7.856×10^6	7.858×10^6	7.858×10^6	7.858×10^6
K_{22} [N]	1.968×10^5	1.974×10^5	1.980×10^5	2.144×10^5
K_{33} [N]	7.896×10^4	8.452×10^4	8.496×10^4	11.78×10^4
K_{44} [N-m^2]	21.8	23.4	23.5	23.0
K_{55} [N-m^2]	249.4	249.4	249.4	249.4
K_{66} [N-m^2]	615.8	616.0	617.0	616.0

Table 3.8: Average stiffness of the symmetric layup composite box beam

Stiffness Term	Calculated from 3-D FEM Strains	Numerical Predictions	
		SectionBuilder	**CLPT**
K_{11} [N]	5.648×10^6	5.674×10^6	6.252×10^6
K_{12} [N]	-7.384×10^5	-7.477×10^5	-10.01×10^5
K_{22} [N]	4.051×10^5	4.109×10^5	5.437×10^5
K_{33} [N]	9.179×10^4	9.974×10^4	11.78×10^4
K_{44} [N-m^2]	34.0	38.5	45.0
K_{45} [N-m^2]	31.0	35.0	52.9
K_{55} [N-m^2]	130.6	134.0	180.2
K_{66} [N-m^2]	454.1	454.1	546.5

no results are available in literature for this layup using VABS, the calculated results are only compared with *SectionBuilder* and those using the CLPT equations. For the stiffness values calculated from 3D FEM and the *SectionBuilder* predictions, the main discrepancies occurred in the flap shear (K_{33}), torsional (K_{44}), and flap bending/torsional coupling (K_{45}) stiffnesses with differences of about 10%. In all cases, the results using the CLPT equations correctly predicted the sign and overall order of magnitude, but overpredicted the actual stiffness values by 10 to 25%. For the antisymmetric layup, the beam presented an extension/torsion coupling and two shear/bending couplings, with the average values of the nine non-zero components compared to the numerical predictions in Table 3.9, with the *VABS* results coming from Yu et al. [29]. The agreement between the calculated values and numerical predictions from *SectionBuilder* was good, with the exception of the flap shear (K_{33}), lag bending (K_{66}), and lag bending/flap shear coupled (K_{36}) stiffnesses, which showed differences of about 20%,

Since both the data reduction algorithm and the 2-D cross-sectional analysis codes rely on calculating the sectional compliance matrix and then inverting to get the sectional stiffness matrix, it can be useful to also compare the compliance components, specifically for the case of the antisymmetric layup where the largest

Table 3.9: Average stiffness of the antisymmetric layup composite box beam

Stiffness Term	Calculated from 3-D FEM Strains	Numerical Predictions		
		SectionBuilder	***VABS***	**CLPT**
K_{11} [N]	6.211×10^6	6.363×10^6	6.363×10^6	6.363×10^6
K_{22} [N]	3.937×10^5	3.940×10^5	2.243×10^5	4.852×10^5
K_{33} [N]	1.351×10^5	1.749×10^5	0.915×10^5	2.665×10^5
K_{14} [N-m]	1.164×10^4	1.203×10^4	1.214×10^4	1.427×10^4
K_{25} [N-m]	-5697	-5840	-3282	-6012
K_{36} [N-m]	-4224	-6307	-3323	-6012
K_{44} [N-m^2]	47.5	48.4	48.2	51.7
K_{55} [N-m^2]	189.0	194.2	152.0	202.0
K_{66} [N-m^2]	398.3	494.6	384.6	498.8

differences were noticed between the results. For this case, the compliance matrices calculated from the 3-D FEM strains and from both *SectionBuilder* and *VABS* are compared in Table 3.10. While large differences were observed between the calculated stiffnesses and those from *SectionBuilder* for the flap shear, lag bending, and lag bending/flap shear coupled components, the difference was primarily observed only

Table 3.10: Average compliance of the antisymmetric layup composite box beam

Stiffness Term	Calculated from 3-D FEM Strains	Numerical Predictions	
		SectionBuilder	***VABS***
S_{11} [1/N]	2.980×10^{-7}	2.966×10^{-7}	3.025×10^{-7}
S_{22} [1/N]	4.505×10^{-6}	4.579×10^{-6}	6.518×10^{-6}
S_{33} [1/N]	1.108×10^{-5}	1.058×10^{-5}	1.593×10^{-5}
S_{14} [1/(N-m)]	-7.300×10^{-5}	-7.379×10^{-5}	-7.620×10^{-5}
S_{25} [1/(N-m)]	1.358×10^{-4}	1.377×10^{-4}	1.407×10^{-4}
S_{36} [1/(N-m)]	1.175×10^{-4}	1.350×10^{-4}	1.376×10^{-4}
S_{44} [1/(N-m^2)]	3.896×10^{-2}	3.904×10^{-2}	3.999×10^{-2}
S_{55} [1/(N-m^2)]	9.384×10^{-3}	9.289×10^{-3}	9.618×10^{-3}
S_{66} [1/(N-m^2)]	3.757×10^{-3}	3.743×10^{-3}	3.789×10^{-3}

in the lag bending/flap shear coupled compliance S_{36}. This shows that, because of the process of inverting the compliance matrix, a discrepancy in a single compliance matrix property S_{ij} can propagate into discrepancies in any of the non-zero stiffness properties with an i or j subscript. Similar observations were observed with the *VABS* predicted properties; large discrepancies in the two shear compliance values, S_{22} and S_{33}, propagated into discrepancies in the six related stiffness properties, K_{22}, K_{25}, K_{33}, K_{36}, K_{55}, and K_{66}, despite the fact that the S_{25}, S_{55}, and S_{66} compliance properties showed good correlation with one another.

3.4 Summary and Conclusions

The proposed strain-based methodology for calculating the sectional stiffness properties was validated using strains predicted from 3D finite element models in *ANSYS*. The first section considered the case of a prismatic beam with a rectangular cross-section and made of an isotropic material; the stiffness values calculated using the data reduction algorithm on the predicted strains from *ANSYS* were validated with analytic solutions. The results agreed very well with one another for all six non-zero stiffness matrix components. Since the beam had a constant cross-section, the stiffness properties were expected to remain constant along the span with the only minor spanwise variations in the calculated properties observed near the beam's edges where the boundary conditions were applied. This simple beam also verified that the proposed methodology can measure all six diagonal stiffness terms, as opposed to only three stiffness values – K_{44}, K_{55}, and K_{66} – that can be measured with existing techniques.

The second section considered a beam with a rectangular cross-section made of an isotropic material, with the cross-sectional dimensions decreasing linearly along the span. Two levels of taper were analyzed to verify the capability of the proposed data reduction algorithm to handle spanwise variations in properties; with exception

to the flap shearing stiffness K_{33}, the calculated stiffness properties showed great correlation with the analytic solutions that were derived for the case of a prismatic beam. For the flap shearing stiffness, the boundary condition and taper cause larger discrepancies of greater than 10% near the clamped end of the beam, but the results end up showing much better correlation near the tip where the cross-sectional dimensions were smallest. Overall, this case verified that the current strain-based method is able to predict the sectional stiffness locally along the beam and allow for measurements on non-prismatic beams, as opposed to most existing methods which can only measure a global stiffness value for the entire beam.

Finally, the capability of the implemented data reduction equations to measure off-diagonal coupling terms is verified using the composite box-beam geometry initially studied by Chandra and Chopra and subsequently used for validating various cross-sectional analysis codes. Calculated stiffness values were presented for three different ply layups, including an uncoupled layup whose only non-zero stiffness values were the six diagonal components, a symmetric layup with non-zero K_{12} and K_{45} stiffness values in addition to the six non-zero diagonal terms, and an antisymmetric layup with nonzero K_{14}, K_{25}, and K_{36} stiffness values in addition to the six non-zero diagonal terms. While some larger discrepancies were observed between the calculated and predicted stiffness values, this case verified that the proposed methodology could measure the full 6×6 stiffness matrix including all expected non-zero off-diagonal terms, in contrast with past experimental techniques that have measured the torsion/flap bending off-diagonal stiffness component only. The discrepancies also highlight a shortcoming of using only the central solution for a composite beam; since composite materials have a much larger diffusion length, the end effects propagate significantly farther along the beam's span than for a beam made of an isotropic material.

Chapter 4: Uncertainty Quantification

This chapter focuses on propagation of the uncertainties from the experimental measurements into the final stiffness matrix calculation. An overview of the types of experimental uncertainties is first discussed, followed by a discussion of two common methods for analysis of uncertainty propagation – a Monte Carlo Method and a Taylor Series Method. A comparison of the two methods is then made by applying the uncertainty propagation to the results of the prismatic aluminum beam and the composite box-beam with extension-torsion coupling from the numerical validation models of Chapter 3.

4.1 Types of Experimental Errors

When working with experimental data, the total error will consist of contributions from *random* (or *precision*) errors and *systematic* (or *bias*) errors [128]. The random errors are associated with the noise, or random variations within the measurement system and, because of this, if the measurement were taken an infinite number of times and averaged, there would be no impact on the total measurement. However, it is often impractical to take a large enough number of samples to completely eliminate the random variations from the measurement and it therefore must be considered in the uncertainty quantification. The random error for a measurement system can be approximated by taking a sample set of data in a controlled environment. Typically, this error will take the form of a Gaussian distribution, as shown in Fig. 4.1(a). If a total of N measurements are obtained in the sample set,

the uncertainty can be estimated from the standard deviation σ_r of these readings given by

$$\sigma_r = \left[\frac{1}{N-1} \sum_{j=1}^{N} (X^{(j)} - \mu)^2 \right]^{1/2} \tag{4.1}$$

where $X^{(j)}$ is the value of the j^{th} measurement and μ is the mean value of the data samples. A common practice when performing an uncertainty analysis is to provide a 95% confidence interval on the measurement which can be approximated by $S_r = \pm 2\sigma_r$ [128].

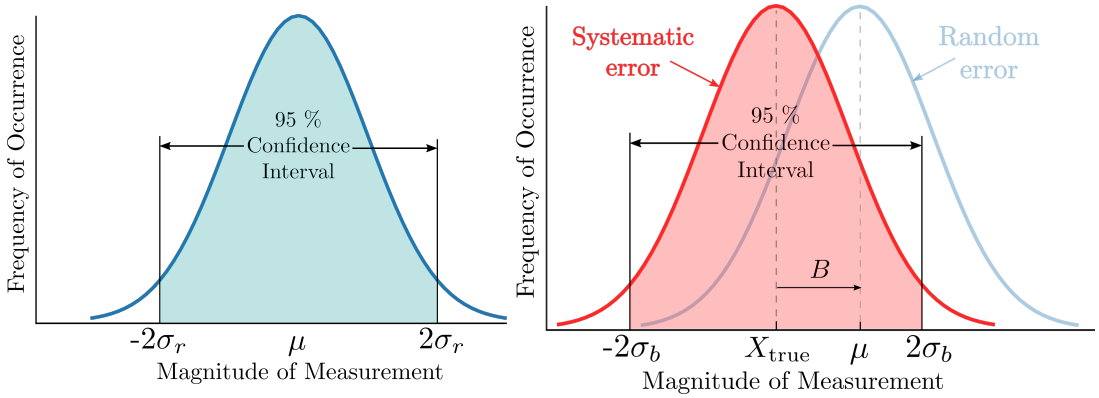

(a) Random error distribution from a sample data set

(b) Possible systematic error distributions

Figure 4.1: Combined random and systematic error distributions.

The second type of error is the systematic error, which is a constant error within the system resulting from the calibration of the measurement device. This a fixed error that will be present in the measurement, regardless of how many times the experiment is performed, which is why it is often regarded as a bias error in the measurement. Because the true value of any experimental variable, such as mass or temperature, is not known with 100% accuracy, the systematic error can not easily be identified or removed from an experiment and must be estimated from knowledge of the calibration procedure, which is typically provided by the vendor of the equipment. It is also typically assumed that the systematic error will take the form of a Gaussian distribution, as seen in Fig. 4.1(b). In this case, the 95%

confidence level means that it is 95% certain that the systematic error B is within the uncertainty range $S_b = \pm 2\sigma_b$ of the true value of the measurement variable, based on expectations from the calibration procedure.

Oftentimes, the desired results are calculated from multiple measured variables, each of which has its own uncertainty distributions. The total uncertainty for the i^{th} measurement variable X_i can then be represented by

$$u_{X_i}^2 = S_{b,i}^2 + S_{r,i}^2 \tag{4.2}$$

where u_{X_i} provides the 95% uncertainty interval. Although it is not possible to reduce the systematic uncertainty of the experiment, the random uncertainty can be reduced if the test is repeated M times using the same test setup. In this case, the results can be averaged across multiple tests allowing for the random noise to be partially filtered out of the experiment and the associated uncertainty interval becomes

$$u_{X_i}^2 = S_{b,i}^2 + \frac{S_{r,i}^2}{M} \tag{4.3}$$

4.2 Experimental Error Quantification

In the measurement of the sectional compliance and stiffness matrices, there are multiple variables being measured and used in the data reduction procedure that have associated errors. These measurements include the loads, the strains, and the locations of the strain measurements. In addition, while not explicitly used in the data reduction equations, the material properties are required to predict the numerical warping field and their associated uncertainties must also be taken into account. The uncertainty intervals can be represented by either a percent of their measured values, which can be the case for loads and material properties, or as a dimensional value, which is more typical for measurement locations and strains.

Considering first the applied loads, these are normally measured through the use of a load cell, either at the root or the tip of the beam. In this work, the test articles were mounted to a 6-axis load cell at their clamped end to measure the three reaction forces and three reaction moments under the applied loading conditions. Extensive calibration was performed for the load cell, as described in Sec. 5.3.2, and was used to estimate the expected systematic and random uncertainties shown in Table 4.1. Calibrations were separately calculated at multiple load levels, described as a low and high loading, so that the 95% confidence intervals could be calculated as a percentage of the applied load instead of a dimensional loading based on the maximum rating of the load cell. This was also done so that the uncertainty levels for low loading conditions would not end up leading to unreasonable uncertainty levels in the calculated stiffness properties. Note however that the load cell was still usually most accurate at load levels closest to its maximum rating, which could generally be observed in comparing the uncertainty bounds between the low and high loading columns in Table 4.1.

In the measurement locations, there are several uncertainties that can impact the calculation of the stiffness properties. Since the loads are only measured at the base of the beam, the cross-sectional loads $\underline{\mathcal{F}}_c$ must be calculated from these measurements based on the spanwise location x and corresponding deflections and rotations at this location. The coordinates measured by DIC are only relative to a local coordinate system assumed by the DIC system; markings on the beams are used to determine the absolute spanwise position which is estimated to have a systematic uncertainty with a 95% confidence interval of $S_{b,x} = \pm 1$ mm. The random uncertainty in the spanwise location comes from the variations in defining this position in the DIC software for each test, with an assumed random uncertainty of $S_{r,x} = \pm 0.25$ mm. In addition to the uncertainties in the spanwise locations, there are also uncertainties of the measurement locations within the cross-section.

Table 4.1: 95% confidence intervals for systematic and random uncertainties of a 6-axis load measurement.

		Low Loading		High Loading	
		Bias, $S_{b,F}$	**Random,**$S_{r,F}$	**Bias,** $S_{b,F}$	**Random,**$S_{r,F}$
F_1	Load bounds	$\lvert F_1\rvert < 800$ N		800 N $< \lvert F_1\rvert <$ 6250 N	
	Uncertainty (%)	0.75	0.87	0.75	0.87
F_2	Load bounds	$\lvert F_2\rvert < 105$ N		105 N $< \lvert F_2\rvert <$ 2500 N	
	Uncertainty (%)	1.02	0.64	1.46	0.89
F_3	Load bounds	$\lvert F_3\rvert < 105$ N		105 N $< \lvert F_3\rvert <$ 2500 N	
	Uncertainty (%)	2.92	1.49	1.29	1.16
M_1	Load bounds	$\lvert M_1\rvert < 40$ N-m		40 N-m $< \lvert M_1\rvert <$ 400 N-m	
	Uncertainty (%)	1.60	1.26	2.01	2.04
M_2	Load bounds	$\lvert M_2\rvert < 60$ N-m		60 N-m $< \lvert M_2\rvert <$ 400 N-m	
	Uncertainty (%)	1.00	0.20	1.00	0.10
M_3	Load bounds	$\lvert M_3\rvert < 60$ N-m		60 N-m $< \lvert M_3\rvert <$ 400 N-m	
	Uncertainty (%)	0.95	0.28	1.10	0.12

From the DIC calibration procedure, the actual measurement locations for the entire cross-section were calculated to have an uncertainty of about 0.02 pixels, which corresponds to a 95% confidence interval of $S_{b,d} = \pm 0.0025$ mm. Comparing the cross-sectional measurement locations across multiple tests provided an estimate for the 95% confidence interval on the random uncertainty of $S_{r,d} = \pm 0.013$ mm. Finally, there were also uncertainties in the actual dimensions of the cross-section; because only two cameras were used in the DIC setup to measure the displacements and strains on a single external surface, the DIC system could not provide an accurate measurement of the external dimensions of the cross-section, particularly in the depth, or thickness, of the cross-section. These dimensions were instead measured using a digital calipers, with an associated 95% confidence level of $S_{b,d_{\text{ext}}} = \pm 0.025$ mm. From measurements of the external dimensions at multiple locations along the span for the various test articles, the 95% confidence interval for the random uncertainty was estimated at $S_{r,d_{\text{ext}}} = \pm 0.8\%$, resulting from manufacturing and

machining tolerances.

The strain is then calculated in the DIC software using derivatives of the measured displacement fields. The accuracy in the relative displacement between two points using the DIC software was estimated to be 0.0025 mm, which corresponded to a 95% confidence interval for the measured strain of 10.9 $\mu\epsilon$. The cameras were also mounted on a tripod that was moved vertically during testing and could result in some rigid body motion between sets of test images; simple tests were performed by translating the cameras, as discussed in Sec. 5.2.6, to estimate the expected uncertainty that could result from this rigid body motion, which was found to introduce about $\pm 16\mu\epsilon$ into the measurement. The total systematic uncertainty in the strain measurement was then estimated to have a 95% confidence interval of about $S_{b,\gamma^+_{\text{mean}}} = \pm 26.9\mu\epsilon$. The random uncertainty was then estimated based on the variations in the unstrained test images, as discussed in Sec. 5.2.7, with a 95% confidence interval of $S_{r,\gamma^+_{\text{mean}}} = \pm 24.0\mu\epsilon$. These two values represent the uncertainty for the entire strain measurement data set, as indicated by using the subscript γ^+_{mean}; however, there were also random variations observed within the cross-section for expected states of constant strain. These variations were then measured to provide a 95% confidence interval on random strain distribution within the cross-section of $S_{r,\gamma^+_{\text{std}}} = \pm 16.1\mu\epsilon$.

Finally, there are also uncertainties in the material parameters that need to be considered. For the case of an isotropic material, any uncertainties in the Young's modulus E and poisson's ratio ν would need to be considered. In this thesis, aluminum 6061 is the only structural isotropic material and the bounds for the 95% confidence intervals on the properties are assumed to be $S_{b,E} = \pm 1$ GPa for the Young's modulus and $S_{b,\nu} = \pm 0.01$ for the poisson's ratio. For the case of a transversely isotropic material, such as the composite materials used in this dissertation, there may be uncertainties in the material properties, such as the

Young's moduli, E_1 and E_2, poisson's ratios, ν_{12} and ν_{23}, and shear modulus G_{12}, as well as in the layup orientation angles given by γ_{ply}. From the Composite Materials Handbook [129], typical coefficients of variance in the measured Young's moduli and shear modulus were between 4% and 7.5%. Assuming the upper bound of these covariances, the 95% confidence intervals for the Young's moduli and shear modulus were taken as $S_{b,E_1} = S_{b,E_2} = S_{b,G_{12}} = \pm 15\%$. Although the coefficient of variance for the poisson's ratio were not described, by comparing materials of similar moduli, a reasonable estimate on the 95% confidence interval for the poisson's ratio was taken as $S_{b,\nu_{12}} = S_{b,\nu_{23}} = \pm 0.025$. For the ply orientation angles, it was assumed that during the manual layup of the plies, the actual layup angle could be produced with a 95% confidence of $S_{b,\gamma_{\text{ply}}} = \pm 3^\circ$. Since the material parameters are only required for the calculation of the warping field, there uncertainties are not expected to impact all the measured stiffness properties in most cases. Indeed, it was seen in Sec. 2.2.4 that the warping correction had no influence on the predicted axial strains in many loading conditions.

4.3 Uncertainty Propagation

Determining the uncertainty for the calculated stiffness matrix components requires propagating the errors from each of the measured variables into the final calculation. Two popular methods for uncertainty propagation were investigated – a Taylor series method and a Monte Carlo method. The nature of the data reduction equations, namely the fact that the use of DIC to measure the strains leads to a system of highly overconstrained equations for the compliance matrix components that is solved using a SVD and that the stiffness matrix is calculated as the inverse of this compliance matrix, presents additional considerations for applying conventional techniques to the uncertainty propagation, particularly for the Taylor Series method.

4.3.1 Taylor Series Method

The stiffness matrix calculation relies on measurements of the strain, force, and strain locations, in addition to the material parameters required to calculate the numerical warping field, all of which have associated uncertainties. A Taylor series method provides the impact of these uncertainties in the measurements on the calculated stiffness values through derivatives of the data reduction equation. To understand the necessary approximations, it is useful to consider the derivation of the Taylor Series uncertainty method as discussed by Coleman and Steele [128]. If the data reduction equation is a function of measured variables X_1 and X_2 and given by

$$f = f\left(X_1, X_2\right) \tag{4.4}$$

then the result for the j^{th} set of measurements is given by $f^{(j)}$. The measurement of each variable X_i will have an associated systematic and random error, given by $B_i^{(j)}$ and $P_i^{(j)}$, respectively. The value of these variables can be determined from their parent distributions whose 95% confidence intervals are described by $S_{b,i} = 2\sigma_{b,i}$ and $S_{r,i} = 2\sigma_{r,i}$. The j^{th} measurement of each of these variables is then given by

$$X_i^{(j)} = X_i^{(true)} + B_i^{(j)} + P_i^{(j)} \tag{4.5}$$

where $X_i^{(true)}$ would be the actual measured value is there were no error present. Approximating the function f about the true measured values using a Taylor series expansion gives

$$f^{(j)} = f^{(true)} + \frac{\partial f}{\partial X_1}\left(B_1^{(j)} + P_1^{(j)}\right) + \frac{\partial f}{\partial X_2}\left(B_2^{(j)} + P_2^{(j)}\right) + \mathcal{O}\left(\left(B_i^{(j)} + P_i^{(j)}\right)^2\right) \tag{4.6}$$

In most cases, the higher-order terms given by $\mathcal{O}((B_i^{(j)} + P_i^{(j)})^2)$ are assumed to be negligible, which is valid as long as the higher-order derivatives are of reasonable

magnitude and the total errors are small. This small error assumption is true of the measured loads and strain locations, whose associated uncertainties are all less than 3%. The small error assumption is also true of the measured strain as long as it is relatively large – several hundred or thousand $\mu\epsilon$; this is normally the case for the axial strain and the shear strain under a torsional load. However, the shear strain under a shear force is typically around 100 $\mu\epsilon$, due to limitations based on the resulting bending moments induced by the shear forces, and may lead to some errors in this approximation, which will be investigated in Sec. 4.4 by comparing results with the Monte Carlo method. Rearranging Eq. (4.6) and neglecting the higher order terms gives

$$\delta_f^{(j)} = (f^{(j)} - f^{(true)}) = \frac{\partial f}{\partial X_1}\left(B_1^{(j)} + P_1^{(j)}\right) + \frac{\partial f}{\partial X_2}\left(B_2^{(j)} + P_2^{(j)}\right) \tag{4.7}$$

where $\delta_f^{(j)}$ is the total error in the j^{th} calculation of $f^{(j)}$. Using the definition for the standard deviation given by Eq. (4.1), the variance of the calculated value f can be computed as

$$\begin{aligned}
\sigma_f^2 =& \frac{1}{N}\sum_{j=1}^{N}\left(\delta_f^{(j)}\right)^2 \\
=& \left(\frac{\partial f}{\partial X_1}\right)^2\left[\frac{1}{N}\sum_{j=1}^{N}\left(B_1^{(j)}\right)^2 + \frac{2}{N}\sum_{j=1}^{N}\left(B_1^{(j)}P_1^{(j)}\right) + \frac{1}{N}\sum_{j=1}^{N}\left(P_1^{(j)}\right)^2\right] + \\
&+ \left(\frac{\partial f}{\partial X_2}\right)^2\left[\frac{1}{N}\sum_{j=1}^{N}\left(B_2^{(j)}\right)^2 + \frac{2}{N}\sum_{j=1}^{N}\left(B_2^{(j)}P_2^{(j)}\right) + \frac{1}{N}\sum_{j=1}^{N}\left(P_2^{(j)}\right)^2\right] + \\
&+ \left(\frac{\partial f}{\partial X_1}\frac{\partial f}{\partial X_2}\right)\left[\frac{2}{N}\sum_{j=1}^{N}\left(B_1^{(j)}B_2^{(j)}\right) + \frac{2}{N}\sum_{j=1}^{N}\left(B_1^{(j)}P_2^{(j)}\right) + \right. \\
&\left. + \frac{2}{N}\sum_{j=1}^{N}\left(P_1^{(j)}B_2^{(j)}\right) + \frac{2}{N}\sum_{j=1}^{N}\left(P_1^{(j)}P_2^{(j)}\right)\right]
\end{aligned} \tag{4.8}$$

Now, assuming that there is no cross correlation between the systematic and random errors and that there is no covariance between the errors, such that the

terms containing products of $B_i^{(j)} P_k^{(j)}$ and the terms containing products $B_i^{(j)} B_k^{(j)}$ and $P_i^{(j)} P_k^{(j)}$ all evaluate to zero, respectively, Eq. (4.8) can be simplified to

$$\sigma_f^2 = \left(\frac{\partial f}{\partial X_1}\right)^2 \left(\sigma_{b,1}^2 + \sigma_{r,1}^2\right) + \left(\frac{\partial f}{\partial X_2}\right)^2 \left(\sigma_{b,2}^2 + \sigma_{r,2}^2\right) \tag{4.9}$$

These two assumptions, that there is no cross correlation and that the covariance is zero, are valid for most cases and should apply to the measurements for the stiffness/-compliance matrix data reduction equation. As an example of a situation where this is not true would be the case of using a thermometer to measure multiple different temperatures needed for a data reduction equation or using two thermometers that are calibrated to the same source.

It is common to represent the uncertainty in the final result f based on a 95% confidence interval. By multiplying Eq. (4.9) by a factor of 2^2 and taking the square root, the 95% confidence interval for the desired result f, denoted by u_f, can then be expressed as

$$u_f = \left[\left(\frac{\partial f}{\partial X_1}\right)^2 u_{X_1}^2 + \left(\frac{\partial f}{\partial X_2}\right)^2 u_{X_2}^2\right]^{1/2} \tag{4.10}$$

For the general case where f is a function of more than two variables, Eq. (4.10) can then be easily extended to give

$$u_f = \left[\left(\frac{\partial f}{\partial X_1}\right)^2 u_{X_1}^2 + \left(\frac{\partial f}{\partial X_2}\right)^2 u_{X_2}^2 + \cdots + \left(\frac{\partial f}{\partial X_n}\right)^2 u_{X_n}^2\right]^{1/2} \tag{4.11}$$

For the case of the sectional stiffness matrix, where the individual components can have various orders of magnitude, it can be desired to have the uncertainty in a non-dimensional form as a fraction of the total stiffness, which can be accomplished by dividing both sides of Eq. (4.11) by f and multiplying the individual variable

uncertainties by X_i/X_i to give

$$U_f = \left[\left(\frac{X_1}{f}\right)^2 \left(\frac{\partial f}{\partial X_1}\right)^2 U_{X_1}^2 + \left(\frac{X_2}{f}\right)^2 \left(\frac{\partial f}{\partial X_2}\right)^2 U_{X_2}^2 + \right. \\ \left. + \cdots + \left(\frac{X_n}{f}\right)^2 \left(\frac{\partial f}{\partial X_n}\right)^2 U_{X_n}^2 \right]^{1/2} \tag{4.12}$$

where $U_{X_i} = u_{X_i}/X_i$ is the 95% confidence interval for the measured variables as a fraction of the measured value and $U_f = u_f/f$ is the 95% confidence interval of the result as a fraction of the actual value.

To provide a simple example of an application of the Taylor Series uncertainty quantification, consider the calculation of the bending stiffness from the measurement of the tip displacement given by Eq. (1.7) ($EI = FL^3/(3w_{\text{tip}})$). In this calculation of the bending stiffness, there are three measured variables, the tip force F, the beam length L, and the tip displacement w_{tip}, each of which has an associated random and systematic error. Using Eq. (4.12) with $f = EI$, $X_1 = F$, $X_2 = L$ and $X_3 = w_{\text{tip}}$, the 95% uncertainty in the measurement of the bending stiffness can be calculated by

$$\begin{aligned} \left(\frac{u_{EI}}{EI}\right)^2 &= \left[\frac{F}{EI}\frac{L^3}{3w_{\text{tip}}}\right]^2 \left(\left(\frac{S_{b,F}}{F}\right)^2 + \frac{1}{M}\left(\frac{S_{r,F}}{F}\right)^2\right) + \\ &+ \left[\frac{L}{EI}\frac{3L^2F}{3w_{\text{tip}}}\right]^2 \left(\left(\frac{S_{b,L}}{L}\right)^2 + \frac{1}{M}\left(\frac{S_{r,L}}{L}\right)^2\right) + \\ &+ \left[\frac{w_{\text{tip}}}{EI}\frac{-FL^3}{3(w_{\text{tip}})^2}\right]^2 \left(\left(\frac{S_{b,w_{\text{tip}}}}{w_{\text{tip}}}\right)^2 + \frac{1}{M}\left(\frac{S_{r,w_{\text{tip}}}}{w_{\text{tip}}}\right)^2\right) \\ &= \left(\frac{u_F}{F}\right)^2 + 9\left(\frac{u_L}{L}\right)^2 + \left(\frac{u_{w_{\text{tip}}}}{w_{\text{tip}}}\right)^2 \end{aligned} \tag{4.13}$$

In this simple example, because the bending stiffness has a cubic dependency on the beam length, any uncertainties in the measurement of the length have an impact nearly an order of magnitude greater then similar uncertainties in the force or the tip on the final results.

Now applying this to the compliance and stiffness matrix calculation discussed in Chap. 2, the calculation requires measurements of the force, strain, and cross-sectional location. In addition, the material properties, although not explicitly used for the calculation of the sectional stiffness properties, are required for the calculation of the numerical warping field that are ultimately used to calculate these properties. The uncertainties in the stiffness properties can then be determined with these inputs using Eq. (4.12), which evaluates to

$$
\begin{aligned}
U_{K_{ij}} = \frac{1}{K_{ij}} \Bigg[& \sum_{k=1}^{6} \left(\mathcal{F}_{c,k} \frac{\partial K_{ij}}{\partial \mathcal{F}_{c,k}} \right)^2 \left(\left(\frac{S_{b,\mathcal{F}_{c,k}}}{\mathcal{F}_{c,k}} \right)^2 + \frac{1}{n} \left(\frac{S_{r,\mathcal{F}_{c,k}}}{\mathcal{F}_{c,k}} \right)^2 \right) + \\
& + \sum_{k=1}^{2} \sum_{l=1}^{6} \left(\frac{\partial K_{ij}}{\partial \gamma^{+}_{1k,\mathcal{F}_{c,l}}} \right)^2 S^2_{b,\gamma^{+}_{\text{mean}}} + \\
& + \sum_{k=1}^{2} \sum_{l=1}^{6} \left(\frac{\partial K_{ij}}{\partial \left| \gamma^{+}_{1k,\mathcal{F}_{c,l}} \right|} \right)^2 \left(\frac{1}{n} S^2_{r,\gamma^{+}_{\text{mean}}} + \frac{1}{nN} S^2_{r,\gamma^{+}_{\text{std}}} \right) + \\
& + \sum_{k=1}^{2} \left(\frac{\partial K_{ij}}{\partial d_k} \right)^2 \left(S^2_{b,d_{\text{ext}},k} + \frac{1}{n} \left(S_{r,d_{\text{ext}},k} \right)^2 \left(d_{\text{ext},k} \right)^2 + S^2_{b,d_k} + \frac{1}{nN} S^2_{r,d_k} \right) \\
& + \sum_{k=1}^{n_E} \left(\frac{\partial K_{ij}}{\partial E_k} \right)^2 S^2_{b,E_k} + \sum_{k=1}^{n_G} \left(\frac{\partial K_{ij}}{\partial G_k} \right)^2 S^2_{b,G_k} + \sum_{k=1}^{n_\nu} \left(\frac{\partial K_{ij}}{\partial \nu_k} \right)^2 S^2_{b,\nu_k} \\
& + \sum_{k=1}^{n_{\text{ply}}} \left(\frac{\partial K_{ij}}{\partial \gamma^{+}_{\text{ply},k}} \right)^2 S^2_{b,\gamma^{+}_{\text{ply},k}} \Bigg]^{1/2}
\end{aligned}
\tag{4.14}
$$

where $U_{K_{ij}}$ is the non-dimensional 95% confidence interval for the stiffness matrix value in the i^{th} row and j^{th} column. Because the data reduction is solved for the compliance matrix entries using a singular value decomposition and the stiffness matrix is then calculated as the inverse of the compliance matrix, the partial derivatives ($\partial K_{ij}/\partial X_k$) can not generally be evaluated analytically and instead must be approximated numerically. Although a finite difference approximation could be

used to estimate these derivatives, a complex step differentiation is used as given by

$$\frac{\partial K_{ij}}{\partial X_k} = \frac{1}{\epsilon_k} \operatorname{Im}\left[K_{ij}\left(X_1, X_2, \ldots, X_k + i\epsilon_k, \ldots, X_n\right)\right] \tag{4.15}$$

where $i\epsilon$ is a small imaginary perturbation to the measured variable. The complex step derivative will typically provide better accuracy in numerical differentiation, as it does not require a difference of function evaluations, with the derivation for the complex step derivative discussed in Appendix B.

Considering Eq. (4.14) in detail, the first line describes the contribution to the total uncertainty from the uncertainty in the loads. From Sec. 2.2.4, it was found that all six components in the j^{th} column of the compliance matrix were calculated from the k^{th} component of the sectional loads $\mathcal{F}_{c,k}$. However, bringing the compliance matrix into symmetric form by $\underline{\underline{S}} = (\underline{\underline{S}}_u + \underline{\underline{S}}_u^T)/2$ and then inverting to calculate the sectional stiffness matrix leads to the possibility that the uncertainty in all the sectional loads can impact the uncertainty in the K_{ij} term, requiring the summation from $k = 1$ to 6 of the partial derivatives with respect to the k^{th} load component $\mathcal{F}_{c,k}$. In fact, this summation can only be simplified for the case when the only non-zero components are the six diagonal stiffness values, in which case the derivative is only non-zero for $i = j = k$. Since the force uncertainties are normally represented as a percent of the applied load, it is generally easier to calculate the complex step derivative by perturbing the measurement by $i\epsilon\mathcal{F}_{c,k}$. In this way, the complex step differentiation gives

$$\mathcal{F}_{c,k}\frac{\partial K_{ij}}{\partial F_{c,k}} = \frac{1}{\epsilon} \operatorname{Im}\left[K_{ij}\left(\mathcal{F}_{c,k} + i\epsilon\mathcal{F}_{c,k}, \ldots\right)\right] \tag{4.16}$$

and the entire quantity $\mathcal{F}_{c,k}\partial K_{ij}/\partial F_{c,k}$ can be easily calculated, allowing the uncertainty quantities $S_{b,\mathcal{F}_{c,k}}/\mathcal{F}_{c,k}$ and $S_{r,\mathcal{F}_{c,k}}/\mathcal{F}_{c,k}$ to be input as their percentage (or fractional) values listed in Table 4.1. This is particularly important because during

the actual experiments, multiple load cases with different magnitudes are often applied to calculate the stiffness matrix, and defining an appropriate value of $\mathcal{F}_{c,k}$ to use in the calculation would otherwise be difficult.

In addition, the data reduction equation requires the forces and moments within the current cross-sectional location and not the directly measured loads from the load cell. Because the measured loads are located at a distance x from the current cross-sectional location, the cross-sectional bending moments will depend on both the measured bending moments and measured shear forces according to

$$\begin{aligned} M_2 &= M_{2,m} + xF_{3,m} \\ M_3 &= M_{3,m} - xF_{2,m} \end{aligned} \tag{4.17}$$

where $F_{2,m}$ and $F_{3,m}$ are the measured forces and $M_{2,m}$ and $M_{3,m}$ are the measured moments in the load cell, while M_2 and M_3 are the cross-sectional bending moments. In this relationship, the additional moments due to the displacement and rotation of the cross-section (see Sec. 5.3.3) are ignored, as these contributions are generally small compared to the bending moment generated directly by the shear force ($xF_{3,m}$ or $xF_{2,m}$). The moment uncertainties from Table 4.1 then need to be updated to account for the load cases where a bending moment and shear force are both present, which can be done by applying a Taylor Series method to Eq. (4.17) to give

$$\begin{aligned} S_{b,M_2} &= \sqrt{S_{b,M_2,o}^2 + \left(S_{b,F_3}^2 + \left(\frac{S_{b,x}}{x}\right)^2\right)\left(\frac{F_3 x}{M_{2,m}}\right)^2} \\ S_{b,M_3} &= \sqrt{S_{b,M_3,o}^2 + \left(S_{b,F_2}^2 + \left(\frac{S_{b,x}}{x}\right)^2\right)\left(\frac{F_2 x}{M_{3,m}}\right)^2} \end{aligned} \tag{4.18}$$

where S_{b,M_2} and S_{b,M_3} are the updated moment systematic uncertainties, $S_{b,M_2,o}$ and $S_{b,M_3,o}$ are the original moment systematic uncertainties from Table 4.1, S_{b,F_3} and S_{b,F_2} are the shear force systematic uncertainties, and $S_{b,x}/x$ is the systematic

uncertainty in the cross-sectional location. The same procedure can then be followed to update the random uncertainties by replacing all the $S_{b,(\cdot)}$ expressions with $S_{r,(\cdot)}$.

The second and third lines of Eq. (4.14) represent the contribution of the strain measurement to the overall uncertainty. Since the axial strain measurements are used to calculate first, fifth, and sixth rows of the compliance matrix and the shear strain to calculate the second, third, and fourth rows, it is necessary to consider their contributions separately as represented by the summation from $k = 1$ to 2. In addition, the derivatives must be calculated separately for each of the six sectional loads, as indicated by the second summation from $l = 1$ to 6. For the mean systematic strain uncertainty, each partial derivative can be calculated by perturbing the measurements of the strain component γ_{1k}^{+} by $i\epsilon$ for each load case separately. However, for the random uncertainty in the strain measurement, as calculated in the third line, it is necessary to account for the sign of the strain component in the perturbation (*i.e.* by taking $\gamma_{1k}^{+} + \text{sgn}\left(\gamma_{1k}^{+}\right) i\epsilon$) when calculating the partial derivative. This is due to the fact that the random uncertainty in the strain will change each time it is measured, as opposed to the systematic uncertainty which only changes if the DIC system gets recalibrated. Since the strain uncertainty levels are represented in dimensional terms ($\mu\epsilon$) and not as a percentage of the measured strain, the imaginary perturbations used to calculate the partial derivatives should be of a constant magnitude and therefore not be multiplied by the value of the strain itself as was done for the case of the load uncertainties.

The fourth line of Eq. (4.14) represents the contribution of the measurement locations to the overall uncertainty. The derivatives must be calculated separately for both of the cross-sectional dimensions, as indicated by the summation from $k = 1$ to 2. The first two uncertainties, $S_{b,d_{\text{ext}},k}$ and $S_{r,d_{\text{ext}},k}$, are the systematic and random uncertainties for the measurements of the external dimensions of the cross-section – for a rectangular shaped cross-section this would be the width and

height and for an airfoil shaped cross-section the chord and thickness. Since the random uncertainty was estimated as a percentage based on manufacturing and machining tolerances, $S_{r,d_{\text{ext}},k}$ is multiplied by its measured dimension $d_{\text{ext},k}$ at the current spanwise location to bring it into a dimensional form. The remaining two uncertainties, S_{b,d_k} and S_{r,d_k}, are the systematic and random uncertainties of the location of the strain measurement on the external surface. In order to approximate the partial derivatives for the measurement locations, the y-coordinates used in defining $\underline{\underline{H}}_i$ (Eq. (2.36)) are perturbed by $i\epsilon$ when $k = 1$ and the z-coordinates are similarly perturbed by $i\epsilon$ when $k = 2$.

Finally, the last two lines of Eq. (4.14) represent the uncertainty with respect to the material parameters. Since the material parameters are only needed for the calculation of the numerical warping field, they only apply to the strain correction term $\underline{\underline{V}}_i \underline{\mathcal{F}}_c^{(k)}$ in the data reduction equation (Eq. (2.39)). For the case of an isotropic material, the material is fully defined by its Young's modulus and poisson's ratio so the uncertainties with respect to the shear modulus and ply orientations disappear. For the case of a composite cross-section, which may consist of layers of isotropic or transversely isotropic materials, it is necessary to consider the uncertainties for each material by applying the imaginary perturbation to each layer separately. For the transversely isotropic materials, the 95% confidence intervals were estimated as a percentage for the Young's and shear moduli; therefore, in order to apply these uncertainties correctly in Eq. (4.14), these percentages must be converted to a dimensional form by multiplying the terms S_{b,E_k} and S_{b,G_k} by their corresponding moduli.

4.3.2 Monte Carlo Method

Alternatively, a Monte Carlo simulation can be used to perform the uncertainty analysis on the measured stiffness properties, without requiring the inherent

approximations used when propagating the uncertainties through the Taylor Series method [128]. In the Monte Carlo method, the data reduction procedure is simulated N times to determine the standard deviations and therefore expected uncertainties in the measured stiffness values. In performing a Monte Carlo simulation for the uncertainty analysis, the first step requires defining the systematic and random error distributions for all the measured variables, which in this dissertation are assumed to follow a Gaussian distribution. In the j^{th} simulation, a random value for the uncertainties of all the measured variables is then determined using a Gaussian random number generator. For each variable, the randomly generated systematic and random uncertainties are summed together with the initially measured value to give an updated "measured" value of the i^{th} variable in the j^{th} simulation as

$$X_i^{(j)} = X_i + B_i^{(j)} + P_i^{(j)} \tag{4.19}$$

where $X_i^{(j)}$ is the current "measured" value, X_i is the initially measured value, and $B_i^{(j)}$ and $P_i^{(j)}$ are the systematic and random uncertainties, respectively, generated randomly from their respective parent distributions defined by $S_{b,i}$ and $S_{r,i}$ for the i^{th} measured variable in the j^{th} simulation. The data reduction procedure is then used

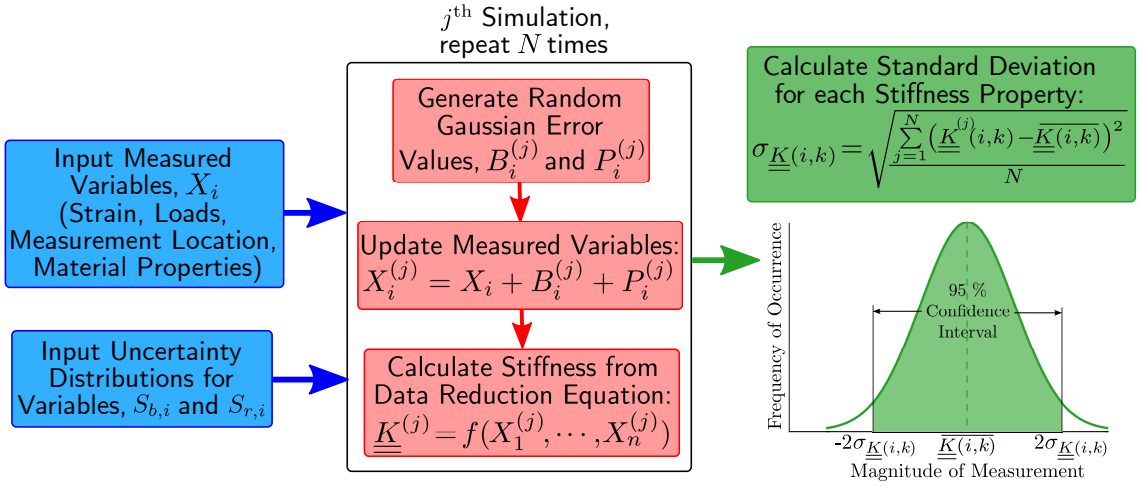

Figure 4.2: Flowchart for uncertainty quantification using Monte Carlo method.

to calculate the stiffness matrix for the current simulation, $\underline{\underline{K}}^{(j)}$, based on the current values of each $X_i^{(j)}$. After completing the N simulations, the standard deviations of each component of the stiffness matrix are calculated and multiplied by a factor of two to provide the 95% confidence intervals based on the measured variables. The number of required simulations can be determined by considering the convergence of standard deviations of each stiffness parameter; typically between 1,000 and 7,000 iterations were required for convergence, thus 10,000 simulations were used in the analysis in this work to ensure sufficient convergence. A summary of this work flow for calculating the uncertainty using the Monte Carlo method is shown in Fig. 4.2.

4.4 Method Comparison

The previous section described two methods for the uncertainty propagation from the experimental measurements into the calculated sectional stiffness components. With the Taylor series method, the total uncertainty in the stiffness properties is estimated based on first order partial derivatives of the data reduction equation with respect to the measured variables – neglecting higher order derivatives. In the Monte Carlo method, the total uncertainty is estimated by performing a large number of simulations with random perturbations of the measured variables, generated from their respective uncertainty distributions. While the accuracy of the Taylor series method depends on the reliability of the assumption that the higher-order derivative terms are negligible, the accuracy of the Monte Carlo method only requires performing a large enough number of simulations such that the standard deviations of the uncertainties in the stiffness properties have converged. However, because the number of simulations for convergence is typically much higher than the number of measurement variables, and therefore numerical derivatives to calculate in the Taylor series method, the Monte Carlo method is expected to be more expensive computationally. To compare the two methods in terms of their accuracy and effi-

ciency, measured in terms of computational time, both methods were applied to the calculation of the stiffness properties for two of the cross-sections from the numerical models considered in Chap. 3. The first comparison was done for the prismatic aluminum beam, to assess the methods in the simplest case of a cross-section made of an isotropic material with the six diagonal entries being the only non-zero stiffness components. A second comparison was then done for the composite box beam, specifically the cross-section with the symmetric layup, to assess the two methods when applied to a cross-section with anisotropic materials and non-zero off-diagonal stiffness components.

4.4.1 Prismatic Aluminum Rectangular Beam

As presented in Sec. 3.1, the stiffness properties were calculated at every cm along the span for the prismatic aluminum beam. To compare the two methods for their accuracy and efficiency, the uncertainty analysis was first applied at a single spanwise location, which was arbitrarily selected to be at 20 cm from the clamped boundary, such that it was sufficiently far away from any effect of the boundary conditions in the 3-D FEM. While the uncertainties are applied based on simulated data from 3-D FEA, experimental measurements will be done using DIC and it is important to try and mimic how its use will impact the uncertainties. Since it is common to only have two cameras for DIC, measuring the strain field on the entire external surface requires taking four separate sets of images – one for each face. Since the calibration doesn't change between sets of images, the bias uncertainty for each measurement type should only be generated once per simulation; however, the random uncertainty would vary for each of the sets of images and therefore needs to be generated four times during each simulation. In addition, since the applied loads from the 3-D FEM are mostly outside the bounds listed in Table 4.1, the uncertainty levels for the high loading condition are used for all the results.

For the Monte Carlo method, 10,000 simulations were run with the 3-D FEA results, applied forces, and material properties perturbed by a randomly generated value from the normal distributions described by the 2σ values from Sec. 4.2. Figure 4.3 shows the variations of the 95% confidence intervals for each of the six non-zero diagonal stiffness matrix components with the number of simulations, from which it can be seen that any significant variations disappeared after about 2,000 simulations. To determine the actual number of iterations required for convergence, the value after 10,000 simulation runs was taken as the reference value and the number of required simulations to converge to within 2% and 1% of this value was calculated as summarized in Table 4.2. With an average run time of about 50 s per 100 simulations, it would take about 870 s (14.5 min.) to converge all the uncertainty bounds to within 2% of their reference value or 3,785 s (63.1 min.) to converge to within 1%.

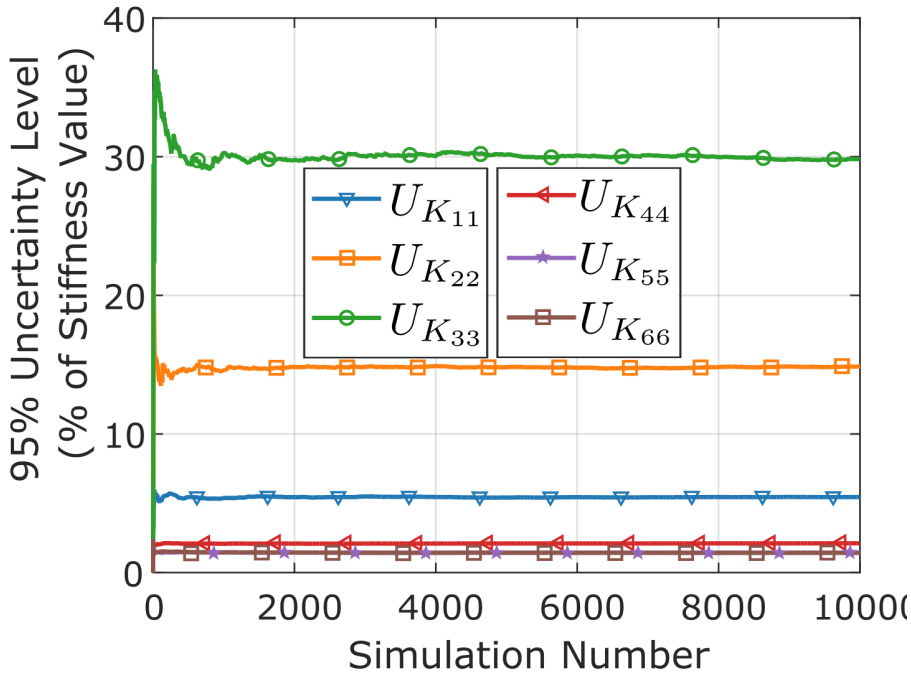

Figure 4.3: Convergence of the Monte Carlo method for the uncertainty levels of the stiffness properties of the prismatic aluminum beam.

The uncertainty levels were then calculated at the same spanwise location using the Taylor series method, with a comparison of the two methods shown in Table

Table 4.2: Number of Monte Carlo iterations required to converge the uncertainty bounds for the prismatic aluminum beam.

Uncertainty Term	Converged Value (%)	Iterations for Convergence	
		within 2%	within 1%
$U_{K_{11}}$	5.46	977	1278
$U_{K_{22}}$	14.9	1008	6464
$U_{K_{33}}$	29.8	810	7567
$U_{K_{44}}$	2.11	120	2993
$U_{K_{55}}$	1.44	644	1221
$U_{K_{66}}$	1.42	1741	4758

4.3. In addition to the total uncertainty level, the contributions from the bias and random uncertainties for each of the input variables were also compared. For the Taylor series method, this is easily evaluated since each of the partial derivative terms is calculated separately; however, to generate these results using the Monte Carlo method, it was necessary to rerun the simulations by perturbing each variable one at a time, increasing the computational expense by about an order of magnitude. From Table 4.3, it can be seen that the uncertainties levels predicted by both methods showed great agreement in terms of the overall uncertainty as well as most of the individual measurement uncertainties, with the Taylor series method typically being slightly more conservative. For the prismatic aluminum beam, the uncertainties in the strain have the biggest impact on the overall uncertainty for the axial and shear stiffness terms, due to the relatively low strain levels that can be achieved under their respective loading; while the uncertainties in the loads and the dimensions have the biggest impact on the total uncertainties for the torsional and bending stiffnesses.

By considering the uncertainty levels from each of the individual variables, some special properties of the data reduction equations and solution process can also be observed. For the case of the systematic strain uncertainty in the DIC system, as shown in the third row of Table 4.3, the only terms that are significantly impacted are the axial and torsional stiffness measurements. The shear and bending loads

Table 4.3: Comparison of 95% uncertainty levels (in %) for the 6 non-zero stiffness properties of the prismatic aluminum beam from the Monte Carlo method (MCM) and Taylor series method (TSM).

Uncertainty Term	Method	K_{11}	K_{22}	K_{33}	K_{44}	K_{55}	K_{66}
Force bias	MCM	0.749	0.952	0.671	1.30	1.01	1.10
U_{K_{ii},B_F} (%)	TSM	0.750	0.950	0.670	1.29	1.03	1.14
Force random	MCM	0.465	0.370	0.324	0.669	0.063	0.062
U_{K_{ii},P_F} (%)	TSM	0.435	0.290	0.301	0.656	0.101	0.097
Strain bias	MCM	4.69	0.005	0.000	0.569	0.000	0.000
$U_{K_{ii},B_{\gamma^+_{\text{mean}}}}$ (%)	TSM	4.70	0.001	0.030	0.621	0.000	0.000
Strain random, mean	MCM	2.65	14.81	29.77	0.304	0.632	0.427
$U_{K_{ii},P_{\gamma^+_{\text{mean}}}}$ (%)	TSM	2.48	14.05	32.43	0.478	0.532	0.608
Strain random, std	MCM	0.116	0.631	1.22	0.018	0.026	0.032
$U_{K_{ii},P_{\gamma^+_{\text{std}}}}$ (%)	TSM	0.164	0.927	2.14	0.032	0.035	0.040
Young's modulus	MCM	0.000	0.503	0.693	0.514	0.000	0.000
U_{K_{ii},B_E} (%)	TSM	0.000	0.507	0.698	0.518	0.000	0.000
Poisson's ratio	MCM	0.000	0.200	0.375	0.264	0.000	0.000
U_{K_{ii},B_ν} (%)	TSM	0.000	0.203	0.381	0.262	0.000	0.000
Dimension bias	MCM	0.000	0.086	0.108	0.294	0.200	0.101
$U_{K_{ii},B_{d_{\text{ext}}}}$ (%)	TSM	0.000	0.082	0.063	0.272	0.215	0.123
Dimension random	MCM	0.000	0.397	0.538	1.25	0.798	0.790
$U_{K_{ii},P_{d_{\text{ext}}}}$ (%)	TSM	0.000	0.329	0.433	1.15	0.860	0.980
Location bias	MCM	0.000	0.001	0.019	0.018	0.010	0.007
U_{K_{ii},B_d} (%)	TSM	0.000	0.014	0.015	0.056	0.037	0.021
Location random	MCM	0.000	0.001	0.016	0.012	0.006	0.003
U_{K_{ii},P_d} (%)	TSM	0.000	0.002	0.002	0.009	0.006	0.003
Total	MCM	**5.45**	**14.87**	**29.82**	**2.11**	**1.44**	**1.43**
$\mathbf{U_{K_{ii},\text{total}}}$(%)	TSM	**5.39**	**14.13**	**32.52**	**2.13**	**1.47**	**1.63**

introduce an antisymmetric strain distribution on the surface of the beam and, when adding a constant offset to the entire strain field, as is the case for the bias uncertainty when using DIC, the SVD filters out this offset resulting in a nearly zero uncertainty level for these stiffnesses. However, since the strain under an axial load and a

torsional load are nearly constant around the cross-section, the bias uncertainty is not filtered out by the SVD for these load cases, resulting in a noticeable uncertainty. For the strain distribution with a random mean strain uncertainty, each measured face would have its own associated uncertainty and the SVD no longer filters out this uncertainty for any of the calculated stiffness components, as can be seen by significant uncertainty levels for all the stiffness components due to a random strain perturbation. For the material uncertainties, in both the Young's modulus and the poisson's ratio, it can be seen that they only impact the shear and torsional stiffnesses, which is a result of the fact that the numerical warping correction is only non-zero for the shear strain under shear and torsional loads. In addition, because the numerical warping correction accounts for only a portion of the overall strain level, the associated uncertainties in the shear and torsional stiffness of about 0.5% for the Young's modulus and 0.3% for the poisson's ratio are significantly less then the overall estimated uncertainties in the material properties of about 1.5% for the Young's modulus and 3% for the poisson's ratio.

The comparison of the two methods was done in Table 4.3 for a single spanwise location; however, it is also important to consider any expected variations that may arise along the span. For the prismatic beam, the bending moments vary linearly along the span when subjected to the tip shear forces. This spanwise variation in bending moment also introduces a change in the axial strain field along the span, with the largest strains near the clamped root of the beam. While the axial strain under the axial force and the shear strains under the shear forces and torsional moment are mostly constant along the span, the boundary conditions introduced strain concentrations at the beam's edges, which can also impact the expected uncertainty levels. The spanwise distributions of the uncertainty levels were calculated using only the Taylor series method, requiring a total of about 16 s to calculate the uncertainty distributions at all 61 spanwise locations, which is roughly two orders of magnitude

faster than the time required to calculate the uncertainty distribution with the Monte Carlo method at only a single cross-section.

The spanwise variations in the uncertainty levels are shown in Fig. 4.4 for the axial and shear stiffnesses and in Fig. 4.5 for the torsional and bending stiffnesses, with all the values normalized by the analytic solutions so that the uncertainty levels could be plotted as a percentage of the expected stiffness. From Fig. 4.4, it can be seen that the uncertainty in the axial stiffness is nearly constant along the span. However, the uncertainty levels for both the lag and flap shear stiffnesses have larger variations along the span due to the strain concentrations arising from the boundary conditions. From Fig. 4.5, it can be seen that the uncertainty levels for the torsional and bending stiffnesses remain nearly constant along the span. Although the uncertainty in the shear forces provided an additional contribution to the uncertainty in the local bending moment, as seen in Eq. (4.18), this had a relatively small impact on the total uncertainty for the bending stiffness, with the contribution from the bending moment varying between 1.0% and 1.1% at the root and tip to 1.04% and 1.15% at the mid-span for the flap and lag stiffnesses, respectively. This small variation across the span is a result of the fact that when the bending moment due to the shear force is largest near the root, the additional uncertainty from the shear force is relatively small since the distance x is small, and, when the additional uncertainty from the shear force is larger due to a large distance x, its magnitude is smaller and the relative weight when using the SVD is roughly proportional to the inverse of the magnitude of the bending moment squared.

4.4.2 Symmetric Composite Box Beam

From Sec. 3.3, the sectional stiffness properties of the composite box beam with a symmetric layup were evaluated and showed a bending/torsion coupling and extension/shear coupling. Therefore, this composite box beam layup was also

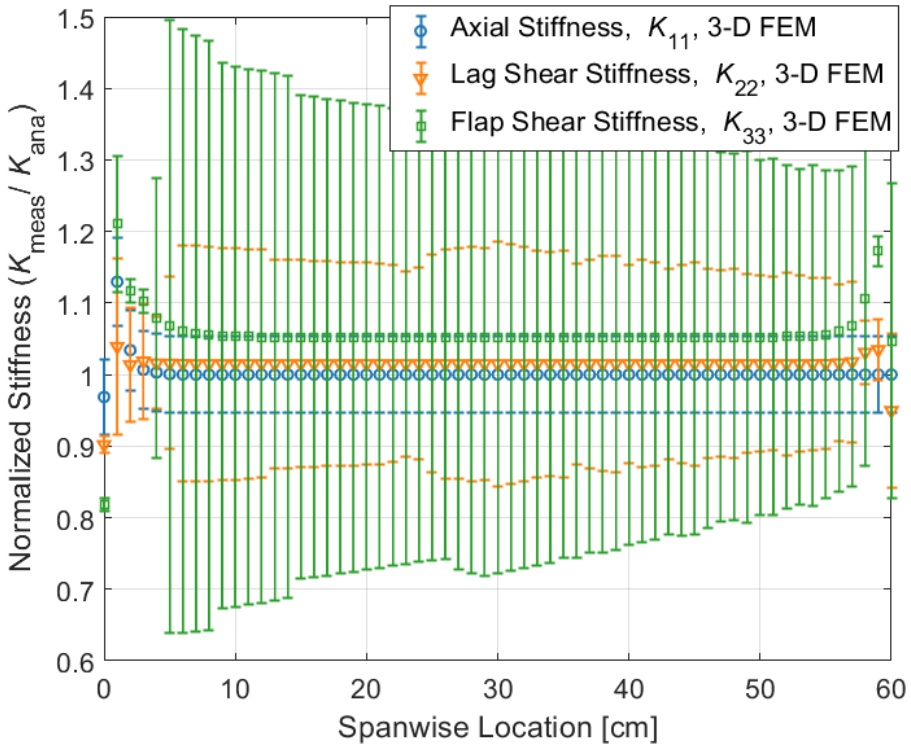

Figure 4.4: Spanwise variation of 95% uncertainty levels for the axial and shear stiffnesses of the prismatic aluminum beam.

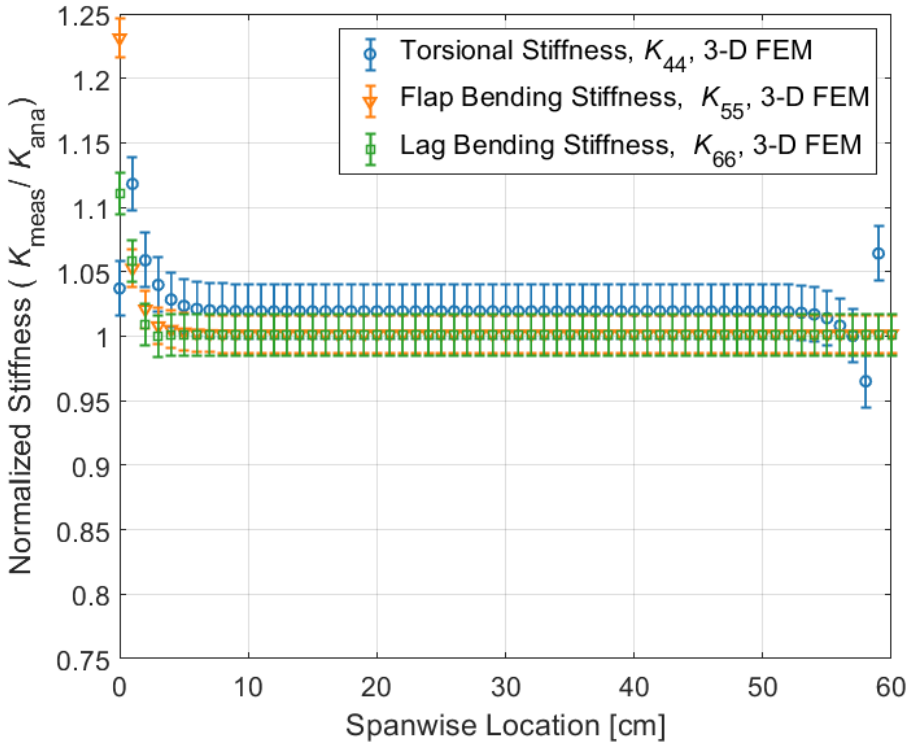

Figure 4.5: Spanwise variation of 95% uncertainty levels for the torsional and bending stiffnesses of the prismatic aluminum beam.

considered to compare the two methods on their accuracy and efficiency when off-diagonal stiffness components are present. The two methods were applied to the data reduction calculation at the mid-span of the beam ($x = 30$ cm), such that they were compared at a location sufficiently far away from any effect of the boundary conditions in the 3-D FEM.

For the Monte Carlo method, 10,000 simulations were again performed with the 3-D FEA results perturbed by a randomly generated value from the normal distributions described by the 2σ values from Sec. 4.2. Figure 4.6 shows the variations of the 95% confidence intervals with the number of simulations for all eight non-zero stiffness components for the composite box beam, with any significant variations again dissipating after about 2,000 simulations. As with the prismatic aluminum beam, the number of required simulations to converge to within 2% and 1% of the reference uncertainty level were calculated and are summarized in Table 4.4. With an average run time of about 51 s per 100 simulations, it would take about 1,425 s (23.7 min.) to converge all the uncertainty bounds to within 2% of their reference value or 3,500 s (58.3 min.) to converge to within 1%. Note that the inclusion of the off-diagonal coupling stiffness values had only a minor impact on the convergence times and number of iterations required for convergence compared to the prismatic aluminum beam.

The uncertainty levels were then computed at this same spanwise location using the Taylor series method, with a comparison of the total and individual uncertainty results shown in Table 4.5. Overall, the two methods still showed good agreement with one another in terms of the total uncertainty and the contribution of individual measured variables; however, the Taylor series method was fairly conservative in its estimation of the uncertainty for the lag shear stiffness K_{22} and the extension/shear coupled stiffness K_{12} due to about a 20% difference in the estimated uncertainty resulting from the systematic strain error. Although the largest relative differences

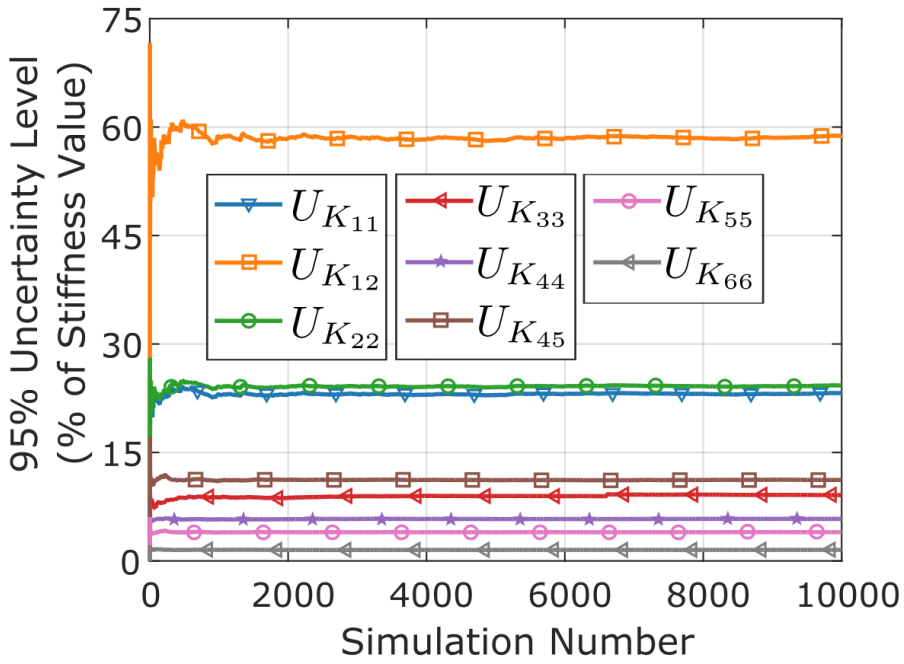

Figure 4.6: Convergence of the Monte Carlo method for the uncertainty levels of the stiffness properties of the composite box beam.

Table 4.4: Number of Monte Carlo iterations required to converge the uncertainty bounds for the composite box beam.

Uncertainty Term	Converged Value (%)	Iterations for Convergence	
		within 2%	within 1%
$U_{K_{11}}$	23.21	961	5160
$U_{K_{12}}$	58.79	913	5160
$U_{K_{22}}$	24.27	913	5160
$U_{K_{33}}$	9.10	2790	6861
$U_{K_{44}}$	5.81	229	1737
$U_{K_{45}}$	11.20	278	1001
$U_{K_{55}}$	3.97	271	1001
$U_{K_{66}}$	1.53	206	2543

between the two methods occurred for the uncertainty in the random location, these uncertainties were several orders of magnitude smaller than the total uncertainty bounds and therefore had almost no impact on the overall results.

For the axial stiffness, lag shear stiffness, and extension/shear coupling stiffness, K_{11}, K_{12}, and K_{22}, respectively, the total uncertainty was almost entirely due

Table 4.5: Comparison of 95% uncertainty levels (in %) from the Monte Carlo method (MCM) and Taylor series method (TSM) for the stiffness properties of the composite box beam with symmetric layup.

Uncertainty Term	Method	K_{11}	K_{12}	K_{22}	K_{33}	K_{44}	K_{45}	K_{55}	K_{66}
Force bias	MCM	0.846	0.602	0.519	0.474	1.37	0.936	1.13	1.10
U_{K_{ii},B_F} (%)	TSM	0.854	0.608	0.517	0.469	1.38	0.969	1.18	1.15
Force random	MCM	0.564	0.811	0.420	0.229	0.720	0.586	0.215	0.062
U_{K_{ii},P_F} (%)	TSM	0.487	0.347	0.163	0.211	0.695	0.200	0.133	0.097
Strain bias	MCM	20.20	50.17	19.91	0.004	3.09	3.10	0.647	0.000
$U_{K_{ii},B_{\gamma^+_{\text{mean}}}}$ (%)	TSM	21.17	60.52	23.76	0.000	3.38	3.61	0.792	0.000
Strain random	MCM	10.66	27.23	11.75	1.76	3.84	10.28	3.54	0.680
$U_{K_{ii},P_{\gamma^+_{\text{mean}}}}$ (%)	TSM	12.35	31.85	12.24	1.43	3.55	9.25	3.17	0.87
Strain random	MCM	0.458	1.16	0.508	0.075	0.174	0.442	0.152	0.045
$U_{K_{ii},P_{\gamma^+_{\text{std}}}}$ (%)	TSM	0.455	1.17	0.450	0.053	0.131	0.341	0.117	0.032
Young's moduli	MCM	0.183	1.17	2.17	0.821	1.38	0.565	0.062	0.000
U_{K_{ii},B_E} (%)	TSM	0.184	1.15	2.16	0.807	1.37	0.545	0.059	0.000
Shear modulus	MCM	0.213	3.03	5.17	8.61	0.982	1.46	0.808	0.000
U_{K_{ii},B_G} (%)	TSM	0.194	2.92	5.03	8.40	0.956	1.42	0.784	0.000
Poisson's ratio	MCM	0.042	0.148	0.119	0.024	0.082	0.115	0.031	0.000
U_{K_{ii},B_ν} (%)	TSM	0.043	0.150	0.121	0.025	0.081	0.115	0.031	0.000
Ply orientation	MCM	0.708	2.733	2.55	0.904	1.88	2.39	0.605	0.004
$U_{K_{ii},B_{\gamma^+_{\text{ply}}}}$ (%)	TSM	0.603	2.50	2.47	0.807	1.88	2.34	0.579	0.000
Dimension bias	MCM	0.027	0.103	0.098	0.180	0.140	0.082	0142	0.102
$U_{K_{ii},B_{d_{\text{ext}}}}$ (%)	TSM	0.053	0.239	0.254	0.070	0.045	0.195	0.137	0.113
Dimension random	MCM	0.150	0.685	0.810	0.37	0.804	0.532	0.631	0.796
$U_{K_{ii},P_{d_{\text{ext}}}}$ (%)	TSM	0.119	0.609	0.815	0.986	1.13	0.693	0.927	1.00
Location bias	MCM	0.018	0.071	0.071	0.032	0.063	0.065	0.011	0.007
U_{K_{ii},B_d} (%)	TSM	0.019	0.083	0.088	0.024	0.016	0.068	0.048	0.039
Location random	MCM	0.192	0.504	0.206	0.029	0.019	0.020	0.004	0.002
U_{K_{ii},P_d} (%)	TSM	0.010	0.043	0.046	0.013	0.008	0.035	0.025	0.020
Total	MCM	**23.21**	**58.79**	**24.27**	**9.10**	**5.81**	**11.20**	**3.97**	**1.53**
$\mathbf{U_{K_{ii},\text{total}}}$(%)	TSM	**24.54**	**68.52**	**27.42**	**8.67**	**5.83**	**10.39**	**3.74**	**1.76**

to the systematic and random uncertainties in the mean strain values. For the systematic uncertainty levels in the mean strain, the corresponding uncertainties in the compliance matrix entries were $U_{S_{11},B_{\gamma^+_{\text{mean}}}} = 2.58\%$, $U_{S_{12},B_{\gamma^+_{\text{mean}}}} = 39.34\%$, and $U_{S_{11},B_{\gamma^+_{\text{mean}}}} = 0.001\%$; this shows the significant impact that the inversion of the compliance matrix can have on the expected stiffness uncertainties when off-diagonal stiffness components are present. Some additional impacts of the off-diagonal stiffness components can also be observed from the systematic uncertainties in both the mean strain and the material property uncertainties. For the uncoupled aluminum beam, the SVD filtered out the contribution of the systematic uncertainty in the mean strain for the lag shear, flap shear, flap bending, and lag bending stiffnesses; however, due to the presence of the extension/shear coupling and the flap bending/torsion coupling terms in the composite box beam, the systematic uncertainty in the mean strain now had a noticeable contribution to both the lag shear stiffness K_{22} and flap bending stiffness K_{55}. In addition, the warping correction factor was shown in Sec. 2.2.4 to only impact the shear and torsional compliance terms and it was found that any uncertainties in the material properties had no impact on the estimated uncertainties for the axial or bending compliances. However, because of the presence of the off-diagonal stiffness components and the requirement to invert the compliance matrix to calculate the stiffness matrix, the material uncertainties ended up propagating into the uncertainties for both the axial and flap bending stiffnesses.

As with the prismatic aluminum beam, the variations in the uncertainty levels along the span were also investigated using the Taylor series method, which required a total of about 28 s for estimating the uncertainty levels at all 61 spanwise locations shown in Figs. 4.7 and 4.8. This again showed the substantial increase in efficiency that the Taylor series method provided compared to the Monte Carlo method, which required nearly two orders of magnitude more time to compute the uncertainty levels at a single cross-sectional location. From Fig. 4.7, which shows the normalized

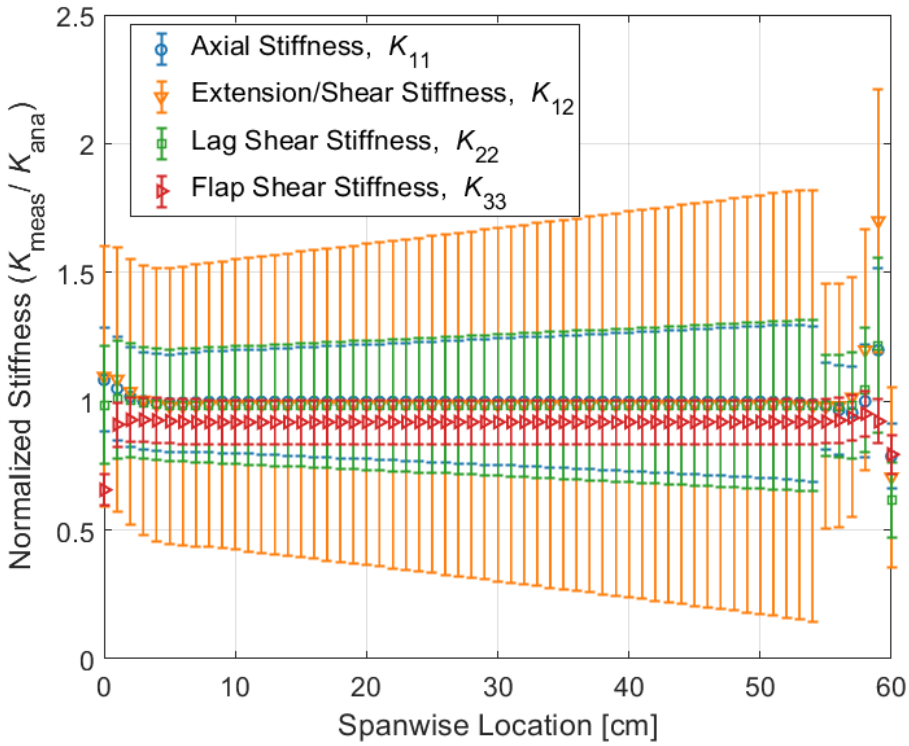

Figure 4.7: Spanwise variation of 95% uncertainty levels for the axial and shear stiffnesses of the composite box beam.

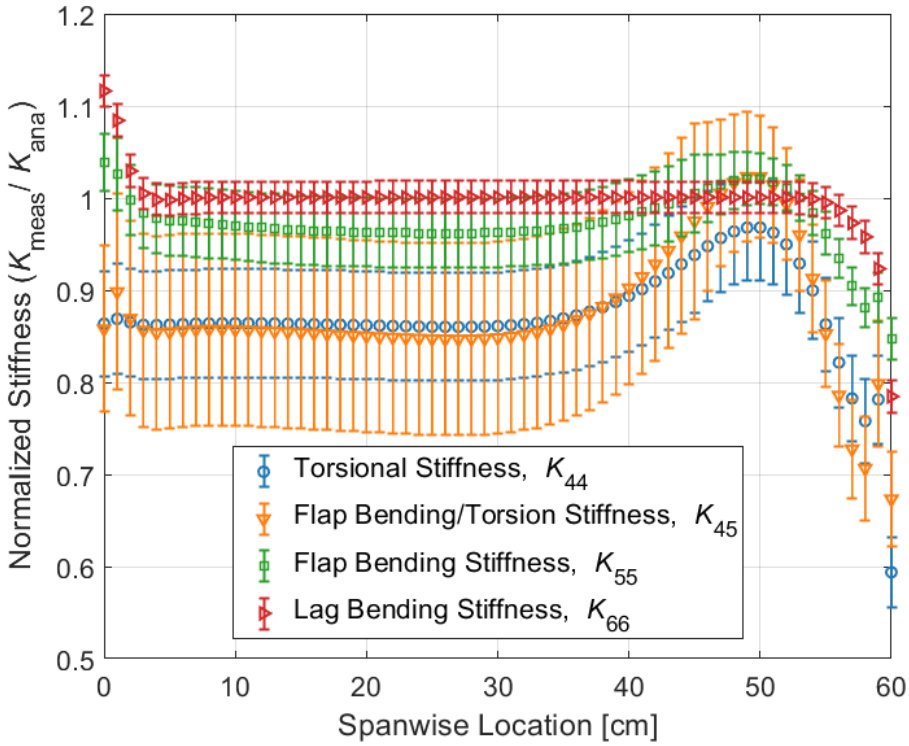

Figure 4.8: Spanwise variation of 95% uncertainty levels for the torsional and bending stiffnesses of the composite box beam.

stiffness values and uncertainty levels for the axial, shear, and extension/shear coupled stiffnesses, it can be seen that while the uncertainty level for the flap shear stiffness is nearly constant along the entire span, the uncertainty levels have fairly large variations along the span for the axial, lag shear, and extension/shear stiffness. These variations are primarily due to the boundary conditions affecting the shear strain distribution along the span, which end up impacting the lag shear and extension/shear compliance uncertainties. From Fig. 4.8, which shows the normalized stiffness values and uncertainties for the torsional, bending, and flap bending/torsional coupled stiffnesses, it can be observed that the strain concentrations, which arose from the applied torsional moment at the tip and persisted from about 45 cm to the tip of the beam, resulted in slightly smaller uncertainty levels in the torsional, flap bending, and flap bending/torsional stiffness components in this region. However, the uncertainty levels for these four stiffness components remained nearly constant over the first two-thirds of the beams length.

4.5 Summary and Conclusions

Uncertainty quantification for the calculation of the stiffness properties from the data reduction equation was investigated in this chapter. A discussion of the two types of error, systematic and random, was first presented followed by an identification of their associated quantities in the experimental measurements. The systematic uncertainty is a fixed quantity, and because it results from calibration in which the true value of the calibration variable is never known with 100% accuracy, is something that can not be eliminated from the test procedure. However, the impact of the random uncertainty, which results from random fluctuations that occur in the measurement apparatus, can be reduced by performing a greater number of tests. The data reduction equation was shown to be dependent on four measured variables, the loads, strains, and measurement locations, and material parameters.

While the first three variables are explicitly measured in the experimental setup, the material parameters, such as the Young's moduli, shear moduli, poisson's ratios, and ply orientations, are normally taken from the manufacturer, but are required to calculate the numerical warping field and their expected uncertainties must therefore also be considered.

For propagating the measurement uncertainties into the final calculated stiffness matrices, two methods were considered – a Taylor series method and a Monte Carlo method. The Taylor series method uses derivatives of the data reduction equation to propagate the uncertainties from the individual variables, while the Monte Carlo method randomly perturbs the measured variables over a large number of simulations to estimate the total uncertainty. Both methods were implemented and compared for two of the numerical validation models from Chap. 3 – the prismatic aluminum beam and the composite box beam with a symmetric layup. While the Taylor series method ignored higher-order derivatives in its uncertainty propagation and the first-order derivatives had to be estimated numerically, it was found to be similarly accurate to the Monte Carlo method for both of the considered models and in most cases, was slightly more conservative. In addition, the Taylor series method was found to be significantly cheaper in terms of computation time, by at least two orders of magnitude and, since the accuracies of the two methods were similar, the Taylor series method was therefore implemented for analysis of the actual experimental results. Based on the considered models, the expected strain uncertainties had the greatest impact on the overall uncertainty level for the stiffness properties; however the errors in the strain could likely be significantly reduced by using additional cameras with higher resolution in the DIC measurements. Moreover, the terms with the largest expected uncertainty levels are generally the shear stiffness components K_{22} and K_{33}, which have the smallest overall impact on the dynamic behavior of composite blades.

Chapter 5: Experimental Methodology

This chapter presents the experimental methodology for the presented dissertation research. A general overview of the design for the experimental test stand is first described. A detailed discussion of the instrumentation used for the strain and force measurements is then presented, highlighting the calibrations and characterizations of their associated uncertainties. Finally, the design and fabrication of the test articles is covered.

5.1 Test Stand

For the experimental test setup, there were two main aspects that needed to be considered – the load application and measurement as well as the optical strain measurement. As discussed in Sec. 2.2.4, the main requirement for the complete characterization of the sectional stiffness matrix is to measure the out-of-plane strain components, γ_{11}^{+} and γ_{12}^{+}, under six independent loading conditions. The requirement for six independent load cases necessitated the ability to apply forces, to produce axial and shear loads, as well as force couples, to produce torsional and bending moments. In addition, the use of an optical measurement technique – digital image correlation (DIC) – required an unobstructed view of the test article, in both its unloaded and loaded states.

With these requirements in mind, a custom test stand was designed and built for the experimental testing, as shown in Fig. 5.1. The main support structure of the test stand consisted of an 80/20 frame, which allowed for the necessary structural

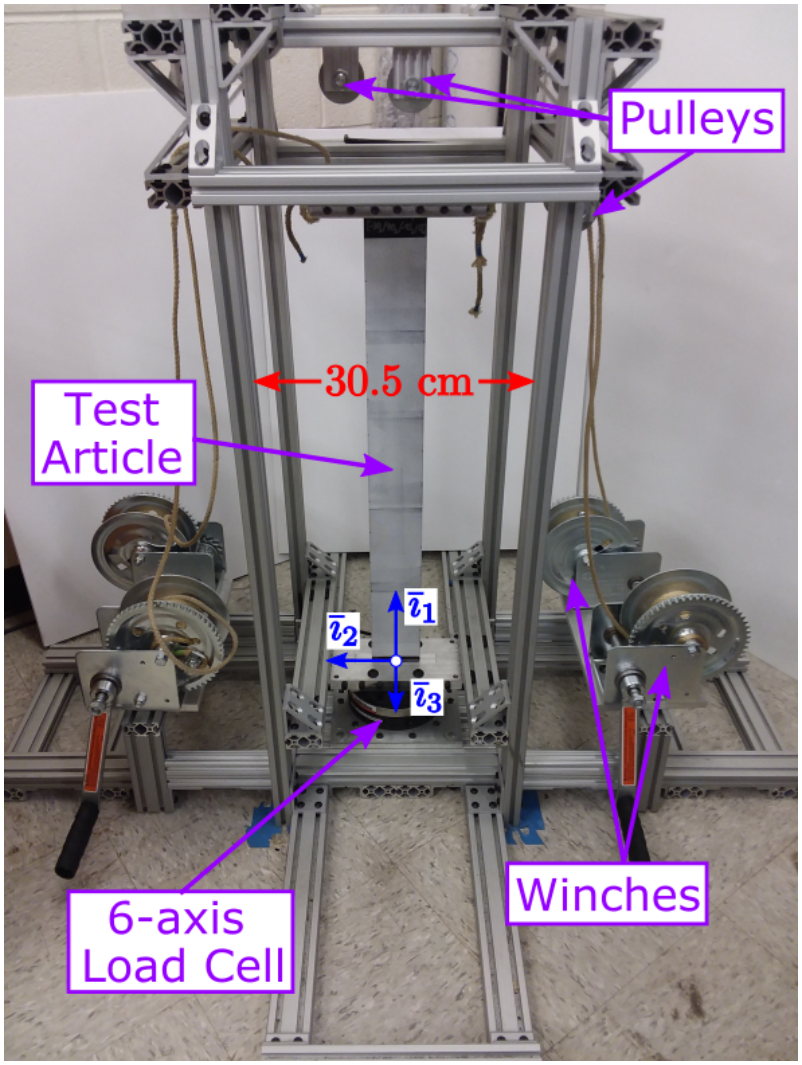

Figure 5.1: Test stand for load application.

rigidity to support the expected load conditions with significant safety factors, while allowing for the modularity needed to accommodate a variety of test articles. The vertical struts of the test stand were spaced with a horizontal separation of 30.5 cm, to ensure that the DIC cameras could capture a fully unobstructed view of the test article under a wide range of expected deformations. A 6-axis load cell was mounted at the base of the structure, between the test stand and test article, for measurement of the full set of reaction loads during testing. A set of four winches, rated up to 5560 N each, were mounted on the sides of the test setup to generate the significant loads needed for certain test cases; however, the winches did have

a minimum load capability of about 50 N. Therefore, in any load cases where the desired forces were sufficiently small, such as the flap shear loading F_3 and the force couples for a torsional moment M_1, a set of hanging weights were instead used. A system of adjustable pulleys was incorporated to reorient the generated forces, from either the winches or weights, into the desired load condition. The entire upper pulley assembly was also designed to be able to translate along the vertical struts between tests, thereby allowing testing to be performed for beams with lengths from 25 cm to 78 cm. Based on the overall design, the limitations on the maximum displacements were about 7 cm in $\bar{\imath}_2$ and 14 cm in $\bar{\imath}_3$. These margins were generally more than sufficient to generate large enough strains in the test articles, with limitations on the maximum measurable loads often becoming the main constraint during testing.

5.1.1 Test Article Mounting

One of the main goals in the design of the test setup was to provide the capability for testing a variety of beams with minimal modifications between test articles. One of the key aspects of producing this modular design was a clamping assembly that could be used for a variety of cross-sectional geometries, with a disassembled schematic shown in Fig. 5.2. The assembly consisted of two outer clamps, made of aluminum 7075, with external dimensions of 20.3 cm $\times$ 5.08 cm and a thickness of 19.1 mm. Two adapter clamps, with maximum external dimensions of 12.7 cm $\times$ 1.27 cm, were then manufactured to match the external geometry of each cross-sectional geometry, with an example of the adapters for an airfoil geometry shown in Fig. 5.2. The external dimensions of the adapter clamps meant that beams with external cross-sectional dimensions of up to 12.7 cm $\times$ 2.54 cm could be easily accommodated in the test setup. The two sets of clamping pieces were then secured together using a nut and bolt assembly, with the entire clamp structure then secured directly to the load cell through the circular four hole pattern on the top face.

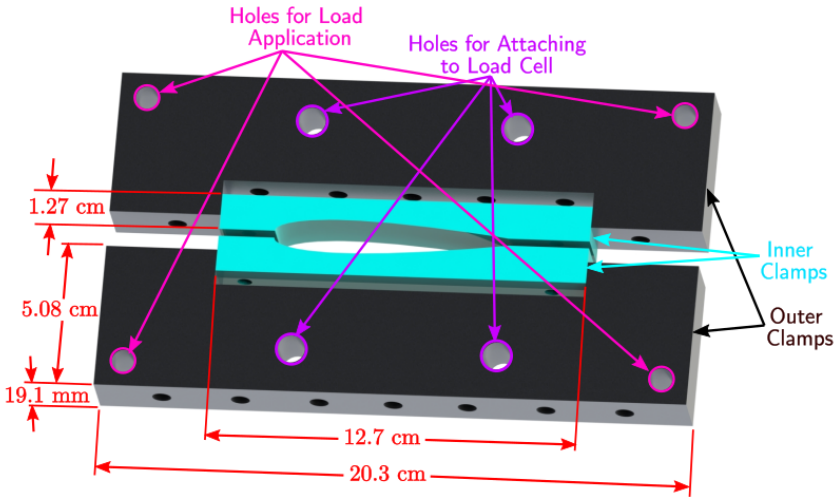

Figure 5.2: Clamp assembly to attach the beams to the test stand and apply loads.

The same clamping structure was also included at the other end of the test article for the load application, with the outer hole pattern used to provide a sufficient moment arm to generate the force couples needed for the torsional and bending moments. The use of the same clamping assembly at both ends of the beam, which was used for attaching the beam to the load cell and applying the loads, reduced the overall number of unique parts that needed to be manufactured for each test article. It also allowed for the beams to be easily flipped during testing, such that either end of the beam (root or tip) could be directly mounted to the load cell, allowing for strain measurements to be collected over a larger portion of the span if necessary.

5.1.2 Load Application

The load application is a crucial step in the experimental procedure. The data reduction procedure requires six independent loading conditions and, as much as possible, it is desired to have only a single force or moment applied at a time in order to maximize the signal to noise ratio for the calculation of each column of the compliance matrix. The three moments, M_1, M_2, and M_3, can be applied separately by carefully aligning the pulleys to produce force couples that generate a single

moment while minimizing the residual forces in the system, with example pulley setups shown in Fig. 5.3 for the application of bending moments about $\bar{\imath}_2$ and $\bar{\imath}_3$. A large axial force F_1 could also be applied by using all four winches, while minimizing

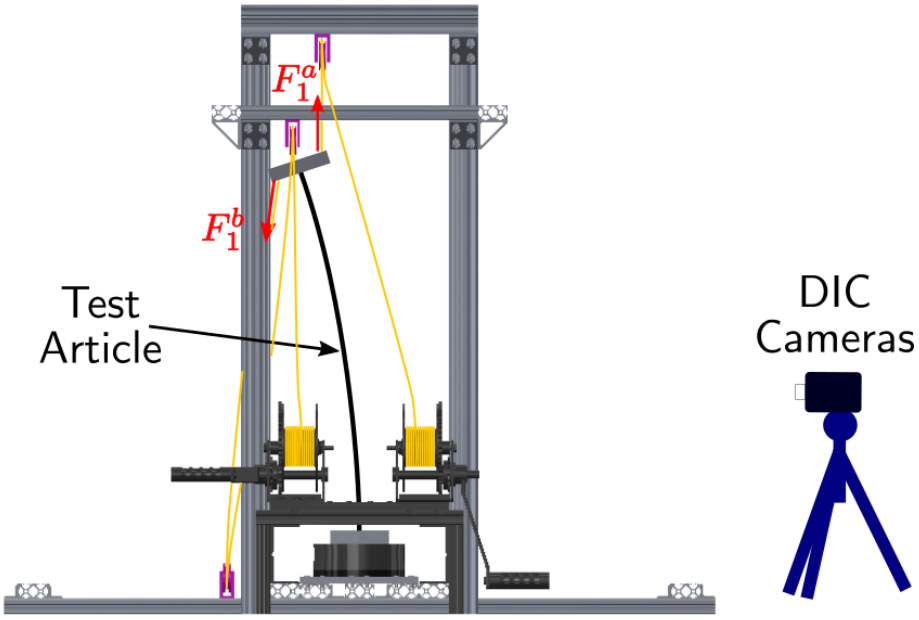

(a) Side view under flap bending moment M_2.

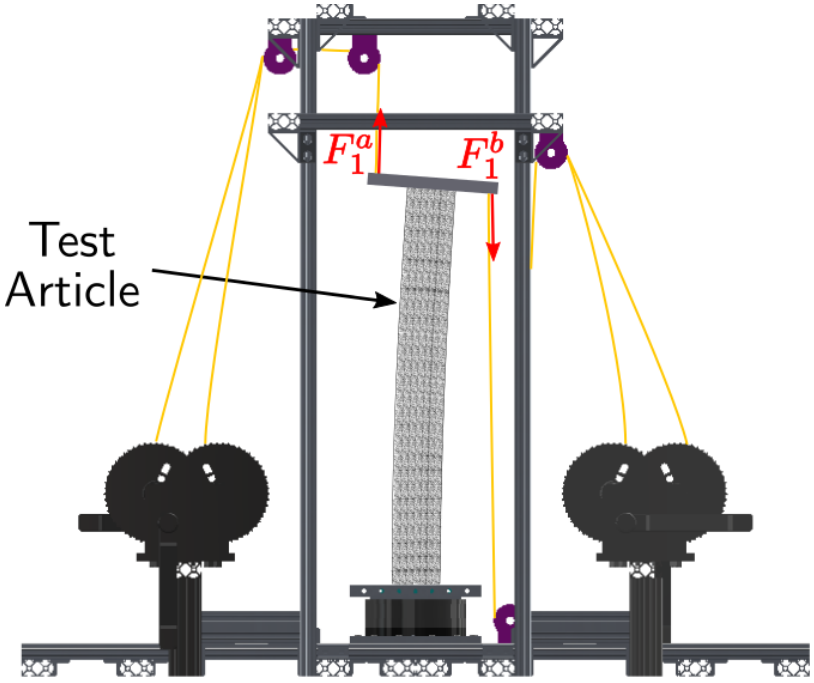

(b) Front view under lag bending moment M_3.

Figure 5.3: Schematics of winch and pulley setups for bending moment application.

the residual in the remaining forces and moments; however the shear forces F_2 and F_3 can not be applied without generating a linearly varying bending moment M_3 and M_2, respectively, along the span of the beams. An additional constraint on the load application arises from the use of an optical strain measurement technique, which necessitates having an unobstructed view of the beam at all points during testing. Therefore, when using hanging weights, which was typically required for applying a flap shear force F_3 or a torsional force couple M_1, it was necessary to make sure that all the weights were placed behind the test article to avoid having either the weights or the ropes block the view of the cameras. A positive and negative load case were also typically applied for all the tests, with the exception of a negative axial force due to limitations associated with buckling, in order to provide additional data and reduce the impact of the random uncertainty.

5.1.3 Digital Image Correlation Setup

Digital image correlation (DIC), described in Sec. 5.2, is used in this dissertation to measure the strain fields under loading by using two cameras pointed at the positive $\bar{\imath}_3$ surface of the beam, with the setup shown in Fig. 5.4. The cameras (5 MP Basler acA2440-75um with Schneider Xenoplan 28 mm lenses) are mounted on an adjustable tripod that allows them to be translated by up to 20.3 cm along the $\bar{b}_1$ axis of the beam during testing, such that images can be captured over a significant portion of the beam's span. Two high-intensity LED arrays (Visual Instrumentation Corp Model 901000H) were used to illuminate the test articles during testing to provide an even light intensity over a significant portion of the beam and reduce the overall exposure time for the images.

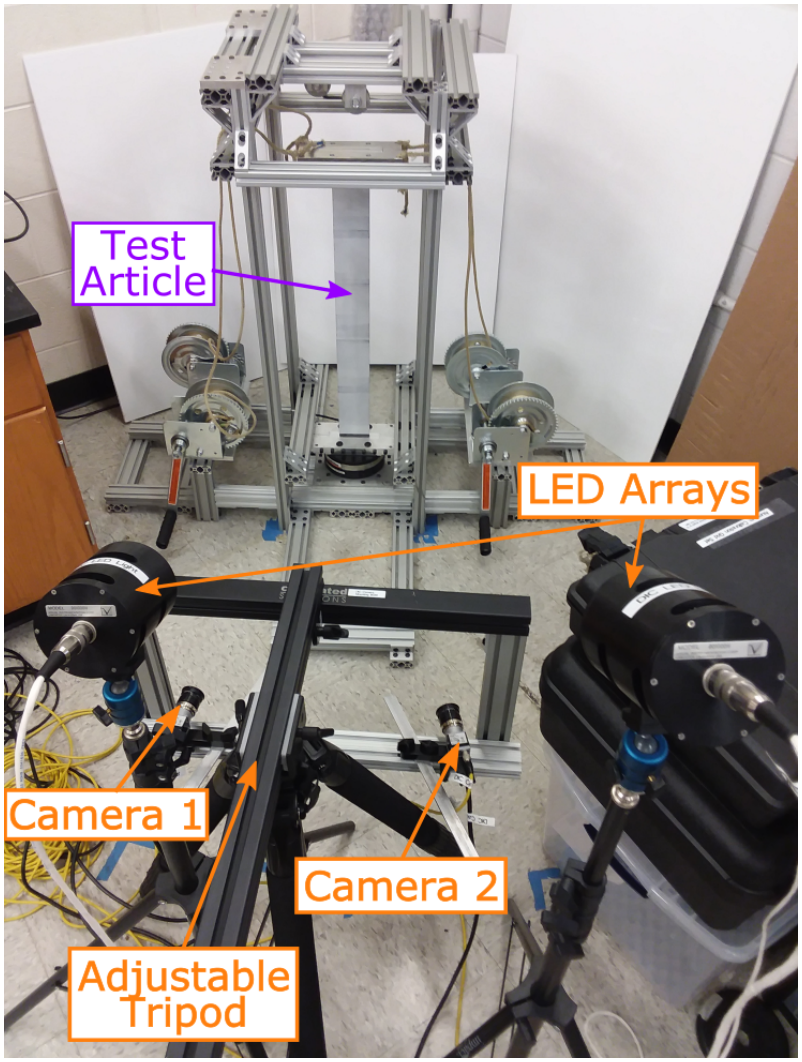

Figure 5.4: Full experimental test setup for stiffness property measurement.

5.2 Digital Image Correlation (DIC)

In the present research, the surface displacements and strains are measured using the VIC-3D digital image correlation (DIC) system from Correlated Solutions, Inc, which included software for both image acquisition (Vic-Snap) and image analysis (Vic-3D v8.0). The two 5 MP Basler cameras are used to capture 2448 × 2048 pixel images during testing that are then analyzed using the Vic-3D software. Extensive documentation for obtaining optimal results from DIC was provided with the software, in the form of both a reference manual and testing guide [130, 131]; the

key aspects of the various steps taken for the current tests are briefly discussed in the following subsections for the purpose of repeatability of the experiments and uncertainty quantification.

5.2.1 DIC Sample Preparation

With DIC, the preparation of the test article is one of the most important steps, as it can significantly impact the quality of the results. Although DIC is a non-contact measurement technique, the test articles are required to have a high contrast, random speckle pattern on the imaging surface to track deformation in the cross-correlation field between images. To achieve this, the surface of each sample is first sanded with a fine grit sand paper to remove any minor surface defects. A base layer of matte white paint is then applied to the surface; it is important to ensure that matte paint is used in order to limit the reflectivity of light that would otherwise arise from a glossy finish and cause a glare in the images. The random speckle pattern is then created using the application kit and black ink provided by Correlated Solutions, Inc, which consisted of rollers and stamps that could generate dot sizes from 0.18 mm to 5.1 mm. The selection of a specific dot size is a tradeoff between spatial resolution and field of view – ideally an individual speckle should be $\approx$ 3 - 5 pixels in the final images. For the current experiments, images were captured over $\approx$ 23 cm of the span and consisted of 2048 pixels in this direction, which meant that the stamp with a 0.33 mm dot size provided the optimal speckle pattern. Since both the stamp and roller have finite dimensions, multiple applications needed to be applied to cover the entire length of the beam. Therefore, it was also important to sufficiently reorient the stamp or roller between applications to ensure that the dot pattern remained stochastic by preventing any repeated patterns from occurring along the span of the beam.

The random speckle pattern itself is the main requirement in preparing the

samples for DIC; however, in order to make use of the DIC results in the data reduction algorithm, two additional steps were necessary. First, the DIC software only has information about the portion of the beam captured within the images themselves, but the actual measurement locations are a main requirement in the data reduction algorithm. Since the full span of the beam normally can not be captured by a single image, it is therefore important to have references within the image for knowing the exact locations of the measurements along the beam. To accomplish this, alphabetic markings were placed every 2.54 cm along the span, such that multiple markings were included within each set of images that could be used to define the measurement locations. Second, the DIC software utilizes a coordinate system aligned with the axes of the images by default, which is not typically the desired coordinate system. To provide a means of orienting the images, pairs of vertical lines, roughly 2.5 mm in length and spaced 2.5 cm apart, were created along the reference axis of the beam, in order to define the orientation of the $\bar{b}_1$ axis within the Vic-3D software. Figure 5.5 shows an example beam at multiple stages within this sample preparation process.

5.2.2 DIC System Setup

The setup and calibration of the imaging system also has a significant impact on the quality of the results, with the arrangement used for the current test shown in Fig. 5.6. When considering the setup of the cameras, selecting an appropriate stereo angle, ϕ_c, is critical for achieving the best results. For the mid-range lenses (28 mm) used in this study, the stereo angle should be between 25° and 60° to maximize the accuracy of the results [131], with an angle of $\phi_c \approx 35°$ used during testing. Maintaining a large enough depth of field (DOF) is also crucial to ensure that the image remains in focus even under large deformations. The depth of field is controlled by the aperture setting (f-number) of the camera F, the lens length f,

a) Sample after sanding external surface

b) Sample after application of layer of matte white paint

c) Sample with speckle pattern applied

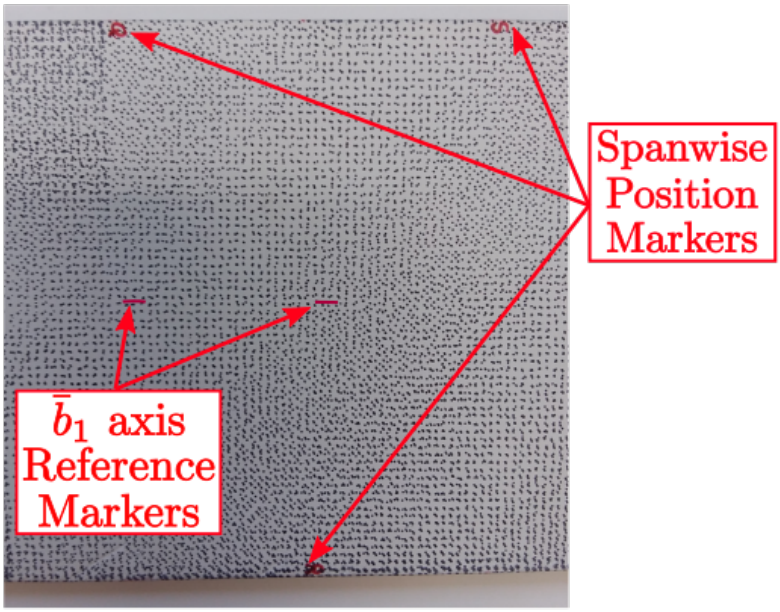

d) Zoomed-in image showing spanwise reference markers

Figure 5.5: Beam at multiple stages in the sample preparation process.

the acceptable diameter of the circle of confusion c, and the object distance s, with the depth of field limits given by [132]

$$\begin{aligned} d_1 &= \frac{sFc(s-f)}{f^2 + Fc(s-f)} \\ d_2 &= \frac{sFc(s-f)}{f^2 - Fc(s-f)} \end{aligned} \tag{5.1}$$

where d_1 and d_2 are the near and far limits, respectively. The maximum acceptable diameter of the circle of confusion, the circle formed when imaging a point source that does not come into perfect focus, can be approximated from the lens focal length as $c \approx f/1720$ [133]. In order to achieve the desired 23 cm image window, the required distance of the cameras from the beam needed to be $s \approx 100$ cm. When combined with an expected maximum displacement of ≈ 9 cm within the imageable portion of the span, this gave a desired f-number of 5.6. For the beams with larger bending stiffness, and therefore smaller expected out-of-plane displacements, the f-number was reduced to 4 to increase the spatial resolution.

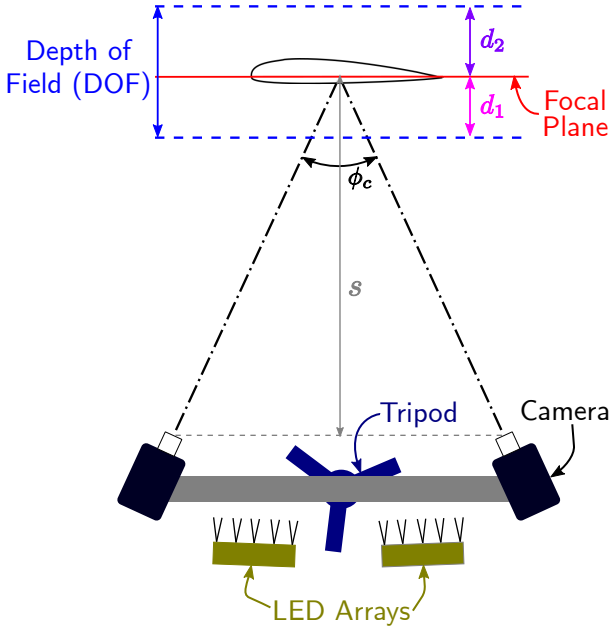

Figure 5.6: Schematic of the overhead view of the DIC setup.

With the camera locations determined, calibration is then used to establish the spatial orientations and positions of both cameras within the Vic-3D software, which are needed to recover the deformations from the cross-correlation procedure. This calibration is done through the use of a calibration plate, shown in Fig. 5.7. Multiple sizes of the calibration plates were provided from the vendor; the appropriate size of the plate is selected based on the requirement that the plate fill up most of the image during calibration. Hollow dots on the plate provide reference axes with a

set of smaller dots providing a reference size that is predefined within the software and used to determine the approximate size and location of the object being imaged. The main requirements for the calibration procedure are to capture images of the plate with significant rotation of the grid about all 3 axes and at multiple distances within the depth of field. Generally 40-50 images were taken for each test to ensure accurate results. Based on the calibration images, the software generates a score describing the average error in pixels between the measured location of a target point on the calibration grid and the theoretical position of this same point, with a score of about 0.02 to 0.025 pixels normally achieved during calibration.

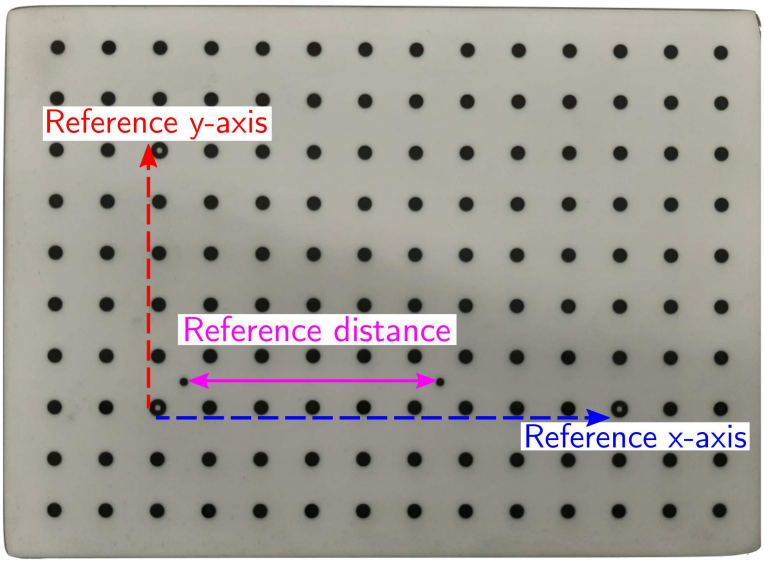

Figure 5.7: Grid used for DIC calibration.

5.2.3 DIC Analysis

Once the test article is prepared and the camera calibration is complete, images of the beams can be collected in the undeformed state as well as in various deformed states under applied loads. For each load state, 10 images are captured that will be averaged together to reduce the impact of any dynamic loads or other variabilities that may arise while capturing the images. In order to provide sufficient data for the

data reduction procedure, images are captured of both the front ($+z$) surface and back ($-z$) surface by rotating the entire beam 180° about its span (axis $\bar{b}_1$) between tests. The crux of the DIC technique is then, as its name suggests, correlating the images between cameras and across loading states to calculate the 3-D shape and deformation field on the imaged surface. The DIC method has been significantly improved over the past three decades since its original development in the early 1980's and a variety of commercial DIC software is now available, with the Vic-3D v8.0 software used in this dissertation. Because the DIC technique is applicable to a wide range of possible tests, multiple steps need to be taken during the analysis and appropriate parameters defined to produce high quality measurements based on the given setup. The following steps were used in this work to generate the experimental DIC data for all of the tested beams:

- **Apply a mask to the images**. A substantial portion of the collected images contain unnecessary information, such as the 80/20 test frame and background behind the test article. An area of interest is therefore defined within the undeformed reference image, encompassing only the speckle pattern, to indicate which portion of the image should be correlated with images of the deformed states. In some cases, if the beam experiences significant movement between images, it may be necessary to define a start point in the image that can be easily tracked across all images. As the DIC software has no knowledge of the absolute position of the images with respect to the inertial frame of the load cell, the alphabetic markings placed on the beams during sample preparation become important for defining the area of interest. By drawing the edges of the area of interest tightly around these alphabetic markings, the spanwise location of the measurements can be easily interpreted on output of the data. These markings can also serve as a useful reference if the definition of a starting point is required.

- **Subdivide the area of interest**. Once the area of interest has been defined, the software needs to subdivide the remaining portion of the image into a subset of pixels that is used to track the displacement between images. The subset size must be large enough to provide a distinctive pattern for correlation purposes, but small enough to maintain an optimal match confidence that minimizes the uncertainty level and noise in the correlation. A subset size of 25 $\times$ 25 pixels was the default suggestion by the software based on these considerations and was used in this work. An additional parameter, the step size, controls the spacing of the points output by the software – a step size of 1 indicates that a data point is placed within every pixel while a larger step size of 5 would correspond to a data point at every 5 pixels. For the DIC software, the area of interest defines a 2-D grid of pixels within the image and the analysis time is therefore inversely proportional to the square of the step size; for the data reduction procedure, the number of cross-sectional points is proportional to the step size and the analysis time is inversely proportional to the step size. Therefore, to maintain a high enough spatial resolution while minimizing the required computational time, a step size of 5 was used for all the experiments, such that data points were evaluated at about 0.06 cm intervals in both $\bar{b}_1$ and $\bar{b}_2$.

- **Calculate the 3-D displacements**. Once the area of interest, subset size, and step size have been selected, the software can compute the cross correlations between undeformed and deformed images to recover the 3-D surface geometry and deformations, with internal algorithms designed to calculate the displacement at a sub-pixel accuracy. Since the cameras have no absolute positional reference, an option for an auto plane fit is used to define the initial orientation of the coordinate system used during the analysis with respect to the calculated undeformed surface geometry. This origin is placed with its

z-coordinate at the "mass" centroid of all the measured points for a given set of undeformed and deformed reference images, with the $\bar{b}_3$ axis defined normal to the best-fit plane of the entire data field. This option is selected to ensure that the average z-coordinate of the measurements is close to 0, making it easier to define the location of the measurement points within the cross-section for use in the data reduction algorithm.

- **Define the coordinate system**. The auto-plane fit option provides a useful means of closely approximating the cross-sectional coordinates of the beam. However, due to the orientation of the cameras on the tripod, the software defaults to the y-coordinate being along the axis of the beam and the cross-sectional coordinates are thus initially defined by axes $\bar{b}_1$ and $\bar{b}_3$, in contrast to the desired axes $\bar{b}_2$ and $\bar{b}_3$. Once the images have been correlated and the positions and displacements calculated, a coordinate transformation can be easily applied within the software by defining the orientation of the $\bar{b}_1$ axis (x-axis), which is done by drawing a line in the software through the axis markers placed on the beams during sample preparation. Once defined, the transformation must be applied to the data by selecting this option within the software. Note that it is important to only apply this transformation once; the transformation is applied in the software using a rotation matrix calculated based on the rotation from the initially calculated coordinate system to the desired coordinate system. If applied more than once, the rotation matrix will then be multiplied through a second time, resulting in data that is no longer in the desired coordinate system.

- **Calculate the surface strains**. After the $\bar{b}_1$ axis has been accurately identified, the surface strains can be calculated in the DIC software to give the three strain components γ_{11}^{+}, γ_{12}^{+}, and γ_{22}^{+} (defined as ϵ_{xx}, ϵ_{xy}, and ϵ_{yy} in the

software). Because the image correlation generates a grid of x, y, z points with high resolution and corresponding u, v, w displacements at these points, the DIC software uses a similar approach to conventional finite element analysis to numerically calculate the strains based on the displacements. Since data is calculated only on the surface of the beam (*i.e.* no through-thickness information is available), the set of data points is analyzed internally using 3-noded triangular elements, similar to conventional plane strain triangular elements. The strain at nearly all the data points is evaluated within multiple triangles and therefore must be smoothed by the software, which is done using a local, center-weighted Gaussian filter. This smoothing is controlled by a filter size given in terms of neighboring data points – too large of a filter size will impact the ability to see local strain concentrations, while too small of a filter will result in a strain measurement with significant noise levels. To determine an appropriate filter size, a prismatic aluminum beam was tested under a tip shear force and the DIC strain measurements were compared to axial strain measurements from four strain gauges attached to the same beam, as shown in Fig. 5.8. The measurements from the strain gauges are shown by the solid lines, with the shaded regions representing $\pm 2.5\%$ of the measured value. The measurements from the DIC setup were extracted at the same locations for various filter sizes. The DIC measurement was extracted for various filter sizes and plotted as points, with an error bar included to represent the two standard deviation result for all the DIC measurement points within a 3 mm $\times$ 3 mm box corresponding to the size of the strain gauge. From these results, it can be observed that above a filter size of about 30 to 40, the noise in the DIC measurement is significantly reduced and the strains show great agreement with the corresponding strain gauges. Based on these results, a filter size of 35 was applied for the experimental measurements in this dissertation. As there

are multiple options for the desired strain tensor, it is also important to make sure that the strain tensor type is set to engineering to ensure that the shear strain matches the convention used in the data reduction algorithm.

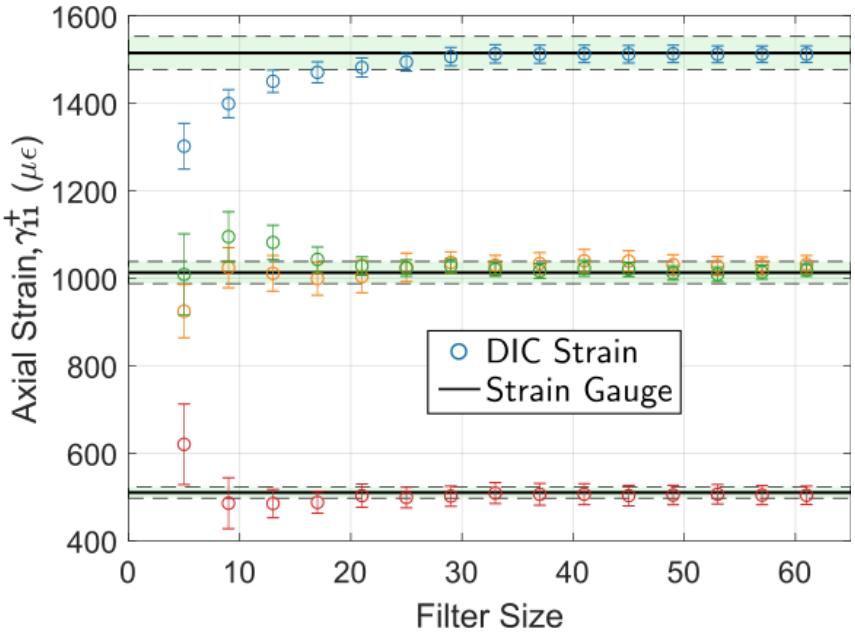

Figure 5.8: Effect of DIC filter size on measured strain.

- **Output the DIC data.** Once all the images have been processed and the displacements and strains calculated, the results of the 10 images taken in each deformed state are averaged within Vic-3D. These results can then be exported to file, with options existing for a comma separated variable (*.csv*) file, Tecplot ASCII file, plain ASCII file, or MATLAB (*.mat*) file. Since the data reduction algorithm was implemented within MATLAB, the DIC data was exported using the option for the *.mat* file.

5.2.4 DIC Data Extraction

Once the images have been processed by the DIC software using the above steps and the data output to file, there are some additional steps that need to be performed in MATLAB to extract the data into a format for use in the data reduction

procedure. These steps include extracting data at discrete spanwise locations and determining the cross-sectional measurement locations, as described below:

- **Extracting data at desired spanwise locations**. Once the images have been processed, the data is output in a 2-D grid, with one dimension along the span and the other along the outer profile of the cross-section. An example data grid is shown in Fig. 5.9 for the measured out-of-plane displacement w_{DIC}. Note that for visualization purposes, the grid lines are only shown for every other point in the DIC data set. Since the data is generated based on the pixels within the images, the grid will generally never be perfectly aligned with the $\bar{b}_1$ and $\bar{b}_2$ axes. Therefore, to extract data at a given cross-section, all data points within ± 0.13 cm of the desired x coordinate are selected, which will normally consist of about five rows of spanwise data from the DIC generated grid. This selection of data points is shown by the red boundary drawn in Fig. 5.9 for x = 24 cm. The important values extracted from this 2-D grid of data at each desired location are then the coordinates $(x_{\text{DIC}}, y_{\text{DIC}}, z_{\text{DIC}})$, the displacements $(u_{\text{DIC}}, v_{\text{DIC}}, w_{\text{DIC}})$ displacements, and the strains γ_{11}^{+} and γ_{12}^{+}.

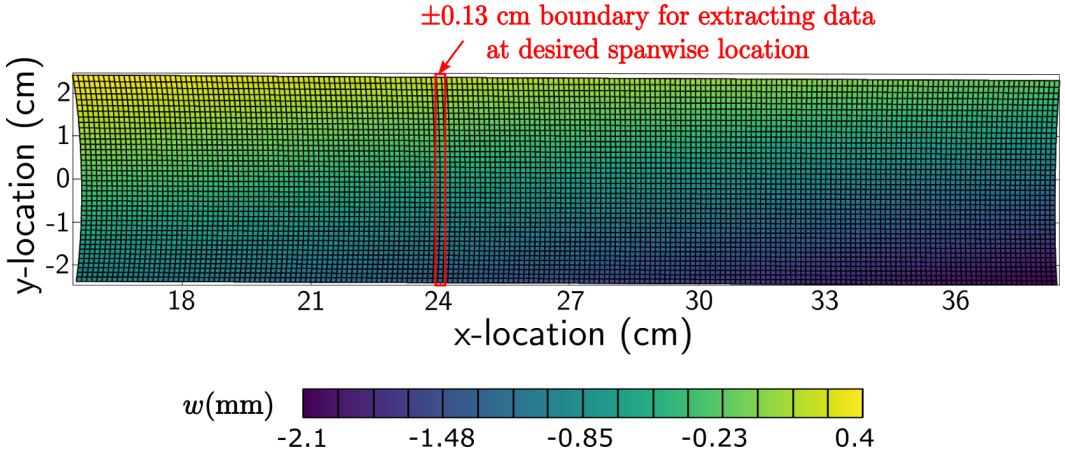

Figure 5.9: Example 2-D grid of w-displacement generated from DIC.

- **Determining the measurement locations**. Because the DIC software works from 2-D images, there is no mean of defining the absolute orientation of

the cross-sectional coordinate system. While the $\bar{b}_1$ axis is defined in the DIC analysis procedure based on its desired orientation, the $\bar{b}_2$ and $\bar{b}_3$ axes cannot normally be aligned within the software in their desired orientations, and both a translation in the $\bar{b}_3$ direction and a rotation about $\bar{b}_1$ will generally be required when processing the data. If selected during analysis, the auto-plane fit option will orient the $\bar{b}_3$ axis normal to the best-fit plane of the cross-section. For the data on the front $(+z)$ surface, the $\bar{b}_3$ axis will therefore be close to its desired orientation; however, for the data on the back $(-z)$ surface, the $\bar{b}_3$ axis is normal to the surface and will be about 180° from its desired orientation. An example of this is shown in Fig. 5.10 for measurements of a VR-7 airfoil. The originally measured y and z coordinates are shown in Fig. 5.10(a), which are not aligned with the coordinates defining the shape of the cross-section. It is therefore necessary to match the measured coordinates with the cross-sectional geometry, which can be done by minimizing the function

$$\psi = \sum_{i=1}^{N} \sqrt{(y_a - y_i)^2 + (z_a - z_i)^2} \tag{5.2}$$

where

$$y_i = y_{\mathrm{DIC},i} C_\phi + (z_{\mathrm{DIC},i} + z_o) S_\phi \tag{5.3a}$$

$$z_i = -y_{\mathrm{DIC},i} S_\phi + (z_{\mathrm{DIC},i} + z_o) C_\phi \tag{5.3b}$$

with i representing a single measurement point, $y_{\mathrm{DIC},i}$ and $z_{\mathrm{DIC},i}$ defining the measurement locations obtained from DIC, and y_a and z_a defining the external profile of the cross-section in basis $\mathcal{B}$. The minimization variables are the offset in the $\bar{b}_3$ direction, z_o, and the rotation angle ϕ that brings the measured coordinates into basis $\mathcal{B}$, such that Eq. (5.3) defines the actual y and z measurement locations. A standard minimization procedure, using the

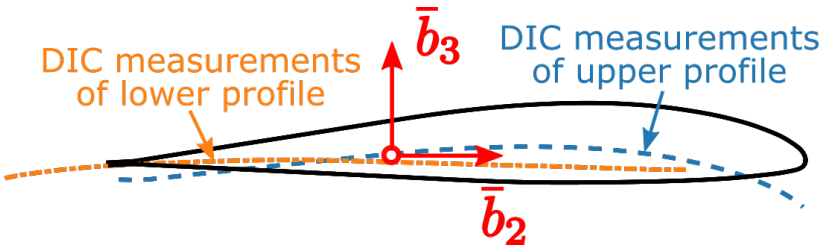

(a) Initial DIC measurement locations

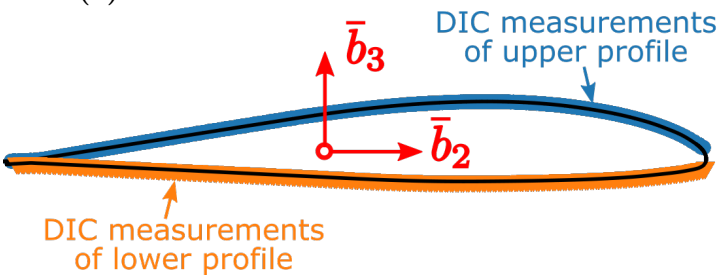

(b) Corrected DIC measurement locations

Figure 5.10: Updating of the DIC measurement locations into the cross-sectional basis $\mathcal{B}$.

fminsearch function in MATLAB, is implemented to determine these variables, which for a VR-7 airfoil leads to an average offset of $z_o = 0.414$ cm and rotation $\phi = -3.55°$ for the measurements along the upper edge of the profile and an average offset of $z_o = -0.172$ cm and rotation $\phi = -181.3°$ along the lower edge of the profile. The resulting corrected measurement locations are then shown in Fig. 5.10(b). Although not explicitly required in the data reduction equation itself, the displacements are needed to calculate the sectional loads based on the loads measured by the load cell. Therefore, the displacements must also be rotated from the DIC coordinate system into the inertial basis $\mathcal{I}$ according to

$$\begin{Bmatrix} u \\ v \\ w \end{Bmatrix} = \begin{bmatrix} 1 & 0 & 0 \\ 0 & C_\phi & S_\phi \\ 0 & -S_\phi & C_\phi \end{bmatrix} \begin{Bmatrix} u_{\text{DIC}} \\ v_{\text{DIC}} \\ w_{\text{DIC}} \end{Bmatrix} \tag{5.4}$$

For the case of a rectangular profile, the minimization procedure can be skipped if the auto plane fit option is used; for measurements on the $+z$ surface,

the parameters can be automatically set to $z_o = h/2$ and $\phi = 0°$, and for measurements on the $-z$ surface, the parameters can be automatically set to $z_o = -h/2$ and $\phi = 180°$.

5.2.5 Strain Measurement Basis

Based on the stated strain analysis procedure from the DIC vendor, it is expected that the measured strain components, γ_{11}^{+}, γ_{12}^{+}, and γ_{22}^{+}, are calculated by the DIC software in the local surface basis $\mathcal{E} = (\bar{e}_1, \bar{e}_2, \bar{e}_3)$. For an airfoil cross-section, the orientation of the surface basis can have significant variations when moving from the trailing edge to the leading edge, particularly for the upper surface of the profile. During DIC testing, images will be taken of both the upper and lower surface of these airfoils and it is therefore important to ensure that the strains are actually calculated in the local surface basis. To verify this, a thin-walled circular cylinder, with an inner radius $d_i = 3.01$ cm and outer radius $r_o = 3.18$ cm as shown in Fig. 5.11(a), was tested under torsion, using the setup shown in Fig. 5.11(b). The tube was made of aluminum 6061 ($E = 68.9$ GPa and $\nu = 0.33$) with a total length of 61 cm and prepared for DIC testing using the process described in Sec. 5.2.1. For this simple circular geometry, the shear strain in the local surface basis (in cylindrical coordinates) should be constant under a torsional load, as given by

$$\gamma_{12}^{+} = -\frac{M_1 r}{\pi/32 G(d_o^4 - d_i^4)} \tag{5.5}$$

where M_1 is the applied torque, r is the radial measurement location ($d_o/2$), and $G = E/(2(1+\nu)) = 25.9$ GPa, with the expression in the denominator representing the torsional stiffness K_{44}. If measured in basis $\mathcal{B}$, the measured strain γ_{12} would depend on the measurement location and vary sinusoidal around the cross-section according to

$$\gamma_{12} = -\frac{M_1 r}{\pi/32G(d_o^4 - d_i^4)}\sin(\alpha) = -\frac{M_1 y}{\pi/32G(d_o^4 - d_i^4)} \tag{5.6}$$

where α measures the rotation angle from $\bar{b}_2$ and $y = r\sin(\alpha)$ is the cross-sectional coordinate of the measurement.

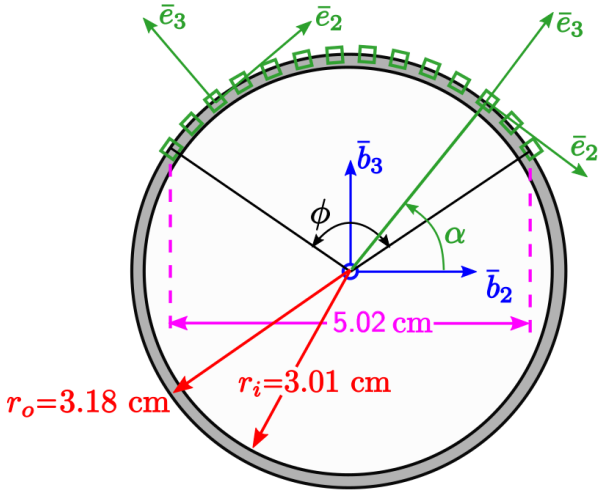

(a) Cross-sectional geometry

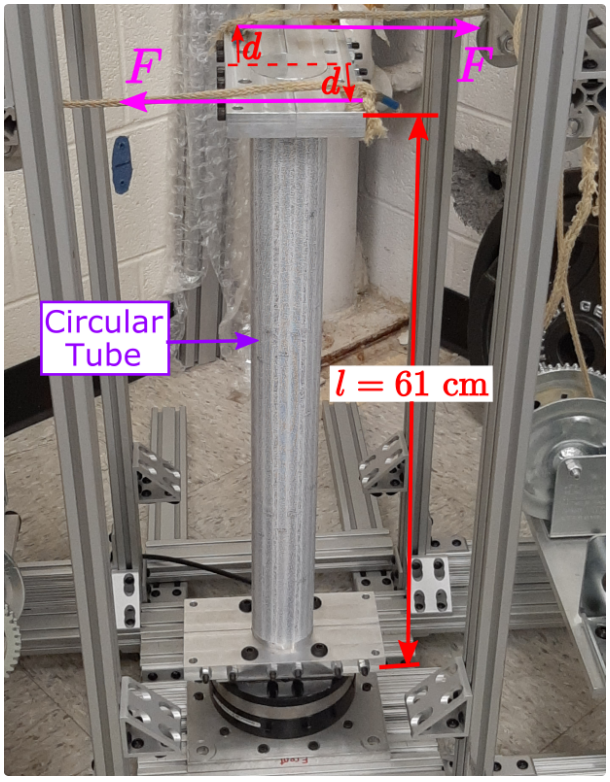

(b) Experimental test setup

Figure 5.11: Experimental setup for torsional testing of a circular aluminum tube.

DIC testing was performed for multiple torques up to -373.5 N-m, in approximately 50 N-m intervals, with the torque applied as a force couple as shown in Fig. 5.11(b); the resultant torque was measured by the load cell at the base of the structure. The cameras were set up to capture images close to the mid-span of the tube, from about $x = 18$ cm to $x = 41$ cm, and from about $y = -2.5$ cm to $y = 2.5$ cm along $\bar{b}_2$, with a grid spacing of about 0.075 cm in the DIC measurement points. An example of the processed strain field component γ_{12}^{+} under a -54.2 N-m applied torque is shown in Fig. 5.12, which showed good agreement with the expected strain from Eq. (5.5) – $\gamma_{12,\text{ana}}^{+} = 218.3\mu\epsilon$ – but did have some larger variations near the boundaries of the image in both the $\bar{b}_1$ and $\bar{b}_2$ directions.

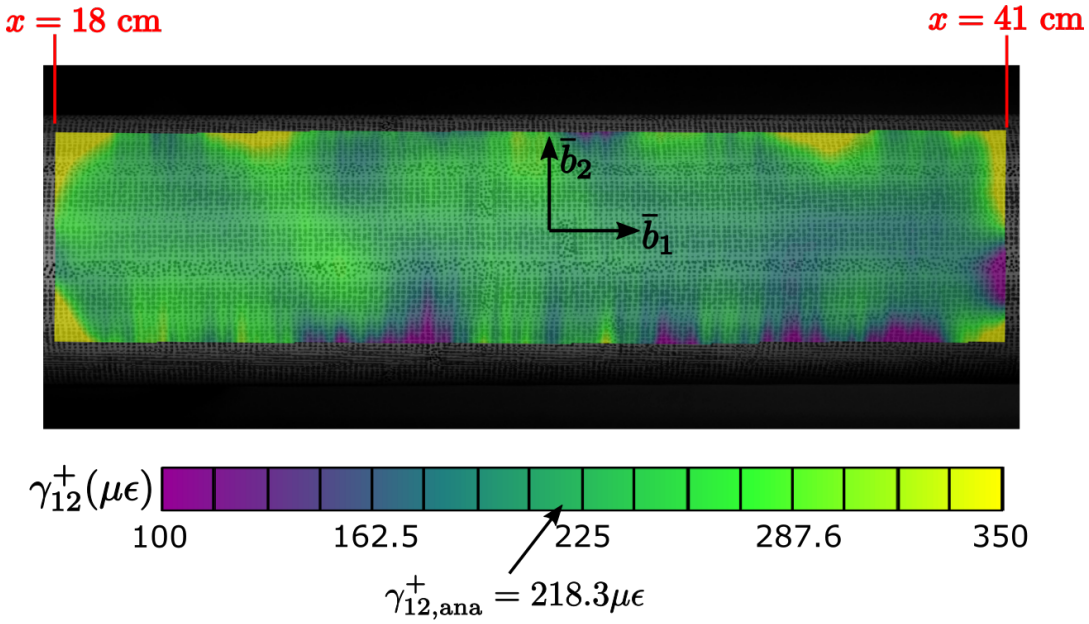

Figure 5.12: Shear strain γ_{12}^{+} measured by DIC for a circular tube under a -54.2 N-m torque.

For each load case, the results were then averaged first along $\bar{b}_1$ to give the variations along $\bar{b}_2$ as shown in Fig. 5.13. These results showed that the shear strain remained nearly constant along y, with the only substantial deviations arising near the outer edges of the DIC measurement window. They were then averaged again along $\bar{b}_2$ to give the mean strain for the entire DIC dataset, with the results for each

load case summarized in Table 5.1. With exception to a few strain concentrations that arose near the outer boundaries of the DIC images, the measured shear strain agreed well with the constant analytic value from Eq. (5.5), which verified that the DIC strains were indeed measured in the local surface basis $\mathcal{E}$.

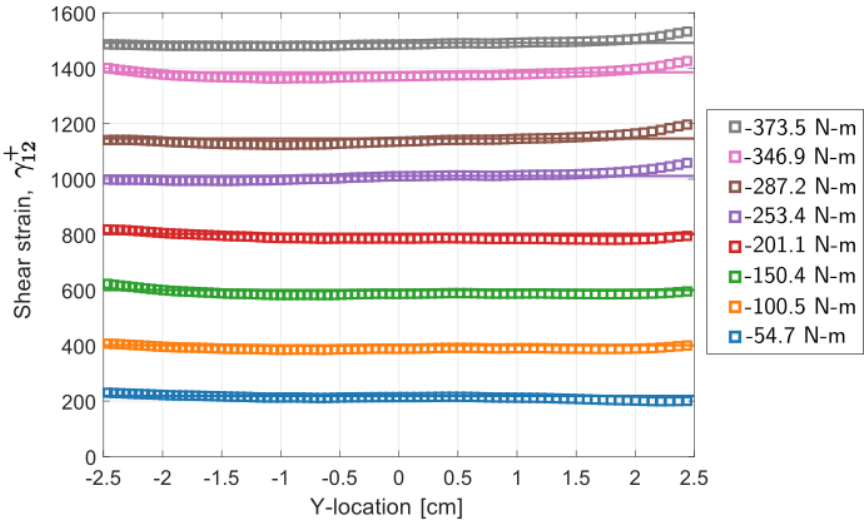

Figure 5.13: Shear strain γ_{12}^{+} distribution along y, measured by DIC under multiple torques for a circular tube.

Table 5.1: Mean shear strain γ_{12}^{+} from DIC under multiple torsional loads.

Torsional Load, M_1 (N-m)	Shear Strain $\gamma_{12}^{+}(\mu\epsilon)$	
	DIC measurement	Analytic
-54.7	213.4	218.4
-100.5	390.8	401.2
-150.4	589.8	600.3
-201.1	790.9	803.0
-253.4	1008.7	1011.6
-387.2	1140.4	1146.5
-346.9	1377.7	1385.2
-373.5	1488.8	1491.3

5.2.6 Rigid Body Motion

An important feature of strain is that a rigid body motion introduces no strain into a structure. In the experimental testing, it is expected that the boundary condition in the experimental setup won't be a perfect clamp condition, due to a finite stiffness in the load cell and some manufacturing tolerances in the clamp assembly, resulting in some rigid body motion under loading. Additional rigid body motion also arises during testing due to the fact that the cameras are translated up and down on the tripod. It is therefore important to verify that the DIC software is able to properly filter out various types of rigid body motion. To assess the impact of a rigid body motion on the strain measurement, two simple tests were carried out. The first test consisted of translating the cameras vertically on the tripod by $h_1 = 2.5$ cm and $h_2 = 5$ cm, while defining the same area of interest within the image, as depicted in Fig. 5.14. These translations were repeated 10 times to assess the average impact on the measurements. Since the test article is undergoing no deformation, the measured strain field should remain 0 in all the DIC measurements; however, some small variations occur during translation of the cameras and the resulting distribution of the mean strain across the data sets is shown in Fig. 5.15. From this distribution, the average offset strain was found to be about -16 $\mu\epsilon$.

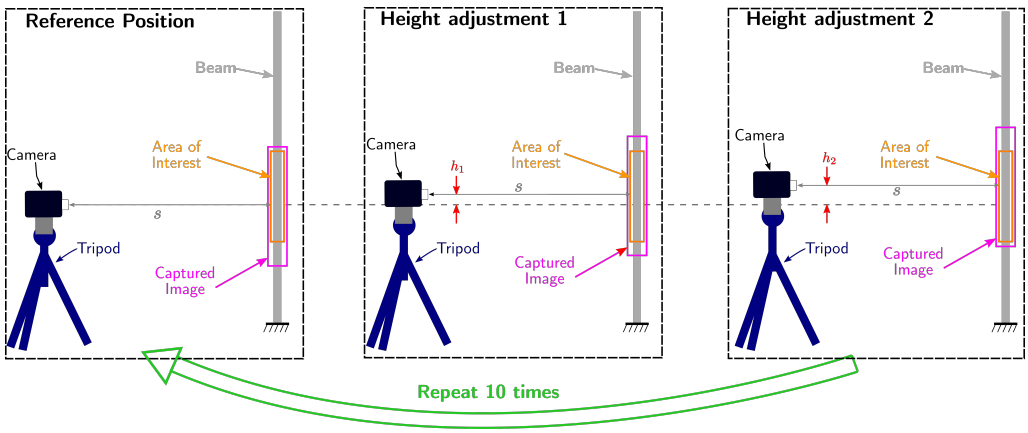

Figure 5.14: Test description for rigid body motion introduced by a vertical translation of the cameras.

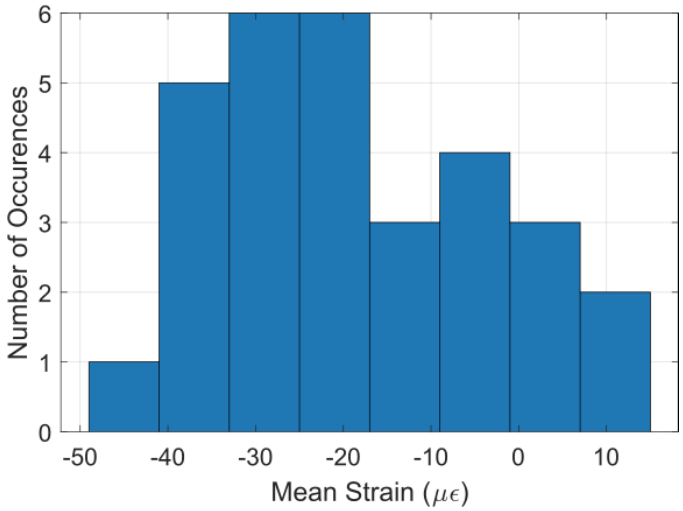

Figure 5.15: Distribution of mean strain values resulting from a vertical translation of the cameras.

The second test involved rigid-body motion in the other in-plane direction, which was accomplished by moving the test article laterally by ±2.5 cm while leaving the cameras stationary, as depicted in Fig. 5.16. This test was again repeated 10 times to assess the average impact on the measurements, with the distribution of the mean strain across the tests shown in Fig. 5.17. From this lateral motion testing, the average offset strain was found to be about 15.2 $\mu\epsilon$, which was similar to the results from the vertical translation of the cameras and therefore provided a good estimate for the systematic strain uncertainty resulting from rigid body motion.

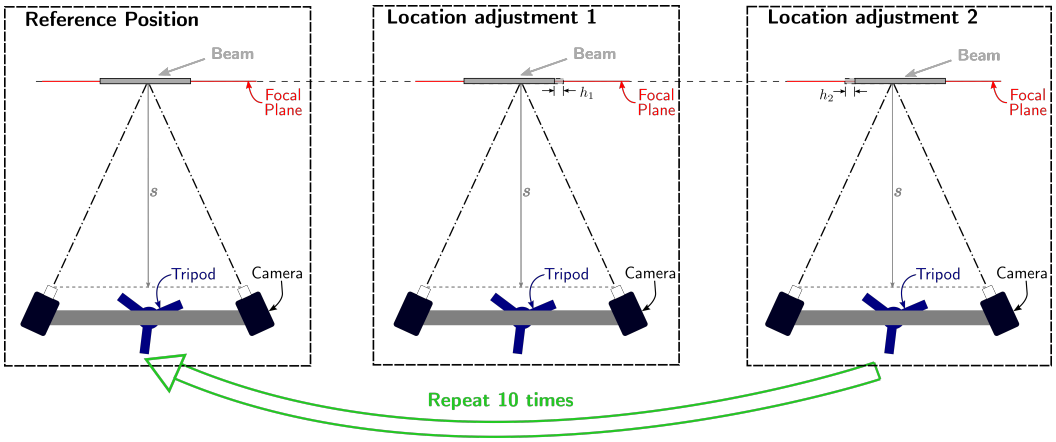

Figure 5.16: Test description for rigid body motion introduced by a lateral translation of the test article.

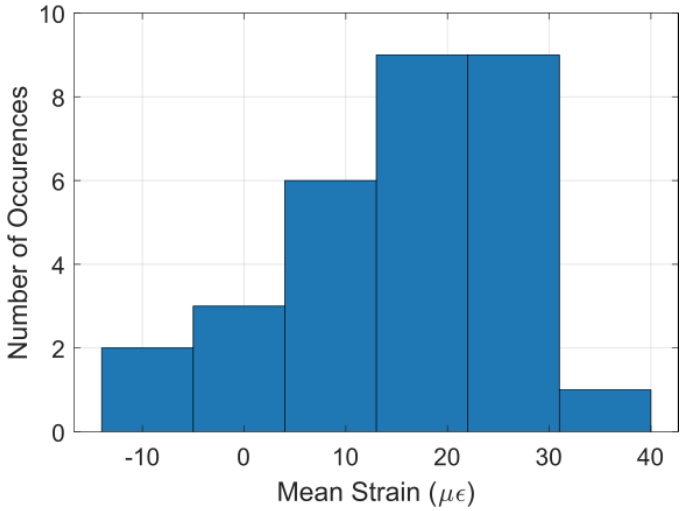

Figure 5.17: Distribution of mean strain values resulting from a lateral translation of the test article.

5.2.7 Uncertainty Identification

As discussed in Chap. 4, a systematic and bias error will be present in every experimental measurement. To determine the systematic strain error, information generated during the calibration of the cameras in the DIC software is used. In particular, a score is displayed that defined the average error in pixels, which generally was around 0.02 pixels, and could be used to provide an estimate on the strain systematic error, based on the total image size, of about 10.9 $\mu\epsilon$. In addition, from the rigid body motion testing, an average offset of about 16 $\mu\epsilon$ was observed when the cameras or test articles were subjected to a rigid body motion. Therefore, the 95% confidence interval for the systematic uncertainty can be estimated to be about 26.9 $\mu\epsilon$.

In order to estimate the random strain error associated with the DIC setup, information from the DIC analysis of the strain is used. During an individual test, ten images are captured of the beam in each reference state, including in the undeformed state. When in the undeformed state, there should be no change between the ten images and the strain field should remain 0; however, a zero strain state is not

actually observed, as seen in Fig. 5.18 which shows an example of the calculated strain from averaging the results of the ten undeformed images. These small, non-

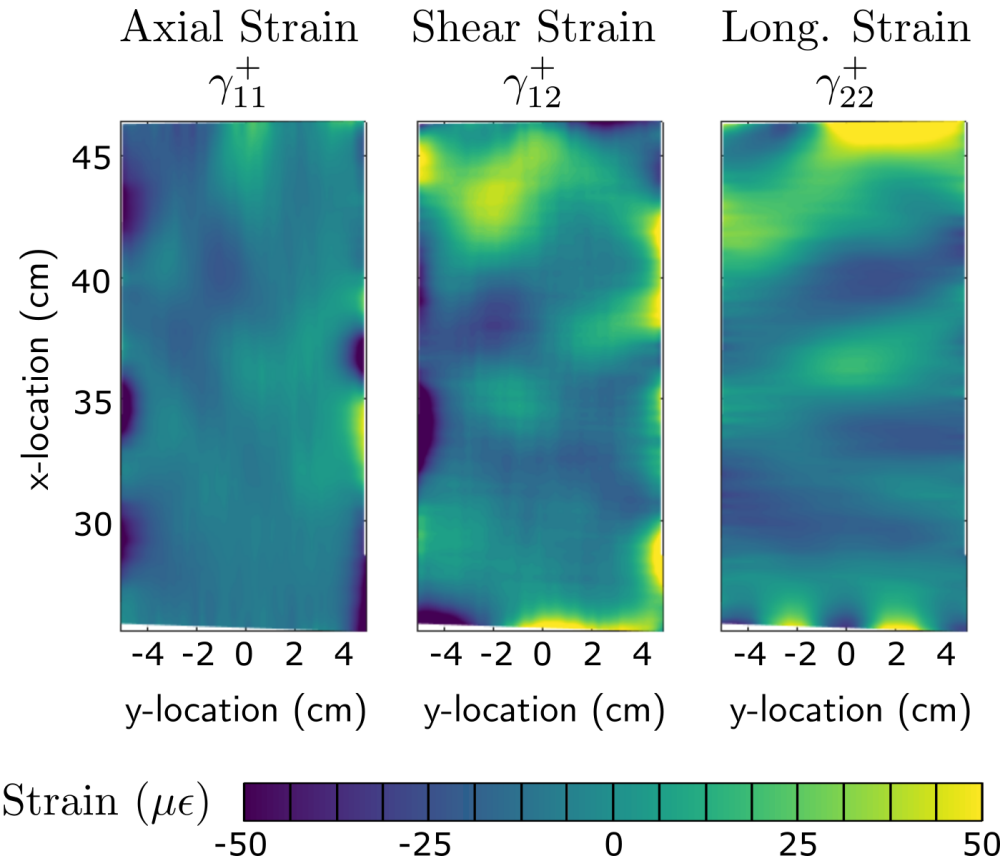

Figure 5.18: DIC strain fields from averaging images in the undeformed state, showing the random error in the DIC system.

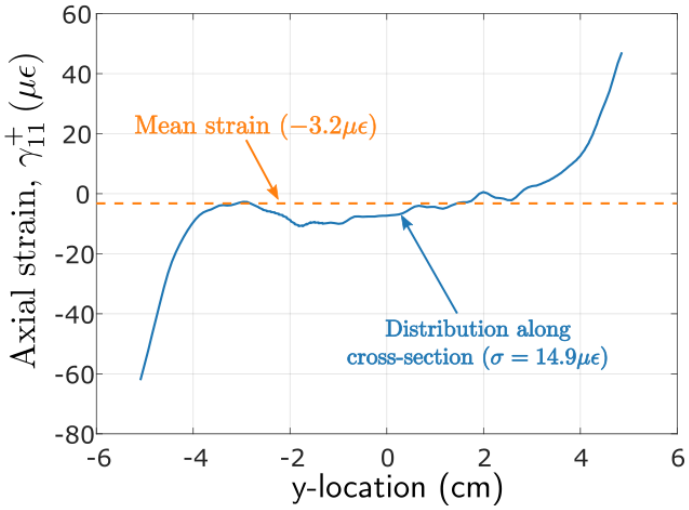

Figure 5.19: Example DIC axial strain distribution in undeformed reference image at $x = 34 \pm 0.05$ cm.

zero strains arise from random variations in the correlation process and result in a mean offset of the average strain. Since the data reduction procedure utilizes all the strain measurements at a given x-location to calculate the stiffness matrix, it is also important to take into account the variations that occur in the $\bar{b}_2$ direction (*i.e.* with respect to y), as this spread will also impact the uncertainty. Figure 5.19 shows the extracted axial strain distribution along y at $x = 34 \pm 0.05$ cm, which had a mean strain offset of -3.2 $\mu\epsilon$ and a standard deviation of 14.9 $\mu\epsilon$. These values, the mean strain offset and standard deviation of the strain along y, were then calculated for each data set generated from the undeformed reference images across all the tests, which consisted of about 1000 data sets in total. The distributions of these results are shown in Figs. 5.20 and 5.21, which can be used to provide an estimate for the 95% confidence levels on the random strain of $S_{r,\gamma^+_{\text{mean}}} = 24\mu\epsilon$ and $S_{r,\gamma^+_{\text{std}}} = 16\mu\epsilon$ for the mean strain and standard deviation along the cross-section, respectively.

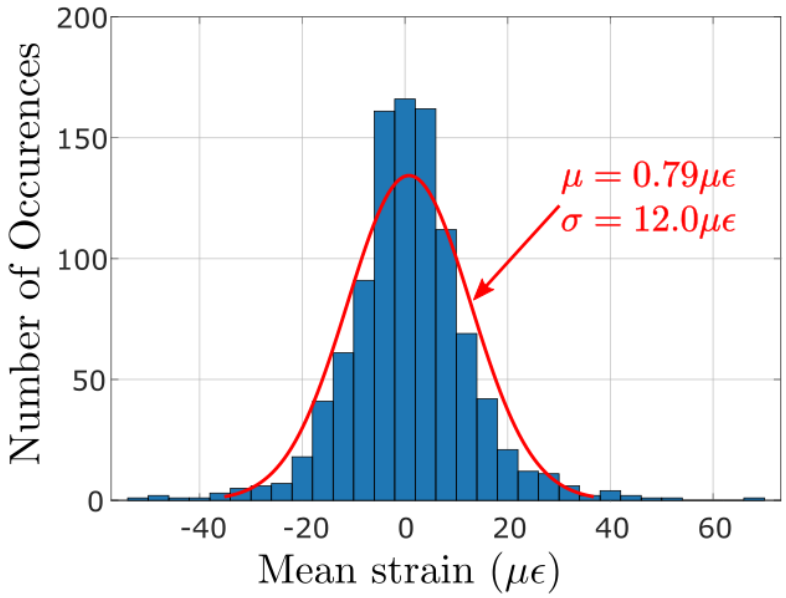

Figure 5.20: Distribution of mean strain offsets in undeformed state.

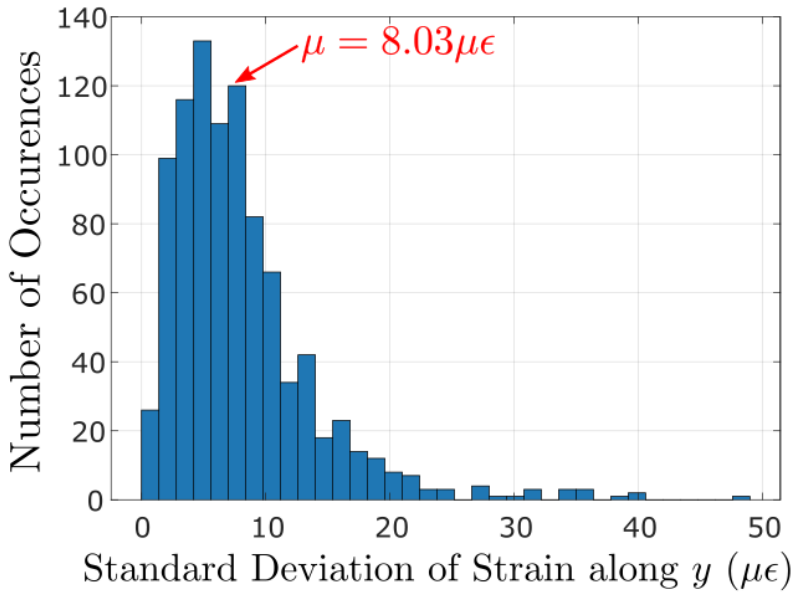

Figure 5.21: Distribution of standard deviation of y-variations in strain in the undeformed state.

5.3 Load Measurement

The other main requirement for the high-quality prediction of the stiffness properties is an accurate knowledge of the applied load. The use of pulleys, which introduce friction to the system, and winches when applying forces requires an independent means of measuring the load during each test. In addition, because the data reduction procedure needs six independent load cases to calculate the full stiffness matrix, it is necessary to be able to measure the loads under three forces (axial and two shears) and three moments (torsion and two bending). To obtain these load measurements, an ATI Omega 160 6-axis load cell, shown in Fig. 5.22, was mounted at the base of the test rig such that the reaction loads at the clamped end of the test articles could be measured. The axes of the load cell were oriented such that $\bar{\imath}_1$ was along the axis of the beams, $\bar{\imath}_2$ was along the chord or width of the beams, and $\bar{\imath}_3$ was in the thickness direction of the beams and pointed outwards towards the DIC camera setup. The load cell was nominally rated up to 6250 N in axial loading, F_1, up to 2500 N in shear, F_2 and F_3, and up to 400 N-m in torsion

and bending, M_1, M_2, and M_3. These maximum load ratings were sufficiently large to generate measureable strain levels for most of the expected test articles.

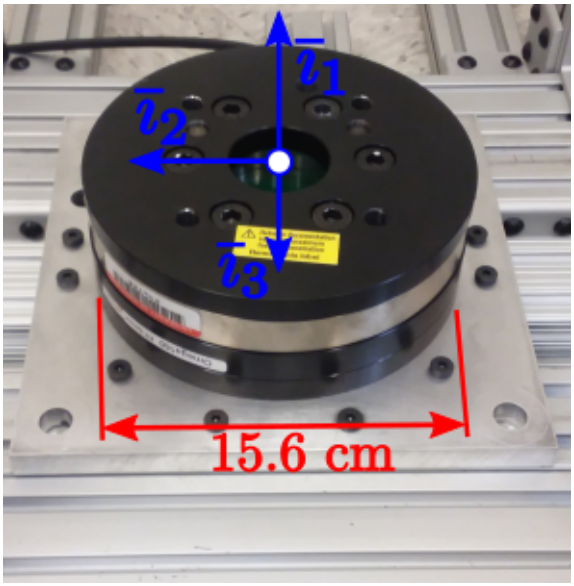

Figure 5.22: 6-axis load cell used to measure reaction loads in the test articles.

5.3.1 Load Cell Testing

In order to estimate the random error in the load cell for the uncertainty analysis, it was necessary to measure applied loads in a controlled environment where the loading condition could be defined with a high degree of accuracy. To accomplish this, the load cell was mounted horizontally on the test stand as shown in Fig. 5.23. A stiff calibration beam was attached to the load cell, which was used to apply loads through hanging weights under gravity, eliminating any friction that could be introduced through the pulley setup of the test stand. This calibration beam, shown in Fig. 5.24, had reference holes placed every 2.54 cm along the span, from 22.9 cm to 73.7 cm, to accurately define the applied bending moments. Simple testing was first performed by applying the dead weight loads in the $\bar{\imath}_3$ direction at multiple locations along the span, to generate various F_3 shear force and M_2 bending moment combinations. The entire stand and beam were then rotated by 90° and the same

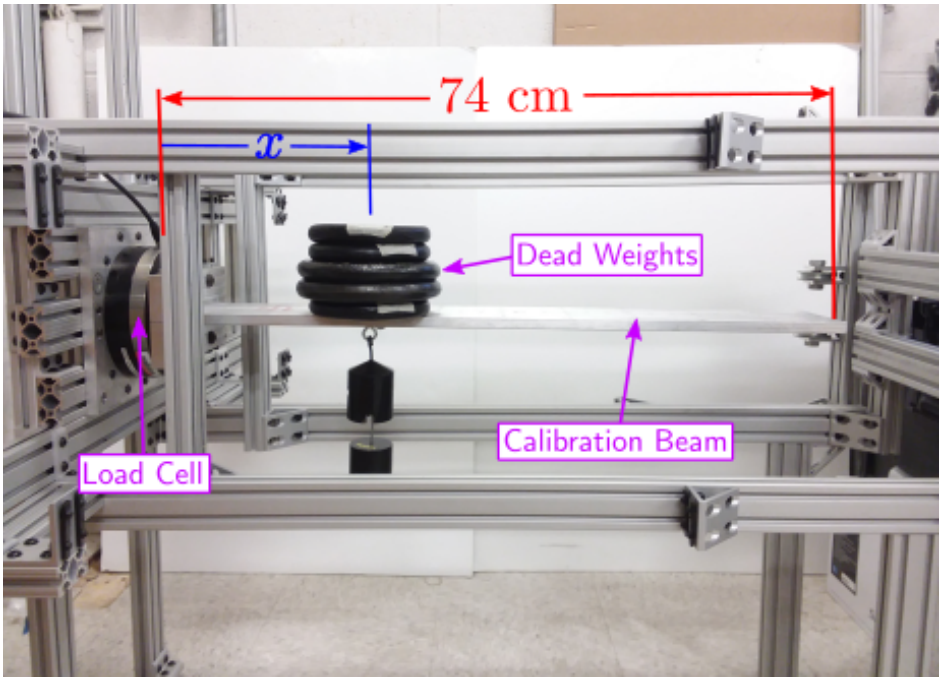

Figure 5.23: Test setup for controlled testing of the 6-axis load cell in shear and bending.

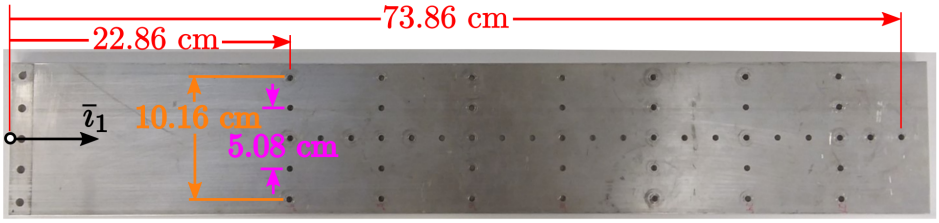

Figure 5.24: Calibration beam used for testing the load cell.

testing was performed with loads now applied in the $\bar{\imath}_2$ direction to consider the shear force F_2 and bending moment M_3. The measured forces and moments are shown in Figs. 5.25 and 5.26, respectively, for applied F_3 loads of 24.5 N, 52.5 N, 105.4 N at various distances x from the origin of the loadcell. From Fig. 5.25, it can be seen that the measured force F_3 (shown as points and dashed lines) had a linear variation with the point of application x from the load cell, despite a constant magnitude force being applied. Since the loads are applied at the tip of the beams during the actual experiments, with the beams expected to have lengths between 0.5 m and 0.75 m, the measured shear force F_3 using the initially supplied calibration could be up to 50% greater than the actually applied load, leading to unreasonable errors in

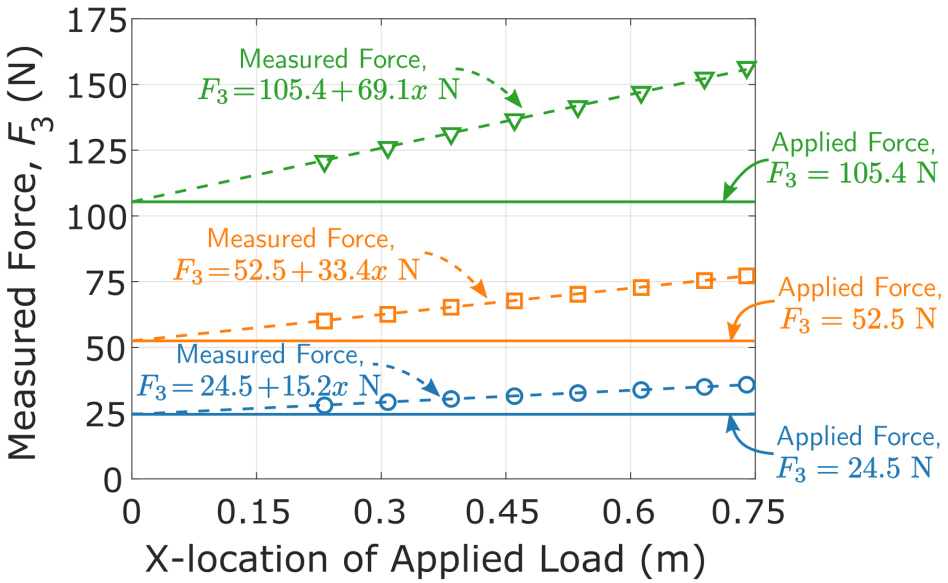

Figure 5.25: Measured force F_3 under multiple applied loads and at multiple locations from the origin of the load cell.

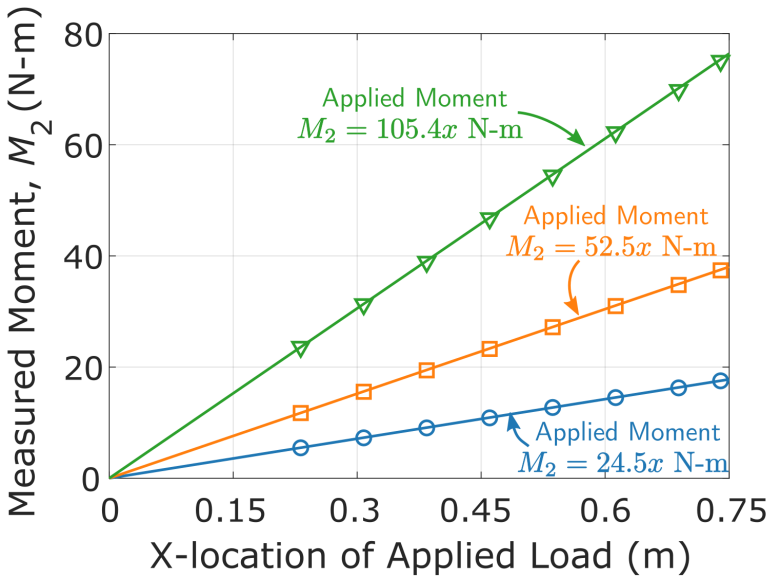

Figure 5.26: Measured moment M_2 under multiple applied loads and at multiple locations from the origin of the load cell.

its measurement. From Fig. 5.26, a linear variation in the measured moment with the point of application of the applied force was also observed; however, this linear variation is expected for a bending moment and the results showed good overall agreement with the expected moment. Similar trends were also observed when the load cell was rotated 90° to apply loads in the $\bar{\imath}_2$ direction as shown in Figs. 5.27 and

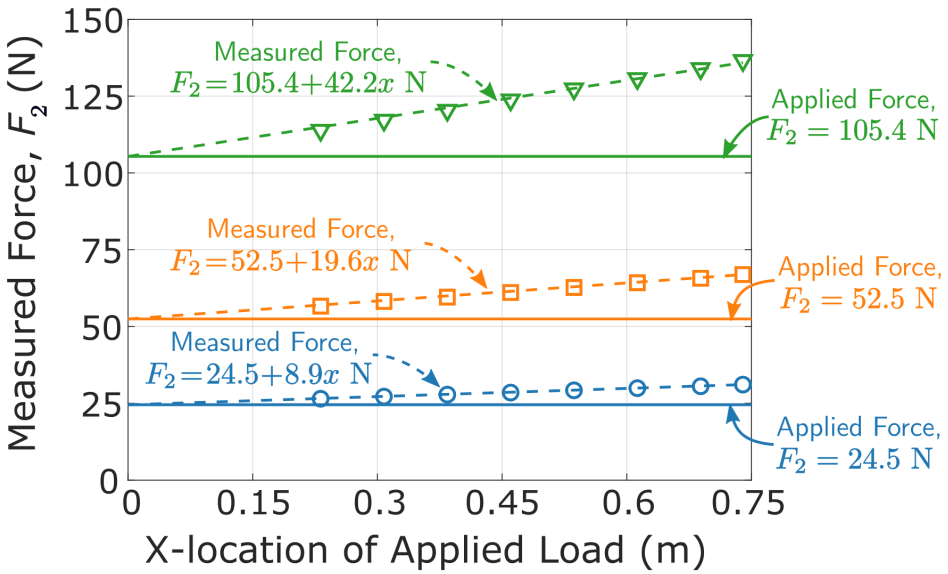

Figure 5.27: Measured force F_2 under multiple applied loads and at multiple locations from the origin of the load cell.

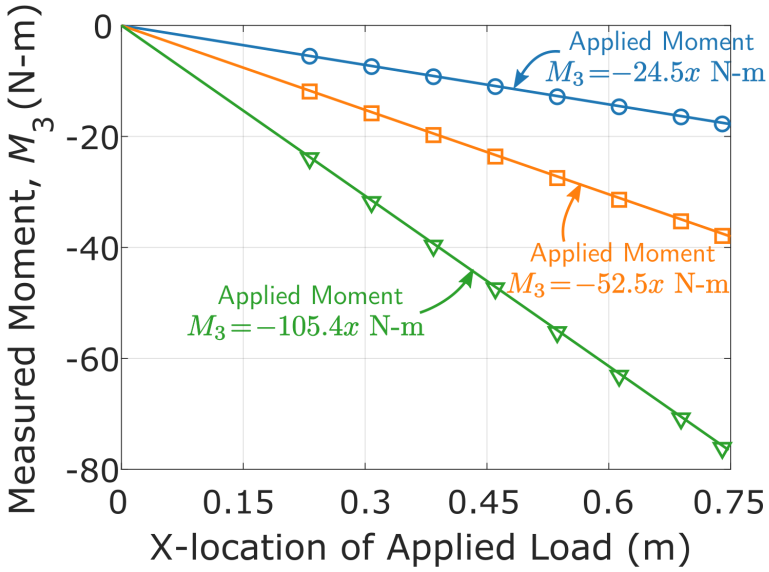

Figure 5.28: Measured moment M_3 under multiple applied loads and at multiple locations from the origin of the load cell.

5.28. The measured bending moment M_3 showed good agreement with the applied moment, while the shear force F_2 had the same erroneous linear variation with point of application, but at a smaller overall maximum error of about 30% of the expected value.

5.3.2 Load Cell Calibration

Results from simple static testing of the load cell showed significant errors in the measurements of the shear force when using the initially supplied calibration matrix. Therefore, to avoid the impact of these large errors on the shear forces in the final measurements, it was necessary to recalibrate the load cell before running the experiments. Because the load cell directly measures and outputs voltages from six internal strain gauges, the reaction loads are defined according to

$$\underline{\mathcal{F}}_m = \underline{\underline{A}}\,(\underline{V} - \underline{V}_o) \tag{5.7}$$

where $\underline{\mathcal{F}}_m = \{F_{1,m}, F_{2,m}, F_{3,m}, M_{1,m}, M_{2,m}, M_{3,m}\}^T$ are the reaction loads, $\underline{\underline{A}}$ is a 6×6 calibration matrix, and $\underline{V} = \{V_1, V_2, V_3, V_4, V_5, V_6\}^T$ are the 6 voltages output by the load cell with $\underline{V}_o$ defining the reference voltage measurements under no load. During the actual experiments, the load cell will be used to measure the reaction loads based on the measured voltages; however, in a controlled environment where the forces are generated by hanging weights of known mass, the loads can be directly calculated based on the mass and distances of application from the reference axes. Since the voltages are also being measured, Eq. (5.7) can then be used to calculate the coefficients of the calibration matrix. A single force or moment is related to the voltages through six calibration coefficients with a total of 36 coefficients required for all six loads. Therefore, to uniquely define the coefficients, it is necessary to apply at least six different non-zero loads for each of the forces and moments. Since the general purpose of this controlled testing is also to quantify the uncertainty in the force measurement, a larger number of different loads are applied and the calibration coefficients are then determined using a linear least squares fit of the data.

To calibrate the shear forces and bending moments, the same gravity loading setup shown in Fig. 5.23 was used. Forces and moments were applied in both the

positive and negative $\bar{\imath}_2$ and $\bar{\imath}_3$ directions and with small and large magnitudes to provide data over the full range of expected test loads. For the forces with a small magnitude, sets of weights ranging from 100g to 2.27 kg were combined together to generate 22 different loads from 100 g up to 10.7 kg. For larger forces and moments, sets of weights ranging from 4.54 kg to 20.4 kg were combined together to generate 12 different loads up to 700 N and bending moments up to 400 N-m. These loads were then applied at up to 28 different positions along the beam, varying the distance along $\bar{\imath}_1$ and either $\bar{\imath}_2$ or $\bar{\imath}_3$, which provided more than 3000 data points for use in the calibration. Since the voltage readings from the load cell tended to have different behavior at the smaller and larger weights and under positive and negative loads, four sets of calibration coefficients were generated for each of the shear forces and bending moments, with the recalibrated shear forces and bending moments shown in Figs. 5.29 - 5.32. In each of these plots, the measured forces and moments are normalized by their expected values, with squares used to indicate the data points used in defining the calibration coefficients and

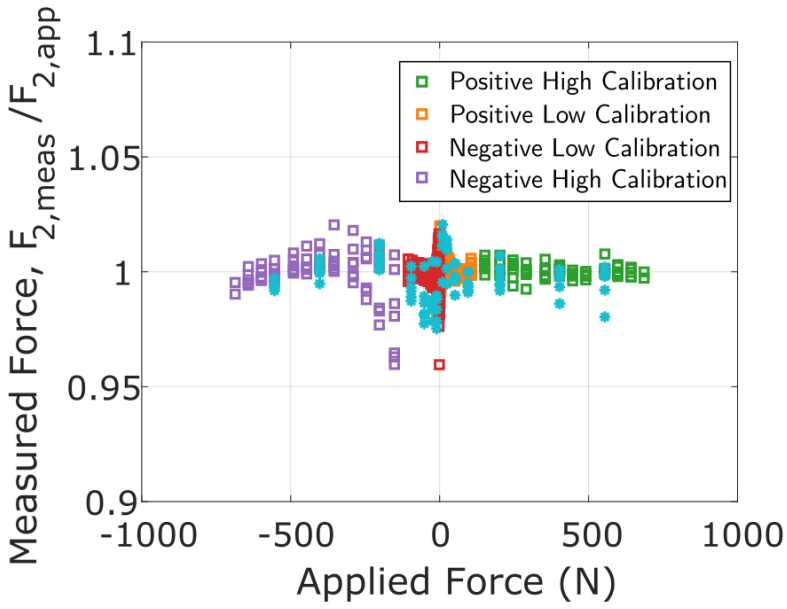

Figure 5.29: Results from static testing of the 6-axis load cell with an updated calibration under a shear force F_2.

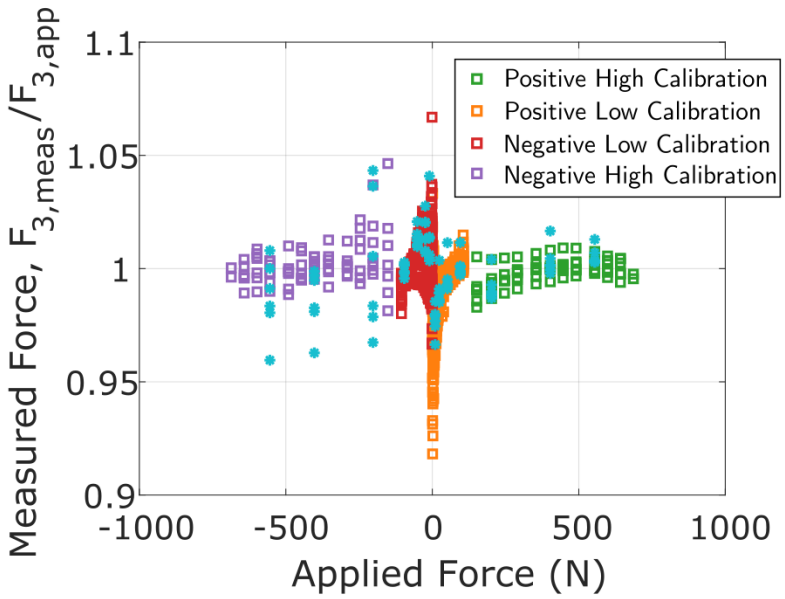

Figure 5.30: Results from static testing of the 6-axis load cell with an updated calibration under a shear force F_3.

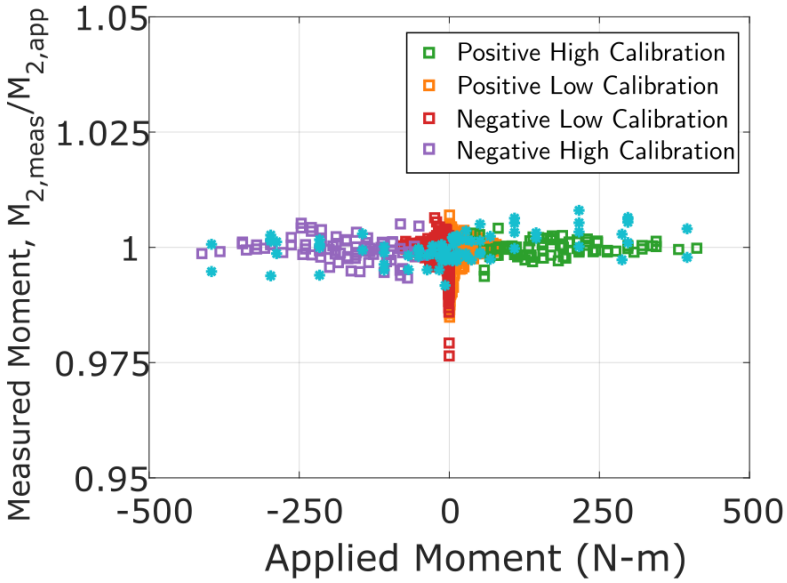

Figure 5.31: Results from static testing of the 6-axis load cell with an updated calibration under a bending moment M_2.

the different colors corresponding to the four different calibration sets. Additional data samples were then collected over subsequent days and the measured loads were calculated based on the updated calibration coefficents to ensure that these coefficients were not substantially impacted by the environmental conditions, with

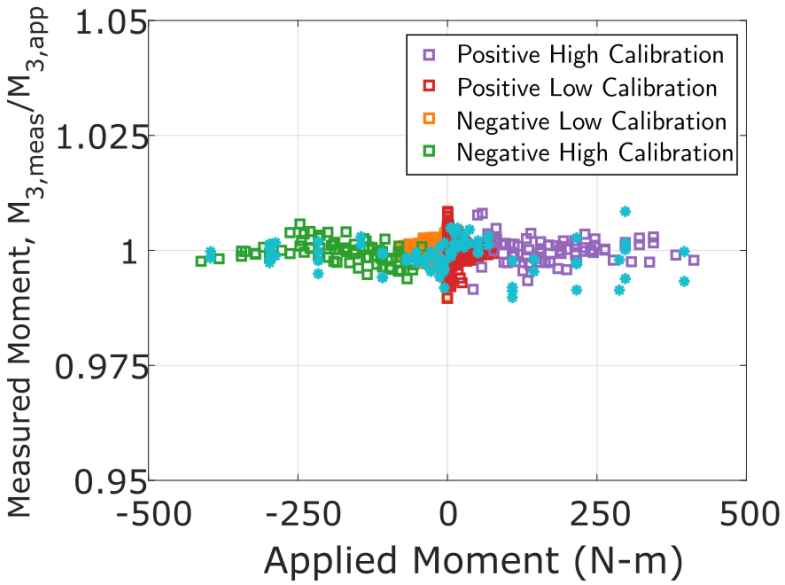

Figure 5.32: Results from static testing of the 6-axis load cell with an updated calibration under a bending moment M_3.

these measurements shown as stars. If using the initially provided calibration matrix, the shear forces exhibited errors of up to 38% and 50% of their expected values for measurements of F_2 and F_3, respectively; however, with the updated calibration matrices, almost all measurements had errors of less than 5% with most having errors under about 2%. Using this large set of measurements, the random uncertainties could then be estimated for each of the shear forces and moments, with separate confidence intervals for the low and high magnitude loads. For the low loading levels, with $|F_{2,3}| < 105$ N and $|M_{2,3}| < 60$ N-m, the 95% confidence intervals for the random uncertainty were $S_{r,F_2} = 0.0064F_2$, $S_{r,F_3} = 0.0149F_3$, $S_{r,M_2} = 0.0020M_2$, and $S_{r,M_3} = 0.0028M_3$. For the high loading levels, the 95% confidence intervals were $S_{r,F_2} = 0.0089F_2$, $S_{r,F_3} = 0.0116F_3$, $S_{r,M_2} = 0.0010M_2$, and $S_{r,M_3} = 0.0012M_3$. To estimate the bias uncertainty, two factors were taken into account. Based on manufacturing data, the bias uncertainty in the mass of the weights used to apply the loads was $S_{b,m} = 0.005m$ and the associated bias uncertainty in the applied bending moment could be estimated as $S_{b,M_i} = 0.006M_i$. In addition, at any given

load level, the average of the resulting measurements calculated from the updated calibrations generally had a small offset from the expected value. Combining these two effects, the 95% confidence intervals for the bias uncertainty could be estimated by $S_{b,F_2} = 0.0102F_2$, $S_{b,F_3} = 0.0292F_3$, $S_{b,M_2} = 0.010M_2$, and $S_{b,M_3} = 0.0095M_3$ at the low loading conditions and $S_{b,F_2} = 0.0146F_2$, $S_{b,F_3} = 0.0129F_3$, $S_{b,M_2} = 0.010M_2$, and $S_{b,M_3} = 0.011M_3$ at the high loading conditions.

To test the load cell under an axial force F_1, the setups shown in Fig. 5.33 were used. For a negative (compressive) force, the load cell was mounted in its normal orientation on the test stand with weights stacked directly on top of it as shown in Fig. 5.33(a), while for a positive (tensile) force, the load cell was mounted upside down at the top of the structure and weights were hung from a bar directly attached to the load cell as shown in Fig. 5.33(b). Since total weights of up to only 800 N could be applied, the full expected axial force range could not be tested using dead weights. However, based on the results from this testing, as shown in Fig. 5.34, it was found that the original calibration provided accurate results for the axial force over the range of applied loads, except for at sufficiently small loads ($|F_1| \lessapprox 10$ N), and a recalibration was not actually required. From these results, the random uncertainty was then estimated to be $S_{r,F_1} = 0.0087F_1$ and assumed to be the same at both the low and high loading conditions. The bias uncertainty for the axial load was taken from the manufacturer data, which gave a 95% percent confidence interval of $S_{b,F_1} = 0.0075F_1$.

Finally, to test the load cell under a torsional moment M_1, the setup from Fig. 5.23 was modified by attaching a piece of 80/20 to the calibration beam to produce a large torsional moment arm d, as shown in Fig. 5.35. More than 1000 different torsional moments, $M_1 = Wd$, were then applied by varying the weight W and moment arm d to generate loading conditions up to 250 N-m, with the results shown in Fig. 5.36. The measurements using the updated calibrations were generally

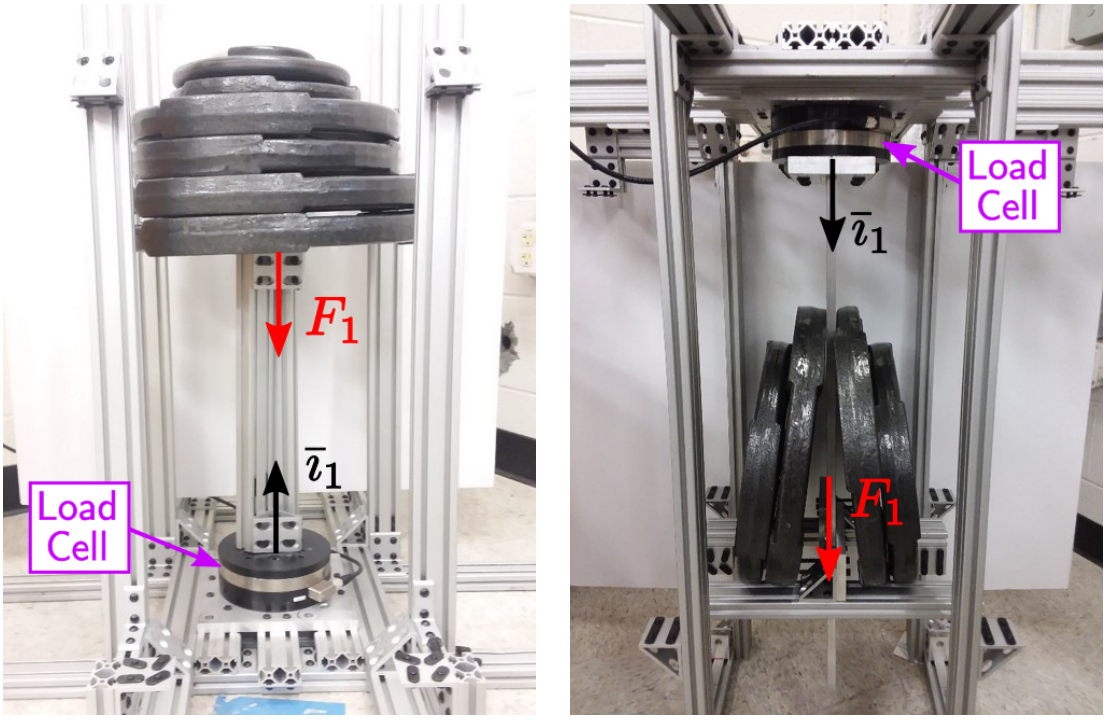

(a) Negative load (b) Positive load

Figure 5.33: Test setup for controlled testing of the 6-axis load cell under an axial force.

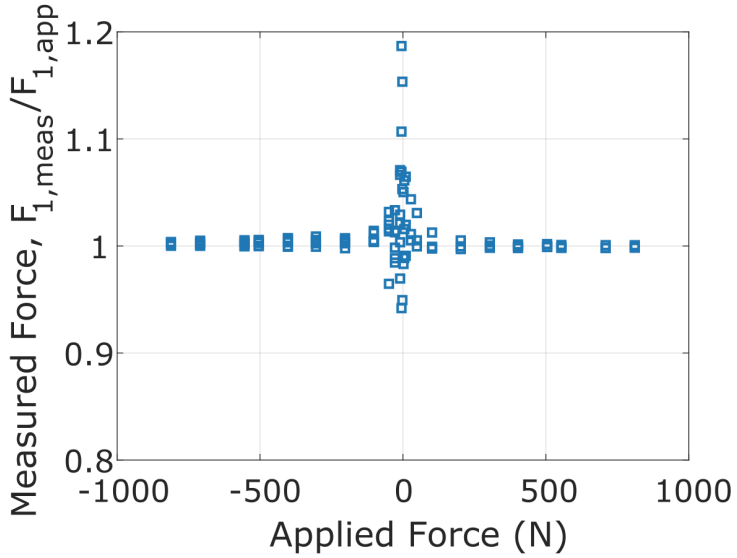

Figure 5.34: Results from static testing of the 6-axis load cell under an axial force F_1.

within 3% of their expected value, which was a significant improvement compared with the measured torsional moments from the original calibration matrix which

showed errors of up to 15%. From these results, the 95% confidence interval for the random uncertainty in the torsional moment measurement was estimated to be $S_{r,M_1} = 0.0126M_1$ for low loading cases ($|M_1| < 40$ N-m) and $S_{r,M_1} = 0.0204M_1$ for high loading cases. Similar to the case of the shear forces and bending moments, the bias uncertainty was estimated by combining the bias uncertainties in the mass and moment arm location with the mean offset of the calibrated results, to give 95% confidence intervals of $S_{b,M_1} = 0.016M_1$ for low loading cases and $S_{b,M_1} = 0.0201M_1$ for high loading cases.

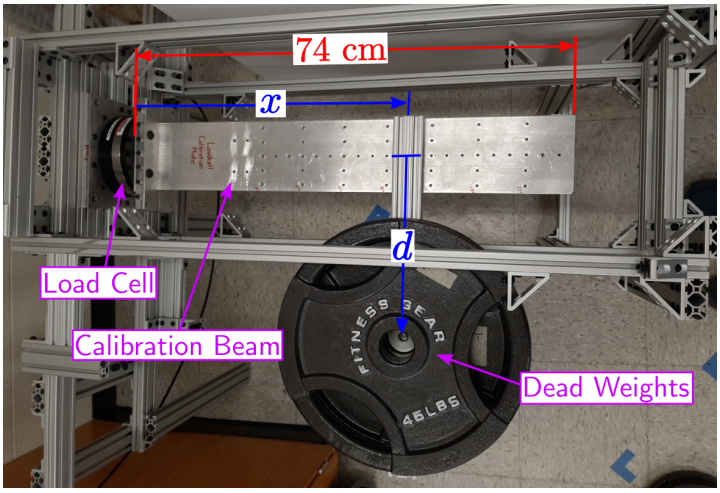

Figure 5.35: Test setup for controlled testing of the 6-axis load cell in torsion.

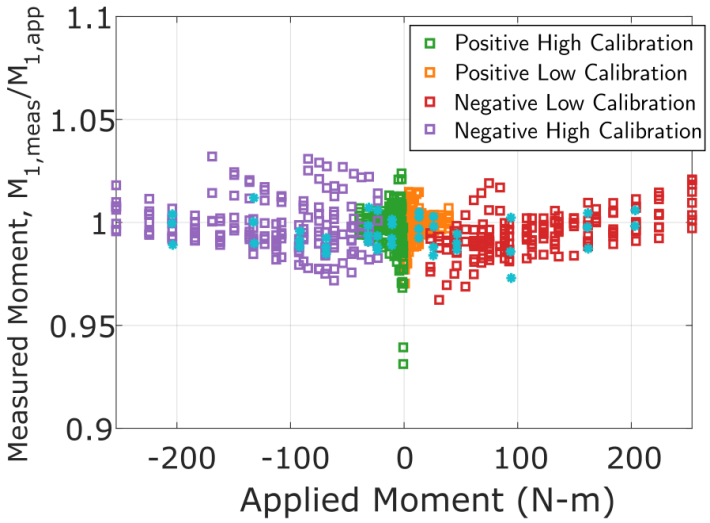

Figure 5.36: Results from static testing of the 6-axis load cell under a torsional moment M_1.

5.3.3 Sectional Load Calculation

The 6-axis load cell measures the applied loads $\underline{\mathcal{F}}_m$ at the root of the beam; however, the calculation of the sectional stiffness properties requires the sectional load vector $\underline{\mathcal{F}}_c$. The transformation of loads from the inertial frame $\mathcal{F}_I = [\mathbf{O}, \mathcal{I} = (\bar{\imath}_1, \bar{\imath}_2, \bar{\imath}_3)]$ to the local cross-sectional frame $\mathcal{F}_b = \left[\mathbf{B}, \mathcal{B} = (\bar{b}_1, \bar{b}_2, \bar{b}_3)\right]$ consists of both a translation, $\underline{r}$, and a rotation $\underline{\underline{R}}$, as shown in Fig. 5.37.

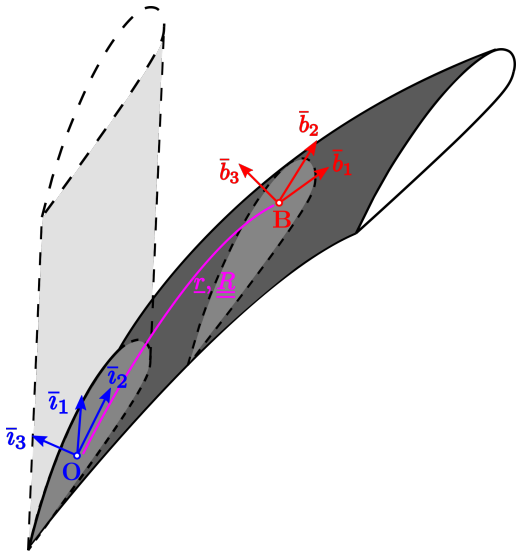

Figure 5.37: Transformation from inertial to local cross-sectional frame.

The translation, $\underline{r}$, can be written as

$$\underline{r} = \underline{r}_u + \underline{r}_d \tag{5.8}$$

with $\underline{r}_u$ denoting the translation to the cross-sectional origin in the local undeformed frame $\mathcal{F}_u = [\mathbf{A}, \mathcal{A}^+ = (\bar{a}_1, \bar{a}_2, \bar{a}_3)]$ and $\underline{r}_d$ the relative displacement of the cross-section into frame $\mathcal{F}_b$ as the beam undergoes deformation. The translation to the local undeformed frame can be written as

$$\underline{r}_u = x_u \bar{\imath}_1 + y_u \bar{\imath}_2 + z_u \bar{\imath}_3 \tag{5.9}$$

where x_u is the spanwise location of the cross-section and y_u and z_u define the offsets of the cross-sectional origin along $\bar{\imath}_2$ and $\bar{\imath}_3$, respectively, from the origin of the inertial frame in which the loads are initially measured, as shown in Fig. 5.38(a). The relative displacement is defined by

$$\underline{r}_d = u\bar{\imath}_1 + v\bar{\imath}_2 + w\bar{\imath}_3 \tag{5.10}$$

where u, v, and w are the displacements along inertial axes $\bar{\imath}_1$, $\bar{\imath}_2$, and $\bar{\imath}_3$, respectively, under the applied load, as seen in Fig. 5.38(b). The 3-D deformation fields, $u(x, y, z)$, $v(x, y, z)$, and $w(x, y, z)$, can be calculated from the DIC measurements using Eq. (5.4) and their mean values can then be used to determine the displacements of the cross-section. Since the tripod is used to manually adjust the vertical position of the cameras between image collections, there will also generally be some relative movement of the camera system between subsequent test points which needs to be taken into account. While not present in the current setup, additional lateral and out-of-plane movement of the camera system may be desired, specifically in the case where large displacements bring the beam out of the focal plane of the cameras. The relative displacements along $\bar{\imath}_1$, $\bar{\imath}_2$, and $\bar{\imath}_3$ can therefore be defined as

$$\begin{aligned} u &= \bar{u}(x_u, y, z) + u_{\text{cam}} \\ v &= \bar{v}(x_u, y, z) + v_{\text{cam}} \\ w &= \bar{w}(x_u, y, z) + w_{\text{cam}} \end{aligned} \tag{5.11}$$

where $\bar{u}(x_u, y, z)$, $\bar{v}(x_u, y, z)$, and $\bar{w}(x_u, y, z)$ are the average values of the 3-D deformation fields from DIC at the spanwise location x_u and u_{cam}, v_{cam}, and w_{cam} are the relative motion of the camera system from the initial position during image collection in the undeformed state.

Next, the rotation matrix, $\underline{\underline{R}}$, bringing the forces and moments into the local

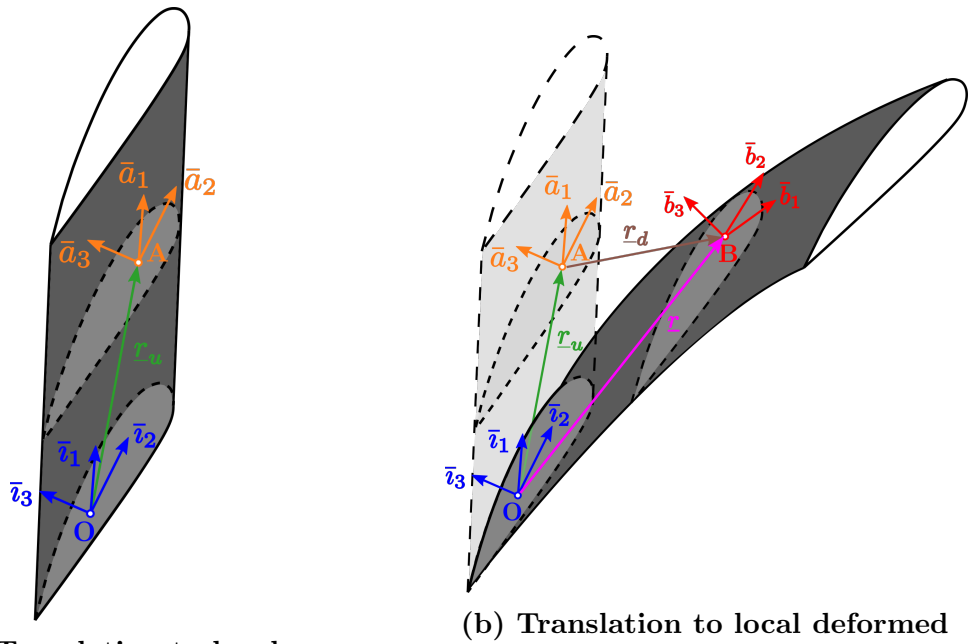

(a) Translation to local undeformed frame

(b) Translation to local deformed frame

Figure 5.38: Translation from inertial frame $\mathcal{F}_I$ to the cross-sectional frame $\mathcal{F}_b$.

cross-sectional frame $\mathcal{F}_b$ must be defined. Conventional means of defining the rotation matrix, using parameters such as Euler angles or quaternions, are not easily applied as rotation angles can not be directly measured. However, if the cross-section is assumed to remain planar after deformation and perpendicular to the elastic axis (*i.e.* no warping and no shear deformation), the rotation can be represented in terms of the beam deflections, v and w, and the elastic twist, ϕ. The rotation matrix written in terms of these parameters is

$$\underline{\underline{R}} = \begin{bmatrix} 1 - \frac{v'^2}{2} - \frac{w'^2}{2} & v' & w' \\ -v'C_\theta - w'S_\theta & \left(1 - \frac{v'^2}{2}\right) C_\theta - v'w'S_\theta & \left(1 - \frac{w'^2}{2}\right) S_\theta \\ v'S_\theta - w'C_\theta & -\left(1 - \frac{v'^2}{2}\right) S_\theta - v'w'C_\theta & \left(1 - \frac{w'^2}{2}\right) C_\theta \end{bmatrix} \tag{5.12}$$

with $()' = \partial/\partial x()$, $C_{()} = \cos()$, $S_{()} = \sin()$, and θ being the total rotation of the

cross section represented by

$$\theta = \phi + \theta_{twist} - \int_0^{x_u} w'v''dx \tag{5.13}$$

where θ_{twist} is the twist pre-built into the blade [44, 134]. Although the displacement derivatives are not a direct output from DIC, the DIC displacements are measured at a high spatial resolution of $h \approx 0.075$ cm and they can be used to numerically approximate the derivatives. Using a second order approximation, the beam slope in the flap direction is

$$w' = \frac{dw}{dx} = \frac{\bar{w}(x_u + h, y, z) - \bar{w}(x_u - h, y, z)}{2h} \tag{5.14}$$

with $\bar{w}$ denoting the average deflection of the cross-section. To maintain a second order approximation, the slopes at the lower and upper boundaries, respectively, are

$$\begin{aligned} w'(x = x_{\min}) &= \frac{4\bar{w}(x_{\min} + h, y, z) - \bar{w}(x_{\min} + 2h, y, z) - 3\bar{w}(x_{\min}, y, z)}{2h} \\ w'(x = x_{\max}) &= \frac{\bar{w}(x_{\max} - 2h, y, z) - 4\bar{w}(x_{\max} - h, y, z) + 3\bar{w}(x_{\max}, y, z)}{2h} \end{aligned} \tag{5.15}$$

The same expressions are used to approximate the beam slope in the lag direction, with all expressions for w replaced with v.

The elastic twist, ϕ, can also be calculated from the beam deflections. Since the beam deflections are defined in the inertial frame $\mathcal{F}_I$, they must first be rotated into the deformed frame using the rotation matrix from Eq. (5.12) and setting $\theta = \theta_{twist} - \int_0^{x_u} w'v''dx$, which gives

$$\begin{Bmatrix} u_c(x_u, y, z) \\ v_c(x_u, y, z) \\ w_c(x_u, y, z) \end{Bmatrix} = \underline{\underline{R}} \begin{Bmatrix} u(x_u, y, z) - \bar{u}(x_u, y, z) \\ v(x_u, y, z) - \bar{v}(x_u, y, z) \\ w(x_u, y, z) - \bar{w}(x_u, y, z) \end{Bmatrix} \tag{5.16}$$

This step is specifically important if the beam exhibits bending/torsion coupling or undergoes a combination of both bending and torsion loads. For the case of an uncoupled beam under pure torsion, this preliminary rotation matrix will become an identity matrix. The elastic twist is then defined as

$$\phi = \tan^{-1}\left(\frac{w_c(x_u, y, z)}{y + v_c(x_u, y, z)}\right) \tag{5.17}$$

With definitions for both the translation $\underline{r}$ and the rotation matrix $\underline{\underline{R}}$, the motion tensor that brings frame $\mathcal{F}_I$ into frame $\mathcal{F}_b$ is defined by

$$\underline{\underline{C}}_{\mathcal{F}} = \begin{bmatrix} \underline{\underline{R}} & \tilde{r}\underline{\underline{R}} \\ \underline{\underline{0}} & \underline{\underline{R}} \end{bmatrix} \tag{5.18}$$

and the sectional loads can be calculated from the measured loads using

$$\underline{\mathcal{F}}_c = \left(\underline{\underline{C}}_{\mathcal{F}}^T\right)^{-1} \underline{\mathcal{F}}_m \tag{5.19}$$

5.4 Test Articles

To verify the proposed data reduction procedure for the calculation of the stiffness matrix, five different test articles were considered. A prismatic aluminum beam was first manufactured with a solid rectangular cross-section. As with the numerical validation model, this beam was the simplest case for the data reduction procedure, as it should have no off-diagonal stiffness matrix components, constant properties along the span, and can be directly compared with an analytic solution. The second beam was a prismatic composite beam with a rectangular cross-section, whose ply layup orientation was tailored to introduce a bending-torsion coupling in the beam. The third and fourth test articles were composite blades, the first of which consisted only of a internal foam core and single layer of carbon-fiber on the

external surface and the second blade with an additional d-shaped spar along its leading edge. The fifth and final experimental test article was an aluminum beam with a solid rectangular cross-section, but whose width was linearly varied along the span of the beam.

5.4.1 Prismatic Aluminum Beam

The prismatic aluminum beam was the first test article considered and was made of aluminum 6061-T6, with a Young's modulus of $E = 68.9$ GPa and Poisson's ratio of $\nu = 0.33$. The beam was nominally designed to have a length of $l = 73.6$ cm, consisting of a solid rectangular cross-section with a width of $w = 10.2$ cm and a thickness of $t = 0.49$ cm as shown in Fig. 5.39. Three separate beams were manufactured to ensure that the experimental procedure was repeatable, with the final prepared samples for DIC testing shown in Fig. 5.40. The geometric parameters of these three beams were then measured at multiple locations along the span, with the average properties summarized in Table. 5.2.

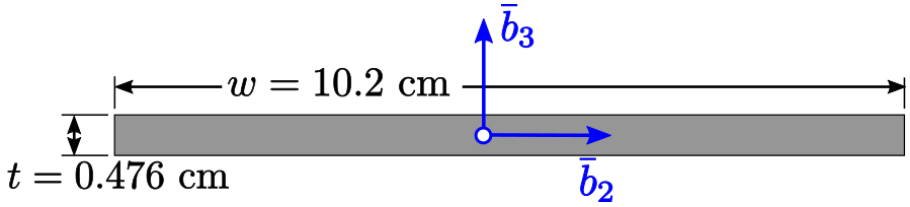

Figure 5.39: Cross-sectional geometry of prismatic aluminum beam for DIC testing.

Table 5.2: Measured geometric properties of the prismatic aluminum beams.

Parameter	Beam 1	Beam 2	Beam 3
Length, l (cm)	73.58	73.58	73.61
Width, w (cm)	10.30	10.27	10.24
Thickness, t (cm)	0.489	0.488	0.489

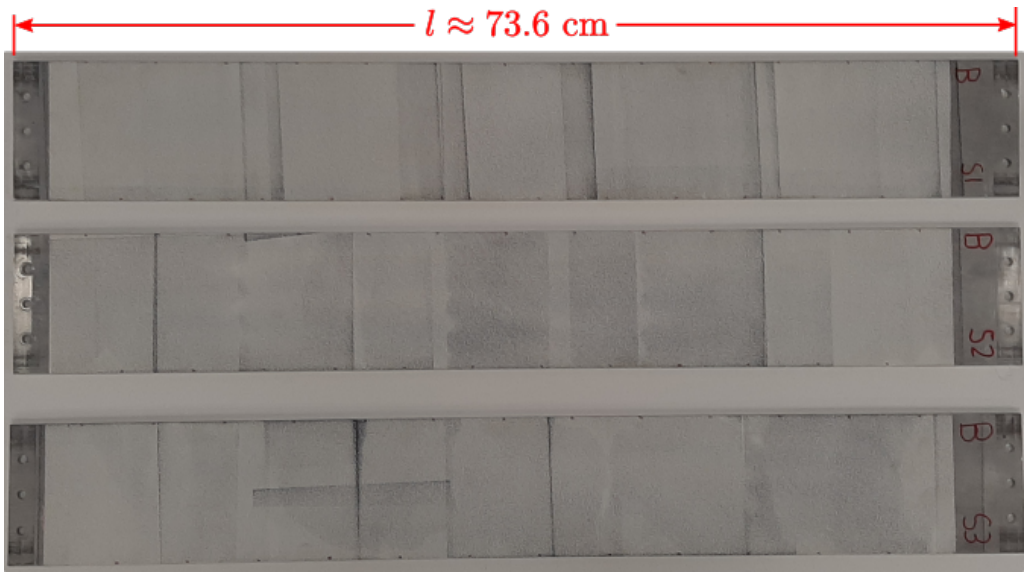

Figure 5.40: Three prismatic aluminum beams with speckle pattern applied for DIC testing.

5.4.2 Tailored Composite Beam

The next test article considered was a prismatic composite beam with a rectangular cross-section as shown in Fig. 5.41. The beam was manufactured in-house using PYROFIL^{TM} TR50S 12K uni-directional prepreg, with 16 total plies in a stacking sequence of $[-30_2^\circ/90_2^\circ/-45_2^\circ/0_2^\circ]_s$ which was selected to provide a significant bending/torsion coupling in the beam. The beam was nominally designed to have a length of $l = 71.1$ cm, with a cross-sectional width of $w = 7.62$ cm and thickness of $t = 0.244$ cm.

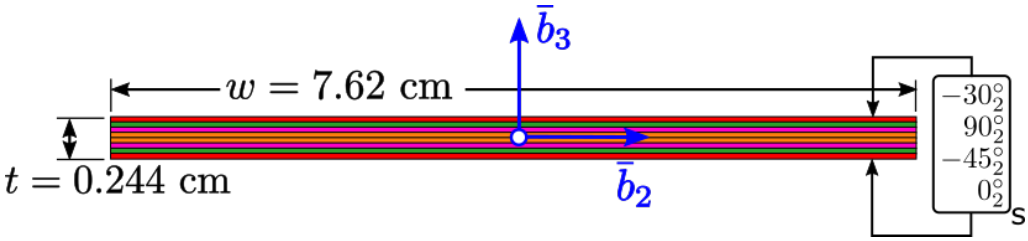

Figure 5.41: Cross-sectional geometry of prismatic aluminum beam for DIC testing.

To fabricate the beam, a simple mold consisting of two 2.54 cm thick plates was used, with the bottom plate containing a 71.8 cm by 8.00 cm cutout to a depth

of 0.244 cm. The 16 prepreg layers were cut from the roll of uni-directional prepreg, using 30 and 45 degree triangular protractors and a steel ruler to precisely cut the plies at the desired angles. The cut plies were then stacked in the $[-30_2^\circ/90_2^\circ/-45_2^\circ/0_2^\circ]_s$ sequence and wrapped with a release film to facilitate the removal of the cured beam from the mold. These main components, the mold, an individual ply, and the release film are shown in Fig. 5.42. Once the plies were assembled and wrapped in the release film, the beam was placed inside the mold, which was then sealed using 16 bolts along the outer perimeter, and cured in a mechanical convection oven by heating the oven up to 135°C (275°F), holding for 90 minutes, and then cooling. Based on this cure cycle, the average material properties provided by the vendor for the cured prepreg have Young's moduli of $E_{1^*} = 130$ GPa and $E_{2^*} = 8.68$ GPa, Poisson's ratios of $\nu_{12} = 0.28$ and $\nu_{23} = 0.33$, and shear modulus of $G_{12^*} = 4.60$

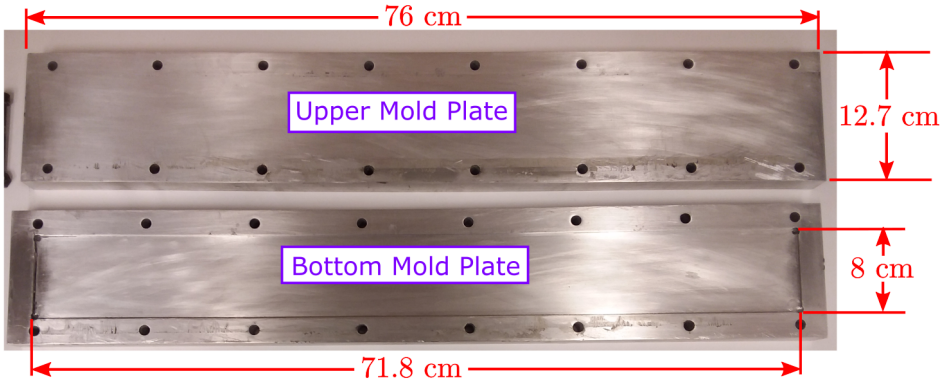

a) Composite beam mold

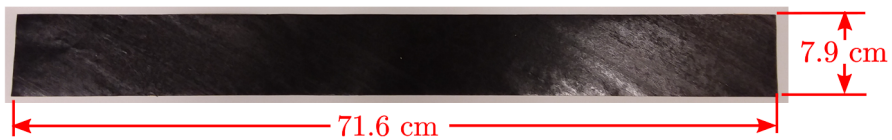

b) Individual ply of Pyrofil™ TR50S 12k prepreg

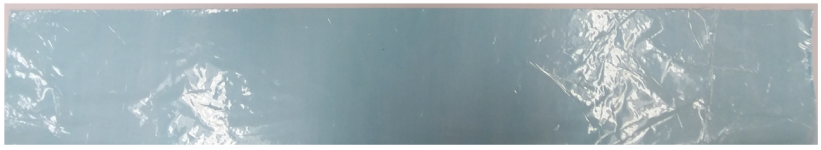

c) Release ply

Figure 5.42: Main components for manufacturing the composite beam with a rectangular cross-section.

GPa [135]. The final geometry was then machined from the cured beam, resulting in dimensions of $l = 70.9$ cm, $w = 7.62$ cm, and $t = 0.244$ cm. Once the composite beam was machined to its correct size, its surface was prepared for DIC testing with the final beam shown in Fig. 5.43.

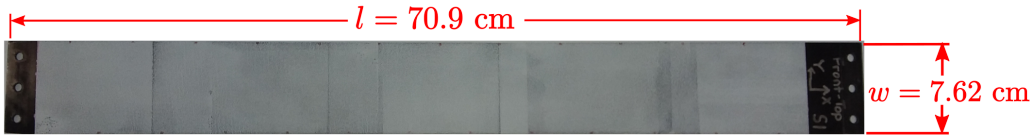

Figure 5.43: Tailored composite beam with speckle pattern applied for DIC testing.

5.4.3 VR-7 Composite Blades

The next two test articles were composite blades with a VR-7 airfoil cross-section. The first blade consisted of a ROHACELL®IG-F 31 foam core with a single ply of HEXPLY®8552 SGP196-PW prepreg wrapped around the exterior at a 45° orientation, with the cross-sectional geometry shown in Fig. 5.44(a). The second blade consisted of the same cross-sectional geometry as the first blade, but with the inclusion of an internal d-shaped spar consisting of two plies of HEXPLY®8552 SGP196-PW prepreg at a 45° orientation and extending from the airfoil leading edge to 38% of the chord, as shown in Fig. 5.44(b). Although a 45° orientation of the composite material is used, the plain weave nature of the prepreg meant that the material properties are nearly identical about $\bar{b}_1^*$ and $\bar{b}_2^*$ and no significant elastic coupling between the shear/torsion and axial/bending deformations was expected. However, due to the lack of symmetry in the cross-sectional geometry, the off-diagonal stiffness components governing the location and orientation of the principle axes of bending (K_{15}, K_{16}, and K_{56}) and the location and orientation of the principle axes of shear (K_{23}, K_{24}, and K_{34}) are all expected to be non-zero for both blades. The blades were nominally designed to have a length of $l = 53.3$ cm, with a chord of

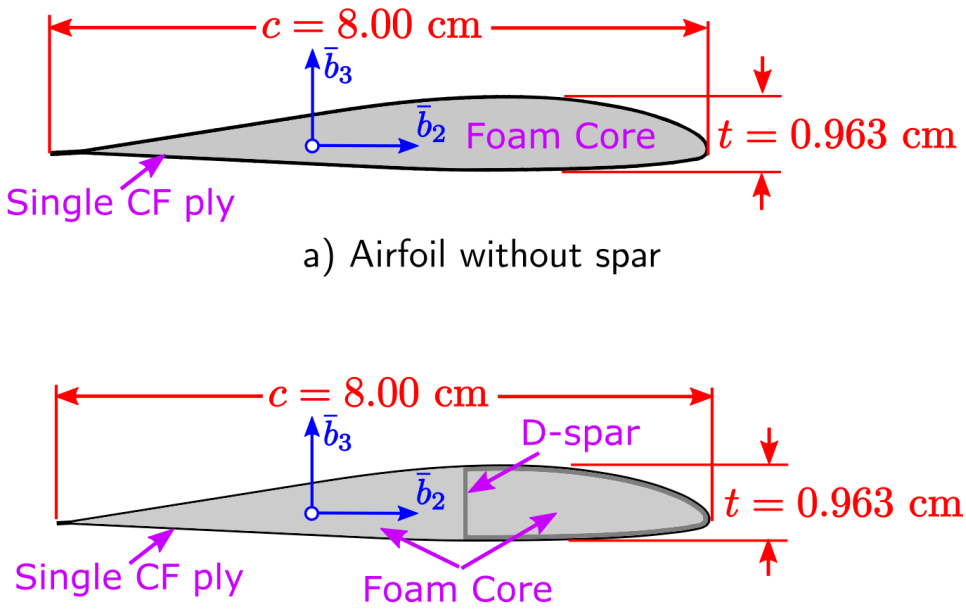

Figure 5.44: Cross-sectional geometries of the composite blades with a VR-7 airfoil.

$c = 8.00$ cm and a thickness of $t = 0.963$ cm.

To fabricate the blades, a two piece mold consisting of two 3.8 cm thick plates containing the external profile of the VR-7 airfoil was used, as shown in Fig. 5.45. A piece of ROHACELL®IG-F 31 foam was first cut into a rectangular block with dimensions of 62.2 cm × 8.75 cm × 1.25 cm. This foam block was then placed into the mold and, after clamping it closed using the 16 bolts along the outer perimeter, was then placed into the oven and heated at 175°C (350 °F) for 90 minutes to form the desired aerodynamic profile. The cooled foam was then removed from the mold and trimmed to a 7.6 cm chord by removing the portion of the foam at the trailing edge tab. For the blade with a d-spar, a 1/16 in. end mill was used to cut the foam at 0.38% of the finished blade chord (3.04 cm from the leading edge). Each piece of foam was then wrapped with a layer of Cytec 300®film adhesive to prevent any bleeding of the resin from the prepreg into the foam.

After the foam was formed to the desired shape and wrapped in the adhesive,

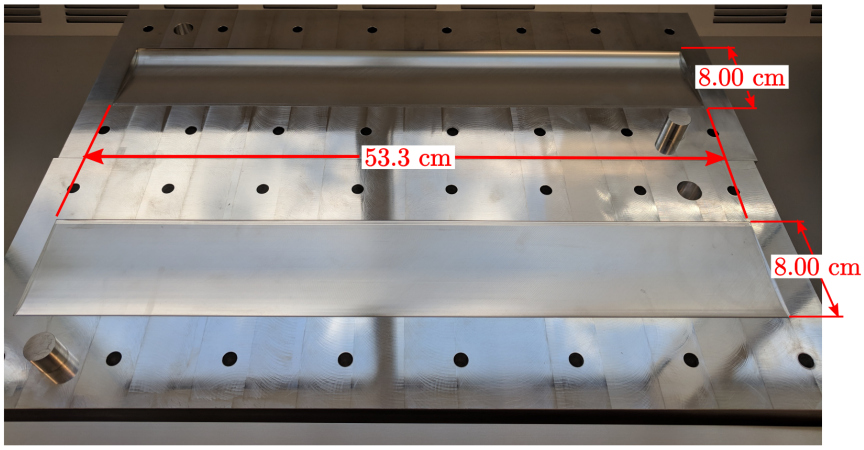

Figure 5.45: Mold used to manufacturing the composite blades with a VR-7 airfoil.

a rectangular aluminum 7075 insert of 5.61 cm in length was machined to the shape of the airfoil near the 1/4 chord to strengthen the blade at the root and tip for transferring loads during testing. For the first blade, two 14.3 cm × 5.61 cm sections of HEXPLY®8552 SGP196-PW prepreg were cut at a 45° orientation to create a d-shaped spar over these inserts, extending only over the first 5.61 cm at both ends of the blade. The remainder of the blade, where the measurements were made, was left as a single piece of foam with no spar. For the second blade a single section of 53.3 × 14.3 cm was cut from the prepreg at a 45° orientation to wrap around the leading edge foam block to form the d-shaped spar that extended along the entire length of the blade. For both blades, a 54 cm × 20.3 cm section of the prepreg was then cut at a 45° orientation and wrapped around the main internal components, starting from the trailing edge up over the leading edge and back to the trailing edge to maintain a smooth aerodynamic profile at the leading edge and avoid potential delamination issues. Any excess material was then trimmed from the trailing edge and the outer layer of the prepreg was then smoothed out using a roller to eliminate any wrinkles or air bubbles, wrapped in a layer of release ply, and placed inside the mold. Once the mold was clamped shut, it was set in the oven to cure at 175°C (350 °F) for 150 minutes and left to cool down. Based on this cure cycle, the average material

properties provided by the vendor for the cured prepreg have Young's moduli of $E_1 = 84.8$ GPa and $E_2 = 79.9$ GPa, Poisson's ratios of $\nu_{12} = 0.30$ and $\nu_{23} = 0.34$, and shear modulus of $G_{12} = 5.60$ GPa [136]. The cured blades were then removed from the mold and trimmed to a length of $l = 53.3$ cm and chord of $c = 8.00$ cm, with the final prepared blades shown in Fig. 5.46. For the blade with only an internal foam core, the maximum thickness was measured at $t = 0.977$ cm, which was about 1.5% larger than the expected thickness. For the blade with the d-shaped spar along its entire span, the additional internal component resulted in a larger measured thickness of $t = 1.001$ cm, which was about 4% larger than the expected thickness.

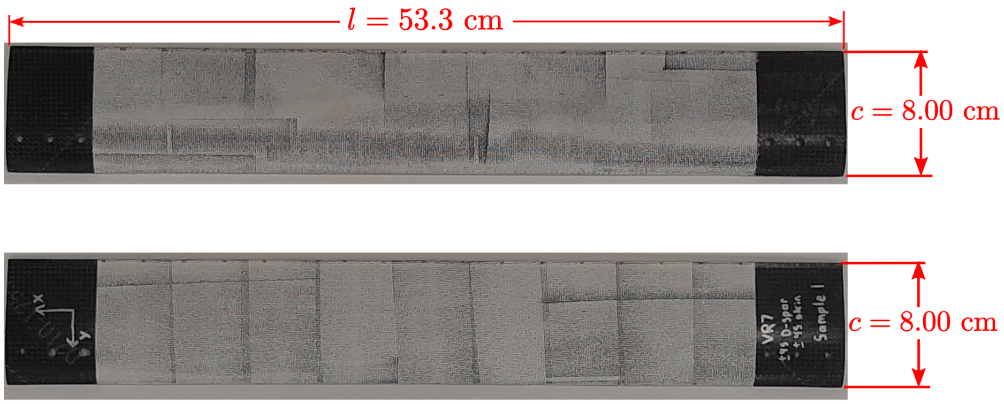

Figure 5.46: Two composite blades with speckle patterns applied for DIC testing.

5.4.4 Tapered Aluminum Beam

The final test article was an isotropic beam made of aluminum 6061-T6 ($E = 68.9$ and $\nu = 0.33$) with a linearly varying width along the span. This beam was designed to experimentally verify the ability of the data reduction procedure to measure spanwise variations in properties. The overall length of the beam was nominally $l = 71.1$ cm, with the beam having a rectangular cross-section with a constant thickness of $t = 0.79$ cm. The beam had a constant cross-sectional width of $w = 7.62$ cm from the root up to $x = 2.54$ cm which was then linearly decreased

down to $w = 3.81$ cm at $x = 34.3$ cm from the root. The width remained constant at $w = 3.81$ cm up to $x = 36.8$ cm and then was linearly increased back up to a width of $w = 7.62$ cm at $x = 68.6$ cm from the root, to produce a symmetric profile about the mid-span. This bi-linear taper was machined out of an aluminum 6061-T6 rectangular block using a CNC mill, with the final prepared sample shown in Fig. 5.47.

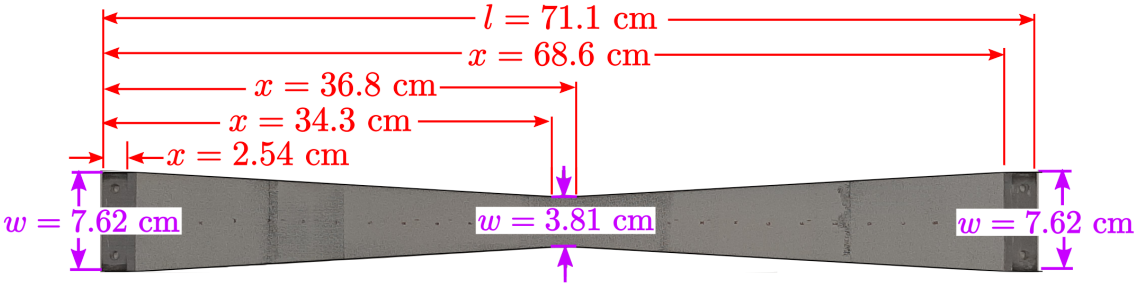

Figure 5.47: Tailored composite beam with speckle pattern applied for DIC testing.

5.5 Summary and Conclusions

The design of an experimental test rig for making the strain and load measurements required to calculate the sectional stiffness matrices was described in this chapter. For the strain measurements, an optical technique, digital image correlation (DIC), is used, with the sample preparation and system calibration first discussed, as these are key factors for obtaining accurate measurements. The DIC analysis and the data extraction process are then highlighted to indicate the required steps for getting the strain and displacement measurements in a form that can be readily used in the data reduction algorithm. A simple test case of a cylindrical tube under torsion was evaluated to ensure that the DIC setup could accurately calculate strains on a highly curved surface. Additional testing was done by applying rigid body motion to the system, to verify that the DIC software could accurately filter out the rigid body motion and produce the expected state of zero strain. The discussion of the DIC

setup concluded with the quantification of the expected uncertainty levels for the strain measurements.

This was followed by a discussion of the load measurement, which was done using a 6-axis load cell mounted at the base of the test stand to measure the reaction forces and moments under applied loading. Significant errors in the shear force measurements based on the original calibration matrix were identified and a rigorous calibration of the load cell was then performed to reduce these errors. Based on the calibration testing under a large number of applied load cases, the systematic and random uncertainties in the loads could be estimated, with most expected errors less than 2%. Since the data reduction procedure requires the sectional loads while the load cell measures the reaction loads, the necessary steps to calculate the sectional loads based on the reaction loads was discussed.

The chapter concluded with a discussion of five different beams fabricated for the experimental testing. Three prismatic aluminum beams were first made, to provide a simple validation case and assess the repeatability of the measurements. A composite beam was then manufactured, with the ply layup tailored to produce significant bending/torsion coupling. Two composite airfoils were then also manufactured with the same external profile but differing internal structure to study the impact of the internal components on the stiffness measurement. An additional aluminum beam was then made with a linearly varying width along its span to verify the capability to measure spanwise variations in properties using the proposed strain-based methodology.

Chapter 6: Experimental Results

This chapter presents the experimental results for the stiffness measurements of the five prepared test articles. For all beams, the spanwise distributions of properties are measured with the detailed uncertainty analysis applied to the measurements. For beams with uniform properties along the span, the average properties are calculated and compared directly with numerical predictions.

6.1 Prismatic Aluminum Beam

For the aluminum beam, the test envelope of anticipated applied loads and maximum expected strains is summarized in Table 6.1. For all but the axial load case, both a positive and negative load were applied to provide a redundant set of data. In the axial load case, the maximum achievable load was limited by the saturation limit of the load cell. A compressive (negative) load was not applied, as the buckling limit was estimated at about 330 N (75 lb), which would only produce a maximum expected strain of 9 $\mu\epsilon$. Both the lag shear and lag bending loads were limited by the maximum rating of the load cell. For the flap shear and flap bending loads, the maximum load was limited by the large deflections that started to bring the upper portion of the beam out of focus in the camera. For the torsional load, no specific limitations were observed, and the load was selected to achieve a desirable strain of about 4000 $\mu\epsilon$.

Table 6.1: Applied load cases for the aluminum test articles.

Test #	Load case	Applied Tip Load	Expected Strain, $\max\{\lvert\underline{\gamma}\rvert\}$
1	Axial	$F_1 = +6250$ N	187 $\mu\epsilon$
2,3	Lag Shear	$F_2 = \pm 670$ N	740 $\mu\epsilon$
4,5	Flap Shear	$F_3 = \pm 89$ N	2200 $\mu\epsilon$
6,7	Torsion	$M_1 = \pm 80$ N-m	4000 $\mu\epsilon$
8,9	Flap Bending	$M_2 = \pm 49$ N-m	1853 $\mu\epsilon$
10,11	Lag Bending	$M_3 = \pm 450$ N-m	778 $\mu\epsilon$

6.1.1 DIC measurements

To maximize the amount of DIC data that could be collected along the span, images were taken at three different locations by adjusting the height of the cameras on the tripod. These three image sets are denoted by image sets 1, 2, and 3, with image set 1 collecting data from 5.24 cm to 27.3 cm along the span, image set 2 collecting data from 15.9 cm to 37.5 cm along the span, and image set 3 collecting data from 26.1 cm to 47.6 cm along the span. All together, this amounted to data provided over a total length of 39.4 cm with significant portions of the span captured by multiple image sets. An example set of results are shown in Fig. 6.1 for the axial strain γ_{11}^{+} measured by the DIC system for all three image sets on both the $z = +h/2$ and $z = -h/2$ faces under a positive flap bending load $M_3 = 49$ N-m. From these results, variations of about 300 $\mu\epsilon$ are observed when moving from a spanwise location of $x = 10$ cm to a spanwise location of $x = 40$ cm. However, while a pure flap bending moment was desired, the load cell also measured a shear force $F_3 \approx 20$ N, which generated a linear variation in the bending moment along the span and accounted for most of the observed variation in the axial strain distribution. This illustrated the importance of being able to directly measure all of the reaction loads, as the desired load condition may not be able to be applied exactly.

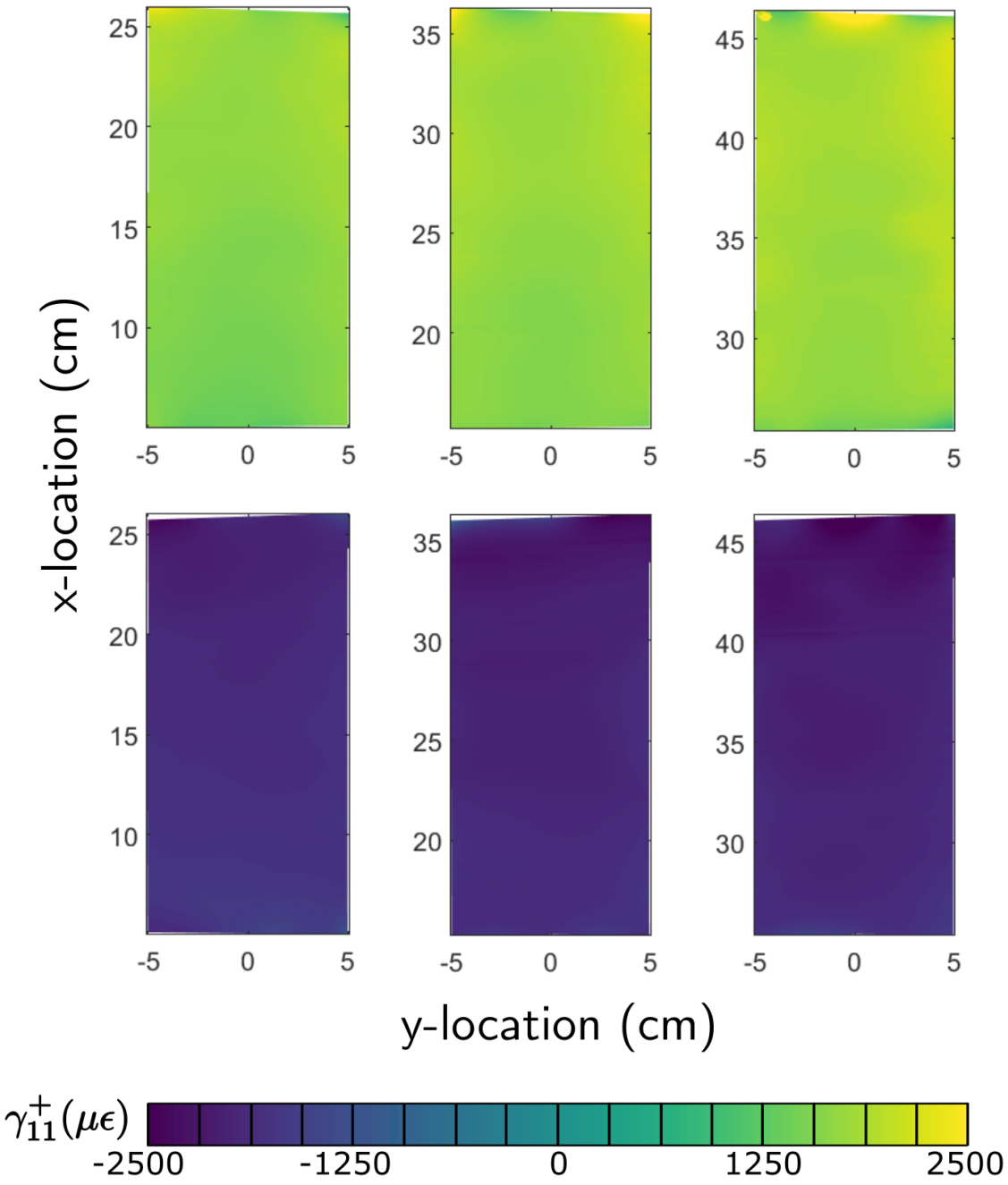

Figure 6.1: Axial strain γ_{11}^{+} under a positive flap bending moment (load case 8). The upper row of images shows the strain on the $z = +h/2$ face and the bottom row shows the strain on the $z = -h/2$ face.

6.1.2 Stiffness Matrix Calculation

DIC measurements were then obtained for the remaining load cases and the strain data was extracted at every 0.64 cm along the span using the procedures discussed in Sec. 5.2. These extracted measurements were then combined with the calculated sectional loads to evaluate the spanwise distributions of the stiffness properties, with the results for the axial, lag shear, torsional, flap bending, and lag bending components of the three beams shown in Figs. 6.2 - 6.6, respectively. For all plots, the results from the three tested beams are shown as points (○,□,▽) with error bars representing the 95% confidence levels based on the expected measurement uncertainties. The analytic solutions were also calculated using Eqs. (3.1-3.3) and shown as solid lines for reference. Since measurements were not able to be performed on the through-thickness faces due to the small thickness of the beam, no data was obtained for measuring the flap shear stiffness component K_{33}.

For both the axial and lag shear stiffness shown in Figs. 6.2 and 6.3, respectively, the average uncertainty levels were fairly large due to the small strains under their corresponding load cases, with about 12% and 23% uncertainty levels for the axial and lag shear stiffness, respectively. While the uncertainty in the axial stiffness could be significantly reduced if a much larger axial load were applied, this is not feasible in the current setup due to the maximum ratings of the load cell. For the lag shear stiffness, the uncertainty level could be reduced by applying a larger lag shear force; however, the maximum appliable shear force is primarily constrained by the bending moment it generates at the root and therefore a substantially larger shear force would not be possible. Despite the large uncertainty levels in both stiffness properties, the results for all three beams showed good agreement with one another and the reference analytic solution. For the lag shear stiffness, the effect of the clamped boundary condition on the shear strain distribution can be seen up to about

15 cm away from the root of the beam, resulting in an increase in the measured shear stiffness in this region.

For the torsional stiffness shown in Fig. 6.4, nearly perfect agreement was observed between all three beams and the predicted stiffness. This great agreement can be largely contributed to the large generated shear strain under the torsional moment; however, the numerical warping field also accounted for a correction factor of nearly 50%, due to the relatively small thickness of the beam, and therefore also significantly contributed to reducing any errors in the measurement. The flap bending stiffness, shown in Fig. 6.5, also showed good correlation across the tests, but did exhibit an increase in the calculated properties at spanwise locations above about 40 cm. At these spanwise locations, the displacement under the flap bending loads tended to bring the beam near the edges of the depth of field of the cameras, and likely introduced additional noise into the measurement that could not be easily accounted for in the uncertainty analysis. For the lag bending stiffness shown in Fig 6.6, the measured results remained fairly constant along most of the span; however, these measurements were about 10% below the predicted value.

Since these aluminum beams had a constant cross-sectional geometry along their span, the average values of the stiffness can also be used to provide a direct comparison across the three test articles, with the calculated average values compared in Table 6.2. Overall, the average torsional and flap bending stiffness values, K_{44} and K_{55}, respectively, showed excellent agreement with the analytic solution, with differences all less than 1.5%. The average measured axial stiffness K_{11} was between 2.4% and 4.5% greater than the analytic solution and the average lag bending stiffness K_{66} was between 6% and 11% lower than the analytic prediction. For the lag shear stiffness K_{22}, the average measured values were calculated over the spanwise locations from 15.3 cm up to 45.7 cm to eliminate the initial increase in stiffness resulting from the strain concentrations near the root. Within this region, the average shear

stiffness showed good agreement within 13% of the predicted value.

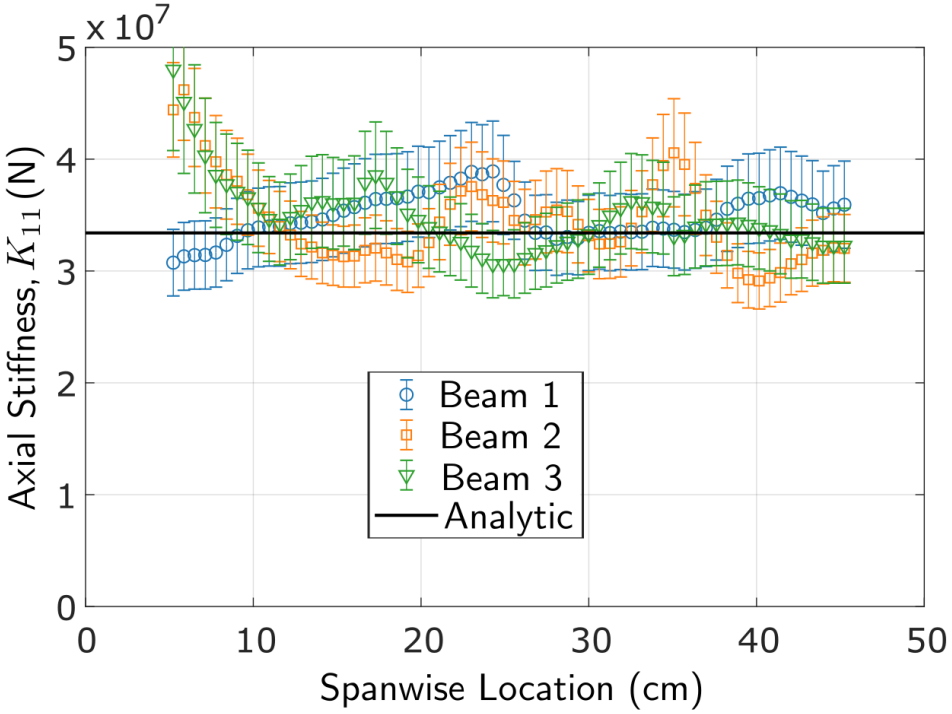

Figure 6.2: Axial stiffness K_{11} measurements for the three prismatic aluminum beams.

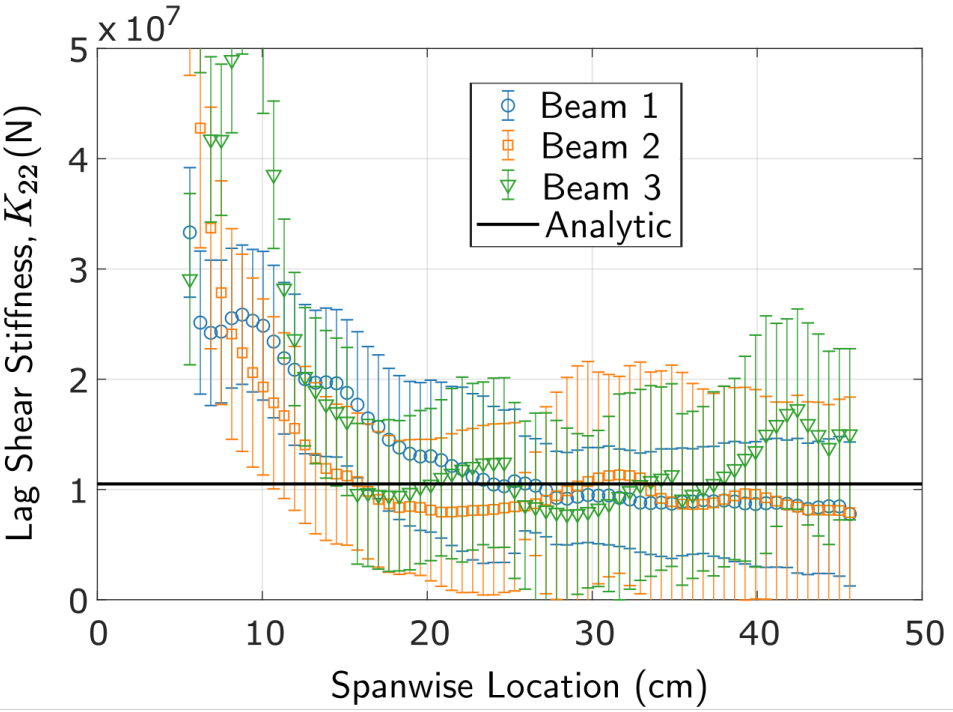

Figure 6.3: Lag shear stiffness K_{22} measurements for the three prismatic aluminum beams.

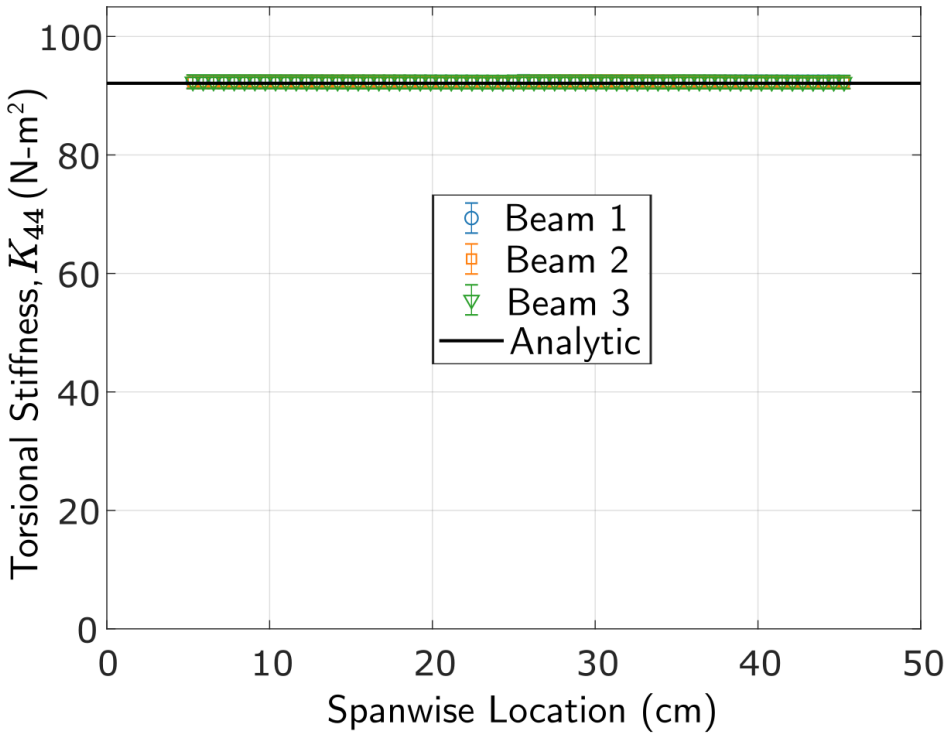

Figure 6.4: Torsional stiffness K_{44} measurements for the three prismatic aluminum beams.

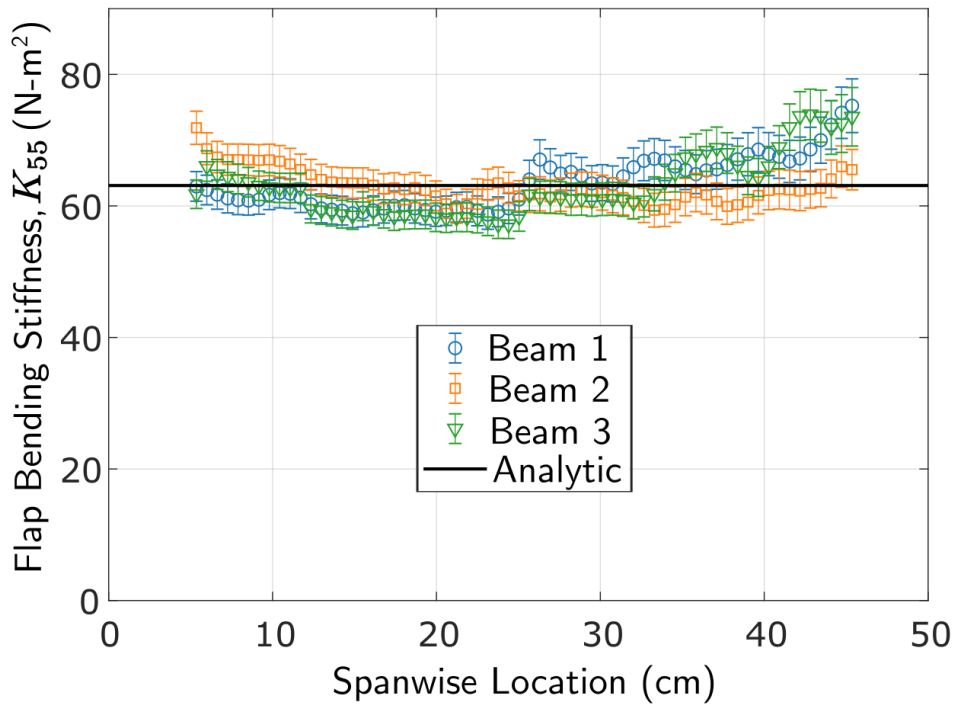

Figure 6.5: Flap bending stiffness K_{55} measurements for the three prismatic aluminum beams.

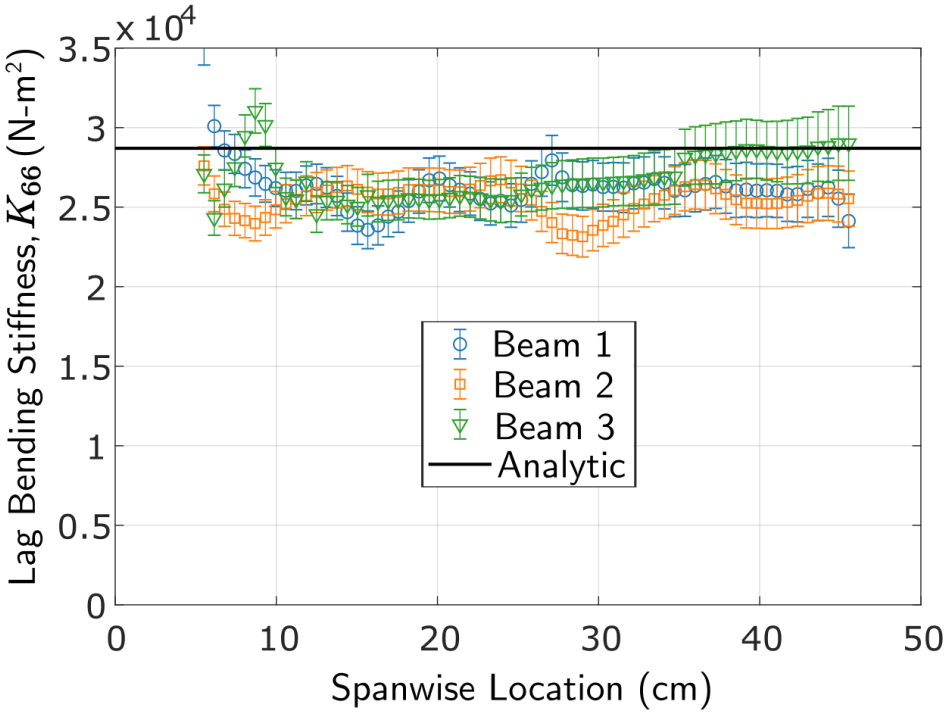

Figure 6.6: Lag bending stiffness K_{66} measurements for the three prismatic aluminum beams.

Table 6.2: Average measured stiffness values of the three aluminum test articles.

Stiffness term	Analytic	Beam 1	Beam 2	Beam 3
K_{11}, N	3.34×10^7	3.49×10^7	3.44×10^7	3.42×10^7
K_{22}, N	1.05×10^7	1.00×10^7	9.15×10^6	1.12×10^7
K_{44}, N-m^2	92.1	92.3	92.3	92.3
K_{55}, N-m^2	63.1	63.6	62.6	63.0
K_{66}, N-m^2	2.87×10^4	2.63×10^4	2.55×10^4	2.69×10^4

6.1.3 Comparison to other methods

In addition to the strain measurements, the DIC setup also directly measures the detailed 3-D displacement fields. These displacements can be used to directly

calculate the bending stiffness under a flap and lag shear load according to

$$K_{55} = \frac{F_3 x^2 (3l - x)}{6z} \tag{6.1a}$$

$$K_{66} = \frac{F_2 x^2 (3l - x)}{6y} \tag{6.1b}$$

where the clamped boundary condition was used to generate these expressions. Because the DIC measurements also generate data at a sufficiently high resolution along the span, the bending slopes can be approximated numerically and used to compare with a rotation-based method. For the clamped-free setup used in these tests, the flap bending and lag bending stiffness values can be calculated along the span according to

$$K_{55} = -\frac{F_3 x (2l - x)}{2w'} \tag{6.2a}$$

$$K_{66} = \frac{F_2 x (3l - x)}{2v'} \tag{6.2b}$$

where w' is the numerical approximation of the flap bending slope and v' is the numerical approximation of the lag bending slope.

The bending stiffness values from the displacement and rotation based methods were then calculated from Eqs. (6.1) and (6.2), respectively, with their measured values shown in Figs. 6.7 and 6.8. The results were also compared with the results from the current strain-based methodology, with the bending stiffness values from all three beams averaged for each method and normalized by the analytic solution. For the flap bending stiffness, shown in Fig. 6.7, the average value calculated from the displacement method was 54.8 N-m^2, which was 86.9% of the predicted value of 63.1 N-m^2. When using the slope method, the average calculated stiffness increased to 58.1 N-m^2, which was still only 92.1% of the predicted value. From the observed spanwise variations for both the displacement and rotation measurements, the flap

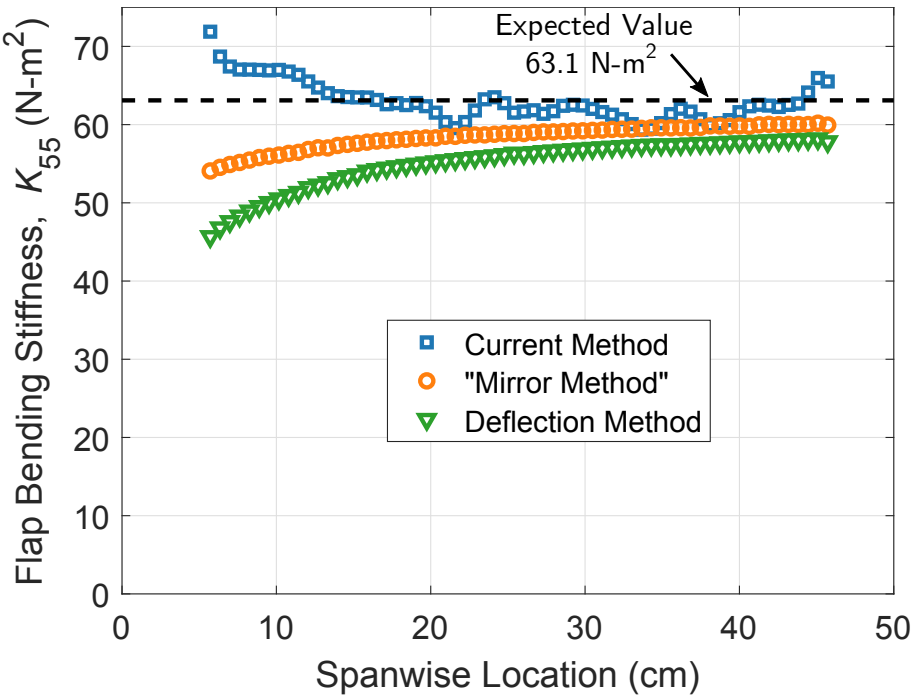

Figure 6.7: Comparison of the current strain-based method to other common measurement techniques for the flap bending stiffness.

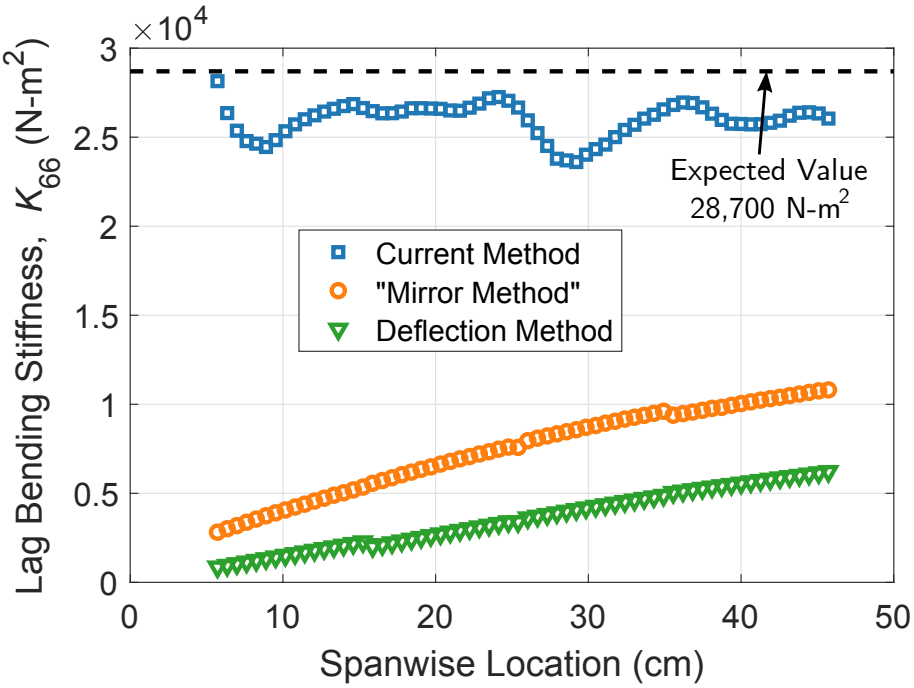

Figure 6.8: Comparison of the current strain-based method to other common measurement techniques for the lag bending stiffness.

bending stiffness was seen to asymptotically approach the predicted stiffness when moving farther away from the root, which is characteristic of the presence of a small

rigid body motion. For the lag bending stiffness, shown in Fig. 6.8, the average stiffness from the displacement method was 3872 N-m^2, which was only 14% of the expected value of 27800 N-m^2. Using the slope method, the average stiffness nearly doubled to 7757 N-m^2, which was still only 27% of the predicted value. These large discrepancies in the lag bending stiffness, seen in both the displacement and slope based measurements, were likely a result of the load cell having a finite stiffness close to the lag bending stiffness of the beam, resulting in a significant rigid body motion of the beam when subjected to the much larger lag shear force. However, the stiffness value was predicted with much better accuracy based on the strain measurements, indicating the expected result that a rigid body motion introduces no strain. This comparison shows the advantage of using strain-based measurements for calculating the stiffness properties, particularly if trying to measure large stiffness values.

6.2 Tailored Composite Beam

The ply layup of the composite beam was carefully selected to produce a significant bending/torsion coupling and thus provided an interesting test case for the developed methodology. The test envelope of anticipated applied loads for this beam, and maximum expected strains under these loads, is summarized in Table 6.3. Tests were again run for 11 different load cases, with the negative load neglected for the axial case due to buckling concerns. Two main constraints arose during testing of the composite beam due to its small thickness and the presence of the flap bending/torsion coupling. First, due to the small thickness, the beam was very unstable when subjected to either a lag shear or lag bending load, which meant that in order to apply either of these load cases, a net axial force also needed to be applied to counteract this instability. This is highlighted in the specified loads for tests 2 and 3 as well as tests 10 and 11 by the inclusion of a large axial force F_1. Second, due to the bending/torsion coupling the beam experienced both a twist and

flap deformation when subjected to a flap bending moment or torsional moment. Therefore, the application of a flap shear load generated a variation in both flap bending and torsional moment along the span that had to be taken into account when positioning the pulleys for applying the loads.

Table 6.3: Applied tip loads for the composite beam.

Test #	Load case	Applied Tip Load	Expected Strain, $\max\{\lvert\underline{\gamma}\rvert\}$
1	Axial	$F_1 = +6250$ N	635 $\mu\epsilon$
2,3	Lag Shear	$F_1 = 5300$ N $F_2 = \pm 725$ N	844 $\mu\epsilon$
4,5	Flap Shear	$F_3 = \pm 3.9$ N	1396 $\mu\epsilon$
6,7	Torsion	$M_1 = \pm 2.7$ N-m	1823 $\mu\epsilon$
8,9	Flap Bending	$M_2 = \pm 2.0$ N-m	1154 $\mu\epsilon$
10,11	Lag Bending	$F_1 = 4500$ N $M_3 = \pm 160$ N-m	1665 $\mu\epsilon$

6.2.1 DIC measurements

For the tailored composite beam, three image sets were again taken for both the front and back surfaces of the beam by adjusting the height of the cameras on the tripod. Image set 1 collected data from 8.26 cm to 27.3 cm along the span, image set 2 collected data from 18.4 cm to 37.5 cm along the span, and image set 3 collected data from 28.6 cm to 47.6 cm along the span, with data provided over a total length of 39.4 cm. An example set of results for the axial and shear strains measured on both the $z = +t/2$ and $z = -t/2$ faces under a positive torsional moment $M_1 = 2.7$ N-m are shown in Figs 6.9 and 6.10. From Fig. 6.9, it can be seen that a significant axial strain γ_{11}^{+}, with a magnitude of about 450 $\mu\epsilon$, is present, even though only a torsional moment is being applied and measured. This strain arose from the bending/torsion coupling in the beam and exhibited the characteristics of the strain under a positive flap bending moment, with a positive axial strain on the

$z = +t/2$ face and a negative axial strain on the $z = -t/2$ face that remain nearly constant along the span. From Fig. 6.10, it can be seen that the applied torsional moment generated a nearly constant shear strain γ_{12}^{+} along both x and y as expected, with the magnitude agreeing well with the predicted 1823 $\mu\epsilon$.

6.2.2 Stiffness Matrix Calculation

The DIC measurements were then made for the remaining 10 load cases and the strain measurements were again extracted at every 0.64 cm along the span. These extracted measurements were combined with the calculated sectional loads to evaluate the spanwise distributions in the stiffness from $x = 8.26$ cm to $x = 47.6$ cm, with the results for the axial, lag shear, torsional, flap bending, and lag bending components shown in Figs. 6.11 - 6.13, respectively. Experimental measurements were plotted as points, with error bars representing the 95% confidence intervals for the measurements. Since no analytic solution was available for this cross-section, measurements were compared to the results predicted by *SectionBuilder*, which are shown as solid lines. Again, because of the small thickness, no data was able to be measured for calculating the flap shear stiffness component K_{33}.

The results for the axial stiffness K_{11}, the lag shear stiffness K_{22}, and the axial/lag shear coupled stiffness K_{12} are shown in Fig. 6.11, with all three components showing relatively good agreement with their respective predicted values. For the lag shear stiffness, some impact of the shear strain concentrations arising from the clamped boundary condition are observed up until about 13 cm from the root. In addition, the axial/lag shear coupling stiffness was only measured in the region of the beam from about 28 cm to 45 cm. For the region closer to the root, the conditions used to imposed symmetry in the compliance matrix, specifically the condition on the off-diagonal components being measured within an order magnitude of each other, eliminated this coupling term within this region. With exception to this coupling

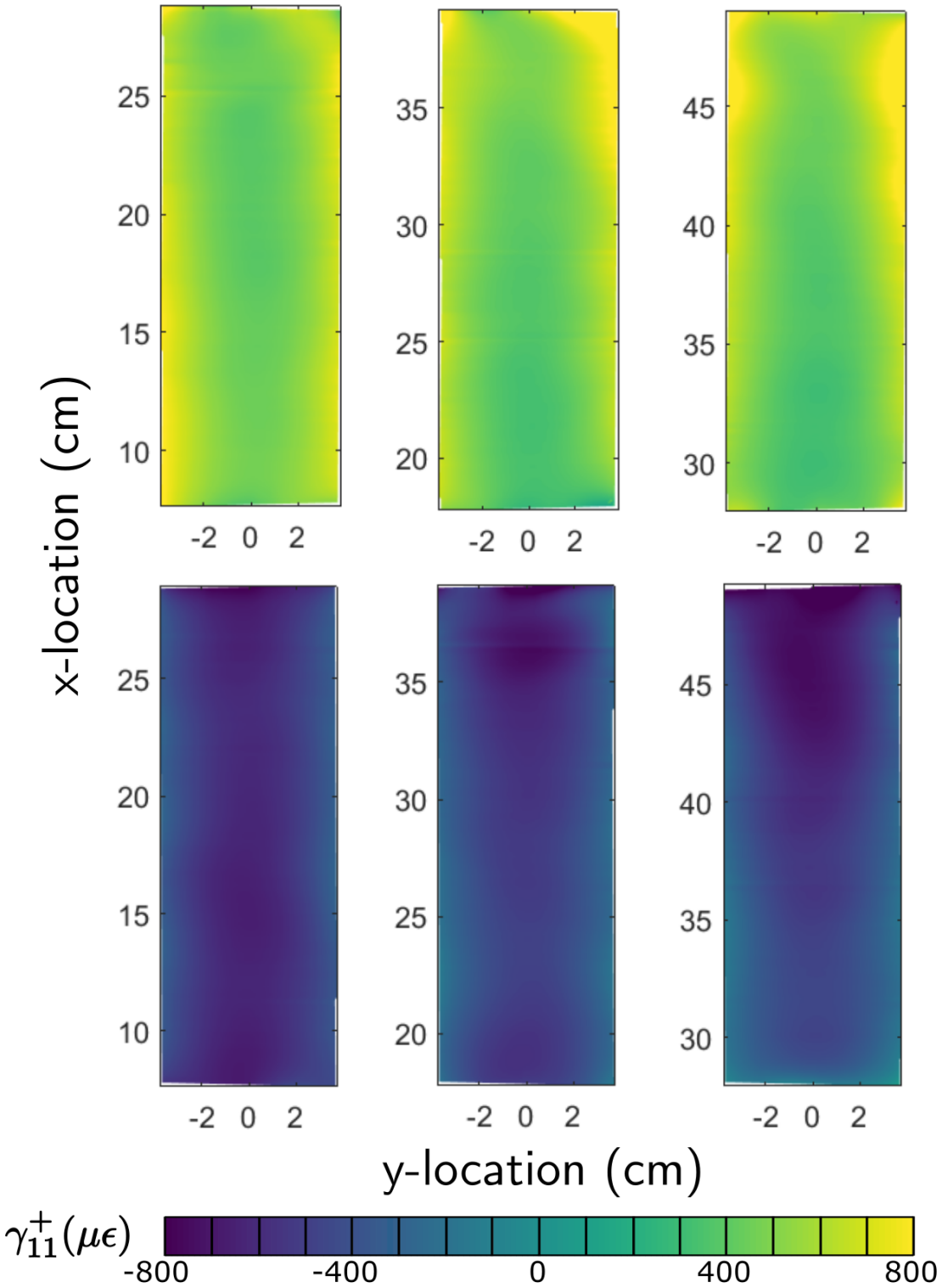

Figure 6.9: Axial strain γ_{11}^{+} under a positive torsional moment (load case 6). The upper row of images shows the strain on the $z = +t/2$ face and the bottom row shows the strain on the $z = -t/2$ face.

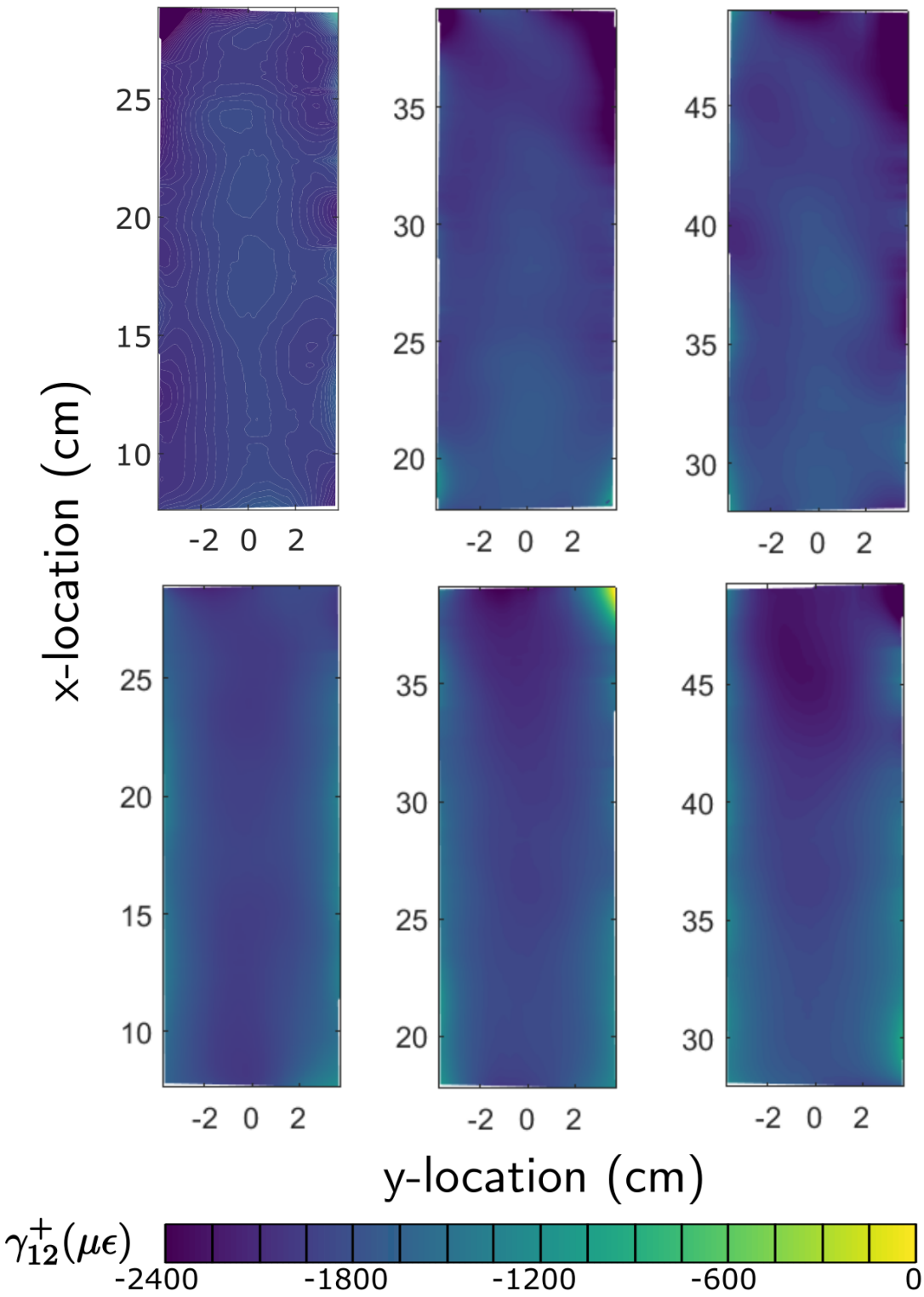

Figure 6.10: Shear strain γ_{12}^{+} under a positive torsional moment (load case 6). The upper row of images shows the strain on the $z = +t/2$ face and the bottom row shows the strain on the $z = -t/2$ face.

stiffness not being measured at certain locations, the predicted stiffness properties were almost always within the 95% confidence intervals of the measured stiffness. For the K_{12} coupling component, these uncertainty levels were calculated to be about 60% of the actual stiffness, primarily due to the small measured strain, while for both the axial and lag shear stiffness components, the uncertainty levels were around 20% of the measured values.

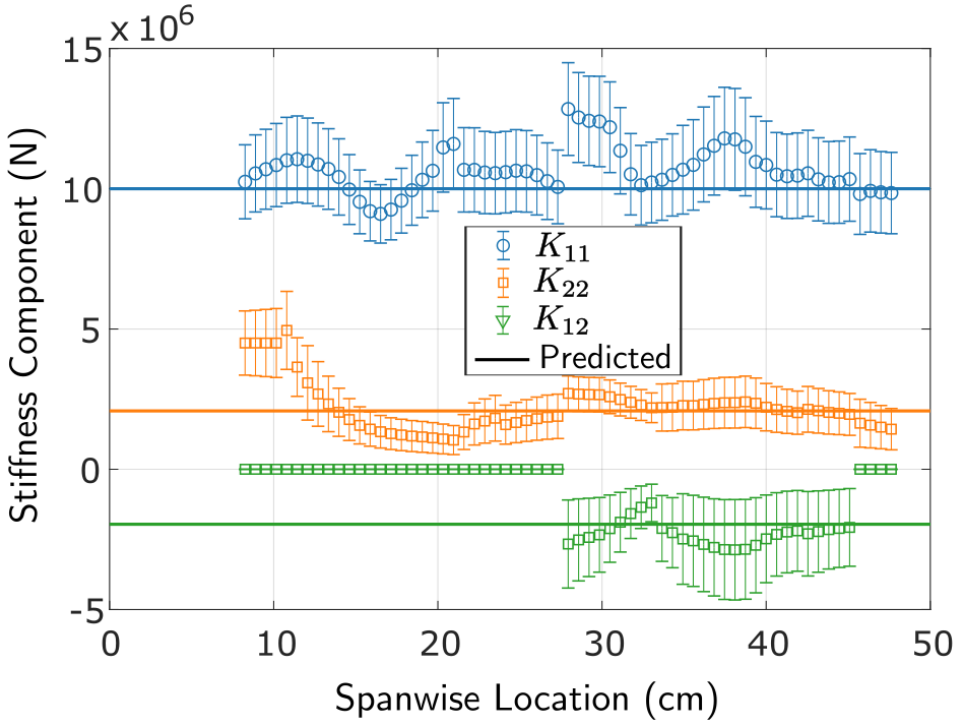

Figure 6.11: Axial and shear stiffness components for the tailored composite beam.

Figure 6.12 shows the measured spanwise variations in the torsional stiffness K_{44}, flap bending stiffness K_{55}, and flap bending/torsional coupling stiffness K_{45}. From these results, it can be seen that the coupled nature of these three stiffness components resulted in similar trends being observed in their variations along the span. The uncertainty levels were again highest in the coupling stiffness component at about 11% of its measured value, with the torsional stiffness and flap bending stiffness having uncertainty bounds of about 5% and 6%, respectively. For the lag bending stiffness K_{66}, shown in Fig. 6.13, the measured value showed good

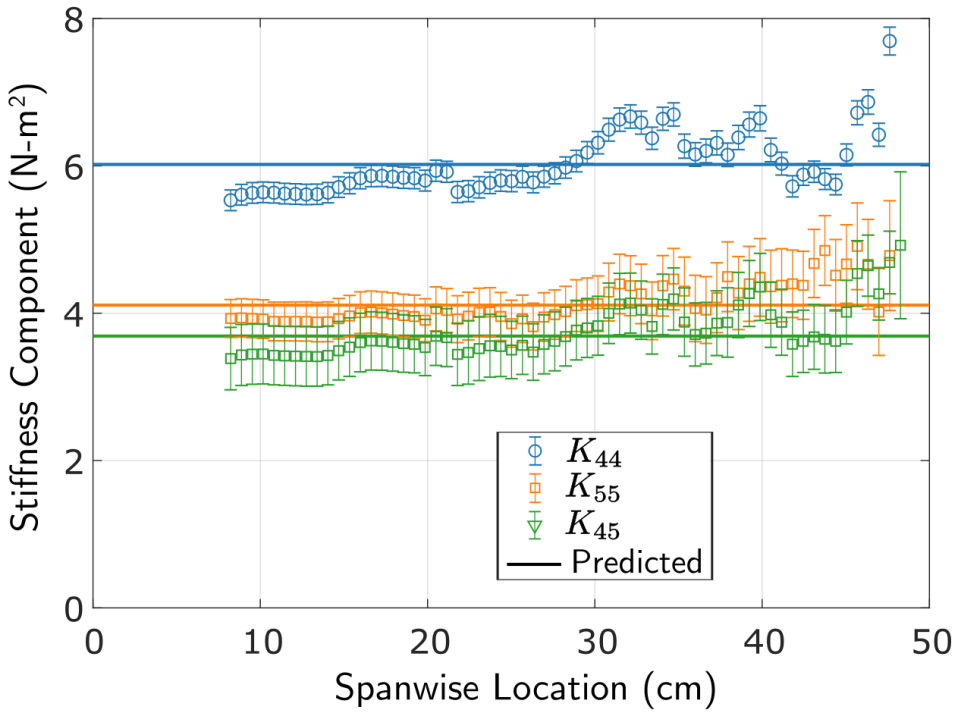

Figure 6.12: Torsional and flap bending stiffness components for the tailored composite beam.

agreement with the predicted value, with exception to unexpected jumps in the measured properties from about 22 cm to 25 cm along the span as well as from about 45 cm to 47.2 cm along the span. For the lag bending stiffness, the average uncertainty level was observed to be about 4% of the measured value.

Since the beam is expected to have constant properties along the span, it can also be useful to compare the average measurements to the predicted properties, as summarized in Table 6.4. In calculating the average stiffness property for the axial/lag shear coupling stiffness, only the locations along the span where the property was measured were used. Great agreement in the average and predicted properties were observed, with differences of less than 1% for the torsional, flap bending, and flap bending/torsional coupled stiffnesses. When compared with the predicted values, the lag bending stiffness and axial stiffness had differences of about 4% and 7%, respectively, with the axial/lag shear stiffness showing the largest difference at about 15%.

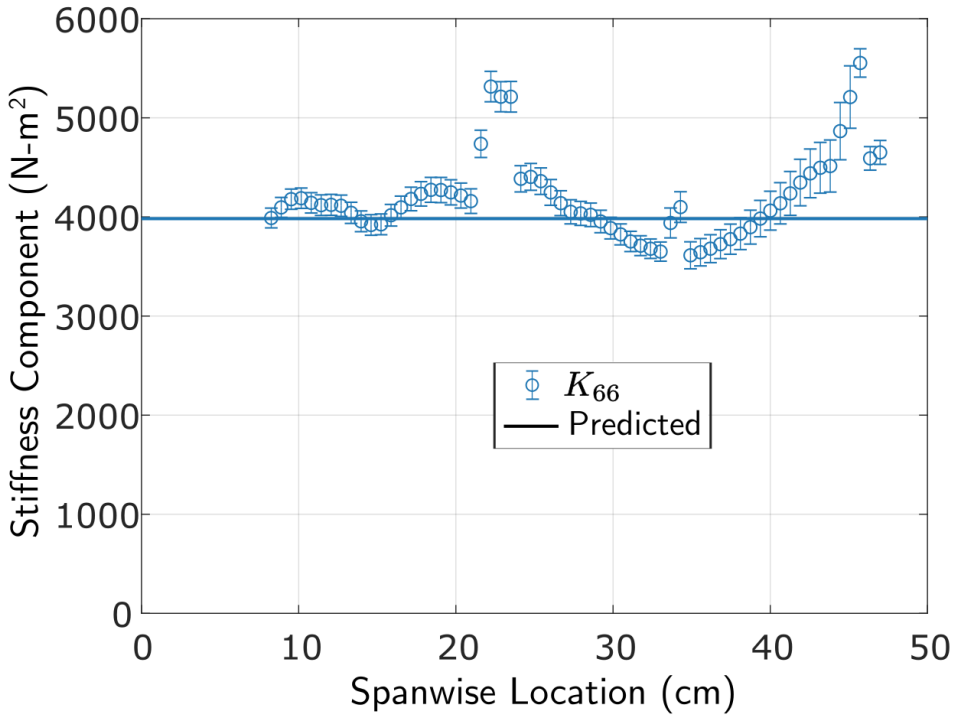

Figure 6.13: Lag bending stiffness for the tailored composite beam.

Table 6.4: Comparison of average composite beam stiffness values.

Stiffness term	Predicted	Measured
K_{11}, N	1.00×10^7	1.07×10^7
K_{12}, N	-1.96×10^6	-2.30×10^6
K_{22}, N	2.08×10^6	2.12×10^6
K_{44}, N-m^2	6.02	6.00
K_{45}, N-m^2	3.69	3.72
K_{55}, N-m^2	4.11	4.13
K_{66}, N-m^2	3.98×10^3	4.17×10^3

6.3 VR-7 Composite Blades

The experimental results for the two blades are considered next, with the test envelope of anticipated applied loads, and maximum expected strains under these loads, summarized in Tables 6.5 and 6.6 for the blades without and with the d-spar, respectively. The loads were selected to provide similar strain levels between the two blades, to provide a good means of comparing the results. Tests were again run for

11 different load cases neglecting the negative axial load. The blades were generally more compliant than the previous beams and also had significant coupling terms, due to the fact that the loads were not applied at the centroid or shear center, and strains of several thousand $\mu\epsilon$ could be generated under all the applied load cases.

Table 6.5: Applied tip loads for the composite blade without a spar.

Test #	Load case	Applied Tip Load	Expected Strain, $\max\{\lvert\underline{\gamma}\rvert\}$
1	Axial	$F_x = +1800$ N	3600 $\mu\epsilon$
2,3	Lag Shear	$F_y = \pm 43$ N	3428 $\mu\epsilon$
4,5	Flap Shear	$F_z = \pm 7.9$ N	2640 $\mu\epsilon$
6,7	Torsion	$M_x = \pm 8.2$ N-m	3040 $\mu\epsilon$
8,9	Flap Bending	$M_y = \pm 3.9$ N-m	2825 $\mu\epsilon$
10,11	Lag Bending	$M_z = \pm 23$ N-m	2712 $\mu\epsilon$

Table 6.6: Applied tip loads for the composite blade with a spar.

Test #	Load case	Applied Tip Load	Expected Strain, $\max\{\lvert\underline{\gamma}\rvert\}$
1	Axial	$F_x = +1550$ N	3610 $\mu\epsilon$
2,3	Lag Shear	$F_y = \pm 57$ N	3428 $\mu\epsilon$
4,5	Flap Shear	$F_z = \pm 11.5$ N	2650 $\mu\epsilon$
6,7	Torsion	$M_x = \pm 13.8$ N-m	3059 $\mu\epsilon$
8,9	Flap Bending	$M_y = \pm 8.2$ N-m	2910 $\mu\epsilon$
10,11	Lag Bending	$M_z = \pm 30.2$ N-m	2692 $\mu\epsilon$

6.3.1 DIC measurements

For both composite blades, the inclusion of inserts for the first 5.61 cm at the root and tip meant that the uniform portion of the blade extended only from 5.61 cm to 47.7 cm along the span. Because of this shorter overall length, only two sets of images were taken along the span, with image set 1 collected from 6.4 cm to 27.5 cm and image set 2 collected from 16.5 cm to 37.7 cm, measured with respect to the beginning of the uniform portion of the blade. An example set of the measured

axial strain γ_{11}^{+} under the applied axial load F_1 is shown in Figs. 6.14 and 6.15 for the blade without and with the spar, respectively. Because the loads were applied and measured at $0.6c$ with respect to the leading edge, a significant variation in the

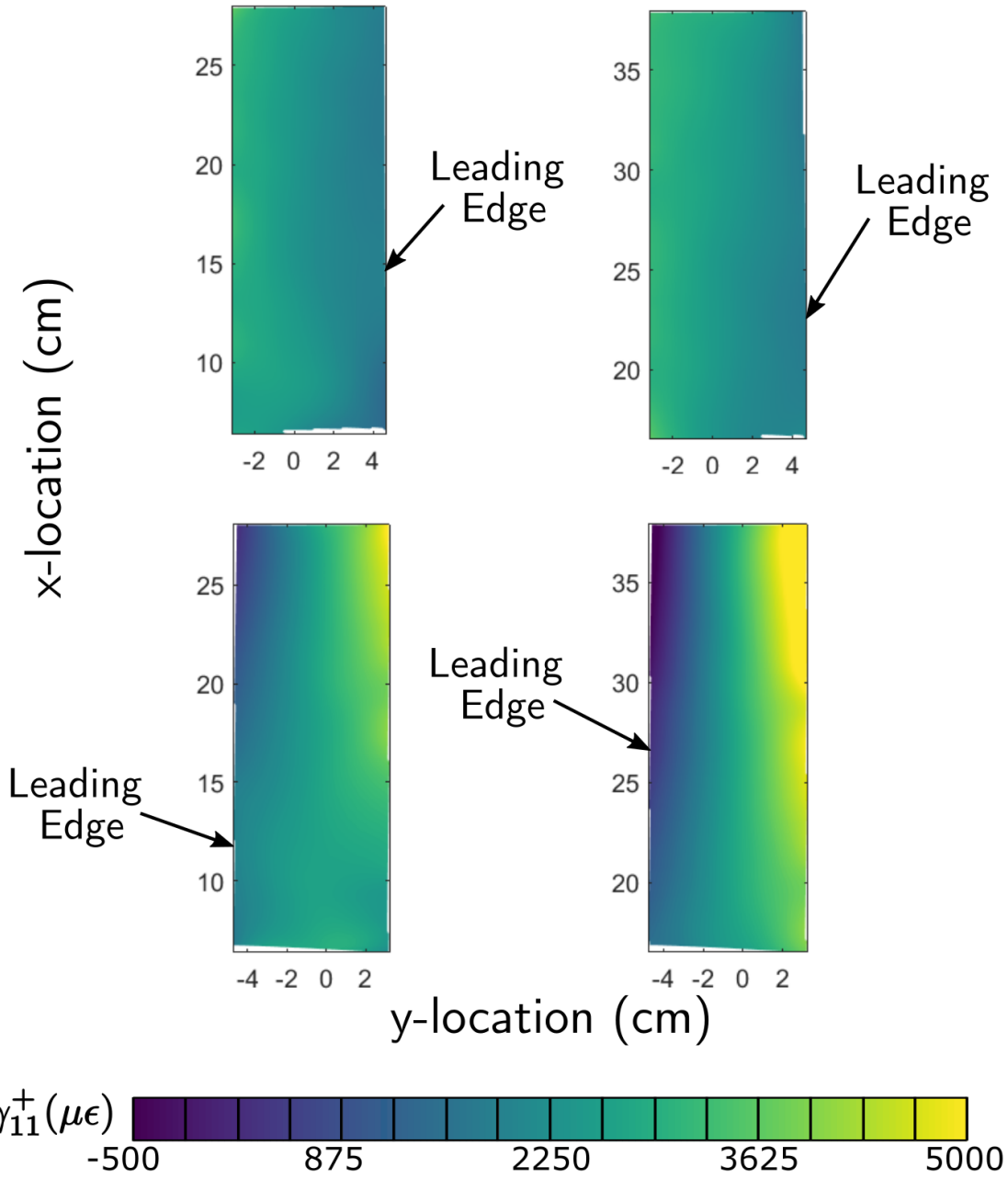

Figure 6.14: Axial strain γ_{11}^{+} under an axial force (load case 1) for the blade without a spar. The upper row of images shows the strain on the upper profile of the airfoil and the bottom row shows the strain on the lower profile.

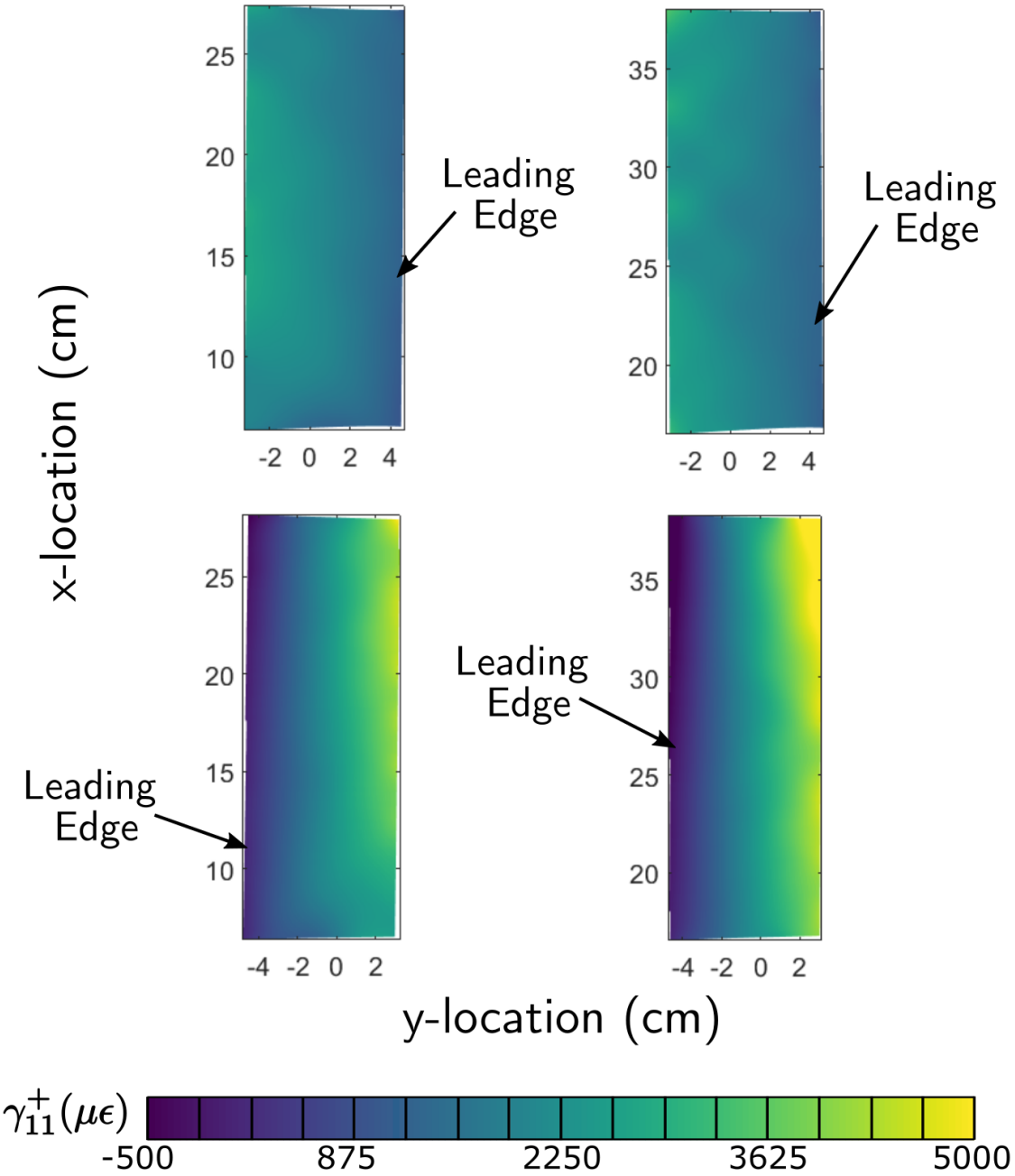

Figure 6.15: Axial strain γ_{11}^{+} under an axial force (load case 1) for the blade with a spar. The upper row of images shows the strain on the upper profile of the airfoil and the bottom row shows the strain on the lower profile.

axial strain along the chord can be observed, particularly on the lower profile of the blade, due to the off diagonal stiffness components coupling the axial and bending stiffnesses. While the loads for both blades were selected with the goal of producing

similar strain levels, the presence of these off-diagonal stiffness components lead to the blade with the spar having slightly larger (more negative) strain magnitudes near the leading edge and slightly smaller (less positive) strains near the trailing edge.

6.3.2 Stiffness Matrix Calculation

The DIC measurements were then made for the remaining load cases and the strain measurements were extracted at every 0.64 cm along the span. These extracted measurements were combined with the calculated sectional loads to evaluate the spanwise distributions in the stiffness from $x = 7.62$ cm to $x = 35.6$ cm, with the results for the six diagonal stiffness components shown in Figs. 6.16 - 6.21, respectively. Experimental measurements were plotted as points, with error bars representing the 95% confidence intervals for the measurements. Since no analytic solution was available for this cross-section, measurements were compared to the results predicted by *SectionBuilder*, which are shown as solid lines. Comparing the results for the blades without and with the spars, it can be seen that in all cases, the inclusion of the spar increases the stiffness, which can be expected due to added structural material. For the blade without the spar, the stiffness properties had small variations along the span and showed great agreement with the predicted stiffness coefficients, with exception to the lag shear stiffness where a difference of about 50% was observed. For the blade with the spar, the measured properties showed much greater variations along the span and also showed larger discrepancies when compared to the predicted properties, with the averaged properties along the span of the blades summarized in Table 6.7. For both blades, the fact that the properties are being measured about $0.6c$ and that the airfoil is not symmetric gives rise to additional off-diagonal stiffness components, whose average properties along the span are summarized in Table. 6.8.

The discrepancies between the predicted and measured properties likely in-

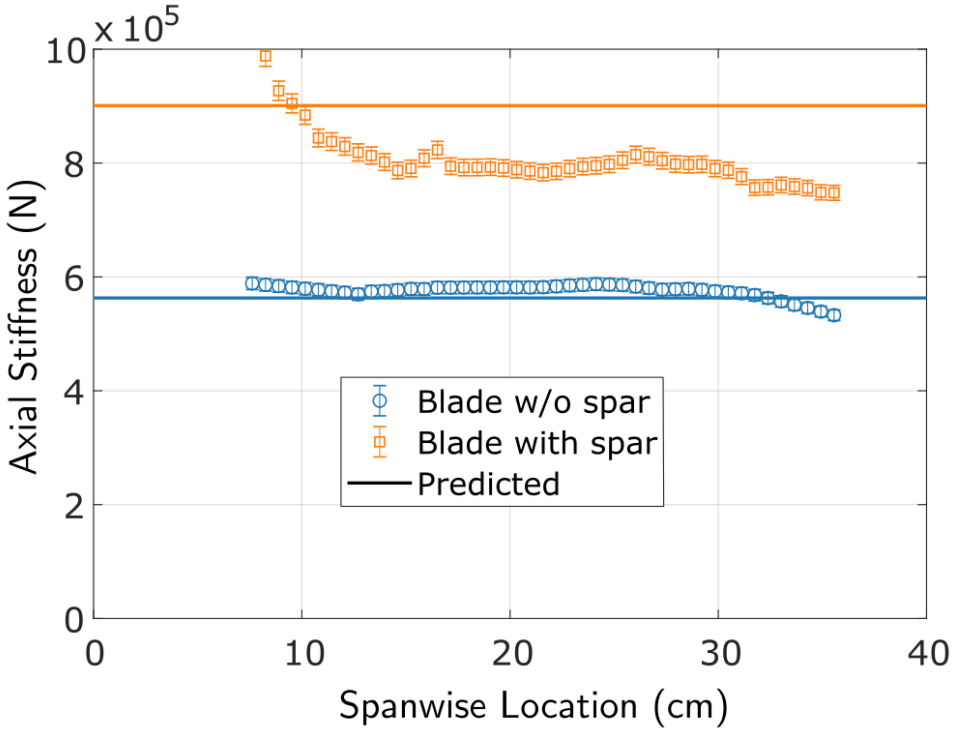

Figure 6.16: Axial stiffness K_{11} measurements for the composite blades.

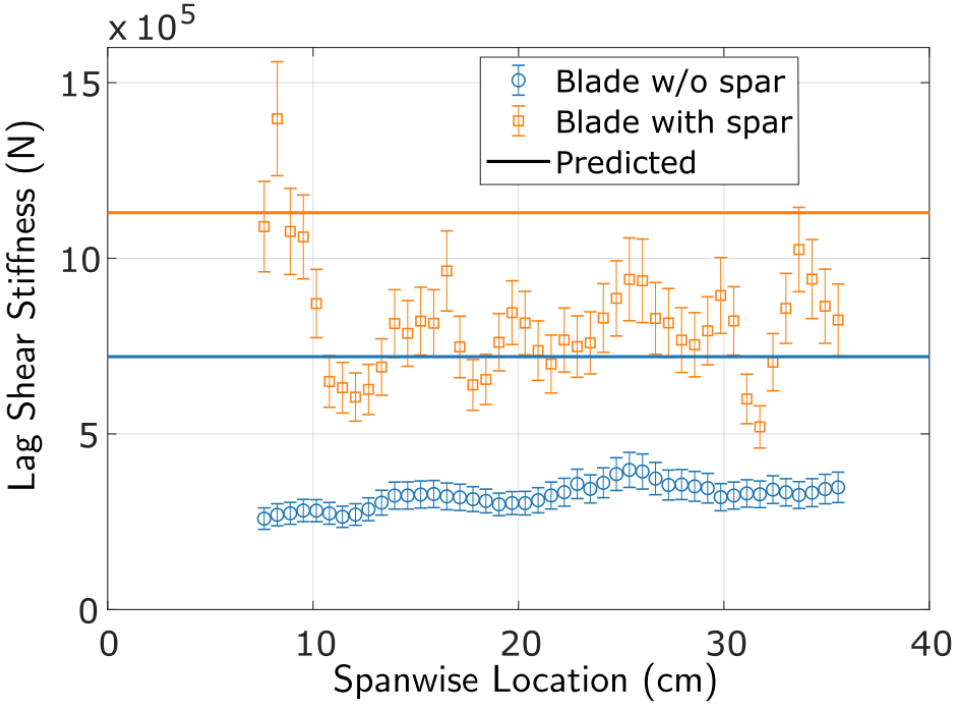

Figure 6.17: Lag shear stiffness K_{22} measurements for the composite blades.

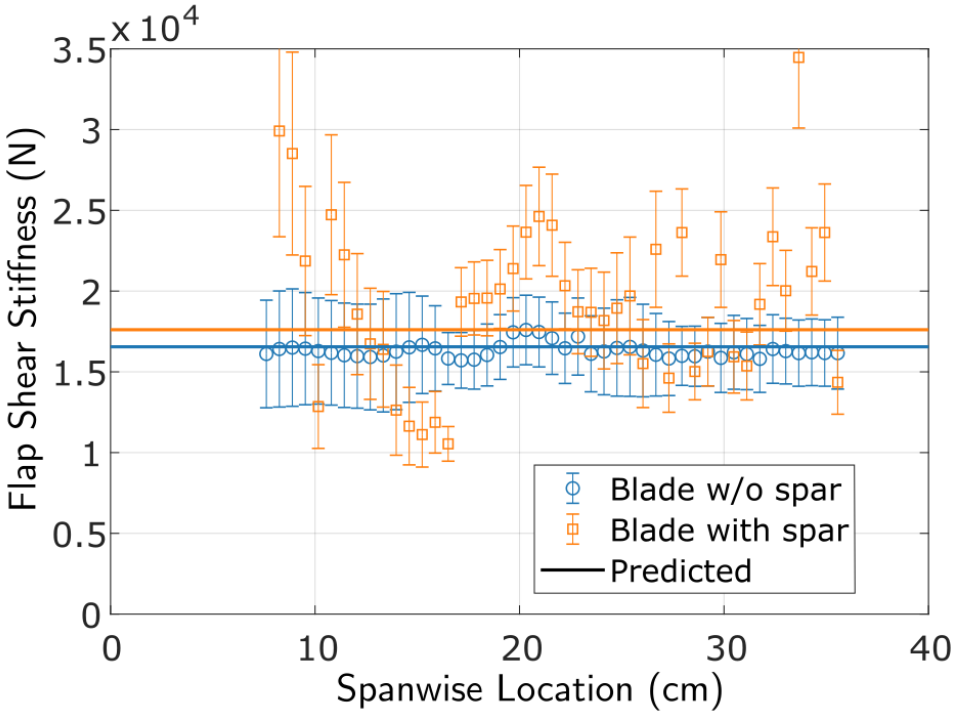

Figure 6.18: Lag shear stiffness K_{33} measurements for the composite blades.

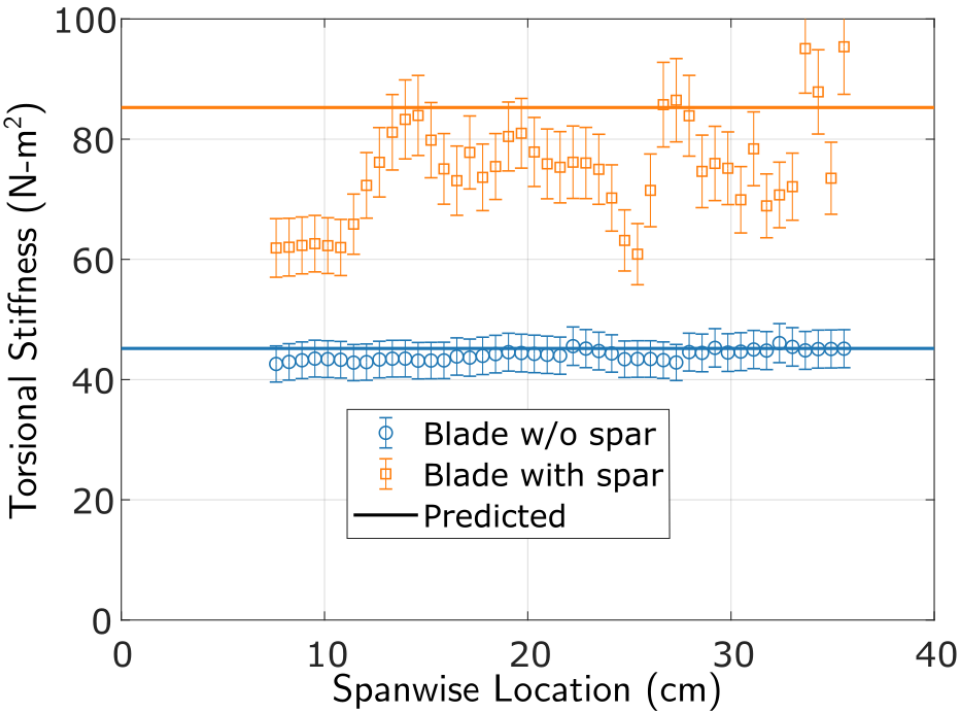

Figure 6.19: Torsional stiffness K_{44} measurements for the composite blades.

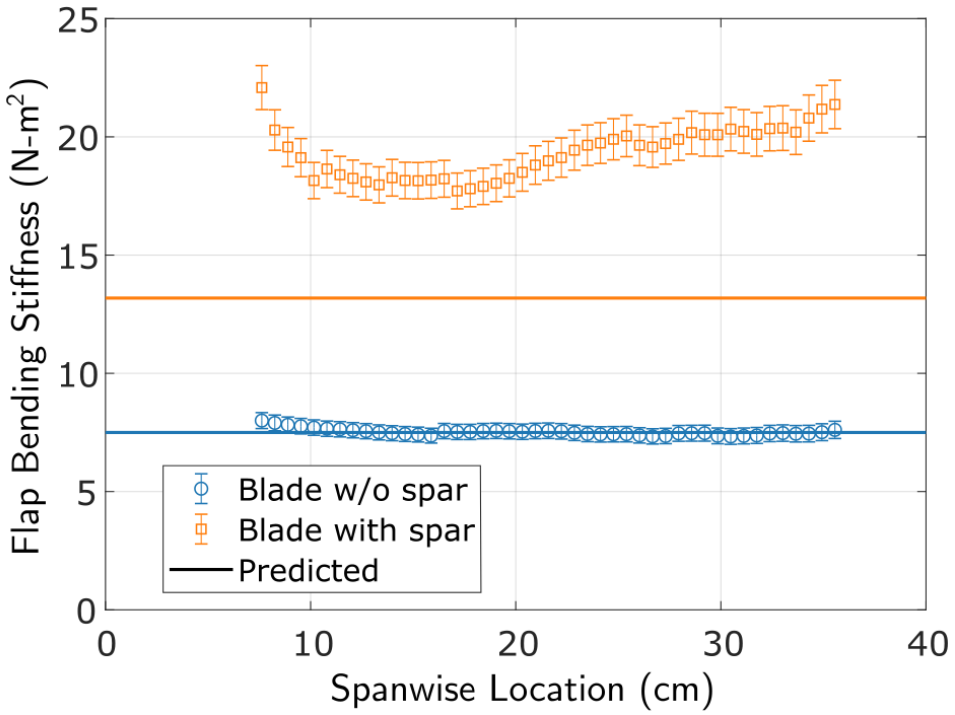

Figure 6.20: Flap bending stiffness K_{55} measurements for the composite blades.

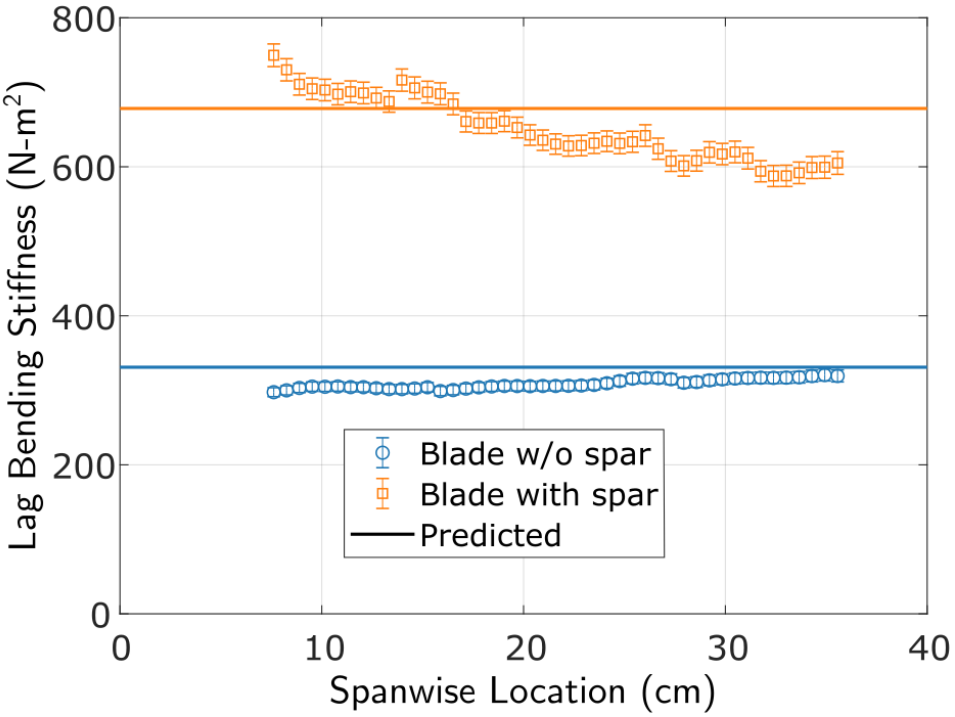

Figure 6.21: Lag bending stiffness K_{66} measurements for the composite blades.

Table 6.7: Comparison of the diagonal stiffness components for the two composite blades.

Stiffness	Without Spar		With Spar	
Entry	Numerical	Measured	Numerical	Measured
K_{11}, N	5.65×10^5	5.74×10^5	9.00×10^5	8.06×10^5
K_{22}, N	7.21×10^5	3.28×10^4	1.13×10^6	8.15×10^5
K_{33}, N	1.66×10^4	1.64×10^4	1.76×10^4	2.00×10^4
K_{44}, N-m^2	44.5	43.6	85.3	74.8
K_{55}, N-m^2	7.49	7.55	13.2	19.3
K_{66}, N-m^2	327	310	678	654

Table 6.8: Comparison of the off-diagonal stiffness components for the two composite blades.

Stiffness	Without Spar		With Spar	
Entry	Numerical	Measured	Numerical	Measured
K_{15}, N-m	780	412	1.40×10^3	1.55×10^3
K_{16}, N-m	-3.39×10^3	-3.54×10^3	-1.40×10^4	-1.28×10^4
K_{56}, N-m^2	-11.3	-0.49	-29.6	-27.5
K_{23}, N	1.53×10^4	7.25×10^3	1.15×10^4	2.20×10^4
K_{24}, N-m	-1.58×10^3	-710	-2.56×10^3	-1.99×10^3
K_{34}, N-m	393	414	362	246

dicates that the manufacturing process for the blade with the spar resulted in a slightly modified geometry than that used for the model. One such difference in geometry was observed by measuring the external geometry of the blade after curing in the oven; for the blade without the spar, the thickness was about 1.5% larger than expected and when including the spar, the difference in the overall airfoil thickness increased to about 4%. This difference in thickness is particularly important for the flap bending stiffness, which generally varies with the thickness cubed. Therefore, a 4% difference would account for about an 12.5% increase in the predicted flap bending stiffness and reduce the discrepancy between the measured and predicted stiffness down to about 35%. However, this thickness difference would only have a marginal impact on the other properties, such as the axial stiffness, that also showed some large discrepancies between the predicted and measured properties.

To ensure that the large difference between the measured and predicted flap bending stiffness was only a result of a difference between the manufactured and modeled blade, and not a result of the developed methodology, the flap bending stiffness was also computed using a displacement based method, with the setup shown in Fig. 6.22. A tip shear force was applied using various weights from 0.2 kg to 2 kg under gravity loading, to eliminate any possible effects of friction generated by the pulleys. The flap bending stiffness was then calculated based on the tip displacement w_{tip} and applied shear force F_3 according to

$$K_{55} = \frac{F_3 l^3}{3 w_{\text{tip}}} \tag{6.3}$$

where $l = 51$ cm is the length of the unclamped portion of the beam. The displacement test was then repeated twice, with the calculated flap bending stiffness results based on the displacement measurement shown in Fig. 6.23 for each of the applied loads. The stiffness values based on the tip displacement measurement showed some spread based on the applied load, but overall showed great agreement with the value calculated using the proposed methodology. However, even when accounting for

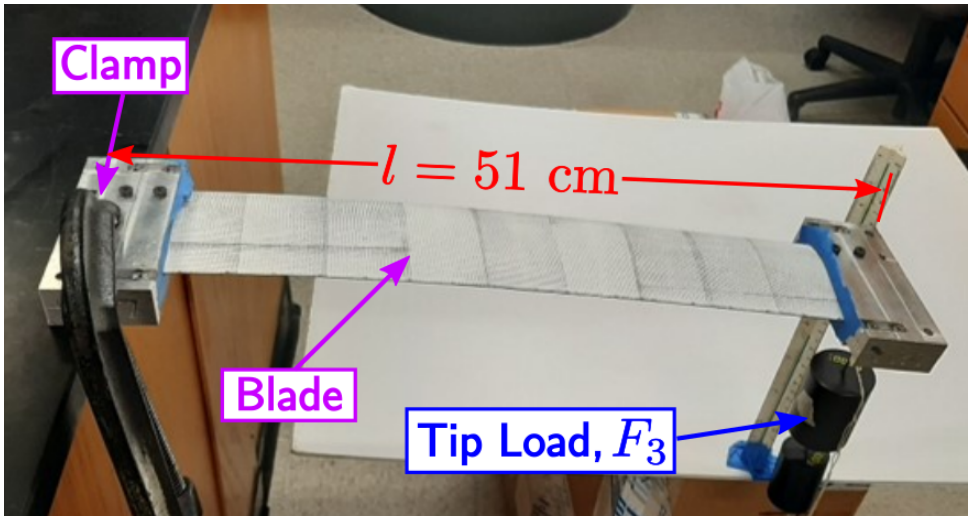

Figure 6.22: Setup for measuring flap bending stiffness of VR-7 composite blade with d-shaped spar using tip displacement.

the 12.5% change in stiffness due to the manufactured airfoil thickness being about 4% greater than that of the model, there was still a significant difference between the predicted stiffness value and the measured stiffness values. This indicates that there are likely some differences between the internal geometry of the modeled and manufactured blades that are not easily identified, which highlights the importance of measuring the properties and not solely relying on the designed blade geometry to predict the stiffness values.

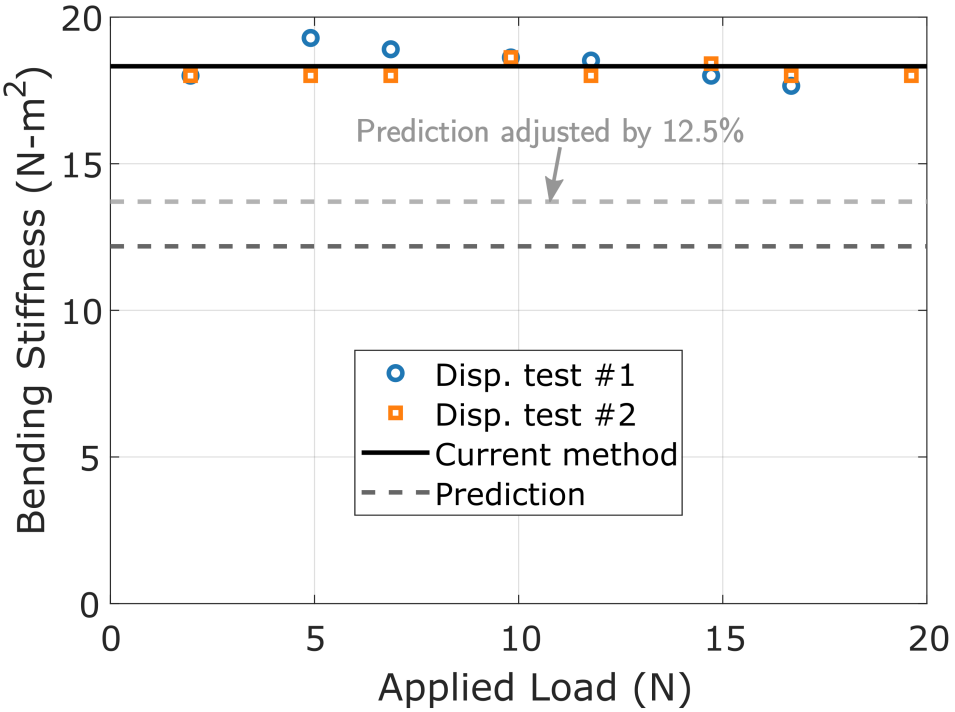

Figure 6.23: Comparison of flap bending stiffness for a VR-7 blade with a d-spar using difference measurement methods.

6.3.3 Centroid and Shear Center

From Sec. 2.3.4 and 2.3.5, it was shown that the stiffness components coupling the axial and bending behavior, K_{15}, K_{16}, and K_{56}, can be used to calculate the centroid and principal axes of bending, while the components coupling the shear and torsion behavior, K_{23}, K_{24}, and K_{34}, can be used to calculate the shear center and principal axes of shear. Based on Eq. (2.50), the centroid location calculated from

the measured properties was found to be $y_{c,m} = 0.62$ cm ($0.52c$ from the leading edge) and $z_{c,m} = 0.07$ cm for the airfoil without a spar and $y_{c,m} = 1.53$ cm ($0.41c$ from the leading edge) and $z_{c,m} = 0.19$ cm for the airfoil with a spar. Based on the predicted stiffness matrices, the centroid location was $y_{c,p} = 0.6$ cm ($0.53c$ from the leading edge) and $z_{c,p} = 0.14$ cm for the airfoil without a spar and $y_{c,p} = 1.71$ cm ($0.38c$ from the leading edge) and $z_{c,p} = 0.17$ cm for the airfoil with a spar. These values were then plotted in Figs. 6.24 and 6.25 for the blades without and with a spar, respectively. For the blade without the spar, the chordwise positions of the measured and predicted centroid are nearly identical but they do have a small offset in the thickness direction, while for the blade with a spar, a larger difference is observed in the chordwise location of the centroid but with the offsets in the thickness direction showing good agreement.

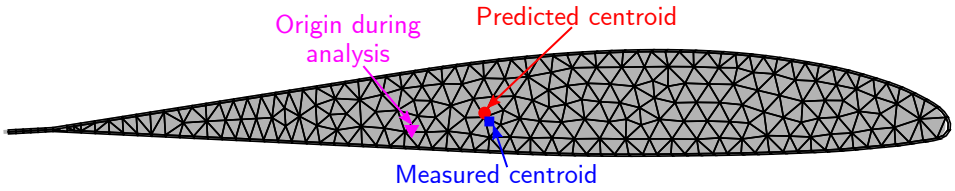

Figure 6.24: Measured and predicted centroid locations for the airfoil without a spar.

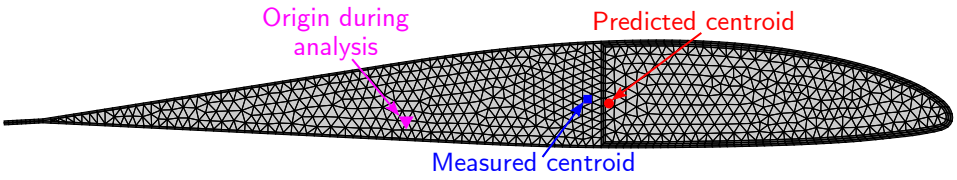

Figure 6.25: Measured and predicted centroid locations for the airfoil with a spar

Based on Eq. (2.54), the shear center calculated from the measured properties was found to be $y_{sc,m} = 2.64$ cm ($0.27c$ from the leading edge) and $z_{sc,m} = 0.27$ cm for the airfoil without a spar and $y_{sc,m} = 1.37$ ($0.43c$ from the leading edge) and $z_{sc,m} = 0.26$ for the airfoil with a spar. Based on the predicted stiffness matrices, the shear center location was $y_{sc,p} = 2.62$ cm ($0.27c$ from the leading edge) and

$z_{sc,p} = 0.28$ cm for the airfoil without a spar and $y_{sc,p} = 2.45$ cm ($0.29c$ from the leading edge) and $z_{sc,p} = 0.28$ cm for the airfoil with a spar. These values were then plotted in Figs. 6.26 and 6.27 for the blades without and with a spar, respectively. For both blades, the predicted shear center was fairly close to the $1/4c$ location, but the measured shear center location for the blade with the spar was significantly farther back. However, both the predicted and measured values had similar offsets in the thickness direction.

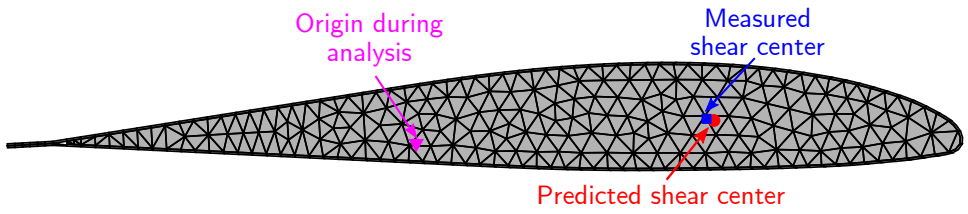

Figure 6.26: Measured and predicted shear center locations for the airfoil without a spar.

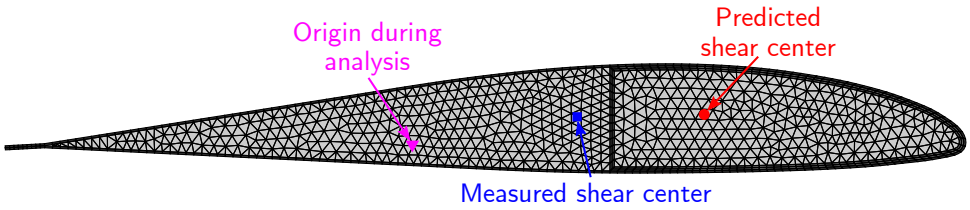

Figure 6.27: Measured and predicted shear center locations for the airfoil with a spar

6.4 Tapered Aluminum Beam

The final test article was the aluminum beam with a tapered width along its span, which provided a means of experimentally verifying the calculation of spanwise variations in properties. The test envelope of the anticipated applied loads for this beam, and the maximum expected strains at the mid-span under these loads, is summarized in Table 6.9. As with all the previous tests, positive and negative load cases were applied for all but the axial force. With exception to the axial force,

applied loads could be generated that produced significant strain of several thousand $\mu\epsilon$ at the mid-span of the beam.

Table 6.9: Applied load cases for the tapered aluminum beam.

Test #	Load case	Applied Tip Load	Expected Strain, $\max\{\lvert\underline{\gamma}\rvert\}$
1	Axial	$F_1 = +6000$ N	380 $\mu\epsilon$
2,3	Lag Shear	$F_2 = \pm 575$ N	1510 $\mu\epsilon$
4,5	Flap Shear	$F_3 = \pm 143$ N	2000 $\mu\epsilon$
6,7	Torsion	$M_1 = \pm 81$ N-m	4000 $\mu\epsilon$
8,9	Flap Bending	$M_2 = \pm 70$ N-m	3000 $\mu\epsilon$
10,11	Lag Bending	$M_3 = \pm 423$ N-m	3000 $\mu\epsilon$

6.4.1 DIC measurements

For the tapered aluminum beam, a total of six image sets were taken along the span. The first three image sets were taken with the root of the beam ($x = 0$ cm) clamped to the load cell with image set 1 collecting data from 5.1 cm to 25.4 cm, image set 2 collecting data from 15.2 cm to 35.6 cm, and image set 3 collecting data from 25.4 cm to 45.7 cm. The entire beam was then rotated 180° such that the tip of the blade was now clamped to the load cell and the same test conditions were repeated, with image set 4 collecting data from 45.7 cm to 66.0 cm, image set 5 collecting data from 35.6 cm to 55.9 cm, and image set 6 collecting data from 25.4 cm to 45.7 cm. This provided data over almost the entire length of the beam, from 5.1 cm all the way up to 66.0 cm, so that the symmetry of the calculations about the mid-span could be assessed. An example set of DIC results for the axial strain γ_{11}^{+} under a negative lag bending moment $M_3 = -423$ N-m is shown in Figs 6.9 and 6.10, for the six image sets on the $z = +t/2$ and $z = -t/2$ faces, respectively. Comparing the images from the upper and lower halves of the span in these two sets of results, it can be seen that the results exhibit symmetry about the mid-span,

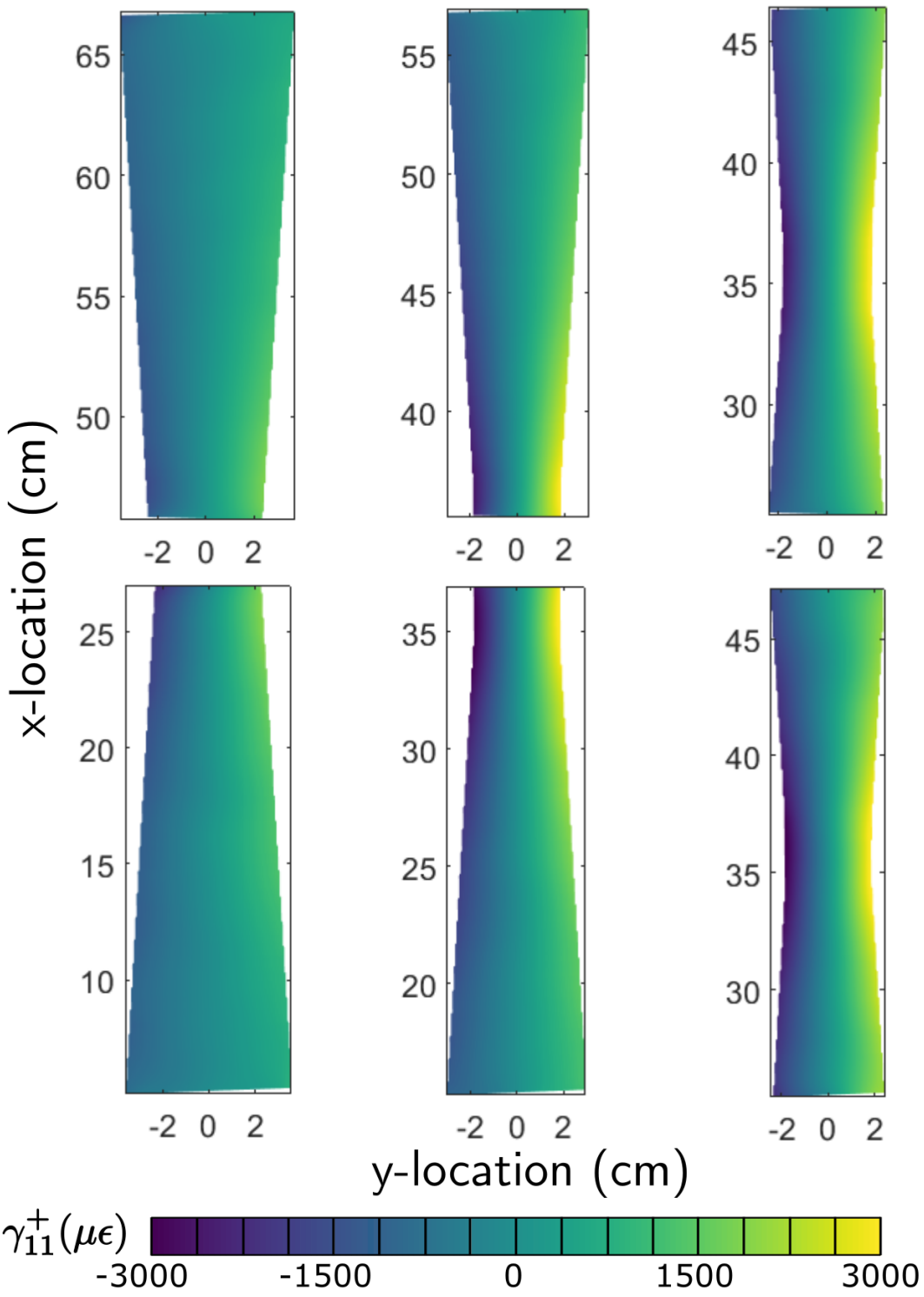

Figure 6.28: Axial strain γ_{11}^{+} under a negative lag bending moment (load case 11) on the $z = +t/2$ face.

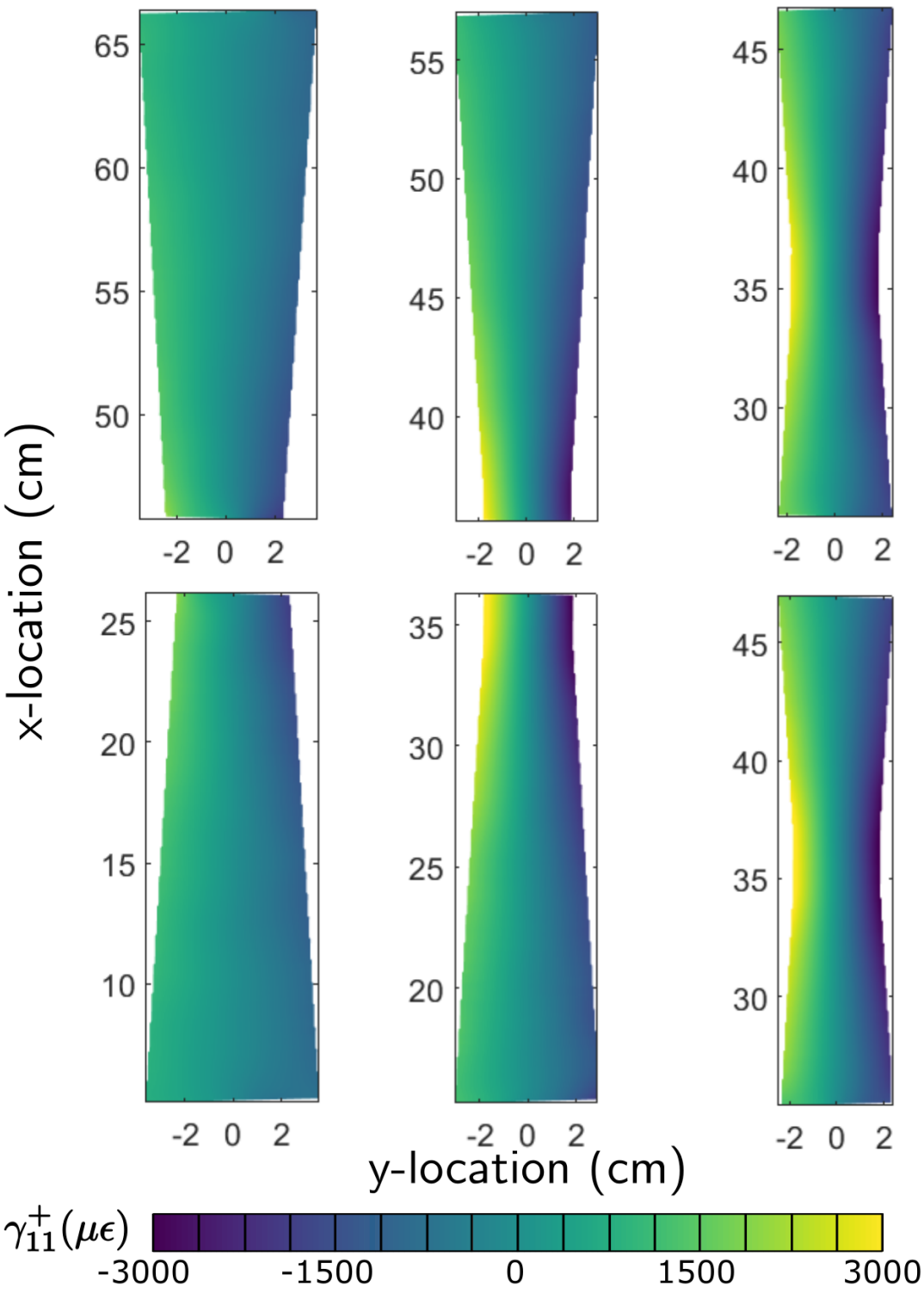

Figure 6.29: Axial strain γ_{11}^{+} under a negative lag bending moment (load case 11) on the $z = -t/2$ face.

which is expected under a constant applied moment.

6.4.2 Stiffness Matrix Calculation

The DIC measurements were then made for the remaining 10 load cases and the strain measurements were extracted at every 0.64 cm along the span, combined with the sectional loads, and used to evaluate the spanwise distributions in the stiffness from $x = 5.1$ cm to $x = 66$ cm. The results for the axial, lag shear, torsional, flap bending, and lag bending stiffness components are shown in Figs. 6.30 - 6.34, respectively. Experimental measurements were plotted as points, with error bars representing the 95% confidence intervals for the measurements. The results are compared with the predictions generated from *SectionBuilder*, which are plotted as solid lines. While the thickness of the tapered aluminum beam was starting to approach the minimum dimension for obtaining DIC measurements in the current setup, the expected shear strain on these faces under the flap shear load was still expected to be very small and the measurement was therefore not attempted, meaning that no data was available for measuring the flap shear stiffness K_{33}.

Figure 6.30 shows the variations in the measured axial stiffness K_{11} along the span. The measured and predicted axial stiffness values have the best correlation closest to the mid-span of the beam, where the axial strain is largest and therefore the associated uncertainty level is smallest. With exception to a jump in the data around 11 cm, the predicted values were generally within the s95% confidence interval for the measured axial stiffness. The results for the spanwise variations of the measured lag shear stiffness K_{22} along the span are then shown in Fig. 6.31, which have relatively large uncertainty levels due to having the smallest associated strain of all the applied load cases. However, with exception to the region from about 20 cm to 25 cm along the span, the experimental and predicted lag shear stiffness values show reasonable correlation.

Figure 6.32 shows the variations in the measured torsion stiffness K_{44} along the span. While the measured and predicted stiffness values showed the same trends, there was a noticeable offset of about 10% between the two sets of results. The effect of the clamped boundary condition can also be seen for the results at both ends of the beam and may contribute to the observed offset in magnitudes. For the flap bending stiffness K_{55}, shown in Fig. 6.33, a similar effect is observed, with the measured and predicted stiffness values having nearly identical trends but with a slight offset in magnitude. The variations in the lag bending stiffness K_{66} are then shown in Fig. 6.34, with exceptional agreement observed between the measurements and predictions. Unlike the other stiffness values that exhibit a linear variation in properties along the span, the lag bending stiffness exhibited a non-linear variation due to its cubic dependence on the width.

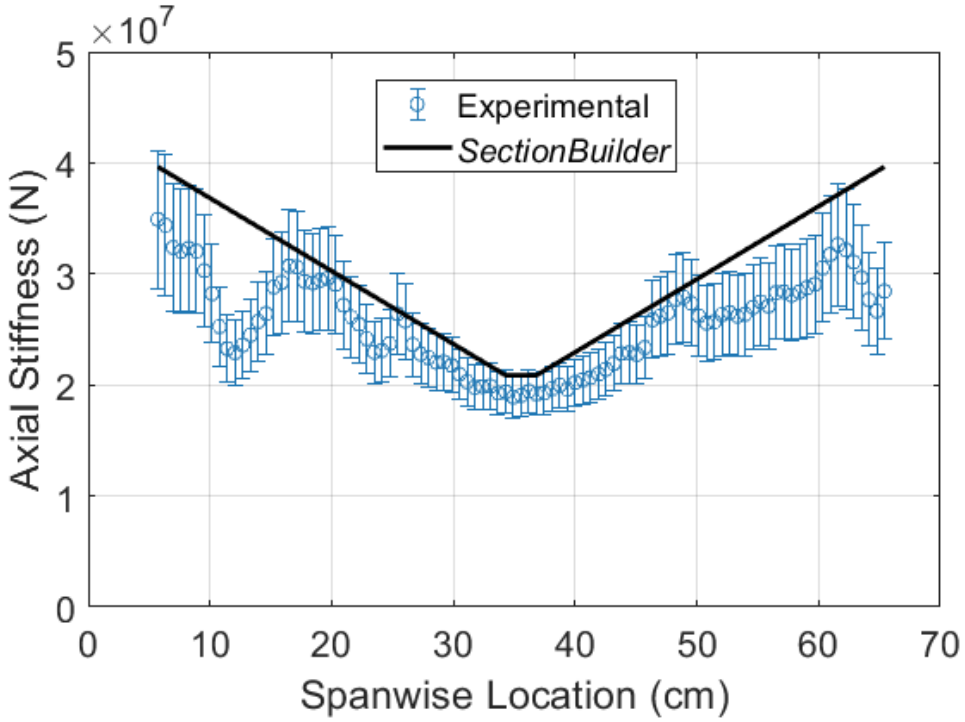

Figure 6.30: Axial stiffness K_{11} measurements for the tapered aluminum beam.

A quantitative comparison between the numerical and measured stiffness values can be considered by taking the average difference along the span. In this

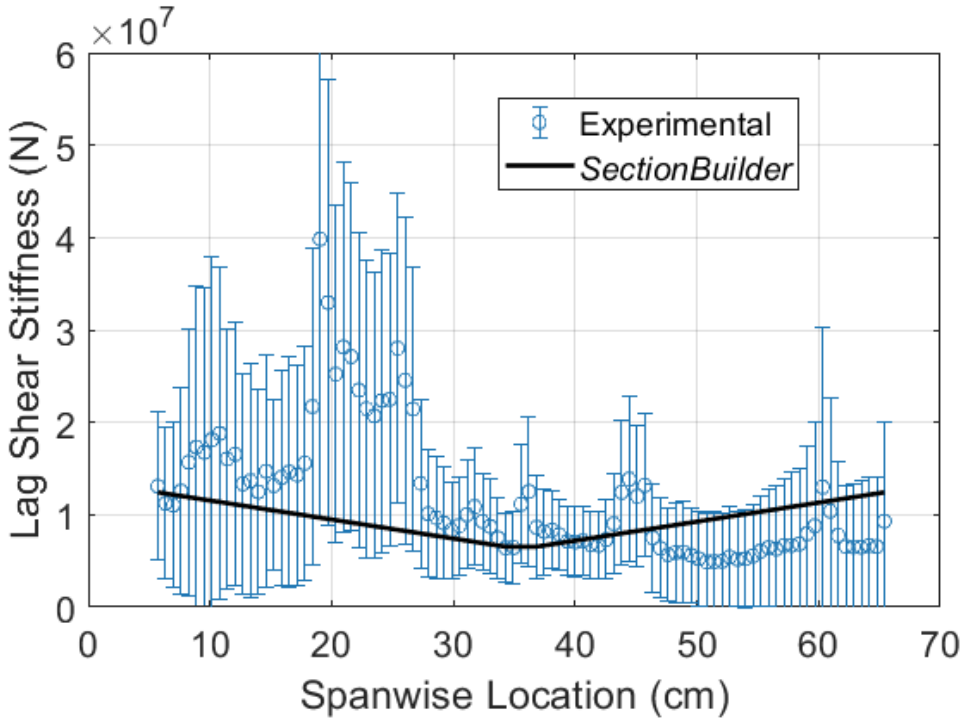

Figure 6.31: Lag shear stiffness K_{22} measurements for the tapered aluminum beam.

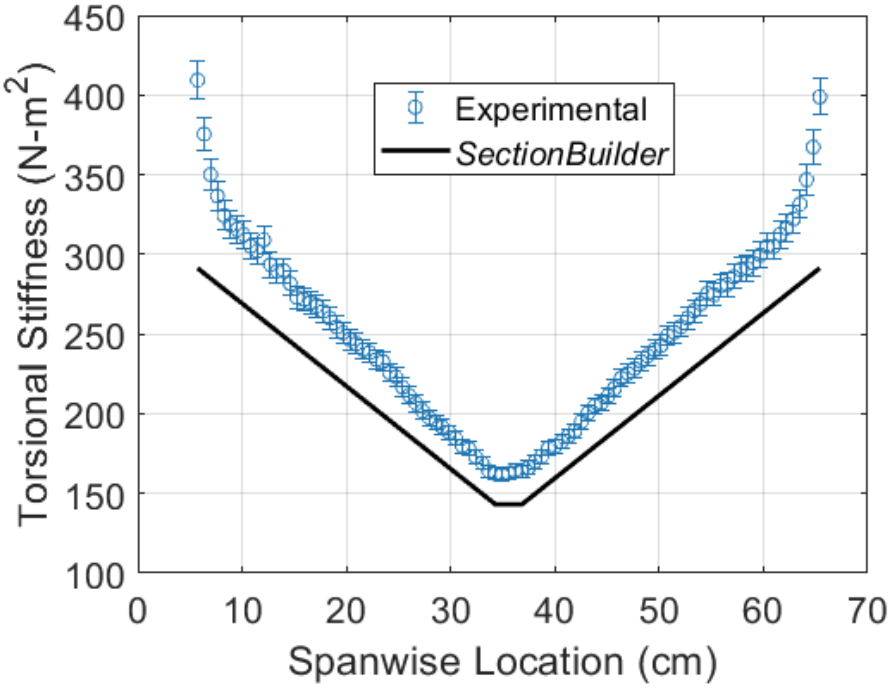

Figure 6.32: Torsional stiffness K_{44} measurements for the tapered aluminum beam.

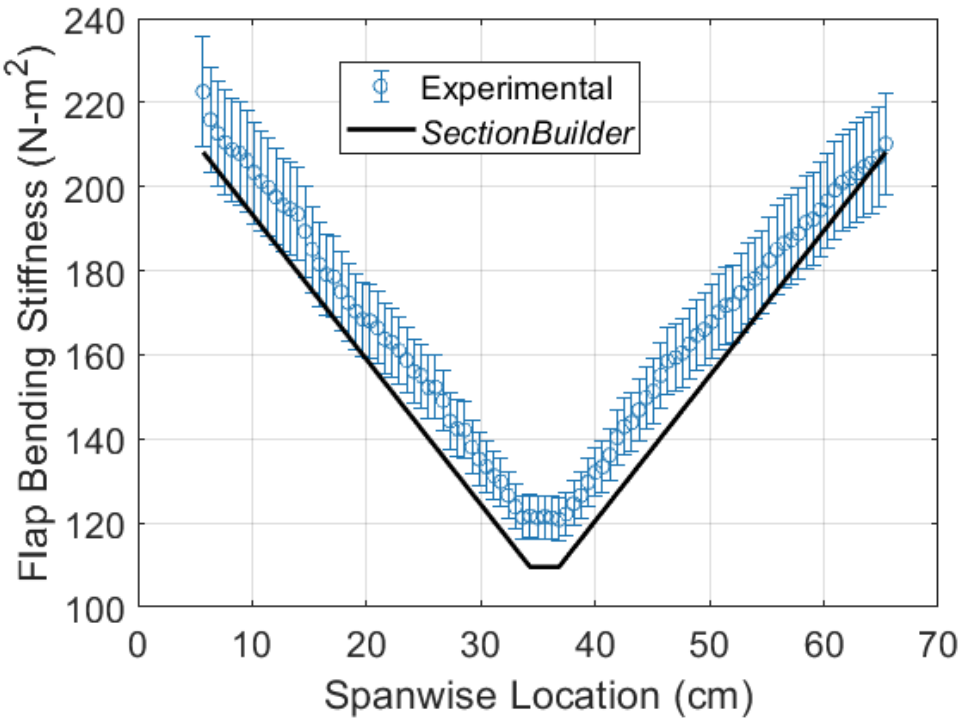

Figure 6.33: Flap bending stiffness K_{55} measurements for the tapered aluminum beam.

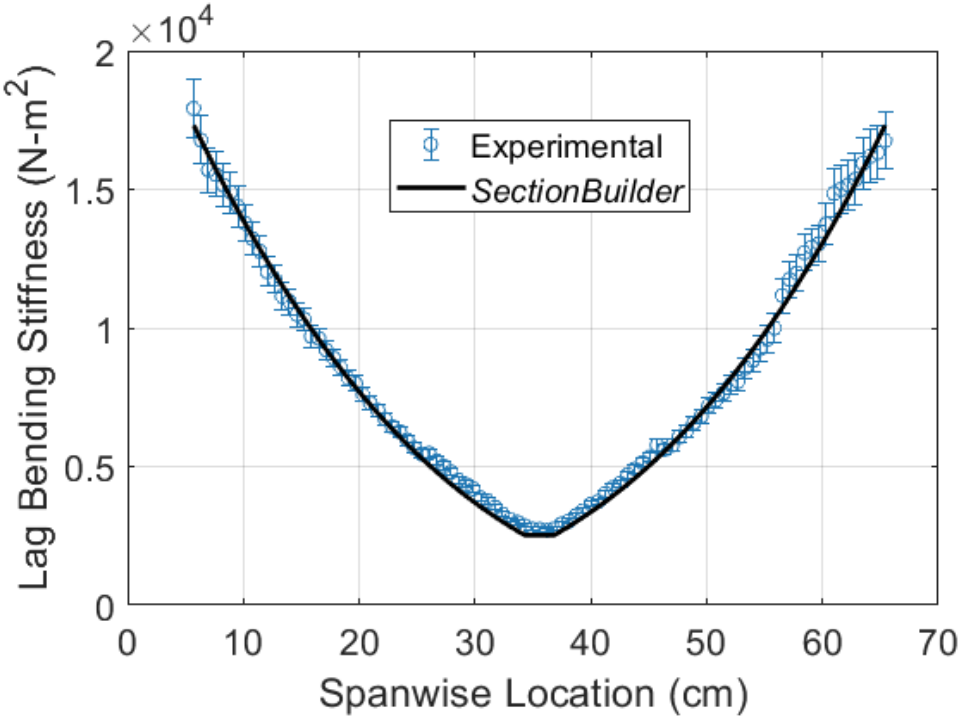

Figure 6.34: Lag bending stiffness K_{66} measurements for the tapered aluminum beam.

case, the axial stiffness was the only stiffness value overpredicted, with an average difference of about 12%. The remaining four stiffness components were all on average underpredicted compared to their corresponding measurements, with a 12%, 15%, 7%, and 3% average difference in the lag shear, torsional, flap bending, and lag bending stiffness components, respectively.

6.5 Summary and Conclusions

The experimental measurements of the sectional stiffness properties for five different beams was presented in this chapter. The first set of tests were presented for three identical prismatic aluminum beams, with the measurements showing overall good agreement with one another. With the exception of the lag shear stiffness, which had a noticeable increase in the measured stiffness close to the clamped boundary, the measured properties were mostly constant along the span, as expected for a beam whose cross-sectional geometry remains uniform along its length. Stiffness measurements were also calculated from these tests based on the displacement and rotation based methods, which showed generally good agreement in the flap bending stiffness but showed substantial differences when considering the much larger lag bending stiffness. In this case, it was expected that rigid body motion resulted in the substantial differences observed using the displacement and rotation based methods, which got filtered out in the current method due to the use of strain measurements, which are invariant to rigid body motion.

Results were next presented for a composite beam whose ply orientation was tailored to produce significant bending/torsion coupling. The use of composite materials and a much smaller thickness resulted in some slightly larger spanwise variations in the measured properties when compare with the aluminum beam; however, the average properties were still shown to be in good agreement with the predicted results. The experiments were also able to accurately capture the

bending/torsion coupling stiffness along the entire length of the beam as well as the extension/lag shear coupling stiffness along the middle portion of the beam.

Two composite blades were then tested to evaluate the impact of internal structural components on the measured stiffness properties. These measurements showed the expected result that the inclusion of a structural spar resulted in larger stiffness values when compared to the same blade without a spar. However, it was also found that the inclusion of the spar resulted in greater spanwise variations in the stiffness measurements, despite the fact that the cross-sectional geometry should be uniform along the span for both blades. A significant difference between the measured and predicted flap bending stiffness of about 50% was observed when including the d-shaped spar in the cross-sectional geometry. While the additional material resulted in a slightly larger thickness than in the designed blade, this would only account for about 12.5% of the observed difference, which would suggest that there are additional differences internal to the blade that can not easily be assessed. However, these large discrepancies highlight the importance of experimental measurements as the manufactured and designed blades can often have unanticipated differences.

Finally, an aluminum beam with a tapered width along its span was tested, with the measurements showing good agreement in the predicted trends in the spanwise variations in properties. Since most traditional approaches can not easily handle these these spanwise variations in properties, these results highlight an important feature that distinguishes the developed methodology from other existing measurement techniques.

Chapter 7: Summary and Conclusions

This chapter presents a summary of this dissertation work, including important conclusions drawn from the presented work, key contributions of this dissertation, and suggestions of alterations and additional tests to continue this work into the future.

7.1 Summary

In this dissertation, a new strain-based methodology for measuring the complete set of cross-sectional stiffness properties of composite rotor blades is developed and presented. The developed method provides improvements over most existing techniques by considering the full 6×6 stiffness matrix, including important off-diagonal elastic coupling terms, as well as providing the ability to measure the properties locally within the blade, as opposed to just average properties for the entire blade.

The technical approach is based on the governing equations for the strain computation from the 2-D cross-sectional analysis code *SectionBuilder* and is presented in Chap. 2. It was shown that to calculate the full 6×6 sectional stiffness matrix, measurements of the applied forces and strains are required, as well as the warping field. Since the warping field cannot be measured experimentally, it is necessary to estimate it numerically based on the cross-sectional geometry and material properties. Investigations on the impact of the numerical warping field were conducted, which showed that the axial and bending compliances could be calculated entirely from the

experimental measurements, but the numerical warping was required for providing a correction to the experimental measurements of the shear and torsional compliances.

Validation of the method is investigated using strain results from the 3-D FEA code *ANSYS* in Chap. 3. The investigated beams had cross-sectional geometries which have received extensive study in past literature, including an aluminum rectangular and composite box beam cross-section. Comparisons were made with analytic solutions, when available, or results from published literature, with the calculated stiffness properties based on the developed data reduction procedure generally showing great agreement. An aluminum beam with a spanwise variation in cross-sectional geometry was also considered, with the calculated results showing great agreement with numerical predictions of the stiffness properties.

Next, a detailed uncertainty analysis was developed for providing confidence intervals on the measured properties. A Taylor series method was implemented for the uncertainty quantification, requiring the calculation of the derivatives of the data reduction equation with respect to the measured variables. The accuracy of this method was assessed by comparing the results to a Monte carlo simulation for the numerical validation models, with the two methods showing good agreement, but with the Taylor series method being several orders of magnitude faster.

A test stand was then developed to carry out an experimental investigation of the methodology, with the key features for the strain and load measurements discussed in Chap. 5. Digital image correlation (DIC) is used to provide an optical measurement of the strain fields, while also providing a measurement of the 3-D deformations needed to accurately calculate the sectional loads. The expected errors in both the DIC system and the 6-axis load cell, used to measure the reaction loads during testing, are investigated for use in the uncertainty quantification. The fabrication of five different beams for experimental testing is also discussed, with the experimental results presented in Chap. 6. The data generated from these tests

showed good agreement with numerical predictions generated by the cross-sectional analysis code *SectionBuilder* for most of the measured stiffness values. For the aluminum beam with a rectangular cross-section, results were also compared to predictions using existing measurement methods, showing the benefits of using a strain-based method over frequency or displacement based methods.

7.2 Key Conclusions

The following is the list of the key conclusions that were drawn based on this work.

1. The general formulation of the developed methodology for calculating the cross-sectional stiffness properties imposed no major restrictions on the types of cross-sectional geometries or materials that could be evaluated.

2. The measurement of the complete 6×6 stiffness matrix is not always feasible. For beams with a rectangular cross-section, if one of the cross-sectional dimensions is too small, then the shear compliance about that dimension cannot be measured. However, the remaining components can all be measured as long as the strain is large enough.

3. The developed data reduction procedure is able to accurately identify the presence of off-diagonal components of the sectional compliance matrix. These off-diagonal components can play a significant role in the analysis of a rotor and can be used to identify the shear center and centroid of the cross-section.

4. Spanwise variations in properties were demonstrated to be accurately captured using the developed methodology, based on both experimental and numerically simulated results.

5. A detailed uncertainty analysis showed that using a highly redundant set of measurements can help reduce the error from the experimental. In addition, the use of the singular value decomposition can almost entirely eliminate certain errors from impacting the calculation of the stiffness properties.

6. Strain measurements are invariant to rigid body motion. Therefore, inaccuracies in the experimental implementation of a boundary condition did not significantly impact stiffness properties calculated based on measured strains.

7. Large strains are required for an accurate calculation of the sectional stiffness properties, although the significant deformations in certain large strain states can bring the beam near the boundary of the depth of field of the DIC cameras. For the most accurate results along the entire span of the blade, it is therefore desired to rotate the beam between tests such that the root and tip portion of the beams are clamped at the base of the test stand. This may be challenging for blades that are used in wind tunnel testing since inserts that facilitate clamping are only included at the root.

8. Prediction of stiffness properties based only on the designed geometry and material can lead to large errors and experimental results showed the importance of measuring the stiffness properties. This was particularly indicated by the measurements of the stiffness properties for the VR-7 airfoil with a spar, where the manufacturing process resulted in a thickness that was 4% larger than the initial design, leading to a much greater flap bending stiffness than initially predicted.

7.3 Original Contributions

The work presented here makes several important original contributions for the structural analysis of composite rotor blades.

1. A new method for calculating the full 6 ×6 sectional stiffness matrix was developed based on the measured strain under static loading. This provided a significant improvement over existing measurement techniques, which focus on only a subset of the matrix and generally include measurements of only the torsional, flap bending, and lag bending stiffnesses for the blade.

2. A new capability to predict spanwise variations in sectional stiffness properties that can arise from common rotor features including taper and twist.

3. A detailed uncertainty analysis method for predicting expected errors in the measured stiffness properties. The effect of each individual parameter can be identified to help improve the quality of the overall measurement, with results from the implemented setup showing that the strain errors had the most significant contributions to the overall uncertainties.

4. A comprehensive experimental database of 3-D displacement and strain fields for composite airfoils under static loading was generated. These data sets can be used in the future to validate the stress and strain predictions of numerical tools for analysis of rotor blades, including 2-D cross-sectional analysis codes such as *SectionBuilder* or VABS as well as 3-D FEM codes such as X3D.

7.4 Future Work

This dissertation focused on the development of a new method for measuring the cross-sectional stiffness properties of composite blades. There are multiple opportunities to expand on the work carried out in this dissertation, with some suggestions for further areas of study listed below.

1. **Additional testing of model scaled beams and composite blades** - this dissertation focused on the development of a new method for measuring the

sectional stiffness properties of beam-like structures, with extensive consideration of how both the numerical and experimental quantities are used in the data reduction equation. While experimental results were obtained for five different beams, which showcased the important features of the method, including measurement of off-diagonal stiffness properties and spanwise variations in stiffness properties, additional testing would prove invaluable for further verification of the method. Possible tests could include:

- *Repeatability of measurements* - Results from the three prismatic aluminum beams showed that the experiments had good repeatability for a simple beam. By manufacturing and testing multiple copies of the remaining test articles, the variations in the composite manufacturing process could be assessed. Specifically, this could help identify the reason for the large discrepancy observed between the measured and predicted flap bending stiffness for the composite rotor with the D-spar.
- *Testing of NACA0012 Airfoils* - Model-scaled rotor blades with a NACA0012 airfoil cross-section have been extensively used for various wind-tunnel tests at the University of Maryland. In most cases, measurements of the torsional and bending stiffness were performed based on displacement or frequency-based techniques and the blades could then be used to provide a comparison with previously measured properties [95, 97, 137].
- *Testing of advanced geometry rotors* - Advanced geometry blades have been fabricated at the University of Maryland for testing on the Maryland Tiltrotor Rig (MTR) in the Glenn L. Martin wind tunnel [138]. Since the blades were manufactured in-house, composite molds exist for a blade with significant twist (37° along its span) and a blade with twist and a swept tip. These molds could be used to manufacture blades for DIC testing of advanced geometry, mach-scaled rotors using the developed

strain-based methodology.

- *Study of the impact of internal structural components* - Two blade models were considered in this work – a blade consisting of only an foam core with a single wrap of carbon-fiber around its exterior and the same blade with the inclusion of an internal d-shaped spar. Most model-scaled rotor blades also have a leading edge weight for stability purposes and may also have various instrumentation, such as pressure sensors or strain gauges, for use in wind tunnel testing. These components are normally neglected in the calculation of the stiffness properties and an interesting case study would be to determine the validity of this assumption.

2. **Updating the experimental setup** - The current experimental setup is capable of testing a wide range of beams; however, there are multiple stages in the analysis that could be automated to help achieve more consistent and possibly accurate results. Since the testing for a single beam requires multiple days to collect data over the full range of necessary load conditions, this would be particularly important if applying the method to full rotor systems, where at least four individual blades need to be fabricated and tested. Camera calibration, test article loading, and the DIC analysis setup are procedures that are often repeated in a very similar manner across tests, and automation of these processes could lead to significant time savings.

   In addition, the uncertainty analysis identified the strain measurements as the key contributor to the overall uncertainty in the stiffness properties. By incorporating multiple sets of cameras along the span, the cameras would no longer have to be translated during testing and would eliminate the corresponding errors arising from this rigid-body motion, which could substantially reduce the overall uncertainty in the measurements. If an array of cameras

were also included to capture images on all external surfaces at the same time, the required time for the experimental tests could be dramatically reduced.

3. **Identifying the material properties** - Accurately identifying the material properties for composites is often difficult, requiring specially shaped samples and specific test procedures. In the developed methodology, a combination of experimental data and a numerical warping field are required for calculating the stiffness matrix; however, it was shown that axial and bending properties are determined entirely from the experimental data. Since the partial derivatives of the stiffness properties with respect to the material inputs are already calculated as part of the uncertainty analysis, an optimization procedure could then be applied based on these derivatives to minimize the residual between the measured and predicted stiffness matrices. This could then be used to identify the material properties (Young's modulus, poisson ratio, and shear modulus), as well as update other input parameters such as the ply orientation.

4. **Measuring the sectional mass properties of the blade** - Extensive studies have been performed at the University of Texas at Austin on the use of DIC to measure the modal properties of blades through an operational modal analysis. The cameras used in the current DIC setup only have a frame rate of 50 fps (frame per second), which is not fast enough to measure the modal properties; however, with high speed cameras, the two methods could be combined to provide a full characterization of the sectional properties of composite blades. The methodology from this dissertation could be used to first calculate the stiffness properties under static loading. The measurement of the mode shapes and frequencies could then be used to extract the mass properties based on the already measured stiffness properties.

5. **Development of a full-scale test rig** - Full scale helicopter rotors have many advanced features, which are well suited for analysis using the developed methodology and normally aren't incorporated on model scaled rotors. Since helicopter companies often already have access to equipment, such as MTS machines, capable of testing rotor blades under a variety of load conditions, generating the static load cases necessary to measure the stiffness properties should be feasible. DIC can be applied at a wide range of scales, but application to a full-scale rotor blade may lead to unique challenges not present at the current scale. However, since DIC is a non-contact measurement technique requiring only a high contrast speckle pattern normally generated using paint and ink, the testing would be minimally invasive and the blades could still be used for normal operations.

Appendix A: Singular Value Decomposition

The *singular value decomposition* (SVD) theorem [122] states that given a matrix $\underline{\underline{A}} \in \mathbb{C}^{m \times n}$, with $m \geq n$ but not necessarily of full rank, it can be factorized into the matrix product

$$\underline{\underline{A}} = \underline{\underline{U}}\,\underline{\underline{\Sigma}}\,\underline{\underline{V}}^* \tag{A.1}$$

where $\underline{\underline{U}} \in \mathbb{C}^{m \times m}$ is unitary, $\underline{\underline{V}} \in \mathbb{C}^{n \times n}$ is unitary, $\underline{\underline{\Sigma}} \in \mathbb{R}^{m \times n}$, and $(\cdot)^*$ indicates the conjugate transpose. Matrix $\underline{\underline{\Sigma}}$ contains real, non-negative numbers along only its main diagonal with the remainder of the components equal to 0. The diagonal entries σ_i of $\underline{\underline{\Sigma}}$, arranged in descending order, are

$$\sigma_1 \geq \sigma_2 \geq \ldots \geq \sigma_r > \sigma_{r+1} = \ldots \sigma_n = 0 \tag{A.2}$$

where σ_i are the *singular values* of $\underline{\underline{A}}$ and $r \leq n$ is the rank of $\underline{\underline{A}}$. If $\underline{\underline{A}}$ is of full rank, $r = n$ and the singular values are all positive. Since $\underline{\underline{U}}$ and $\underline{\underline{V}}$ are unitary matrices, meaning they are square matrices whose inverse is equivalent to their conjugate transpose, the inverse of $\underline{\underline{A}}$ can be written as

$$\begin{aligned} \underline{\underline{A}}^{-1} &= \left(\underline{\underline{U}}\,\underline{\underline{\Sigma}}\,\underline{\underline{V}}^*\right)^{-1} \\ &= \underline{\underline{U}}^{-1}\underline{\underline{\Sigma}}^{-1}\underline{\underline{V}}^{-1*} \\ &= \underline{\underline{U}}^*\underline{\underline{\Sigma}}^{-1}\underline{\underline{V}} \end{aligned} \tag{A.3}$$

where, because $\underline{\underline{\Sigma}}$ is non-square, $\underline{\underline{\Sigma}}^{-1}$ is the left inverse defined by $\underline{\underline{\Sigma}}^{-1}\,\underline{\underline{\Sigma}} = \underline{\underline{I}}$, whose only non-zero elements are the reciprocals of the singular values located along its main diagonal.

A.1 Computation of the SVD

A simple way to compute the SVD is to solve the eigenvalue problem for the matrix product $\underline{\underline{A}}^*\underline{\underline{A}} = \underline{\underline{V}}\,\underline{\underline{\Sigma}}^2\,\underline{\underline{V}}^*$ and then use the eigenvalues and eigenvectors to solve the system $\underline{\underline{U}}\,\underline{\underline{\Sigma}} = \underline{\underline{A}}\,\underline{\underline{V}}$ for the unitary matrix $\underline{\underline{U}}$. However, the condition number of $\underline{\underline{A}}^*\underline{\underline{A}}$ is the square of the condition number of $\underline{\underline{A}}$ and this becomes much more sensitive to perturbations and may become unstable. An alternative, stable method for reducing the SVD to an eigenvalue problem is to form the $(m+n)\times(m+n)$ Hermitian matrix defined by

$$\underline{\underline{H}} = \begin{bmatrix} \underline{\underline{0}} & \underline{\underline{A}}^* \\ \underline{\underline{A}} & \underline{\underline{0}} \end{bmatrix} \tag{A.4}$$

The decomposition given by Eq (A.1) implies that $\underline{\underline{A}}\,\underline{\underline{V}} = \underline{\underline{U}}\,\underline{\underline{\Sigma}}$ and $\underline{\underline{A}}^* = \underline{\underline{V}}\,\underline{\underline{\Sigma}}$ which means that the following equation holds

$$\underline{\underline{H}} \begin{bmatrix} \underline{\underline{V}} & \underline{\underline{V}} \\ \underline{\underline{U}} & -\underline{\underline{U}} \end{bmatrix} = \begin{bmatrix} \underline{\underline{V}} & \underline{\underline{V}} \\ \underline{\underline{U}} & -\underline{\underline{U}} \end{bmatrix} \begin{bmatrix} \underline{\underline{\Sigma}} & \underline{\underline{0}} \\ \underline{\underline{0}} & -\underline{\underline{\Sigma}} \end{bmatrix} \tag{A.5}$$

and describes the eigenvalue decomposition of $\underline{\underline{H}}$. Since the singular values of $\underline{\underline{A}}$ must be non-negative, they are equivalent to the absolute values of the eigenvalues of $\underline{\underline{H}}$, as seen by the last matrix in Eq. (A.5). This approach will be stable since the condition number of $\underline{\underline{H}}$ is the same as that of $\underline{\underline{A}}$. The eigenvalue problem for the Hermitian matrix can then be solved numerically using a two-part computation, first reducing the matrix to a bidiagonal form and then diagonalizing the bidiagonal matrix; depending on the size of $\underline{\underline{A}}$, this can be efficiently computed using the *Golub-*

Kahan bidiagonalization ($m < 5/3n$) or the *LHC bidiagonalization* ($m > 5/3n$) [122]. In practice, algorithms for computing the SVD are readily available in the scientific computing packages available for most scripting languages.

A.2 Reduced SVD

While the SVD given in Eq. A.1 provides a full factorization of $\underline{\underline{A}}$, if $\underline{\underline{A}}$ is not square (i.e. $m \neq n$) then this generally provides additional information that is not needed in most applications. Consider first the matrix $\underline{\underline{\Sigma}}$; this can be partitioned according to

$$\underline{\underline{\Sigma}} = \begin{bmatrix} \hat{\underline{\underline{\Sigma}}} \\ \underline{\underline{0}} \end{bmatrix} \tag{A.6}$$

where $\hat{\underline{\underline{\Sigma}}} \in \mathbb{R}^{n \times n}$ is a square diagonal matrix of the singular values σ_i, $\hat{\underline{\underline{\Sigma}}} = \mathrm{diag}\,(\sigma_i)$. The matrix of left singular vectors $\underline{\underline{U}}$ can be partitioned according to

$$\underline{\underline{U}} = \begin{bmatrix} \hat{\underline{\underline{U}}} & \underline{\underline{\Gamma}} \end{bmatrix} \tag{A.7}$$

where $\hat{\underline{\underline{U}}} \in \mathbb{C}^{m \times n}$ and $\underline{\underline{\Gamma}} \in \mathbb{C}^{m \times (m-n)}$. The SVD can then be written as

$$\begin{aligned} \underline{\underline{A}} &= \underline{\underline{U}}\,\underline{\underline{\Sigma}}\,\underline{\underline{V}}^* \\ &= \begin{bmatrix} \hat{\underline{\underline{U}}} & \underline{\underline{\Gamma}} \end{bmatrix} \begin{bmatrix} \hat{\underline{\underline{\Sigma}}} \\ \underline{\underline{0}} \end{bmatrix} \underline{\underline{V}}^* \\ &= \hat{\underline{\underline{U}}}\,\hat{\underline{\underline{\Sigma}}}\,\underline{\underline{V}}^* + \underline{\underline{\Gamma}}\,\underline{\underline{0}}\,\underline{\underline{V}}^* \end{aligned} \tag{A.8}$$

Since the second term $\underline{\underline{\Gamma}}\,\underline{\underline{0}}\,\underline{\underline{V}}^*$ evaluates to $\underline{\underline{0}}$, the SVD can be factorized more compactly as $\underline{\underline{A}} = \hat{\underline{\underline{U}}}\,\hat{\underline{\underline{\Sigma}}}\,\underline{\underline{V}}^*$ which is known as the *reduced SVD*. While $\hat{\underline{\underline{U}}}$ is not unitary, it still forms an orthonormal basis and the equality $\underline{\underline{A}}^{-1} = \hat{\underline{\underline{U}}}^*\,\hat{\underline{\underline{\Sigma}}}^{-1}\,\underline{\underline{V}}$ holds. Moreover this only requires knowledge of the first n left singular vectors, which can

result in significant savings over the full SVD, in terms of both computational time and storage, when $m \gg n$.

Appendix B: Complex Step Derivative

When calculating the derivative of a function, an alternative to finite difference approximations is a complex step derivative. The derivation of the complex step derivative can be considered by using a Taylor Series expansion of the function $f(x)$ about $x + i\epsilon$ given by:

$$f(x + i\epsilon) = f(x) + i\epsilon\frac{df(x)}{dx} - \epsilon^2\frac{h^2}{2!}\frac{d^2f(x)}{dx^2} - i\epsilon^3\frac{h^3}{3!}\frac{d^3f(x)}{dx^3} + \cdots \tag{B.1}$$

Taking the imaginary components of both sides ($\mathrm{Im}\,(\cdot)$), dividing by ϵ, and rearranging in terms of $df(x)/dx$ gives

$$\frac{df(x)}{dx} = \frac{1}{\epsilon}\,\mathrm{Im}\,(f(x + i\epsilon)) + \mathcal{O}(\epsilon^2) \tag{B.2}$$

For a small $\epsilon \ll 1$, the derivative is then

$$\frac{df(x)}{dx} \approx \frac{1}{\epsilon}\,\mathrm{Im}\,(f(x + i\epsilon)) \tag{B.3}$$

This is advantageous compared to the conventional central difference approximation given by

$$\frac{df(x)}{dx} \approx \frac{f(x + \epsilon) - f(x - \epsilon)}{2\epsilon} \tag{B.4}$$

as it allows the derivative to be calculated without evaluating a difference of function, which provides a better accuracy. In addition, taking the real part of Eq. (B.1) gives

$$f(x) = \mathrm{Re}(f(x + i\epsilon)) + \mathcal{O}(\epsilon^2) \tag{B.5}$$

which means that $f(x) \approx \mathrm{Re}(f(x + i\epsilon))$ and therefore both the functional value and its derivative can be calculated using a single complex function evaluation.

If considering a function of multiple variables, the partial derivatives can be evaluated by perturbing each variable separately. For example, if $f = f(X_1, X_2, \cdots, X_n)$ then the partial derivatives evaluate to

$$\begin{aligned}
\frac{\partial f}{\partial X_1} &\approx \frac{1}{\epsilon_1} \mathrm{Im}(f(X_1 + i\epsilon_1, X_2, \cdots, X_n)) \\
\frac{\partial f}{\partial X_2} &\approx \frac{1}{\epsilon_2} \mathrm{Im}(f(X_1, X_2 + i\epsilon_2, \cdots, X_n)) \\
&\vdots \\
\frac{\partial f}{\partial X_n} &\approx \frac{1}{\epsilon_2} \mathrm{Im}(f(X_1, X_2, \cdots, X_n + i\epsilon_n))
\end{aligned} \tag{B.6}$$

requiring n complex functional evaluations to compute all the partial derivatives.

Bibliography

[1] Rastogi, P. K., *Digital Optical Measurement Techniques and Applications*, Artech House, Norwood, MA, 2015.

[2] Glauert, H., "The Theory of the Autogyro," *The Journal of the Royal Aeronautical Society*, Vol. 31, (198), June 1927, pp. 483–508.

[3] Datta, A., Nixon, M. W., and Chopra, I., "Review of Rotor Loads Predictions with the Emergence of Rotorcraft CFD," *Journal of the American Helicopter Society*, Vol. 52, (4), October 2007, pp. 287–317.

[4] Murugan, S., Ganguli, R., and Harursampath, D. K., "Stochastic Aeroelastic Analysis of Composite Helicopter Rotor," *Journal of the American Helicopter Society*, Vol. 56, (1), January 2011, pp. 1–13.

[5] Pflumm, T., Rex, W., and Hajek, M., "Propagation of Material and Manufacturing Uncertainties in Composite Helicopter Rotor Blades," 45th European Rotorcraft Forum, September 17-20 2019.

[6] Yeo, H. and Johnson, W., "Prediction of Rotor Structural Loads with Comprehensive Analysis," *Journal of the American Helicopter Society*, Vol. 53, (2), April 2008, pp. 193–209.

[7] Rabbott, J. P., A., L. A., and Paglino, V. M., "A Presentation of Measured and Calculated Full-Scale Rotor Blade Aerodynamic and Structural Loads," USAAVLABS TR 66-31, 1966.

[8] Bousman, W. G., Young, C., Gilbert, N. E., Strawn, R. C., Miller, J. V., Maier, T. H., Costes, M., and Beaumier, P., "A Comparision of Lifting-Line and CFD Methods with Flight Test Data from a Research Puma Helicopter," NASA TM 110421, October 1996.

[9] Heffernan, R. M. and Gaubert, M., "Structural and Aerodynamic Loads and Performance Measurements of an SA 349/2 Helicopter with an Advanced Geometry Rotor," NASA TM 88370, November 1986.

[10] Yeo, H., Bousman, W. G., and Johnson, W., "Performance Analysis of a Utility Helicopter with Standard and Advanced Rotors," *Journal of the American Helicopter Society*, Vol. 49, (3), July 2004, pp. 250–270.

[11] Ormiston, R., "An Investigation of the Mechanical Airloads Problem for Evaluating Rotor Blade Structural Dynamics Analysis," AHS Fourth Decennial Specialists' Conference on Aeromecanics, January 21-23 2004.

[12] Datta, A. and Chopra, I., "Validation and Understanding of UH-60A Vibratory Loads in Steady Level Flight," *Journal of the American Helicopter Society*, Vol. 49, (3), July 2004, pp. 271–287.

[13] Jung, S. N., You, Y. H., Lau, B. H., Johnson, W., and Lim, J. W., "Evaluation of Rotor Structural and Aerodynamic Loads Using Measured Blade Properties," *Journal of the American Helicopter Society*, Vol. 58, (4), October 2013, pp. 1–12.

[14] Jung, S. N., You, Y. H., Dhadwal, M. K., Riemenschneider, J., and Hagerty, B. P., "Study on Blade Property Measurement and Its Influence on Air/Structural Loads," *AIAA Journal*, Vol. 53, (11), November 2015, pp. 3221–3232.

[15] Datta, A. and Johnson, W., "An Assessment of the State-of-the-Art in Multidisplinary Aeromechanical Analyses," American Helicopter Society Specialist's Conference on Aeromechanics, January 23-25 2008.

[16] Johnson, W., "A History of Rotorcraft Comprehensive Analyses," American Helicopter Society 69th Annual Forum, May 21-23 2013.

[17] de Saint-Venant, J. C. B., "Mémoire sur la torsion de prismes," *Receuil des Savants Étrangers*, Vol. 14, 1855, pp. 233–560.

[18] de Saint-Venant, J. C. B., "Mémoire sur la flexion de prismes," *Journal de Mathématiques de Liouville*, Vol. 1, 1856, pp. 89–189.

[19] Timoshenko, S. P., "On the Correction for Shear of the Differential Equation for Transverse Vibrations of Prismatic Bars," *Philosophical Magazine and Journal of Science*, Vol. 41, (245), 1921, pp. 744–746.

[20] Ieson, D., "Saint-Venant's Problem for Inhomogeneous and Anisotropic Elastic Bodies," *Journal of Elasticity*, Vol. 6, (3), July 1976, pp. 277–294.

[21] Ieson, D., "On Saint-Venant's Problem," *Archive for Rational Mechanics and Analysis*, Vol. 91, (4), December 1986, pp. 363–373.

[22] Dong, S. B., Kosmatka, J. B., and Lin, H. C., "On Saint-Venant's Problem for an Inhomogeneous, Anisotropic Cylinder-Part I: Methodology for Saint-Venant Solutions," *Journal of Applied Mechanics*, Vol. 68, (3), May 2001, pp. 376–381.

[23] Kosmatka, J. B., Lin, H. C., and Dong, S. B., "On Saint-Venant's Problem for an Inhomogeneous, Anisotropic Cylinder-Part II: Cross-Sectional Properties," *Journal of Applied Mechanics*, Vol. 68, (3), May 2001, pp. 382–391.

[24] Lin, H. C., Kosmatka, J. B., and Dong, S. B., "On Saint-Venant's Problem for an Inhomogeneous, Anisotropic Cylinder-Part III: End Effects," *Journal of Applied Mechanics*, Vol. 68, (3), May 2001, pp. 392–398.

[25] Berdichevsky, V. L., "On the Energy of an Elastic Rod," *Journal of Applied Mathematics and Mechanics*, Vol. 45, (4), January 1981, pp. 518–529.

[26] Atilgan, A. R. and Hodges, D. H., "Unified Nonlinear Analysis for Nonhomogeneous Anisotropic Beams with Closed Cross-sections," *AIAA Journal*, Vol. 29, (11), November 1991, pp. 1990–1999.

[27] Atilgan, A. R., Hodges, D. H., and Fulton, M. V., "Nonlinear Deformation of Composite Beams: Unification of Cross-sectional and Elastic Analyses," *Applied Mechanics Reviews*, Vol. 44, (11), November 1991, pp. S9–S15.

[28] Hodges, D. H., *Nonlinear Composite Beam Theory*, AILL, Reston, Virginia, 2006.

[29] Yu, W. B., Hodges, D. H., Volovoi, V. V., and Cesnik, C. E. S., "On Timoshenko-like Modeling of Initially Curved and Twisted Composite Beams," *International Journal of Solids and Structures*, Vol. 39, (19), September 2002, pp. 5101–5121.

[30] Kim, J. S., Cho, M., and Smith, E. C., "An Asymptotic Analysis of Composite Beams with Kinematically Corrected End Effects," *International Journal of Solids and Structues*, Vol. 45, (7), April 2008, pp. 1954–1977.

[31] Giavotto, V., Borri, M., Mantegazza, P., Ghiringhelli, G., Carmaschi, V., Maffioli, G. C., and Mussi, F., "Anisotropic Beam Theory and Applications," *Computer and Structures*, Vol. 16, (1-4), December 1983, pp. 403–413.

[32] Borri, M. and Merlini, T., "A Large Displacement Formulation for Anisotropic Beam Analysis," *Meccanica*, Vol. 21, March 1986, pp. 30–37.

[33] Borri, M., Ghiringhelli, G. L., and Merlini, T., "Linear Analysis of Naturally Curved and Twisted Anisotropic Beams," *Composites Engineering*, Vol. 2, (5-7), January 1992, pp. 433–456.

[34] Mielke, A., "Saint-Venant's Problem and Semi-inverse Solutions in Nonlinear Elasticity," *Archive of Rational Mechanics and Analysis*, Vol. 102, September 1988, pp. 205–229.

[35] Mielke, A., "Normal Hyperbolicity of Center Manifolds and Saint-Venant's Principle," *Archive of Rational Mechanics and Analysis*, Vol. 110, December 1990, pp. 353–372.

[36] Zhong, W. X., "Plane Elasticity Problem in Strip Domain and Hamiltonian System," *Journal of Dalian University of Technology*, Vol. 4, 1991, pp. 373–384.

[37] Zhong, W. X., "Plane Elasticity in Sectorial Domain and the Hamiltonian System," *Applied Mathematics and Mechanics*, Vol. 15, December 1994, pp. 1113–1123.

[38] Morandini, M., Chierichetti, M., and Mantegazza, P., "Characteristic Behavior of Prismatic Anisotropic Beam via Generalized Eigenvectors," *International Journal of Solids and Structures*, Vol. 47, (10), May 2010, pp. 1327–1337.

[39] Druz, A. N. and Ustinov, Y. A., "Green's Tensor for an Elastic Cylinder and its Applications in the Development of the Saint-Venant Theory," *Journal of Applied Mathematics and Mechanics*, Vol. 60, (1), January 1996, pp. 97–104.

[40] Druz, A. N., Polyakov, N. A., and Ustinov, Y. A., "Homogeneous Solutions and Saint-Venant Problems for a Naturally Twisted Rod," *Journal of Applied Mathematics and Mechanics*, Vol. 60, (4), January 1996, pp. 657–664.

[41] Bauchau, O. A. and Han, S. L., "Three-Dimensional Beam Theory for Flexible Multibody Dynamics," *Journal of Computational and Nonlinear Dynamics*, Vol. 9, (4), 2014.

[42] Bauchau, O. A. and Han, S. L., "Nonlinear Three-Dimensional Beam Theory for Flexible Multibody Dynamics," *Multibody System Dynamics*, Vol. 34, (3), July 2015, pp. 211–242.

[43] Houbolt, J. and Brooks, G., "Differential Equations of Motion for Combined Flapwise Bending, Chordwise Bending, And Torsion of Twisted Nonuniform Rotor Blades," NACA TN 3905, February 1957.

[44] Hodges, D. H. and Dowell, E. H., "Nonlinear Equations of Motion for the Elastic Bending and Torsion of Twisted Nonuniform Rotor Blades," NASA TN D-7818, December 1974.

[45] Rosen, A. and Friedmann, P., "Nonlinear Equations of Equilibrium for Elastic Helicopter or Wind Turbine Blades Undergoing Moderate Deformation," NASA CR-159478, December 1978.

[46] Hodges, D. H., Ormiston, R. A., and Peter, D. A., "On the Nonlinear Deformation Geometry of Euler-Bernoulli Beams," NASA TP 1566, April 1980.

[47] Hodges, D. H., "Nonlinear Equations for Dynamics of Pretwisted Beams Undergoing Small Strains and Large Rotations," NASA TP 2470, May 1985.

[48] Bauchau, O. A., "A Beam Theory for Anisotropic Materials," *Journal of Applied Mechanics*, Vol. 52, June 1985, pp. 416–422.

[49] Bauchau, O. A. and Hong, C. H., "Nonlinear Composite Beam Theory," *Journal of Applied Mechanics*, Vol. 55, March 1988, pp. 156–163.

[50] Hodges, D. H., "A Mixed Variational Formulation Based on Exact Instrinsic Equations for Dynamics of Moving Beams," *International Journal of Solids and Structures*, Vol. 26, (11), December 1990, pp. 1253–1273.

[51] Smith, E. C. and Chopra, I., "Aeroelastic Response, Loads, and Stability of a Composite Rotor in Forward Flight," *AIAA Journal*, Vol. 31, (7), July 1993, pp. 1265–1273.

[52] Bauchau, O. A. and Kang, N. K., "A Multibody Formulation for Helicopter Structural Dynamic Analysis," *Journal of the American Helicopter Society*, Vol. 38, (2), April 1993, pp. 3–14.

[53] Bauchau, O. A., Bottasso, C. L., and Nikishkov, Y. G., "Modeling Rotorcraft Dynamics and Finite Element Multibody Procedures," *Mathematical and Computer Modeling*, Vol. 33, (10), May 2001, pp. 1113–1137.

[54] Johnson, W., "Rotorcraft Dynamic Models for a Comprehensive Analysis," American Helicopter Society 54th Annual Forum, May 20-22 1998.

[55] Saberi, H., Khoshlahjeh, M., Ormiston, R., and Rutkowski, M., "Overview of RCAS and Application to Advanced Rotorcraft Problems," 4th AHS Decennial Specialist's Conference on Aeromechanics, January 21-23 2004.

[56] Abishek, A., Datta, A., and Chopra, I., "Prediction of UH-60A Structural Loads Using Multibody Analysis and Swashplate Dynamics," *Journal of the American Helicopter Society*, Vol. 46, (2), March 2009, pp. 474–490.

[57] Hodges, D. H., Atilgan, A. R., Cesnik, C. E. S., and Fulton, M. V., "On a Simpified Strain Energy Function for Geometrically Nonlinear Behaviour of Anisotropic Beams," *Composites Engineering*, Vol. 2, (5-7), 1992, pp. 513–526.

[58] Cesnik, C. E. S. and Hodges, D. H., "VABS: A New Concept for Composite Rotor Blade Cross-sectional Modeling," *Journal of the American Helicopter Society*, Vol. 42, (1), January 1997, pp. 27–38.

[59] Yu, W. B., Volovoi, V. V., Hodges, D. H., and Hong, X., "Validation of the Variational Asymptotic Beam Sectional Analysis," *AIAA Journal*, Vol. 40, (10), October 2002, pp. 2105–2112.

[60] Han, S. L. and Bauchau, O. A., "Nonlinear Three-Dimensional Beam Theory for Flexible Multibody Dynamics," *Multibody System Dynamics*, Vol. 34, (3), July 2015, pp. 211–242.

[61] Han, S. L. and Bauchau, O. A., "High-fidelity, 3D Stress Prediction for Composite Rotor Blades," American Helicopter Society 73rd Annual Forum, May 9-11 2017.

[62] Blasques, J. P., Bitsche, R. D., Fedorov, V., and Eder, M. A., "Applications of the Beam Cross Section Analysis Software (BECAS)," 26th Nordic Seminar on Computational Mechanics, October 23-25 2013.

[63] Mansfield, E. and Sobey, A., "The Fibre Composite Helicopter Blade; Part 1: Stiffness Properties; Part 2: Prospects for Aeroelastic Tailoring," *Aeronautical Quarterly*, Vol. 30, (2), May 1979, pp. 413–449.

[64] Winckler, S. J., "Hygrothermally Curvature Stable Laminates with Tension-Torsion Coupling," *Journal of the American Helicopter Society*, Vol. 3, (1), July 1985, pp. 56–58.

[65] Bauchau, O. A., "An Approach to Ideal Twist Distribution in Tilt Rotor VTOL Blade Designs," Rensselaer Polytechnic Institute Rotorcraft Technology Center Report No. D-86-2, July 1986.

[66] Smith, E. C. and Chopra, I., "Formulation and Evaluation of an Analytical Model for Composite Box-Beams," *Journal of the American Helicopter Society*, Vol. 36, (3), July 1991, pp. 23–35.

[67] Chandra, R., Stemple, A. D., and Chopra, I., "Thin-Walled Composite Beams under Bending, Torsional, and Extensional Loads," *Journal of Aircraft*, Vol. 27, (7), July 1990, pp. 619–626.

[68] Soykasap, O. and Hodges, D. H., "Performance Enhancement of a Composite Tilt-Rotor Using Aeroelastic Tailoring," *Journal of Aircraft*, Vol. 37, (5), October 2000, pp. 850–858.

[69] Ozbay, S., Bauchau, O. A., Dancila, D. S., and Armanios, E. A., "Stability Analysis of Extension-Twist Coupled Composite Rotor Blades," American Helicopter Society 60th Annual Forum, June 8-10 2004.

[70] Haynes, R. A. and Armanios, E. A., "New Families of Hygrothermally Stable Composite Laminates with Optimal Extension-Twist Coupling," *AIAA Journal*, Vol. 48, (12), December 2010, pp. 2954–2961.

[71] Lake, R. C., Nixon, M. W., Wilbur, M. L., Singleton, J. D., and Mirick, P. H., "Demonstration of an Elastically Coupled Twist Control Concept for Tilt Rotor Blade Application," *AIAA Journal*, Vol. 32, (3), July 1994, pp. 1549–1551.

[72] Bao, J., Nagaraj, V. T., Chopra, I., and Bernhard, A. P. F., "Development of Mach Scale Rotors with Tailored Composite Coupling for Vibration Reduction," *Journal of Aircraft*, Vol. 43, (4), July-August 2006, pp. 922–931.

[73] Bao, J., Nagaraj, V. T., Chopra, I., and Bernhard, A. P. F., "Wind Tunnel Test of Five Sets of Mach Scale Composite Tailored Rotor with Flap-Bending/Torsion Couplings for Vibration Reduction," *Journal of the American Helicopter Society*, Vol. 53, (3), July 2008, pp. 215–225.

[74] Fedorov, V. and Berggreen, C., "Bend-twist Coupling Potential of Wind Turbine Blades," *Journal of Physics: Conference Series*, Vol. 524, 2014, pp. 1–10.

[75] Stäblein, A. R., *MARE-WINT New Materials and Reliabiliy in Wind Turbine Technology: Analysis and Design of Bend-Twist Coupled Wind Turbine Blades*, Springer, Dordrecht, Heidelberg, London, New-York, 2016.

[76] Bauchau, O. A. and Hong, C. H., "Large Displacement Analysis of Naturally Curved and Twisted Composite Beams," *AIAA Journal*, Vol. 25, (11), November 1987, pp. 1469–1476.

[77] Cesnik, C. E. S. and Hodges, D. H., "Variational Asymptotical Analysis of Initially Twisted and Curved Composite Beams," *International Journal for Engineering Analysis and Design*, Vol. 1, (2), April 1994, pp. 177–187.

[78] Hodges, D. H., "Unified Approach for Accurate and Efficient Modeling of Composite Rotor Blade Dynamics: The Alexander A. Nikolsky Honorary Lecture," *Journal of the American Helicopter Society*, Vol. 60, (1), January 2015, pp. 1–28.

[79] Epps, J. and Chandra, R., "The Natural Frequencies of Rotating Composite Beams with Tip Sweep," *Journal of the American Helicopter Society*, Vol. 41, (1), January 1996, pp. 29–36.

[80] Sinotte, T. and Bauchau, O. A., "Experimental Strain Measurements of Highly-Curved Blades," American Helicopter Society 75th Annual Forum, May 13-16 2019.

[81] Bauchau, O. A., Choi, J. Y., and Bottasso, C. L., "On the Modeling of Shells in Multibody Dynamics," *Multibody System Dynamics*, Vol. 8, January 2002, pp. 459–489.

[82] Bauchau, O. A., Choi, J. Y., and Bottasso, C. L., "Time Integrators for Shells in Multibody Dynamics," *International Journal of Computers and Structures*, Vol. 80, March 2002, pp. 871–889.

[83] Bottasso, C. L., Bauchau, O. A., and Choi, J. Y., "An Energy Decaying Scheme for Nonlinear Dynamics of Shells," *Computer Methods in Applied Mechanics and Engineering*, Vol. 191, March 2002, pp. 3099–3121.

[84] Pardo, D. R. and Branner, K., "Finite Element Analysis of the Cross-Section of Wind Turbine Blade; a Comparision Between Shell and 2D-Solid Models," *Wind Engineering*, Vol. 29, (1), January 2005, pp. 25–31.

[85] Fedorov, V., Dimitrov, N. K., Berggreen, C., Krenk, S., Branner, K., and Berring, P., "Investigation of Structural Behavior due to Bend-Twist Couplings in Wind Turbine Blades," Proceedings of the 17th International Conference of Composite Materials, July 2009.

[86] Bazilevs, Y., Hsu, M. C., Kiendl, J., Wuchner, R., and Bletzinger, K. U., "3D Simulation of Wind Turbine Rotors at Full Scale. Part II: Fluid-Structure Interaction Modeling with Composite Blades," *International Journal for Numerical Methods in Fluids*, Vol. 65, October 2010, pp. 236–253.

[87] Kang, H., Chang, C., Saberi, H., and Ormiston, R., "Assessment of Beam and Shell Elements for Modeling Rotorcraft Blades," *Journal of Aircraft*, Vol. 51, (2), March 2014, pp. 520–531.

[88] Ortun, B., Petot, D., Truong, K. V., and Ohayon, R., "Towards a New Generation of Rotorcraft Comprehensive Analysis; Coupling with CSM and CSD," 34th European Rotorcraft Forum, September 16-19 2008.

[89] Yeo, H., Truong, K., and Ormiston, R., "Assessment of 1-D Versus 3-D Methods for Modeing Rotor Blade Structural Dynamics," 51st AIAA/ASME/ASCE/AH-

S/ASC Structures, Structural Dynamics, and Materials Conference, April 12-15 2010.

[90] Truong, K., Yeo, H., and Ormiston, R., "Investigation of Finite Element Approaches for Rotor Blade Structural Dynamics," 36th European Rotorcraft Forum, September 7-9 2010.

[91] Datta, A. and Johnson, W., "Three-Dimensional Finite Element Formulation and Scalable Domain Decomposition for High-Fidelity Rotor Dynamic Analysis," *Journal of the American Helicopter Society*, Vol. 56, (2), April 2011, pp. 1–14.

[92] Datta, A. and Johnson, W., "An Assessment of the State-of-the-Art in Multidisplinary Aeromechanical Analyses," American Helicopter Society Technical Meeting on Aeromechanics Design for Vertical Lift, January 20-22 2016.

[93] Staruk, W. and Datta, A., "Gimbaled Tiltrotor Conversion Flight Loads Prediction Using Three-Dimensional Structural Analysis," *Journal of Aircraft*, Vol. 56, (2), March-April 2019, pp. 758–770.

[94] Ward, E., Chopra, I., and Datta, A., "Rotation-Frequency-Driven Extension-Torsion Coupled Self-Twisting Rotor Blades," *Journal of Aircraft*, Vol. 55, (5), September-October 2018, pp. 1929–1941.

[95] Trollinger, L. N., *Refined Performance and Loads of a Mach-Scale Rotor at High Advance Ratios*, Master's thesis, University of Maryland, College Park, 2017.

[96] Wang, X. and Trollinger, L. N., "Refined Performance Results on a Slowed Mach-Scaled Rotor at High Advance Ratios," *Journal of the American Helicopter Society*, Vol. 65, (1), January 2020, pp. 28–40.

[97] Saxena, A. and Chopra, I., "Wind Tunnel Testing of a Swashplateless Rotor with Compact Brushless Motor Actuated Flaps for Primary Control," American Helicopter Society Technical Meeting on Aeromechanics Design for Vertical Lift, January 20-22 2016.

[98] Cameron, C. G., *Comprehensive Aeromechanical Measurements of a Model-Scale, Coaxial, Counter-Rotating Rotor System*, Ph.D. thesis, University of Texas at Austin, 2016.

[99] Chandra, R. and Chopra, I., "Experimental and Theoretical Analysis of Composite I-Beams with Elastic Couplings," *AIAA Journal*, Vol. 29, (12), December 1991, pp. 619–626.

[100] Cameron, C. G., Karpatne, A., and Sirohi, J., "Performance of a Mach-Scale Coaxial Counter-Rotating Rotor in Hover," *Journal of Aircraft*, Vol. 53, (3), May-June 2016, pp. 746–755.

[101] Jung, S. N., Dhadwal, M. K., Kim, Y. W., Kim, J. H., and Riemenschneider, J., "Cross-sectional Constants of Composite Blades using Computed Tomography Technique and Finite Element Analysis," *Composite Structures*, Vol. 129, (1), October 2015, pp. 132–142.

[102] Hoffmann, K., *An Introduction to Measurements using Strain Gages*, Hottinger Baldwin Messtechnik GmbH, Alsbach, Germany, 1989.

[103] Kufeld, R., Balough, D. L., Cross, J. L., Studebaker, K. F., Jennison, C. D., and Bousman, W. G., "Flight Testing the UH-60A Airloads Aircraft," American Helicopter Society 50th Annual Forum, May 11-13 1994.

[104] Norman, T. R., Shinoda, P., Peterson, R. L., and Datta, A., "Full Scale Wind Tunnel Test of the UH-60A Airloads Rotor," American Helicopter Society 67th Annual Forum, May 3-5 2011.

[105] Berry, B. and Chopra, I., "Wind Tunnel Testing for Performance and Vibratory Loads of a Variable-Speed Mach-Scale Rotor," American Helicopter Society 67th Annual Forum, May 3-5 2011.

[106] Wang, X., Saxena, A., and Chopra, I., "Measurement and Validation of a Mach-Scale Rotor Performance and Loads at High Advance Ratios," American Helicopter Society 72nd Annual Forum, May 16-19 2016.

[107] Baz, A. and Poh, S., "A New Class of Distributed Sensors," *Journal of Vibration and Acoustics*, Vol. 119, (4), October 1997, pp. 582–589.

[108] Copp, P., "In-flight Rotorcraft Blade Elastic Twist Sensor," *Smart Materials and Structures*, Vol. 23, (4), March 2014, pp. 045021.

[109] Liu, Y., Lacher, A., Wang, G., Purekar, A., and Yu, M., "Wireless Fiber Optic Sensor System for Strain and Pressure Measurements on a Rotor Blade," *Proceedings of SPIE - The International Soceity for Optical Engineering*, Vol. 6770, 2007.

[110] Fairbanks-Smith, M. S., "Use of Fibre-Optic (FBG) Sensors in the Structural Health Monitoring of a Battlefield Helicopter Rotor Blade," Bachelor thesis, University of Southern Queensland, 2014.

[111] Gryzagoridis, J., "Laser Based Nondestructive Inspection Techniques," *Journal of Nondestructive Evaluation*, Vol. 31, (4), December 2012, pp. 295–302.

[112] Fleming, G. A. and Gorton, S. A., "Measurement of Rotorcraft Blade Deformation Using Projection Moiré Interferometry," *Shock and Vibration*, Vol. 7, (3), January 2000, pp. 149–165.

[113] Fleming, G. A., Soto, H. L., and South, B. W., "Projection Moiré Interferometry for Rotorcraft Applications: Deformation Measurements of Active Twist Rotor Blades," American Helicopter Society 58th Annual Forum, June 11-13 2002.

[114] Sekula, M. K., "The Development and Hover Test Application of a Projection Moiré Interferometry Blade Displacement Measurement System," American Helicopter Society 68th Annual Forum, May 1-3 2012.

[115] Sirohi, J. and Lawson, M. S., "Measurement of Helicopter Rotor Blade Deformation using Digital Image Correlation," *Operational Engineering*, Vol. 51, (4), April 2012, pp. 043603.

[116] Sicard, J. and Sirohi, J., "Measurement of the Deformation of an Extremely Flexible Rotor Blade using Digital Image Correlation," *Measurement of Science and Technology*, Vol. 24, (6), May 2013, pp. 065203.

[117] Uehara, D. and Sirohi, J., "Full-Field Optical Deformation Measurement and Operational Modal Analysis of a Flexible Rotor Blade," *Mechanical Systems and Signal Processing*, Vol. 133, (1), November 2019, pp. 106265.

[118] Annett, M. S. and Littell, J. D., "Evaluation of the Second Transport Rotorcraft Crash Testbed (TRACT 2) Full Scale Crash Test," American Helicopter Society 71st Annual Forum, May 5-7 2015.

[119] Bauchau, O. A. and Craig, J. I., *Structural Analysis with Application to Aerospace Structures*, Springer, Dordrecht, Heidelberg, London, New-York, 2009.

[120] Bauchau, O. A., Callejo, A. I., Han, S. L., and Sonneville, V., *The Motion Formalism for Flexible Multibody Dynamics*.

[121] Acree, C. W., "Effects of V-22 Blade Modifications on Whirl Flutter and Loads," *Journal of the American Helicopter Society*, Vol. 50, (3), July 2005, pp. 269–278.

[122] Trefethen, L. N. and Bau, D., *Numerical Linear Algebra*, Society for Industrial and Applied Mathematics, Philadelphia, 1997.

[123] Ho, J. C., "Stiffness Constants of Homogeneous, Anisotropic, Prismatic Beams," *AIAA Journal*, Vol. 53, (2), February 2015, pp. 473–478.

[124] Ho, J. C., "Shear Stiffness of Homogeneous, Orthotropic, Prismatic Beams," *AIAA Journal*, Vol. 55, (12), December 2017, pp. 4357–4363.

[125] Bauchau, O. A. and Hodges, D. H., "Analysis of Nonlinear Multi-Body Systems with Elastic Couplings," *Multibody System Dynamics*, Vol. 3, (2), May 1999, pp. 163–188.

[126] Popescu, B. and Hodges, D. H., "On Asymptotically Correct Timoshenko-like Anisotropic Beam Theory," *International Journal of Solids and Structures*, Vol. 37, (3), January 2000, pp. 535–558.

[127] Jung, S. N., Nagaraj, V. T., and Chopra, I., "Refined Structural Model for Thin- and Thick-Walled Composited Rotor Blades," *International Journal of Solids and Structures*, Vol. 40, (1), January 2002, pp. 105–116.

[128] Coleman, H. W. and Steele, W. G., *Experimentation and Uncertainty Analysis for Engineers – 2nd Ed.*, John Wiley & Sons, New York, NY, 1999.

[129] Wichita State University, *Composite Materials Handbook, Volume 2: Materials Properties*, SAE International, Warrendale, Pennsylvania, 2012.

[130] Simonsen, M. and Adkins, I., *VIC-3D 8 Software Manual*, Correlated Solutions Inc., http://www.correlatedsolutions.com/supportcontent/VIC-3D-8-Manual.pdf, 2019.

[131] Simonsen, M. and Adkins, I., *VIC-3D 8 Testing Guide*, Correlated Solutions Inc., http://www.correlatedsolutions.com/supportcontent/Vic3D-8-Guide.pdf, 2018.

[132] Greenleaf, A. R., *Photographic Optics*, Macmillan Publishers, New York, 1950, pp. 24–28.

[133] Kodak, *Optical Formulas and Their Applications*, Kodak Publication No. AA-26, Eastman Kodak Company, New York, 1972.

[134] Datta, A., *Fundamental Understanding, Prediction and Validation of Rotor Vibratory Loads in Steady Level Flight*, Ph.D. thesis, University of Maryland, College Park, 2004.

[135] "Newport 321 Product Data Sheet," `https://www.rockwestcomposites.com/media/wysiwyg/Product_Categories/Materials_Tools/Newport_321_-_Resin_System.pdf`, 2006.

[136] "HexPly 8552 Product Data Sheet," `https://www.hexcel.com/user_area/content_media/raw/HexPly_8552_us_DataSheet.pdf`, 2016.

[137] Wang, X., *Wind Tunnel Test on Rotor Aeromechanics at High Advance Ratios*, Ph.D. thesis, University of Maryland, College Park, 2020.

[138] Tsai, F., Sutherland-Foggio, J., Datta, A., and Privett, D., "The Maryland Tiltrotor Rig (MTR): The Baseline Gimballed Hub," American Helicopter Society 75th Annual Forum, May 13-16 2019.